PHD

The processing of intermetallic matrix composites

Palmer, D. G. W.

Award date:
1997

Awarding institution:
University of Bath

THE PROCESSING OF INTERMETALLIC MATRIX COMPOSITES

Submitted by

D.G.W.Palmer

for the degree of PhD

of the University of Bath

1997

ProQuest LLC
789 East Eisenhower Parkway
P.O. Box 1346
Ann Arbor, MI 48106-1346

ABSTRACT

The production of intermetallic matrix composites by various processing routes was investigated. Initial attempts at producing aluminide matrices by solid-state diffusion, between transition metals and aluminium at 640°C, were unsuccessful. The diffusion process was time consuming and formed a porous microstructure. In addition, high aluminium content aluminides were formed, not the required XAl formula, where X was iron, nickel or titanium.

Reactive synthesis initiated a reaction between the reactants required to form the aluminide phase and used the energy released to sustain the reaction. The liquid-state reactions which occurred in reactive synthesis were found to rapidly produce the desired aluminide phases and to reduce porosity in the final materials, provided that the correct proportions of reactants were thoroughly mixed together.

The thermal explosion mode of reactive synthesis initiated reactions in powder compacts of the reactants. Thermal explosions were initiated by the exothermic formation of high aluminium content intermetallics, by solid-state diffusion, as the compacts were heated. The extent of reaction was found to be dependent on the rate of heat accumulation and the rate of heat loss from the reaction. The rate of heat accumulation was affected by the energy available for release, the proportion of liquid formed, the dimensions of the reactants, the green density of the compact, the rate of heat accumulation and the application of pressure. The rate of heat loss was affected by the surroundings and the application of pressure. The porosity in the final materials was reduced by forming a large proportion of liquid phase, using low density green compacts and by applying pressure during the reaction.

Alumina additions to the compacts remained inert to the reactants and diluted the reactions. This reduced the amount of liquid formed and increased the porosity of the final materials. Silicon carbide additions to the compacts interacted with the reactants during the thermal explosions to form a variety of phases and to increase the porosity of the final materials. A method using a thermal explosion and a liquid metal

infiltration was used to introduce continuous fibres into an intermetallic matrix. Using this, a fibre preform was infiltrated with a liquid formed by the initiation of a thermal explosion in a powder compact.

The reactive liquid metal infiltration route of aluminide formation was attempted by infiltrating a porous nickel and alumina preform with aluminium. However, the preform collapsed under the infiltration pressure and the rate of heat loss from the reaction was too great to support the reactive synthesis.

Acknowledgements

I would like to thank my supervisors, Prof.V.Scott and Mr.M.Phillips, for their guidance and support during my time as a PhD student. I would like to acknowledge the financial and material support of the DRA Farnborough under the direction of Dr.N.Lindsay, the School of Materials Science Bath, EPSRC and INCO London.

Further thanks go to the support and technical staff, Mr.M.Deven, Mr.S.Bowman, Mr.I.Trussler, Rev.B.Chapman, Mr.F.Hammond and Mr.C.Arnold for their expertise and help.

Finally, I would also like to thank my parents Guy and Monica Palmer and my brother Julian for their essential support throughout my life.

Contents

"It's better to regret something that you have done,
than to regret something that you haven't done"

Section 1

INTRODUCTION

1.1 General Features of Intermetallic Compounds

Intermetallic phases are currently under development as the next generation of high temperature structural materials. They occupy a position between present day superalloys and possible future engineering ceramics, Figure 1.1. The main driving force behind their development has come from the aerospace industry, where money is readily available for research and development into more efficient propulsion systems[1,2]. Greater efficiency may be achieved in turbine units by the use of lighter materials and by increasing the engine operating temperatures[3]. Materials able to operate at higher temperatures also require less cooling which brings additional weight savings[4].

The present nickel base superalloys and titanium alloys used in engines have reached their upper temperature limits[5] and whilst engineering ceramics are able to operate at

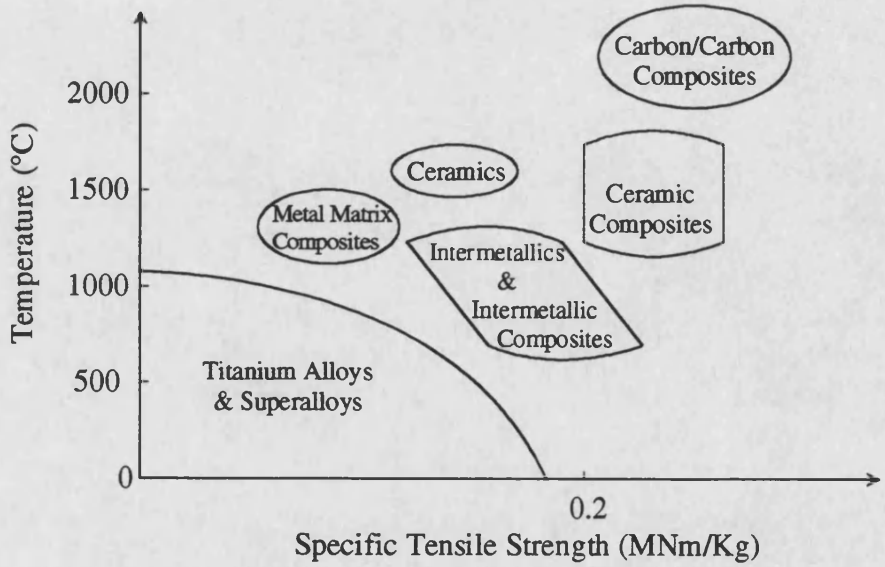

Figure 1.1 Performance map of high temperature engine materials (after Tanaka[6])

Material	M.Pt. (°C)	Density (Kg/m^3)	Specific TS (MNm/Kg)	Specific YS (MNm/Kg)	Specific E (GNm/Kg)	Duct. (%)	Creep limit (°C)	Oxidation limit (°C)
Ti alloys	1650	4500	0.187	0.170	0.022	20	600	600
Superalloys	1400	8300	0.116	0.061	0.023	3	1100	1100
Ceramics	>2500	6100	0.164	-	0.066	-	-	>2000
FeAl	1330	5600	0.075	0.061	0.046	2	-	-
Fe_3Al	1540	6700	0.052	0.031	0.021	4	-	-
NiAl	1638	5900	0.081	0.042	0.050	1	1100	>1000
Ni_3Al	1390	7500	0.031	0.028	0.024	2.5	-	-
TiAl	1460	3900	0.205	0.167	0.045	1	1000	900
Ti_3Al	1600	4200	0.190	0.236	0.035	2	900	650

Table1.1 Properties of selected materials[13,16,19-22]
TS - tensile stress, YS - yield stress, E - elastic modulus

higher temperatures, they suffer from very low ductility and fracture toughness. This low damage tolerance has prevented their use in engines in the near future and has left intermetallic compounds as the most promising next generation of high temperature structural materials. Table 1.1 compares the room temperature properties of some of these materials.

Possible applications for intermetallics are in the compressor and turbine areas of turbine engines[4,7], as heat protectors[8] and as elevated temperature structural materials[9,10].

Intermetallics are based on an integral ratio of metallic atoms of at least two species[2]. A superlattice is formed below a critical temperature, the critical ordering temperature, with each atomic species occupying a particular sublattice. A superlattice possesses long-range-order and an alloy phase is said to be ordered when two or more sublattices are required to describe its structure[11]. Dislocation mobility is reduced in a superlattice[12] and they exhibit good elevated-temperature strength and stiffness, but poor ambient temperature ductility and fracture toughness. The unit slip vector in body-centred cubic metals is $\frac{1}{2}\langle 111\rangle$ and in face-centred cubic metals is $\frac{1}{2}\langle 110\rangle$. In the ordered state these are not lattice translation vectors and moving dislocations leave behind a surface of disorder known as an anti-phase boundary and an increase in energy. Order may be restored by a second dislocation and dislocations therefore have

to travel in pairs, known as superdislocations, which restricts their movement. The number of slip systems available to most intermetallic systems at ambient temperatures are low, less than the five independent slip systems required for a ductile material. This results in the poor formability of intermetallics, which is a major hindrance to their utilisation[13].

Diffusion processes are also restricted in the superlattice as atoms have to occupy specific lattice points to maintain the ordered structure and consequently activation energies for diffusion are high[14,15]. The reduced diffusion rates are responsible for the good creep strengths of intermetallics at elevated temperatures.

Property	$FeAl_3$ (θ)	FeAl (β_2)	Fe_3Al (β_1)	$NiAl_3$ (ε)	Ni_2Al_3 (δ)	NiAl (β')	Ni_3Al (α')	$TiAl_3$ (β)	TiAl (γ)	Ti_3Al (α_2)
Melting Pt. (°C)	1150	1250	1500	854	1133	1638	1390	1340	1460	1600
Lattice Type	D_{2h} Mono-clinic	B2 Cubic	DO_3 Cubic	Ortho-rhom-bic	Hexa-gonal	B2 Cubic	$L1_2$ Cubic	DO_{22} Tetra-gonal	$L1_0$ Tetra-gonal	DO_{19} Hexa-gonal
ΔH_f (KJ/mol)	-56.2	-54.4	-18.0	-150.7	-282.6	-118.5	-150.7	-142.4	-74.0	-110.4
Density (Kg/m^3)	3800	5600	6700	4000	4700	5900	7500	3400	3900	4200
E (GPa)	-	260	141	-	-	186→ 294	178	215	160→ 176	100→ 145
TS (MPa)	-	420	350	-	-	330→ 480	230	-	450→ 800	800→ 1140
YS (MPa)	-	340	210	-	-	250	193	-	400→ 650	700→ 990
Ductility (%)	-	2	4	-	-	0→1	2.5	-	1	2
K_{IC} ($MPam^{½}$)	-	-	24	-	-	4→6	-	-	25	13→ 25
Oxidation Limit (°C)	-	-	-	-	-	>1000	-	-	900	650
Hydrogen Embrittlement	-	dislⁿ hinder	dislⁿ hinder	-	-	dislⁿ hinder	dislⁿ hinder	-	hydride forming	hydride forming
Creep Limit (°C)	-	-	-	-	-	1100	-	-	950	900

Table 1.2 Properties of aluminides[13,16-22]

1.2 Transition Metal Aluminides

Of all the intermetallic groups, the aluminides have received the most development attention. This is due to their low densities, coupled with good environmental resistance through the formation of protective alumina layers[23]. In turn, the majority of work carried out on intermetallics has taken place on the iron, nickel and titanium aluminide systems. Attempts have been made at improving high temperature strength, stiffness and creep resistance and ambient temperature fracture toughness and ductility through the addition of alloying elements and by producing multiphase microstructures[24]. Further work has concentrated on improving resistance to environmental attack at both ambient and elevated temperatures. Details of these investigations are summarised below.

Within the three aluminide systems detailed in this section, the majority of development work has concentrated on the XAl and X_3Al compounds (where X is either iron, nickel or titanium). Therefore, the brief reviews that follow will concentrate on these two compounds. Table 1.2 compares properties relevant to the high temperature use of intermetallics and to their use as structural materials. These are high temperature oxidation and creep resistance and strength, ductility and fracture toughness at ambient temperature.

1.2.1 Iron Aluminides

The phase diagram for the iron-aluminium binary system is shown in Figure 1.2. FeAl (β_2) has a B2 structure similar to a body-centred cubic lattice as shown in Figure 1.3. Fe_3Al (β_1) possesses three possible crystal structures. Below 550°C it has a $D0_3$ structure, whilst between 550°C and 1100°C a B2 structure exists and above 1100°C a solid solution based upon the body centred cubic (b.c.c.) lattice forms[25].

Both FeAl and Fe_3Al have low strength and creep resistance above 600°C[9]. The strength of FeAl is dependent on its exact stoichiometry. Increasing the aluminium content at low temperatures increases the yield strength, whilst at temperatures above 600°C the effect is reversed. Grain refinement of FeAl has been shown to increase yield strength[10]. Fe_3Al has a maximum yield strength at a composition of 75at%

(atomic percent) iron and 25at% aluminium, Fe-25at%Al, which decreased with increasing aluminium up to Fe-30at%Al[10].

A large amount of work has been carried out on the fracture of both FeAl and Fe_3Al. It was initially thought that these intermetallics were brittle since they both have low ductilities at ambient temperatures when tested in air, ~2% for FeAl and ~4% for Fe_3Al. But recent investigations have shown that they are in fact intrinsically ductile, but susceptible to extrinsic effects. The major cause for these low ductilities has been identified as hydrogen embrittlement. Water vapour in the air reacts with the aluminium to form atomic hydrogen which drives into the intermetallic and causes brittle crack propagation along cleavage planes and grain boundaries[10,26,27].

$$2Al + 3H_2O \rightarrow Al_2O_3 + 6H^+ + 6e^-$$

When tested in vacuum, FeAl had a ductility of 6% and when tested in dry air a ductility of 18%. It is thought that the greater ductility in dry air is due to rapid oxide

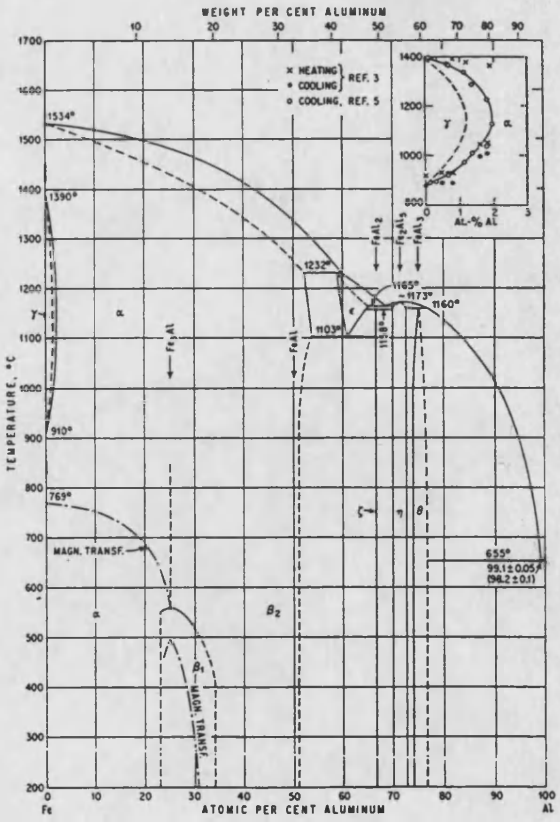

$\beta_2 = Fe_3Al$

$\beta_1 = FeAl$

$\xi = FeAl_2$

$\eta = Fe_2Al_5$

$\theta = FeAl_3$

Figure 1.2 Iron-Aluminium phase diagram[28]

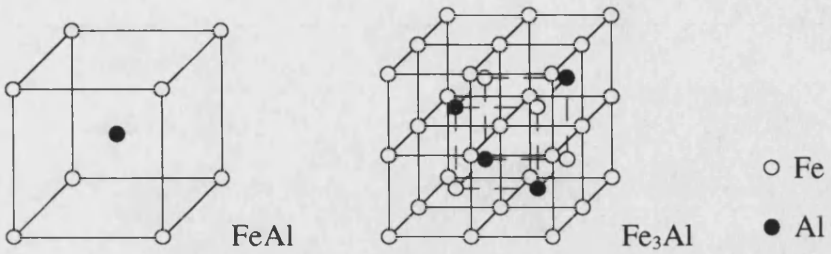

Figure 1.3 Structure of FeAl and Fe_3Al

formation on the intermetallic surface which suppresses the water vapour reaction[9]. At high temperatures FeAl appears to be insensitive to environment due to rapid oxide formation[9,26].

The iron aluminides have been alloyed with a wide variety of elements to increase strengths and ductilities and to reduce environmental attack, these are listed in Appendix B. Adding molybdenum, zirconium, niobium or boron to FeAl and Fe_3Al increases their elevated temperature strengths[9,10], whilst adding boron to FeAl (>38at%Al) increases ambient temperature ductility by segregating to and strengthening grain boundaries[9,26,29].

Additions of chromium to Fe_3Al reduce embrittlement by promoting the formation of a protective oxide film which prevents ingression of atomic hydrogen[5,9,10]. Chromium also reduces the yield strength and increases the fracture and cleavage strengths of Fe_3Al.

1.2.2 Nickel Aluminides

Figure 1.4 is the phase diagram of the nickel-aluminium system. NiAl (β') possesses a B2 structure based on the body-centred cubic lattice[9] and Ni_3Al (α') a $L1_2$ structure similar to a face-centred cubic structure[9], Figure 1.5b[33]. The nickel aluminides have received much attention because of their good oxidation resistances and high melting points[5,33,34]. NiAl has a higher melting point, lower density and a superior oxidation

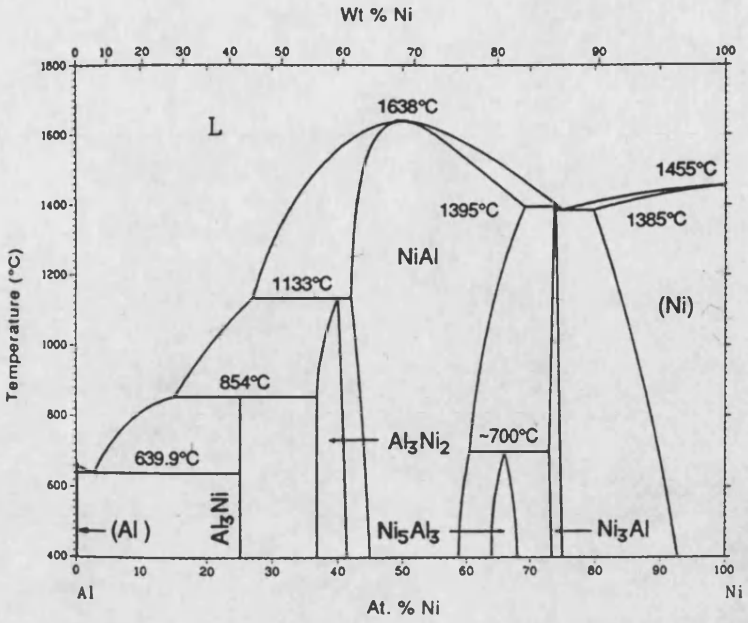

Figure 1.4 Nickel-Aluminium phase diagram[35]

than resistance Ni_3Al and it exists over a wider compositional range. However the ductility of Ni_3Al is readily increased by alloying it with boron.

The ambient temperature strengths of NiAl and Ni_3Al are both inferior to the iron aluminides and are low from an engineering viewpoint[5]. Even though Ni_3Al is the main strengthening component in superalloys, monolithic Ni_3Al is not strong enough to compete with them. However, it does possess a yield anomaly, its yield strength increases with increasing temperature up to a peak of 550MPa at temperatures around 700°C[9,35,36].

Many investigations have been made into the strengthening of nickel aluminides. Two-phase alloys are much stronger[30] as demonstrated by the addition of titanium which forms dual Ni/Ni_2AlTi phases[5,33]. Other elements added to strengthen NiAl include boron, carbon, gallium, iron, molybdenum and zirconium[2,33]. Whilst cobalt, hafnium, iron, molybdenum and zirconium increase the strength of Ni_3Al[9,33]. Increases in hardness and strength can also be achieved by off-stoichiometric compositions which introduce defects into the lattices[9,33], though ductilities are reduced.

Both NiAl and Ni_3Al suffer from poor ambient temperature ductility and fracture toughness. At ambient temperatures, polycrystalline NiAl is below the ductile/brittle transition temperature of approximately 277°C for a 50/50at% composition. As only

three slip systems are operative[30,33], it is brittle and fails by intergranular fracture[4,9,34]. Above this temperature, thermally activated deformation processes become operative. The brittle intergranular fracture can be reduced by enriching the grain boundaries with aluminium or boron which increase grain boundary cohesion[9,122]. Iron, gallium and molybdenum have also been found to increase the ductility of NiAl[9,33,37]. Finally, refining the microstructure has been found to have a beneficial effect on ductility above 400°C[30].

Although single crystal Ni_3Al is ductile[9,26], polycrystalline Ni_3Al fails by brittle intergranular fracture at both ambient and elevated temperatures[9,38]. This was initially thought to be solely due to weak grain boundaries[9,26,30], but recent tensile tests in vacuum and air have shown that environmental embrittlement is a contributory factor[9,30]. At ambient temperatures, Ni_3Al is affected by hydrogen embrittlement[26,27], as hydrogen from water vapour penetrates along grain boundaries causing intergranular fracture. Above 500°C, oxidation embrittlement occurs as oxygen is absorbed along grain boundaries ahead of crack tips and embrittles the surrounding material. Once the material is sufficiently embrittled the crack jumps forward and the process repeats[9,26,27].

Boron additions to Ni_3Al have been found to dramatically improve the ambient temperature ductility[4,23,39]. It has been reported that by adding 0.2at% boron to polycrystalline Ni_3Al, its ductility increases from 2.5% to 39.3% when tested in air[9]. It is known that the boron segregates to grain boundaries and changes the fracture mode from intergranular to transgranular. The boron appears to increase the cohesive strength of grain boundaries by occupying the interstitial sites that hydrogen would

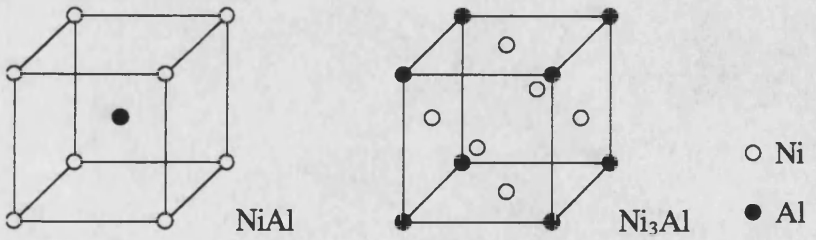

Figure 1.5 Structure of NiAl and Ni_3Al

occupy and thus blocking hydrogen diffusion along the grain boundaries[9,39,40]. This makes the Ni_3Al insensitive to environmental embrittlement at ambient temperatures. It has also been reported that beryllium improves ambient temperature ductility, but as it does not segregate to grain boundaries, the Ni_3Al is still susceptible to embrittlement[30]. Elevated temperature environmental embrittlement may be partially alleviated by alloying with 8at% chromium[9]. This promotes the formation of a self healing oxide film over crack tips which blocks oxygen diffusion along grain boundaries[26,27].

NiAl has excellent oxidation resistance and is used as a high temperature protective coating for other materials[33,41]. It forms protective oxide scales more readily at temperatures above 700°C[42-44], but suffers from the drawback of the scale cracking and spalling on cooling to room temperature[33]. This problem may be lessened by alloying with yttrium and zirconium which help bond the oxide scale to the substrate[9,33]. Cavities may also form below the alumina scale, but by using off stoichiometric, high aluminium content NiAl[43] and by alloying with chromium this may be overcome[33,44].

Ni_3Al has an inferior oxidation resistance. This trend is noticed in the majority of the aluminide systems with the higher aluminium content aluminides tending to form more highly protective oxide scales since more aluminium is available to form alumina. A mixed NiO, $NiAl_2O_4$ and Al_2O_3 scale forms over Ni_3Al which is not oxidation resistant. However, chromium does appear to improve oxidation resistance[38].

NiAl has lower creep resistance than FeAl, but several methods have been found to improve this property[24]. Off stoichiometric compositions possess higher creep resistances[24], whilst two-phase microstructures have also been found to improve creep resistance[5,33]. Alloying with hafnium and zirconium is also beneficial[9].

1.2.3 Titanium Aluminides

Low density and good mechanical properties combine to give the titanium aluminides very favourable specific properties. When the good retention of strengths, stiffnesses and creep resistances at high temperatures are also taken into account, this explains why a large amount of development work has been performed on the titanium-

aluminium system. But, as with the previous systems, the titanium aluminides suffer from poor ambient temperature ductilities and fracture toughnesses[45-47].

The phase diagram for the titanium-aluminium system is shown in Figure 1.6. TiAl (γ) possesses a $L1_0$ ordered face-centred tetragonal structure and Ti_3Al (α_2) possesses a hexagonal structure as shown in Figure 1.7.

For single-phase intermetallics, Ti_3Al has a higher melting point and greater strength and ambient temperature ductility than TiAl. But TiAl possesses a higher elastic modulus, greater high temperature creep and oxidation resistance and a lower density[3,48]. However, most work has been carried out on the two-phase alloys which allow greater scope for property variation.

In the case of TiAl, a two-phase TiAl/Ti_3Al alloy has undergone extensive investigation. By careful heat treatment, a variety of microstructures may be produced[4,49,50]. These range from a fully lamellar structure, through a duplex structure of lamellar and equiaxed grains, to a fully equiaxed structure, Figures 1.8a-b. The lamellar grains consist of alternate plates of TiAl and Ti_3Al whilst the equiaxed grains consist of TiAl only. By altering the material composition, the volume fraction of lamellae, the quantity of Ti_3Al present in the lamellae and the width of the lamellae, large variations in properties may be produced[51-53].

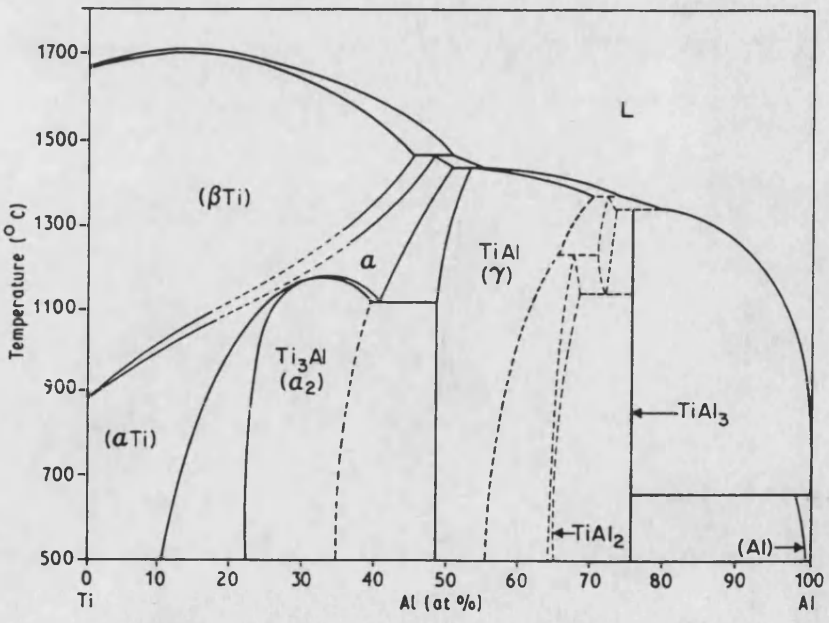

Figure 1.6 Titanium-aluminium phase diagram[3]

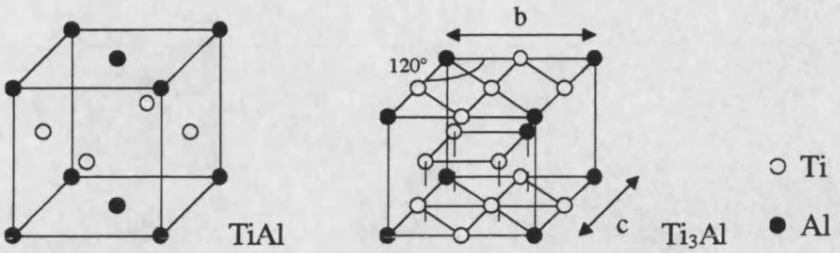

Figure 1.7 Structure of TiAl and Ti_3Al

Increasing the amount of lamellar phase has been shown to increase ambient temperature ductility and fracture toughness[5,8,39] and high temperature creep resistance[15,54,55]. But it also reduces strength and oxidation resistance[7]. An alloy consisting of Ti-48at%Al, with approximately 30vol% of lamellar phase has been shown to give the best combination of properties, with good high temperature creep resistance, acceptable tensile strength and usable ductility[3,8,15].

Further property improvements may be induced by the addition of alloying elements. Additions of chromium, manganese or vanadium have all been shown to increase the ambient temperature tensile ductility and fracture toughness of TiAl[30,39,48], though they also reduce the oxidation resistance[7]. Additions of niobium, manganese or tantalum promote strengthening[3], whilst increasing the aluminium content[7] or adding carbon or tungsten[3,15] increase creep resistance.

The Ti_3Al two-phase alloy consists of Ti_3Al and β phases[3] and have strengths nearly double those of monolithic Ti_3Al[7]. Additions of molybdenum, niobium, tantalum or vanadium are required to act as β phase stabilisers and have the effect of enhancing ambient temperature ductility and fracture toughness[3,27,47]. Strength is increased with additions of chromium, zirconium or the aforementioned β stabilisers and creep strengths are improved by molybdenum, silicon or zirconium[3,7]. Both the two-phase alloys are very susceptible to oxygen content which reduces ductilities[4,15,56].

The main limitation on the high temperature use of titanium aluminides is that of oxidation resistance[15]. TiAl has a limit of 900°C[4,8] and Ti_3Al has a limit of 650°C[57], which shows that lowering the aluminium content of the intermetallic reduces

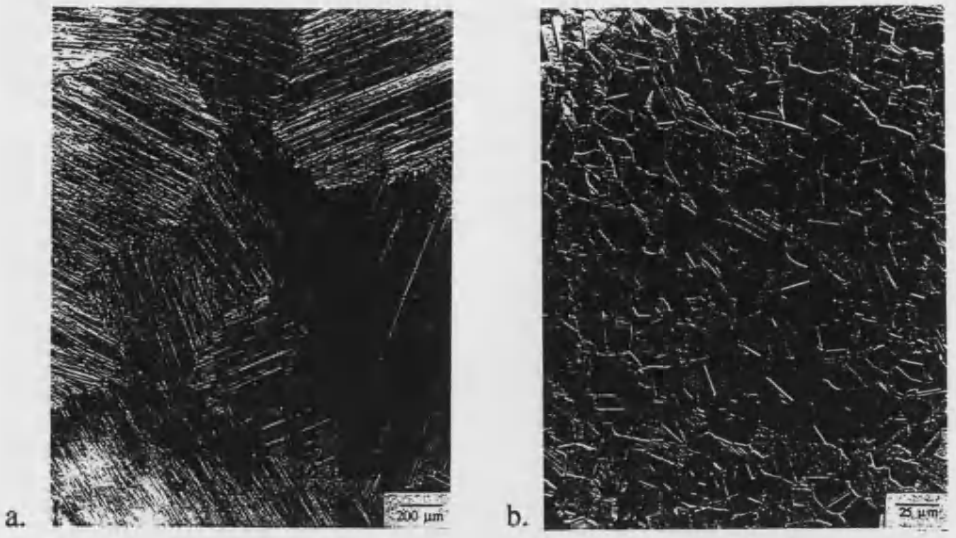

Figure 1.8 a. fully lamellar structure, b. duplex structure[4]

oxidation resistance[7]. Monolithic TiAl only forms a continuous alumina scale up to 900°C and above this temperature titania grows more rapidly[15,58,59] to form a mixed scale containing many voids and pores. This results in cracking and spallation of the oxide layer[3]. In the two-phase alloy, as the volume fraction of Ti_3Al phase increases, the oxidation resistance decreases[7,60]. By adding molybdenum, niobium, silicon, tantalum or tungsten to TiAl, the oxidation resistance is improved, but the ambient temperature tensile ductility is reduced[3,15,39].

Ti_3Al forms a mixed alumina/titania oxide layer which is prone to cracking and spallation[56], resulting in the low oxidation limit of 650°C. This may be improved by adding molybdenum, niobium, tantalum or tungsten[3,7,57].

The environment has a major effect on the ambient temperature tensile ductility of TiAl. It has been shown that TiAl has a higher ductility in vacuum than it does in air[30,39]. However, the largest ductilities have been achieved in pure oxygen[61] In air, water vapour reacts with TiAl to form oxides which embrittle the intermetallic[61], but in pure oxygen a protective oxide film forms and prevents any water vapour from reaching the TiAl.

Hydrogen embrittlement takes place in Ti_3Al by the formation of titanium hydride precipitates[3,7,62]. Exposure to hydrogen at elevated temperatures increases the yield strength but reduces ambient temperature ductility and fracture toughness[3,27,62].

1.3 Production Methods for Intermetallic Compounds

1.3.1 Casting

This is the most widely employed method of intermetallic production. The constituent elements are heated in a crucible to a temperature above the melting points of the elements and the intermetallic. The constituent elements rapidly form the intermetallic at this temperature, which is then cast into a mould[2].

1.3.2 Powder Metallurgy

Due to their poor low temperature ductilities and fracture toughnesses, intermetallics are not easily worked. An alternative method by which intermetallic components may be fabricated is to use powder metallurgy[2]. Compacts of intermetallic powders are heated and pressed, usually isostatically (HIP), into the shape of the component. However, high temperatures and pressures are needed to form a dense product since solid-state diffusion rates in intermetallics are slow.

1.3.3 Reactive Synthesis

The conventional production routes detailed above require the use of high temperature furnaces for long periods of time. The equipment required is usually complex and the process is time and energy intensive[63]. However, by initiating an exothermic reaction between the reactants and thus utilising their chemical energy, high temperatures can be attained within seconds without the need for high temperature furnaces[2,25,64]. This gives large savings in both time and energy and thus reduces costs[65,66].

These are not the only advantages that may be gained from using reactive synthesis. High purity products are usually formed, since volatile contaminants in the reactant materials are vapourised during the reaction[67,68]. Rapid cooling rates are also achieved as the surrounding apparatus has not experienced the combustion temperatures of the reactant materials. This leads to fine grain sizes which improve mechanical properties[25] and high defect concentrations which give a more reactive material which is more sinterable[67,68].

There are a few disadvantages of using the reactive synthesis route. The reactant materials are usually in powdered form, which is expensive to produce and is easily contaminated[69] due to the large surface area to volume ratio. Porosity is a major problem in all powder processing routes and reactive synthesis is no exception[69]. Highly porous materials are produced due to the voids present in the green compact, outgassing of gases trapped between the reactants and absorbed on their surfaces, volume changes in producing a product denser than its reactants[67,70,71] and solidification shrinkage[72]. These problems may be partially remedied by compacting and degassing the reactants[64,67], by forming a liquid phase during the reaction which provides solidification through capillary action between the powders[72] and through the application of pressure during or immediately after the reactive synthesis[25,69].

Self-Propagating High-Temperature Synthesis (SHS): The reactants are usually in the form of powder compacts. One region of the compact is heated until an exothermic reaction is initiated and energy is released. This energy heats the surrounding reactants to the initiation temperature whereupon a combustion wave is set up and propagates through the remaining reactants leaving product phases as it passes, Figure 1.9.

A large amount of work has been carried out on producing intermetallic compounds by SHS[73-75]. The velocity of the combustion wave, the manner in which it propagates through the compact and the final product phases are all dependent on several processing parameters. These are the system used[68], the dimensions of the reactants[76],

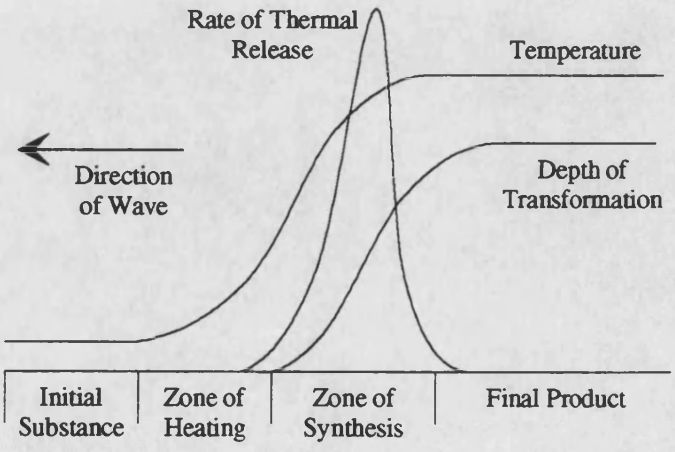

Figure 1.9 Schematic of SHS profile[73]

the green density of the compact[64], the rate of heating[77], the application of pressure[67], the addition of diluents[78] and the initial temperature of the compact[64].

Thermal Explosion: As in the SHS route, the reactants are usually in the form of a powder compact. The whole compact is heated until an exothermic reaction is initiated simultaneously throughout its bulk. This can be considered as a whole multitude of SHS reactions occurring simultaneously. After initiation, the energy released sustains the reaction, converting the reactants to product phases, and no further energy input is required. This method is commonly used for weakly exothermic systems since all the energy released is used to sustain the reaction and none is used to raise the reactants to the initiation temperature. The same processing parameters which affect SHS also affect the thermal explosion mode of reactive synthesis. The effect of the system used[79], the dimensions of the reactants[34], the green density of the compact[64], the rate of heating[70], the application of pressure[35] and the addition of diluents[80] have all been investigated.

Metal Foils: Reactive synthesis of metal foils has also been performed[12,81]. Instead of using powdered reactants, the compacts are comprised of alternate layers of metal foils. The whole compact is then heated to the initiation temperature, as in a thermal explosion mode of reactive synthesis. However, the reaction has not been successfully continued to completion and reactants have been found to be present in the final material. This has produced a composite metal-intermetallic structure[17,82], which is a novel material in its own right, but thinner metal foils may have to be used to produce a homogenous intermetallic.

Reactive Liquid Metal Infiltration: In liquid metal infiltration a porous preform is infiltrated by a liquid to form an intermetallic material[83,84]. The infiltrating liquid is a melt of the reactant with the lowest melting point and the preform consists of the remaining reactants required to form the final compound[85,86]. As the preform is infiltrated, a reactive synthesis reaction is initiated between the reactants and the heat released allows the reaction to continue to completion to form the final compounds. A positive gas pressure or mechanical pressure is applied to force the liquid into the preform. This pressure also serves to close any porosity generated by this process. Processing parameters such as preform temperature, melt temperature and application

of pressure[86] are all important in infiltrating the preform to form a homogeneous final material.

Apparatus: A variety of apparatus is used to produce reactive synthesis reactions. SHS reactions are usually initiated by means of a heating coil in contact with one end of the compact, whilst for thermal explosions the whole compact is heated uniformly in a furnace. To minimise possible reactions with the atmosphere, the syntheses are usually performed in vacuum or in an inert gas atmosphere.

If pressure is to be applied during the reaction, then a press has to be incorporated into the furnace. This obviously makes the apparatus more complicated and expensive when a vacuum or protective atmosphere is also required. Uniaxial presses are widely used, but recently, hot isostatic pressing (HIP) has been used to heat and pressurise thermal explosion reactions.

1.4 The Reactive Synthesis Method

1.4.1 Principles

This is a novel processing route for materials with large negative enthalpies of formation, including intermetallics, ceramics and cermets. Loose mixtures or compacts of the reactants are heated until an exothermic reaction is initiated. The heat released by the exotherm is then utilised to perpetuate the reaction, making it self-sustaining. A collective term for this type of processing is reactive or combustion synthesis. Reactive synthesis can be divided into several modes, detailed above, of which the two most widely used are self-propagating high-temperature synthesis (SHS) and thermal explosion.

As mentioned previously, in the SHS mode, the reaction is initiated by only heating one region of the compact to the initiation temperature. From this point a reaction wave front self-propagates throughout the remainder of the sample converting the reactants into product. With the thermal explosion mode, also known as reactive sintering, the whole sample is raised to the initiation temperature, whereupon the synthesis reaction occurs simultaneously throughout the bulk. This has been found to be a more suitable route for the production of less exothermic materials[70] such as the

intermetallics. The thermal explosion route does not use energy released during the reaction to heat the reactants to the initiation temperature, and the low initiation temperatures of most intermetallic systems means that the whole compact is easily heated to initiation in a furnace. By using identical compacts, both these two modes have been found to produce identical products[77], though adjustments to processing parameters were made.

An alternative to initiating a reactive synthesis by heating a powder compact of the reactants is to subject it to a compressive shock[87]. This is known as shock-induced reactive synthesis (SRS) and uses the simultaneous application of high pressure and temperature generated during the passage of shock waves through a powder mixture. This process has not received much attention to date and is beyond the scope of this review.

The reactants involved in reactive synthesis may themselves be either elements or compounds and initially be in either a solid or gaseous state[78].

1.4.2 The Process

Several papers have been published detailing the SHS and thermal explosion modes of reactive synthesis of binary aluminides. The majority of work has concentrated on the three systems involved in this project, the iron, nickel and titanium aluminides[70,88,89]. A general consensus on the steps involved in reactive synthesis has been reached[2,90], Figure 1.10.

i) The compact is heated until a transient, aluminium rich, liquid phase is formed. This may be either at the melting point of aluminium or at a composition with a lower melting point, depending on the system and the rate of heating.

ii) This liquid phase quickly surrounds the remaining reactants and starts to rapidly dissolve the transition metal.

iii) Once the liquid phase becomes saturated with the transition metal, one of the higher aluminium content intermetallics starts to precipitate out. This is an exothermic process which generates heat and sustains the reaction.

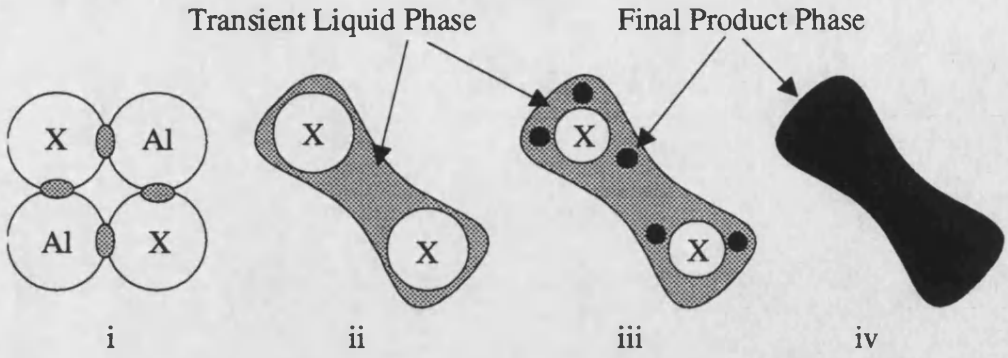

Figure 1.10 Steps of reactive synthesis

iv) Depending on the system and the stoichiometric composition of the compact, several intermedate phases may be formed, through either liquid-state or solid-state reactions, before the final product phase is reached.

This is a simplified overview of the process as the following reaction route for Ni_3Al shows. This has been constructed from various references since Ni_3Al is a well investigated system and has been formed by both SHS and thermal explosion modes of reactive synthesis[74,23,64].

By heating a compact comprised of aluminium (25at%) and nickel (75at%) powders, two solid-state reactions occur prior to initiation.

$$3Al + Ni \rightarrow NiAl_3$$

$$NiAl_3 + Ni \rightarrow Ni_2Al_3$$

These reactions are exothermic, Table 1.2, and the heat released raises the temperature of the compact and helps in the formation of an aluminium rich liquid phase between the nickel particles, thus triggering the reactive synthesis. The liquid phase spreads around the nickel particles and starts to dissolve their outer surfaces, which raises the nickel content of the liquid. Once the liquid phase becomes saturated with nickel and providing the temperature is below 854°C, then the liquid + $NiAl_3$ region of the phase diagram is entered and $NiAl_3$ starts to precipitate out, Figure 1.4. This is another exothermic reaction which further increases the temperature of the compact:

$$liquid + Ni \rightarrow NiAl_3$$

However, the temperature of the compact rapidly exceeds the melting point of $NiAl_3$ and it decomposes into a liquid phase and Ni_2Al_3:

$$NiAl_3 \rightarrow \text{liquid} + Ni_2Al_3$$

This reaction is endothermic, but this has a negligible effect on the temperature of the reacting compact as the proportion of $NiAl_3$ that forms during the rapid temperature rise is small. The liquid rapidly dissolves more nickel and precipitates out Ni_2Al_3, releasing more energy:

$$\text{liquid} + Ni \rightarrow Ni_2Al_3$$

Before all the liquid is converted to Ni_2Al_3, the peritectic temperature is exceeded, and the Ni_2Al_3 decomposes to liquid + NiAl:

$$Ni_2Al_3 \rightarrow \text{liquid} + NiAl$$

Further nickel is dissolved by this liquid phase and NiAl and Ni_3Al are precipitated directly from the liquid:

$$\text{liquid} + Ni \rightarrow NiAl + Ni_3Al$$

If the melting point of NiAl (1638°C) is not exceeded by the combustion temperature, the maximum temperature attained by the reaction, then the NiAl remains in the solid-state once it is formed. Combustion temperatures of 1329°C[35] and 1390°C[23,74] have been reported. Nickel diffuses into nickel rich phases faster than aluminium at temperatures greater than 1000°C[23] and the NiAl phases become saturated with nickel and precipitate out Ni_3Al. The remaining nickel cores, at the centres of the original nickel particles, also become enriched with aluminium until they become saturated, whereupon Ni_3Al is precipitated out. Growth of the Ni_3Al grains by diffusion then produces the final microstructure:

$$NiAl + 2Ni \rightarrow Ni_3Al$$

This final stage will only continue to completion if the compact is maintained at a high temperature for a sufficient time.

However, minor variations to the processing parameters may alter the reaction path taken and the final compounds produced.

1.4.3 Processing Parameters

It will be shown that a high combustion temperature is necessary during reactive synthesis for a high extent of reaction and to form a dense product. The extent of reaction is a measure of the conversion of reactants to the final phases predicted by the relevant phase diagram. Many papers have been published detailing the effects of processing parameters on the combustion temperature. These parameters include, the reaction mode, the ratio of reactants, the dimensions of the reactants, the green density of the compact, the rate of heating of the reactants, the pressure applied during reactive synthesis, the quantity of diluents, the compact thickness and the initial temperature of the reactants.

Reaction Mode: Several authors have investigated the formation of aluminides by both the SHS and thermal explosion modes of reactive synthesis. They report that by carefully adjusting the processing parameters mentioned above, the same product phases may be formed[68,77,78].

Ratio of Reactants: The atomic ratio governs the amount of energy available for release and is critical to the extent of reaction and the final density of the material. For the aluminide systems studied in this investigation, a high aluminium content in the green compact will form a large volume fraction of aluminium rich liquid phase during the reaction[89]. This liquid spreads to all the transition metal surfaces and results in a large area of reaction and a rapid release of energy. With a rapid release of energy, little is lost to the surroundings and a large proportion is used to heat the compact to a high combustion temperature[91]. This promotes faster diffusion, converting more reactants to products and leads to a higher extent of reaction in a shorter time.

Several authors have stated that there is an optimum amount of liquid phase required to form the most dense reacted compact[71,92,93]. Too little liquid and there is insufficient available to provide densification through capillary action. Too much liquid phase and the compact swells as it tries to accommodate the increased volume[70,92,93]. This results in increased porosity since any densification by capillary action is insufficient to compensate for the swelling. If pressure is applied during the reactive synthesis of a high aluminium content compact, then the liquid phase may be squeezed out from its centre, altering the local composition[69].

Reactant Dimensions: All the authors investigating reactant dimensions mention the need for a continuous aluminium network when producing aluminides[71,77,94]. This eases the spread of the aluminium rich liquid phase through the compact to increase the area of reaction. An interrupted network prevents the liquid phase reaching all the transition metal surfaces, lowering the combustion temperature. In order to form a connected network the aluminium particles have to be able to pack around the transition metal particles. An optimum ratio of 3.0 has been proposed[64,94] for the transition metal particle diameter to aluminium particle diameter.

Increasing the transition metal surface area by altering its morphology or reducing its size also increases the possible contact area with the liquid, increasing the extent of reaction[64,77].

Green Density: The green density has an impact on the final porosity in two ways. Reducing the porosity of the green compact will lead to a denser product by a reduction of volume[93]. Also, it is necessary that the liquid formed spreads easily and rapidly through the compact to form a large area of reaction. Any hindrance to the spread of the liquid results in a reduction in the combustion temperature which affects the extent of reaction and the final density[64,94]. Since the spread of liquid is aided by capillary action, a high green compact density is necessary to provide narrow channels between the transition metal powders and to reduce voids which hinder capillary action.

Rate of Heating: Authors investigating the reactive synthesis of nickel and titanium aluminides have demonstrated that a slower heating rate reduces the combustion temperature[77,93]. Slower heating rates allow more solid-state diffusion to occur before the reaction is initiated and this forms greater quantities of high aluminium content intermetallics. The formation of product phases is less rapid when these intermetallics are present since diffusion is slower through these intermetallics and they reduce the quantity of aluminium rich liquid phase formed, which results in a smaller area of reaction. Consequently, the rate of energy release is reduced and densification through capillary action is affected.

The authors investigating the formation of nickel aluminides[77] found no change in the reaction products when altering the heating rate, unlike those investigating titanium

aluminides[77,93]. If a significant amount of $TiAl_3$ is formed by solid-state diffusion during slow rates of heating, then some remains in the final material. The melting point of $TiAl_3$ is above the combustion temperature of the reaction and it can only be transformed into other titanium aluminides through diffusion which is a slow process in the titanium-aluminium system[93]. However, the $NiAl_3$ and Ni_2Al_3 intermetallics have melting points well below the combustion temperature and they are readily melted and incorportaed into the liquid phase, which eradicates any evidence of their formation during heating.

The initiation temperatures of the thermal explosions also vary with heating rate. The initiation temperature in the nickel-aluminium system decreases as the heating rate decreases[77], but remained constant in the titanium-aluminium system[70]. In the nickel-aluminium system, solid-state diffusion to form high aluminium content intermetallics is relatively rapid and a slow heating rate allows a substantial amount to form. If energy is released fast enough to raise the local temperature at a point in the compact to a temperature at which a liquid phase is formed, then the reaction will be initiated at a lower compact temperature. In the titanium-aluminium system, solid-state diffusion is slow and the energy is not released rapidly enough to produce a significant change in the initiation temperature over the same range of heating rates.

Finally, the effect that the heating rate has on SHS reactions will be mentioned. Since the exothermic reaction is only initiated at one point, heat is conducted away from the ignition point during heating. A slow heating rate allows the surrounding compact to be heated to a higher temperature, and this raises the initial temperature of the reactants. The effects of which are detailed in a subsequent section.

Pressure: Another method used to reduce the final porosity of the product is the application of pressure to the compact during or immediately after reactive synthesis. This is known as reactive hot pressing (RHP) when heat and a uniaxial pressure are applied and reactive hot isostatic pressing (RHIP) when heat and an isostatic pressure are applied. It has been reported that the final density of reactively formed Fe_3Al is increased from 54% to 98% of the theoretical maximum by applying a pressure of 120MPa through a RHIP process[71].

However, care has to be taken to avoid the build up of absorbed gases which are released as the compact is heated. These gases originate from the decomposition of hydroxides on the surface of the powders[70] and if they are not properly vented, their build-up may breach the die. One investigation into the formation of TiC, which used a die which was sealed when pressure was applied[73], was forced to apply the pressure one to two seconds after the reactive synthesis was initiated to allow the gases time to escape. A product with a density of 95% of theoretical was formed, whereas the same reaction performed without the application of pressure only formed a product with a final density of 50% of theoretical[67]. Alternatively, the reactants may be degassed before the reactive synthesis, to reduce the amount of gas evolution, or an open die arrangement, which lets the gases escape, may be used. The open die allows pressure to be applied prior to the initiation of the reactive synthesis and using this method a Ni-25at%Al compact, pressurised to 50MPa, formed a Ni_3Al product with a density of 99.3% of the theoretical value[35]. As mentioned in the previous section on the ratio of reactants, care has to be taken with this last arrangement since liquid from the centre of the compact may be squeezed out by the application of pressure.

Another effect of applying pressure to the reacting compact is to increase heat loss from the reaction to the surroundings. The applied pressure closes pores and voids in the reacting compact and increases its thermal conductivity. In some cases, where high pressure is applied to a small compact, the reactive synthesis is quenched since too much heat is lost from the reaction[35].

Diluents: Diluents are added to control the reaction and these are usually in the form of the final product phases so that a homogeneous microstructure is formed. However, any phases that remain inert during the reactive synthesis may be classed as diluents. This includes reinforcements which may act as undesired diluents, as described in subsequent sections.

The introduction of diluents to the green compact has three effects. First, it reduces the proportion of energy releasing reactants in the green compact. Second, it acts as a heat sink absorbing some of the heat generated from the exothermic reactions[78,94]. Third, it disrupts the flow of the liquid phase through the compact, reducing the area

of reaction[94]. All these reduce the amount of liquid phase formed and lower the combustion temperature.

To control a reactive synthesis, diluents may be added to keep the combustion temperatures below the disassociation temperature of the required product or to reduce the amount of liquid phase formed during the reactive synthesis to retain the shape of the green compact. If diluents in the form of reinforcements are added, then the undesired diluting effect may lead to a lower extent of reaction and lower final density.

Compact Thickness: The outer regions of reactively synthesised compacts often undergo a lower extent of reaction than the inner regions[69]. The energy released by the exothermic reaction in the outer regions is rapidly lost to the cooler surroundings and this lowers the combustion temperature and the extent of reaction. In some cases the heat loss is so great that the reaction is effectively quenched without further input of energy from an external source.

The closer a region is to the edge of the compact, the faster the heat is lost to the surroundings. This was demonstrated through the thermal explosion of nickel-aluminium compacts of varying thicknesses[69]. The extent of reaction was lowest at the surfaces of the compacts in contact with the apparatus and increased towards their centres, but some of the compacts were too thin to possess a fully reacted central region.

Initial Reactant Temperature: This variable only applies to the SHS mode of reactive synthesis. In the thermal explosion mode the whole compact is heated uniformly so the initial temperature of the reactants is effectively the initiation temperature of the reaction.

In SHS the reaction is ignited by heating one part of the compact to the initiation temperature. The combustion wave propagates outwards from this point by the exothermic reaction raising the temperature of the reactants ahead of the wave to the initiation temperature. The closer these reactants are to the initiation temperature, the less energy is used in heating them and therefore more energy remains to increase the

combustion temperature of the reaction[64,74,78]. The combustion temperature and volume of liquid phase affect the rate at which the combustion wave propagates[64].

Summary of Processing Parameters: All the processing parameters detailed above; reaction mode, ratio of reactants, reactants dimensions, green density, rate of heating, pressure, diluents, compact thickness and initial temperature, ultimately affect the phases formed and the final density. For a reaction to continue to completion, the combustion temperature must achieve a sufficiently high level for a long enough time to allow all the reactants to fully react and produce a homogenous structure. This depends on the rate of heat accumulation and the rate of heat loss.

The rate of heat accumulation is related to the rate of energy release. A rapid rate of energy release, brought about by the formation of highly exothermic phases and a large area of reaction, results in little energy loss to the surroundings and a greater proportion available to heat the compact. The ratio of reactants, their dimensions, the rate of heating and the spread of the liquid phase all affect the area of reaction for a specific system.

The rate of heat loss is dependent on the surroundings of the reaction, the dimensions and thermal conductivity of the compact, the presence of diluents and whether pressure is applied. A rapid rate of heat loss will result in the reaction being quenched before completion.

A high final density is dependent on the spread of an optimum amount of a liquid phase through the reacting compact. This liquid phase refers to both transient liquid phases and molten product phases. If no liquid phase was formed, then only solid-state diffusion would occur during the reaction and this would have no densifying effect on the compact. A large amount of liquid phase and the compact swells to accommodate it, increasing poroisty.

The quantity of transient liquid phase formed by a specific system is dependent on the ratio of reactants and the rate of heating, whilst the quantity of molten product is dependent on the combustion temperature and thus the rate of heat accumulation. The spread of the liquid phases is affected by the reactant dimensions, the green density and the presence of diluents. Other factors affecting density are initial porosity of the compact, outgassing of absorbed gases which would otherwise become trapped within

the material, differences in molar volume between reactants and products, the Kirkendall effect and the application of pressure.

1.4.4 Thermodynamic Modelling

A significant amount of effort has been put into the thermodynamic modelling of reactive syntheses. Values for the maximum temperature reached and the fraction of molten product formed have been calculated for both SHS and thermal explosions[95-98]. The following explanation gives a brief description of the thermodynamic formulae used to calculate these values. A few simplifying assumptions have to be made.

i) The reactions are carried out under adiabatic conditions so that there is no heat loss from the system. Therefore, the values calculated are usually higher than those obtained by experimental means and thus describe an upper limit.

ii) The final product phases are produced directly from the reactants. The inclusion of intermediate phases into the calculations requires knowledge of the exact route taken by the reactive synthesis, including the molar fractions of each phase present over a range of temperatures. Combined with the need for a large amount of thermodynamic data on each phase, which is not readily available, this would take the calculations beyond the scope of this report.

iii) All the product is formed simultaneously at the same temperature, above which no reactants remain. This implies that each atom of a reactant species is simultaneously in contact with a sufficient number of atoms of every other reactant species required to form the final phases. This is impossible to produce with particulate reactants. In reality, the atoms at the centre of particles can only react after those at the outer surface and therefore, they form product phases over a temperature range. In the calculations below, the two extreme cases, of the product being formed at the initiation temperature of the reactive synthesis[68,78,99] and the product being formed at its melting point[72,86], are taken. The actual values will therefore lie between these two bounding cases.

Consider a simple reaction of

$$A + B \rightarrow AB$$

and assume that the product is formed at the initiation temperature of the reactive synthesis, T_i. As adiabatic conditions apply then the enthalpy of the reactants at T_i must be equal to the enthalpy of the products at T_{ad}. If the reaction is initiated under standard conditions, then $T_i = 298K$, and this is illustrated in Figure 1.11.

This figure shows the enthalpy-temperature relationships for the reactant (A+B) and product (AB) phases. At 298K the reactants have an enthalpy of $H(R)_{298}$ and the products an enthalpy of $H(P)_{298}$ and the energy released by the formation of the product phase, Q_{298} is:

$$Q_{298} = H(P)_{298} - H(R)_{298} \tag{1}$$

Q_{298} is the negative of the standard enthalpy of formation of AB, $\Delta H_{f,298}$, and T_{ad} may be easily calculated from:

$$-\Delta H_{f,298} = \int_{298}^{Tad} C_p(P)dT \tag{2}$$

were $C_p(P)$ is the heat capacity of the product AB.

In practice, reactive syntheses are rarely initiated at 298K, but at elevated temperatures.

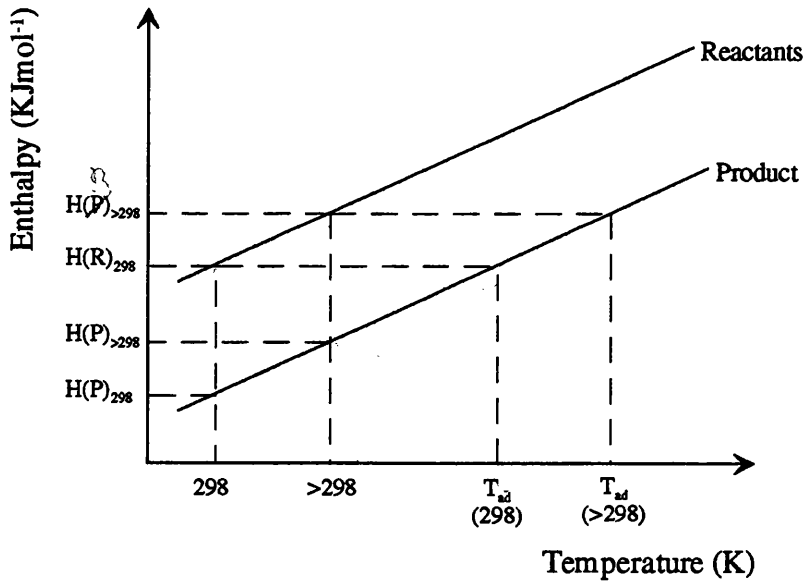

Figure 1.11 Enthalpy vs temperature plot[100]

Figure 1.11 shows the effect of raising the reactants to an initiation temperature, T_i > 298K, by means of an external heat source. The reactants now possess an enthalpy of $H(R)_i$ and for energy to be conserved, the products are raised to a higher value of T_{ad}. For an initiation temperature of T_i , the enthalpy of formation, $\Delta H_{f,Ti}$, is calculated using Kirchoff's equations[101]:

$$\Delta H_{f,Ti} = \Delta H_{f,298} + \int_{298}^{Ti} \Delta C_p(PR)dT \tag{3}$$

Where $\Delta C_p(PR) = C_p(P) - C_p(R)$. $C_p(R)$ is the sum of the heat capacities of the reactants A and B. Even though it is not used here, some authors[63,67,78] simplify the calculations by applying the Neumann-Kopp rule of $\Delta C_p(PR) = 0$ and thus $\Delta H_{f,Ti} = \Delta H_{f,298}$.

The adiabatic temperature is calculated from:

$$-\Delta H_{f,Ti} = \int_{Ti}^{Tad} C_p(P)dT \tag{4}$$

All the above equations assume that no phase transformations occur within the reactants or products. To allow for solid/solid and solid/liquid phase transformations, at temperatures T_{ss} and T_m respectively, the following terms have to be included in equations (3) and (4).

Equation (3) becomes:

$$\Delta H_{f,Ti} = \Delta H_{f,298} + \int_{298}^{Ti} \Delta C_p dT + \Delta \sum_{298 \rightarrow Ti} L(PR)_{ss} + \Delta \sum_{298 \rightarrow Ti} L(PR)_m \tag{5}$$

Where $\Delta \sum_{298 \rightarrow Ti} L(PR)_{ss}$ is the difference in the sums of the enthalpies of solid/solid transformations and $\Delta \sum_{298 \rightarrow Ti} L(PR)_m$ is the difference in the sums of the enthalpies of melting of the products and reactants between 298K and T_i.

Equation (4) becomes:

$$-\Delta H_{f,Ti} = \int_{Ti}^{Tad} C_p(P)dT + \sum_{Ti \to Tad} L(P)_{ss} + \nu L(P)_m \tag{6}$$

$\sum_{Ti \to Tad} L(P)_{ss}$ is the sum of the enthalpies of solid/solid transformations in the product between T_i and T_{ad}. $L(P)_m$ is the enthalpy of melting of the product phase and ν is the molar fraction of molten product formed during the reactive synthesis.

$\nu = 0$ when $T_{ad} < T_m$

$0 < \nu < 1$ when $T_{ad} = T_m$

$\nu = 1$ when $T_{ad} > T_m$,

where T_m is the melting point of AB. It is tempting to use ν as the molar fraction of liquid phase formed during the reaction, but this assumes that all the liquid phase formed has the composition of product AB and does not take into account the intermediate liquid phases formed during the reactive synthesis.

The heat capacities of the materials also vary with each transformation and the integrals in equations (5) and (6) may have to be split into several temperature ranges.

If the reactants are initially at a temperature T_s where $T_s < T_i$, the reactants have to be raised to the initiation temperature using the energy released by the reactive synthesis. This occurs in SHS reactions where a combustion wave travels through a mixture of reactants. Equation (6) is modified as follows:

$$-\Delta H_{f,Ti} = \int_{Ti}^{Tad} C_p(P)dT + \sum_{Ti \to Tad} L(P)_{ss} + \nu L(P)_{sl} + \int_{Ts}^{Ti} C_p(R)dT + \sum_{Ts \to Ti} L(R)_{ss} + \sum_{Ts \to Ti} L(R)_m \tag{7}$$

If we now consider the other bounding condition that the product is formed at its melting point. The reactants first have to be raised to T_m and equation (7) is modified to give:

$$-\Delta H_{f,Tm} = \int_{Tm}^{Tad} C_p(P)dT + \nu L(P)_{sl} + \int_{Ts}^{Tm} C_p(R)dT + \sum_{Ts \to Tm} L(R)_{ss} + \sum_{Ts \to Tm} L(R)_m \tag{8}$$

No solid/solid transformations can occur in the product since it is formed at its melting point. Using these two equations, the adiabatic temperature and the molar fraction of liquid product produced during the reaction may be calculated for the two bounding conditions. Graphs of initial reactant temperature against adiabatic temperature and initial reactant temperature against molar fraction of liquid product were calculated in Appendix C for the formation of NiAl and TiAl by the thermal explosion mode of reactive synthesis. Unfortunately there were insufficient data available to produce the corresponding graphs for FeAl.

Figure 1.12 compares the calculated adiabatic temperatures for the product formed at the initiation temperature of the thermal explosion (plot A) and at its melting point (plot B). The graph only covers an initial reactant temperature range of room temperature to the lowest temperature at which a liquid phase may form, nickel-aluminium (639.9°C) and titanium-aluminium (660.1°C), since the thermal explosions are initiated at these temperatures. A full explanation of the calculations is given in Appendix C.

Both calculation methods indicate that the reaction is sufficiently exothermic to raise NiAl to its melting point. As T_{ad} does not increase over the range of T_i, the extra energy made available by the higher reactant temperatures is used to melt the product. All the product must become molten before there is any further temperature increase. This does occur at the highest reactant temperature on the line calculated for the formation of the product at the initiation temperature.

The horizontal plots for TiAl also predict that the product is raised to its melting point and that an increasing fraction becomes molten over the initial reactant temperature range. The plot calculated from the formation of the product at its melting point only reaches the melting point at an initial reactant temperature of 275°C. Below this temperature, insufficient energy is released to raise the reactants to the melting point of TiAl and the reaction is not self-sustaining.

The plots of molar fraction of liquid product formed are displayed in Figure 1.13. This graph again contains plots of both calculation methods. A much larger molar fraction of the NiAl is molten in comparison with the TiAl for the same initial reactant temperatures. Both calculation methods produce an almost identical plot for NiAl, but

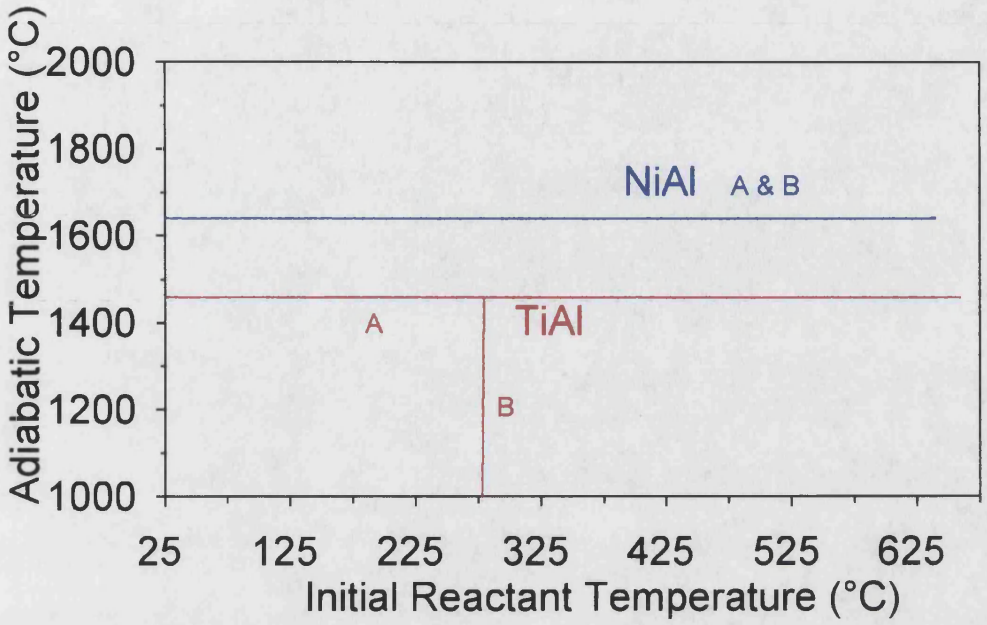

Figure 1.12 Effect of initial reactant temperature on adiabatic temperature

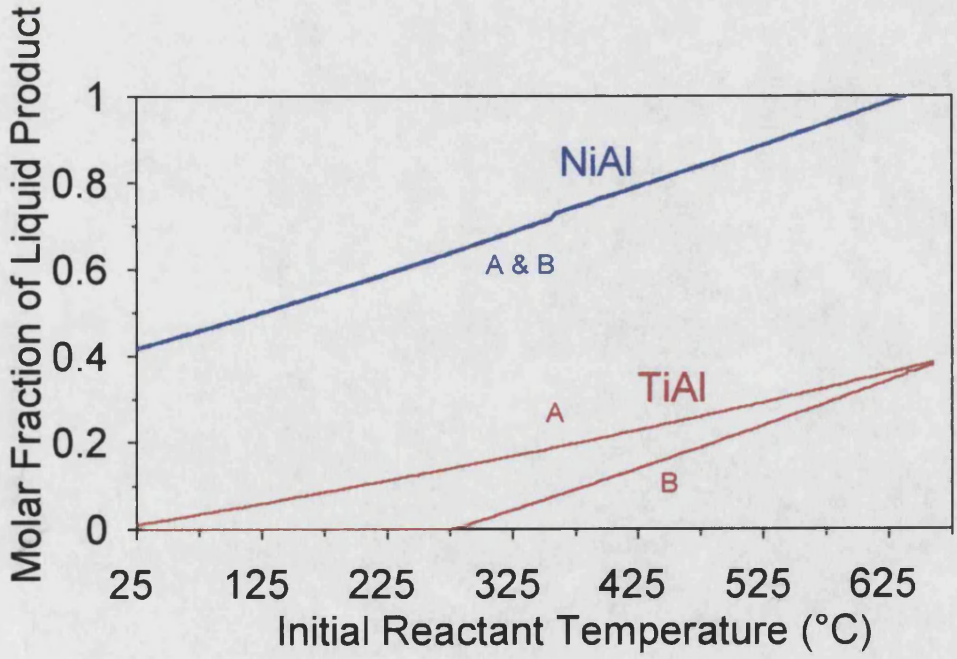

Figure 1.13 Effect of initial reactant temperature on the molar fraction of liquid product formed

varying plots for TiAl. Although the formation of the product at the initiation temperature (plot A) initially produces a larger molar fraction of molten product, this increases at a slower rate than the molar volume of the product formed at its melting point (plot B).

The above equations may be modified to allow for the presence of diluents (D) or reinforcements if it is assumed that they remain solid and completely inert throughout the reaction. If x is the molar fraction of diluent added to the reactants, then for the formation of the product at the initiation temperature, equation (7) becomes:

$$-\Delta H_{f,Ti} = (1-x)\left[\int_{Ti}^{Tad} C_p(P)dT + \sum_{Ti\rightarrow Tad} L(P)_{ss} + vL(P)_{sl} + \int_{Ts}^{Ti} C_p(R)dT + \sum_{Ts\rightarrow Ti} L(R)_{ss} + \sum_{Ts\rightarrow Ti} L(R)_{sl}\right] + x\left[\int_{Ts}^{Tad} C_p(D)dT + \sum_{Ts\rightarrow Tad} L(D)_{ss}\right] \quad (9)$$

$C_p(D)$ is the specific heat capacity of the diluent and $\sum_{Ts\rightarrow Tad} L(D)_{ss}$ is the sum of the enthalpies of solid/solid transformations of the diluent.

For the formation of the product at its melting point, equation (8) becomes:

$$-\Delta H_{f,Tm} = (1-x)\left[\int_{Tm}^{Tad} C_p(P)dT + vL(P)_{sl} + \int_{Ts}^{Tm} C_p(R)dT + \sum_{Ts\rightarrow Tm} L(R)_{ss} + \sum_{Ts\rightarrow Tm} L(R)_{sl}\right] + x\left[\int_{Ts}^{Tad} C_p(D)dT + \sum_{Ts\rightarrow Tad} L(D)_{ss}\right] \quad (10)$$

Figures 1.14a-b detail the changes in adiabatic temperature with additions of 5 and 10wt% alumina to the reactive syntheses. These quantities reflect those commonly used in industry[102] and it is assumed that the alumina remains inert during the reactive synthesis.

Both calculation methods show that the addition of 5 and 10wt% alumina to the formation of NiAl have no effect on the adiabatic temperature for the range of initial reactant temperatures covered, Figures 14a-b. However, the addition of alumina to the formation of TiAl does reduce the adiabatic temperature. With the addition of 10wt% alumina to the formation of the product at the initiation temperature, the

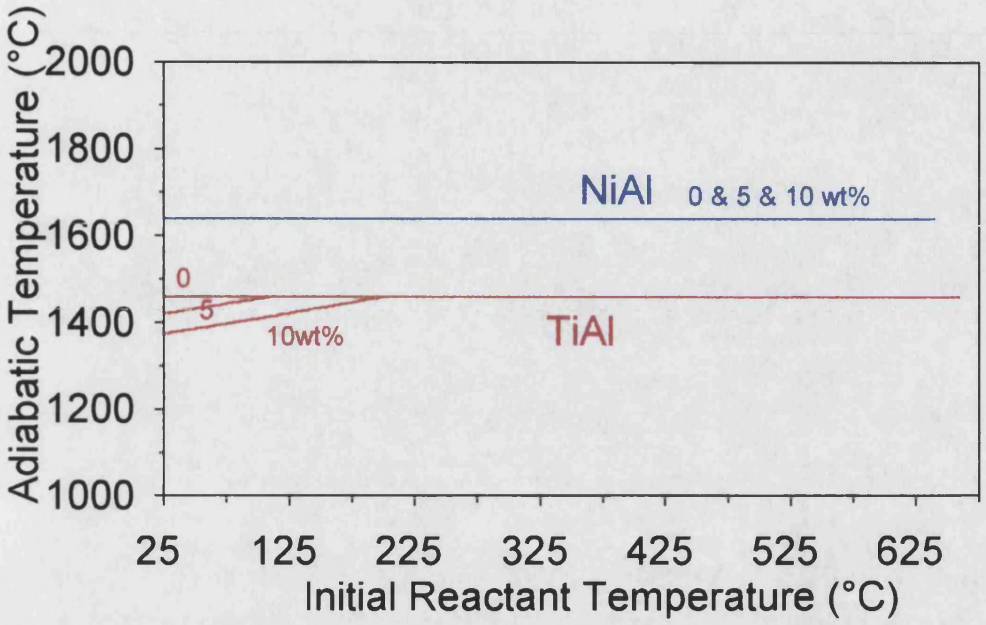

Figure 1.14a Effect of initial reactant temperature on adiabatic temperature for varying additons of alumina. Product formed at the initiation temperature.

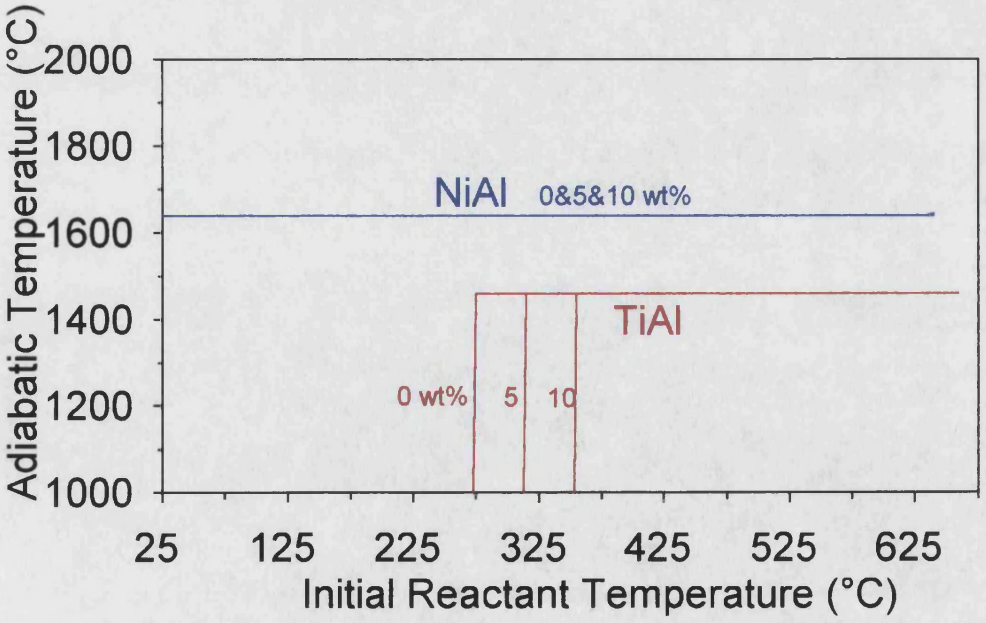

Figure 1.14b Effect of initial reactant temperature on adiabatic temperature for varying additions of alumina. Product formed at its melting point.

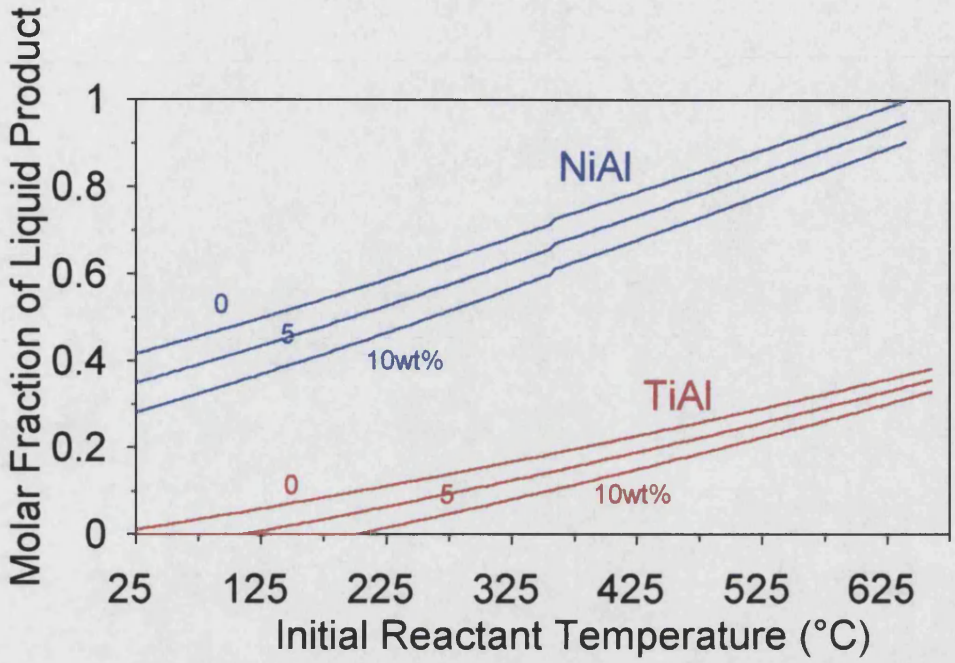

Figure 1.15a Effect of initial reactant temperature on molar fraction of liquid product formed for varying additions of alumina. Product formed at the initiation temperature.

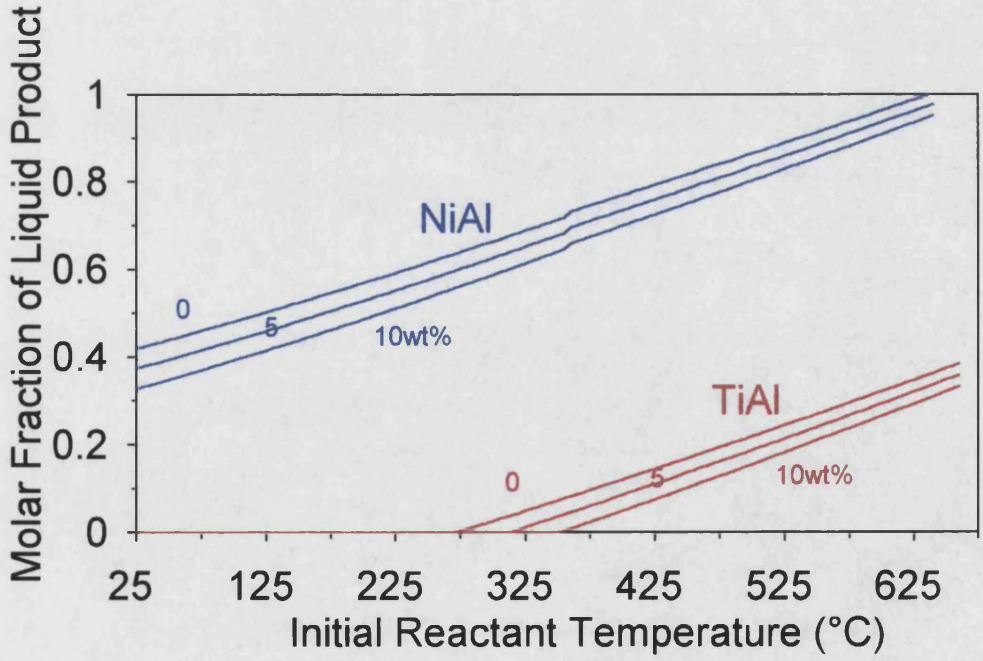

Figure 1.15b Effect of initial reactant temperature on the molar fraction of liquid product formed for varying additions of alumina. Product formed at its melting point

product remains below its melting point until the initial reactant temperatures is raised above 200°C. The calculation for the formation of the product at its melting point gives a much more drastic effect. This shows that the reaction containing 10wt% alumina is not self-sustaining until the reactants are raised above 355°C.

Both calculation methods show that adding progressively greater quantities of alumina reduces the molar fraction of liquid product for both NiAl and TiAl, Figures 15a-b. The molar fractions of liquid product formed are smaller for the formation of the product at its melting point. However, the reduction in molar fraction of molten product with the addition of alumina is greater using the calculation method for the formation of the product at the initiation temperature.

1.5 Reinforcing Intermetallic Compounds

A composite is defined as a combination of at least two chemically distinct materials, with an interface separating the constituents. The separate materials forming the composite must be combined three dimensionally and must produce properties which would not otherwise be achieved by any of the individual constituents[6].

Ductile reinforcing phases are added to intermetallic matrices in an attempt to increase ductility and fracture toughness[19,103,104], but only a few investigations have been undertaken in this area.

Most work is concentrated on property modifications brought to intermetallics by the addition of brittle reinforcing phases. The majority of reinforcement materials are ceramics. Borides, carbides and oxides are all hard brittle materials which constrain the matrix, increasing high temperature strength, stiffness and creep resistance and ambient temperature fracture toughness, though ambient temperature ductility is usually reduced. Additionally, if the reinforcement phase has a lower density than the matrix, this will lead to a decrease in the composite density[12,90,105].

There are two forms of reinforcement which may be introduced into an intermetallic matrix, continuous reinforcements in the form of long fibres and discontinuous reinforcements in the form of particles or short fibres.

1.5.1 Long Fibres

Long fibres run the length of the composite and confer the greatest increases in strength, stiffness and creep resistance to the intermetallic matrix. They can also increase the ambient temperature fracture toughness[106]. This is achieved by debonding of the fibre from the matrix ahead of the crack tip, followed by deflection of cracks along the matrix/fibre interface[107].

However, they also produce a very anisotropic material and the fibre directions have to be carefully tailored to the component. They are also difficult and expensive to produce since the fibres have to be woven into a preform and are susceptible to fracture during composite fabrication.

1.5.2 Particles

Discontinuous reinforcements only provide improvements to stiffness and creep resistance and reduce fracture toughness and ductility. But, they are cheaper to produce and form a more isotropic material than long fibres. They are easier to incorporate into a matrix and some production methods for unreinforced intermetallics may be used with little or no modification.

1.5.3 Composite Systems

Compatibility: A satisfactory reinforcement for the matrix should have suitable chemical, thermal and mechanical properties[90,107,108].

Chemical compatibility is a problem for intermetallic composites which are intended for use at high temperatures. These high temperatures hasten the formation of any unwanted reaction products and reduce the reinforcement volume[12,103].

As regards thermal properties, the coefficients of thermal expansion (CTEs) for reinforcement and matrix must be similar. Any significant difference results in the build-up of internal stresses as the composite is thermally cycled. Again this is a problem for intermetallic composites which experience large temperature ranges[109,110].

Finally, in the case of continuous reinforcements, there should be sufficient mechanical strength between the fibres and the matrix at their interface to maintain a coherent

structure, yet still allow some fibre pull-out to give a measure of toughness to the composite[10,12,110].

At present, no intermetallic composite system appears to fulfil all three criteria perfectly, but the situation may be improved by the application of suitable coatings to the reinforcements. These coatings may act as a reaction barrier or as a material with an intermediate CTE to smooth the sharp change from fibre to matrix or as a material to provide a small amount of reaction between the fibre and matrix.

Examples of Systems: A range of intermetallic composite systems have been produced and the majority of investigations are concerned with the chemical compatibility of the matrix and reinforcement. Work has concentrated on the iron, nickel and titanium-aluminium systems for the matrices.

In the iron-aluminium matrices, alumina[10], aluminium nitride[72], tungsten[10] and yttrium oxide[10] are all stable in FeAl, whilst titanium diboride exhibits a limited reaction[10]. This is desirable for good mechanical bonding between the matrix and reinforcement. In Fe_3Al, aluminium nitride[72] is stable, but alumina[111] and zirconium oxide[112] are not.

A more extensive set of investigations have been performed on nickel-aluminium matrices. NiAl is inert to alumina[72,85,103] and carbon[72], but stoichiometric NiAl is only inert to titanium diboride below 1000°C[34,85,113]. As the activity of the nickel increases in nickel rich NiAl or in Ni_3Al, then the titanium from TiB_2 diffuses more rapidly into the matrix to form Ni_2AlTi[12,108,114]. Ni_3Al is stable with alumina[94,88,115,116], carbon[72], titanium carbide[72], yttrium oxide[84,72] and zirconium oxide[112]. Both NiAl and Ni_3Al react with silicon carbide to form carbon and either $Ni(Si_{0.5}Al_{0.5})$[107,117] or Ni_5Si_3[12,94] respectively.

Both TiAl and Ti_3Al are stable to alumina[3,73,84], titanium diboride[72,123] and titanium carbide[72], but react with zirconium oxide[112]. They also react with silicon carbide[107,109,119] to form a variety of reaction products, depending on the reinforcement content. These include Ti_5Si_3, $Ti_4Al_2C_2$ and $Ti_7Al_5Si_{12}$[72].

Table 1.3 summarises the chemical compatibility of these composite systems.

	AlN	Al_2O_3	C	SiC	TiB_2	TiC	W	Y_2O_3	ZrO_2
FeAl	inert	inert	-	-	reacts	-	inert	inert	-
Fe_3Al	inert	reacts	-	-	-	-	-	-	reacts
NiAl	-	inert	inert	reacts	reacts	-	-	-	-
Ni_3Al	-	inert	inert	reacts	-	inert	-	inert	inert
TiAl	-	inert	-	reacts	inert	inert	-	-	reacts
Ti_3Al	-	inert	-	reacts	inert	inert	-		reacts

Table 1.3 Chemical stability of composite systems

1.6 Production Methods for Reinforced Intermetallic Compounds

Several routes are used in the production of reinforced intermetallic compounds.

1.6.1 Casting

Perhaps the simplest way to introduce discontinuous reinforcements is to mix them into the molten matrix. However, the reinforcement is not evenly distributed in the matrix and it is exposed to high temperatures for a considerable time, a factor which may promote matrix/reinforcement reactions[12].

1.6.2 Powder Metallurgy

Another composite production method limited to discontinuous reinforcements is powder metallurgy[2,105]. The reinforcement is mixed with intermetallic powders before being pressed into compacts which are HIPed to form a dense product. As mentioned earlier, high temperatures and pressures are required when applying powder metallurgy to intermetallic powders. This may promote matrix/reinforcement reactions again.

A variation on powder metallurgy which attempts to introduce long fibres into a matrix is the powder cloth technique. Intermetallic powders are mixed with a binder and rolled into sheets. These are placed in alternating layers with the reinforcing fibres and hot pressed[2,111] to consolidate the powders.

1.6.3 Diffusion Bonding

This method has been successfully used in the production of continuously reinforced composites[2,105]. Layers of matrix foils are separated by layers of reinforcement and the whole arrangement is then pressed and heated, allowing the matrix foils to diffuse together. Problems arise when this is applied to intermetallics since high temperatures and pressures are needed to consolidate the matrix and the production of intermetallic foils is not easily or cheaply accomplished.

1.6.4 Liquid Metal Infiltration

Liquid metal infiltration is widely used for the production of metal matrix composites. A preform of the fibres is placed into a mould and the matrix material is heated separately to a temperature above its melting point. The molten matrix is introduced into the mould and pressure is applied to force the molten matrix into the preform[105,112,120]. When producing an intermetallic matrix composite, a high temperature is needed to melt the matrix material and this may cause a significant reaction to occur between the matrix and the reinforcement.

1.6.5 Spray Forming

Intermetallic powder is fed into a plasma to melt it and then immediately sprayed over continuous fibres, wound onto a rotating mandrel. This forms thin layers of composite material which are stacked and HIPed to form a thicker section of material and to reduce porosity[2,105,111].

1.6.6 Reactive Synthesis

By mixing the reinforcement with the reactants prior to initiation, intermetallic matrix composites may also be formed by reactive synthesis. The reinforcement has to remain inert throughout the reactive synthesis, otherwise unwanted reaction products are formed. However, thermodynamic calculations in Section 1.4 indicate that if the reinforcement remains inert it acts as a heat sink and draws heat away from the reaction. The reinforcement not only draws heat from the reaction, but also dilutes the reactant mixture, reducing the quantity of heat released per unit volume of compact.

This limits the quantity of reinforcement that may be added before the reaction is quenched. Even though the desired phases are formed, the presence of the reinforcement may increase porosity by altering the quantity of liquid formed and by hindering its spread throughout the reactants.

Self-Propagating High-Temperature Synthesis: The reinforcement is mixed and compacted with the reactants, which necessitates the use of discontinuous reinforcements[12,99]. The SHS mode of reactive synthesis uses some of the heat released to raise the temperature of the reactants ahead of the combustion wave. This reduces the energy available to raise the temperature of the reaction, making this method particularly sensitive to any further reduction in energy through the diluting and heat absorbing effects of the reinforcement.

Thermal Explosion: A reinforced compact of reactants is produced using the same method as SHS[2,106,116]. This method is less sensitive to the presence of reinforcements as the whole compact is raised to the initiation temperature by an external heat source and all the heat released is available to sustain the reaction. Figures 1.14a-b detail the effect that the initial temperature of the reactants has on the adiabatic temperature of the reaction, for three different reinforcement levels.

Metal Foils: This method may be used to form continuously reinforced intermetallic composites. It is similar to the metal foils method to form unreinforced intermetallics by initiating a self-sustaining reaction between alternating layers of reactant foils. The continuous fibres are inserted between the foils and the whole lay-up is hot pressed to initiate the reaction and to consolidate the material formed[2].

Reactive Liquid Metal Infiltration: When used to form intermetallic composites, reactive liquid metal infiltration uses the reactant with the lowest melting point to infiltrate a modified preform. The preform consists of the remaining reactants and the reinforcement[86]. The easiest way to introduce the reinforcement is to mix it with the reactants and then to sinter this mixture into a porous preform. Only discontinuous reinforcements may be added since there is no method to introduce continuous reinforcements into the preform at present.

As mentioned in previous sections, either gas or mechanical pressure may be used to force the molten reactant into the preform[72,83,85]. Besides the reinforcement diluting the reactants and acting as a heat sink, it also brings additional problems to reactive liquid metal infiltration. If insufficient liquid phase is formed during this method, porosity is closed off and the preform is not fully infiltrated. The reinforcement size is also vital to the porosity of the preform and careful study of the packing of the reactant and reinforcement powders is necessary to obtain the correct porosity.

In-Situ Reinforcement: The reactant materials required to form the matrix are mixed with reinforcement forming constituents which may be in either a solid or gaseous form[78,99,108]. The matrix reactants are heated until an exothermic reaction is initiated and a transient liquid phase is formed. This liquid phase reacts with the reinforcement forming constituents and a reinforcement phase is precipitated from the liquid. The size of the reinforcement and its distribution may be adjusted by controlling the exothermic reaction[3,12].

This process allows a large volume fraction of fine reinforcement phases to be added to the matrix. Further, the matrix/reinforcement interface is free from reaction products[3] or externally developed contamination[2,108,121].

1.7 Project Aims and Strategy

The proposal for this project was to produce an intermetallic matrix composite by a reactive synthesis route. This required a large amount of background research into intermetallic systems to provide the matrix phases and into compatible reinforcements. Further background reading was required to apply the novel and still developing field of reactive synthesis to their production.

The iron, nickel and titanium-aluminium systems were chosen to provide the matrix phases as they were the most extensively investigated intermetallics and possessed the largest database of material properties. From these systems, FeAl, NiAl and TiAl were selected because of their superior specific strengths and stiffnesses. For the reinforcements, alumina was chosen since it was inert to both NiAl and TiAl and was available in the form of particles and fibres. Carbon was also selected since it was inert

to NiAl and was available in fibres. Silicon carbide was chosen as a contrast to the inert alumina.

As reactive synthesis was still a developing science, there was little literature available on the subject other than journal papers, which were sometimes contradictory. Therefore, a preliminary series of experiments was required to gain experience of reactive synthesis and to bulid up progressively to the thermal explosion and reactive liquid metal infiltration routes of intermetallic matrix composite production.

First, Section 2 covering the analysis techniques used in all of the subsequent sections is included. To reflect the progressive nature of this investigation, the remainder of the thesis is set out in a series of self-contained sections. Each subsequent section contains sub-sections detailing the materials used, experimental procedures, results, a discussion and a summary. The summaries also contain explanations for the development of the next experiment in the progression.

Sections 3 and 4 cover the preliminary experiments undertaken to gain experience of reactive synthesis. The low temperature diffusion work in Section 3 proved that a reactive synthesis route was desirable, both to produce the required material and for

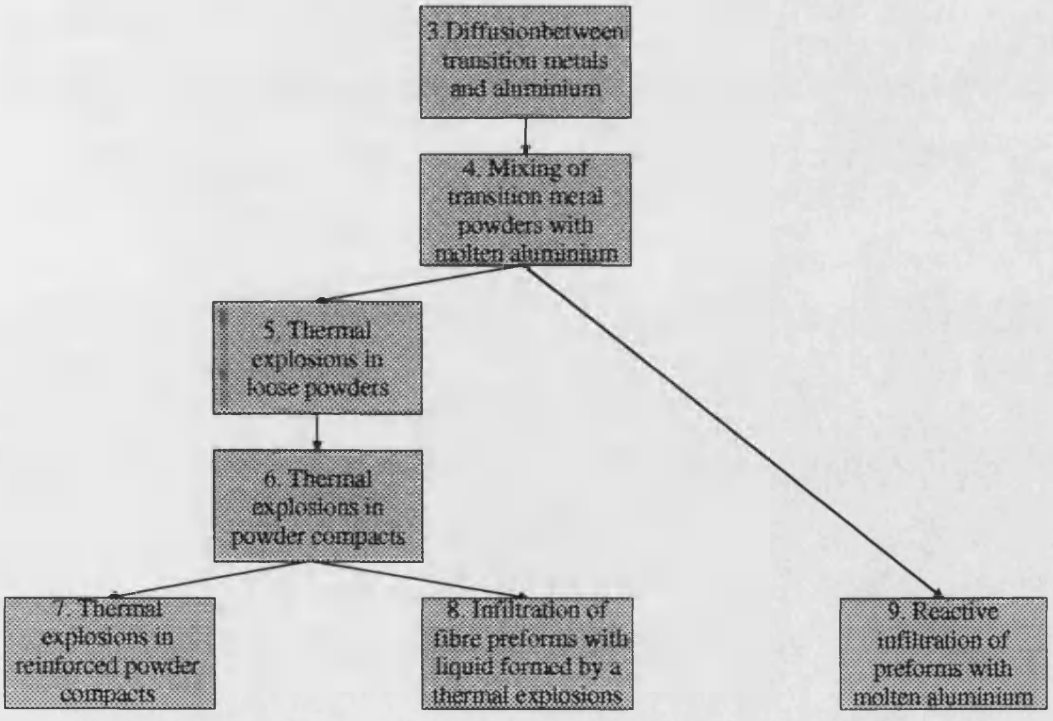

Figure 1.16 Flow chart of investigation

economic reasons. Section 4 details an intermediate experiment prior to the basic thermal explosion described in Section 5 and the set of thermal explosions in Section 6 which formed the intermetallic matrices. In Section 7, particulate reinforcements were added to the thermal explosions. Section 8 details the attempts to introduce continuous reinforcements into matrices formed by thermal explosions and Section 9 describes the formation of a intermetallic matrix composite by reactive liquid metal infiltration. Figure 1.16 illustrates the connection between the experiments in the investigation.

The thesis is concluded with a final section summarising all the experiments and with suggestions for further areas of investigation. References and appendices are included at the end of the thesis.

Section 2

MATERIALS CHARACTERISATION AND ANALYSIS

2.1 Starting Materials

2.1.1 Bulk Metal

Bulk super-pure aluminium was used in Sections 3, 4 and 9 for mixing with transition metals, Table 2.1.

2.1.2 Wires and Fibres

Metal wires were used in the production of diffusion couples in Section 3 and fibres were used as reinforcements in Section 8, Table 2.2.

2.1.3 Powders

Metal powders were used in Sections 4 to 9 and ceramic powders were used as reinforcements in Sections 7 and 9, Table 2.3.

Material	Form	Dimensions	Purity	Source
Aluminium	Bar	-	99.95%	DRA, Holton Heath

Table 2.1 Bulk metals

Material	Form	Diameter	Purity	Source
Iron	Wire	125μm	99.5%	Advent, Halesworth
Nickel	Wire	125μm	99.98%	Advent, Halesworth
Titanium	Wire	125μm	99.6%	Goodfellow, Cambridge
Alumina	Fibre	110μm	99.9%	Goodfellow, Cambridge
Carbon	Fibre	5μm	99.9%	Thornel, London

Table 2.2 Wires and fibres

Material	Form	Dimensions	Purity	Source
Aluminium	Powder	Ø60μm max.	99.9%	Goodfellow, Cambridge
Iron	Powder	Ø450μm max	99.0%	Goodfellow, Cambridge
Nickel	Powder	Ø100μm max	99.8%	Iconel, London
Nickel	Powder	Ø149μm max	99.5%	Alfa, Royston
Nickel	Powder	Ø250μm max	99.5%	Goodfellow, Cambridge
Titanium	Powder	Ø200μm max	99.5%	Goodfellow, Cambridge
Alumina	Powder	Ø40μmax	99.9%	Plasmatex, London
Silicon Carbide	Powder	Ø20μm max	99.5%	Logitech, Manchester

Table 2.3 Powders

The supplier specifications of the metal powders are given in Table 2.3. Particle size distributions (PSDs) were not provided, but these were measured using a Malvern System 3601 Particle Size Analyser. A small quantity of powder was added to one of the suspending solutions listed in Table 2.4 and the suspension was passed in front of a laser. The extent to which the laser was diffracted by the powder particles gave an indication of their sizes.

The iron and titanium powders were sieved to provide the particle size ranges in Table 2.5 and this provided each transition metal element with the three PSDs shown in Figures 2.2-2.4. The particle size distribution for the aluminium powder is shown in Figure 2.1 and those of the ceramic powders are shown in Figures 2.5-2.6.

Powder	Suspending Solution
Aluminium	Isopropanol
Iron	Distilled Water + Ethyleneglycol
Nickel	Acetone + Rape Seed Oil
Titanium	Distilled Water + Sodium Carbonate
Alumina	Distilled Water
Silicon Carbide	Distilled Water

Table 2.4 Suspending solutions

Material	Designation	Particle Size Range
Aluminium	-	0→60μm
Iron	PSD1	0→190μm
Iron	PSD2	0→190μm
Iron	PSD3	130→190μm
Nickel	PSD1	0→20μm
Nickel	PSD2	0→100μm
Nickel	PSD3	0→275μm
Titanium	PSD1	0→75μm
Titanium	PSD2	0→200μm
Titanium	PSD3	75→200μm
Alumina	-	0→40μm
Silicon Carbide	-	0→20μm

Table 2.5 Particle size distribution (PSD) details

For the iron powders, PSD1 and PSD2 covered the same range of particle sizes, but PSD1 contained a greater proportion of small particles. PSD3 was restricted to particles larger than 130μm.

The maximum size of the nickel particles increased from 20μm in PSD1 to 275μm in PSD3.

The titanium particle size distributions were all produced from PSD2. This was sieved to give a maximum particle size of 75μm in PSD1 and the remainder was used for PSD3.

2.2 Analysis of Intermetallic Compounds

2.2.1 Metallography

Sectioning: All the samples produced for optical microscopy and scanning electron microscopy underwent a rigorous preparation routine.

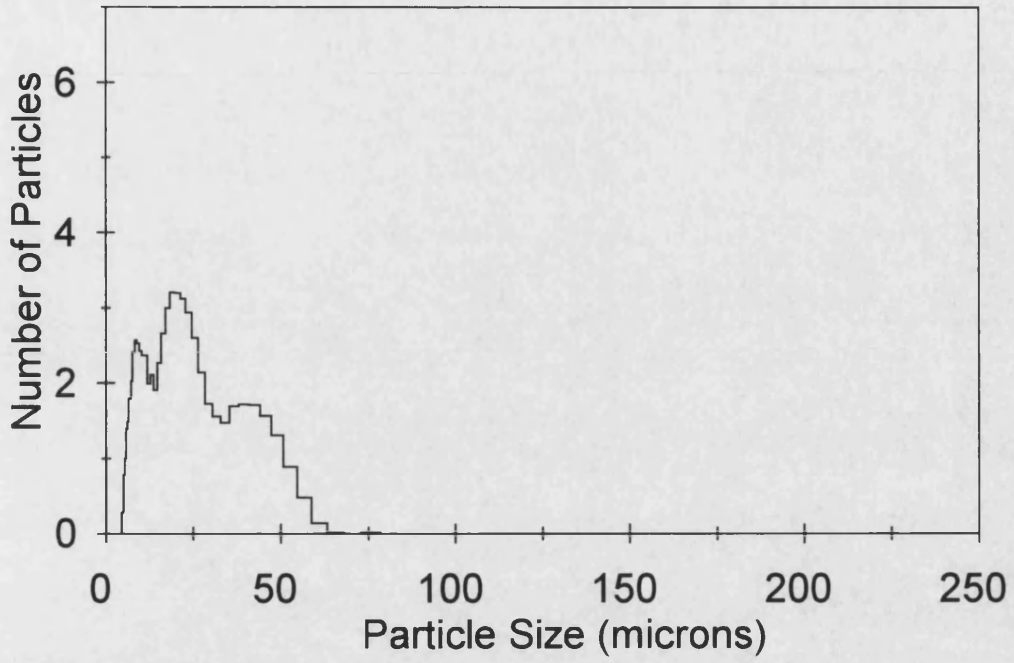

Figure 2.1 Aluminium powder size distribution

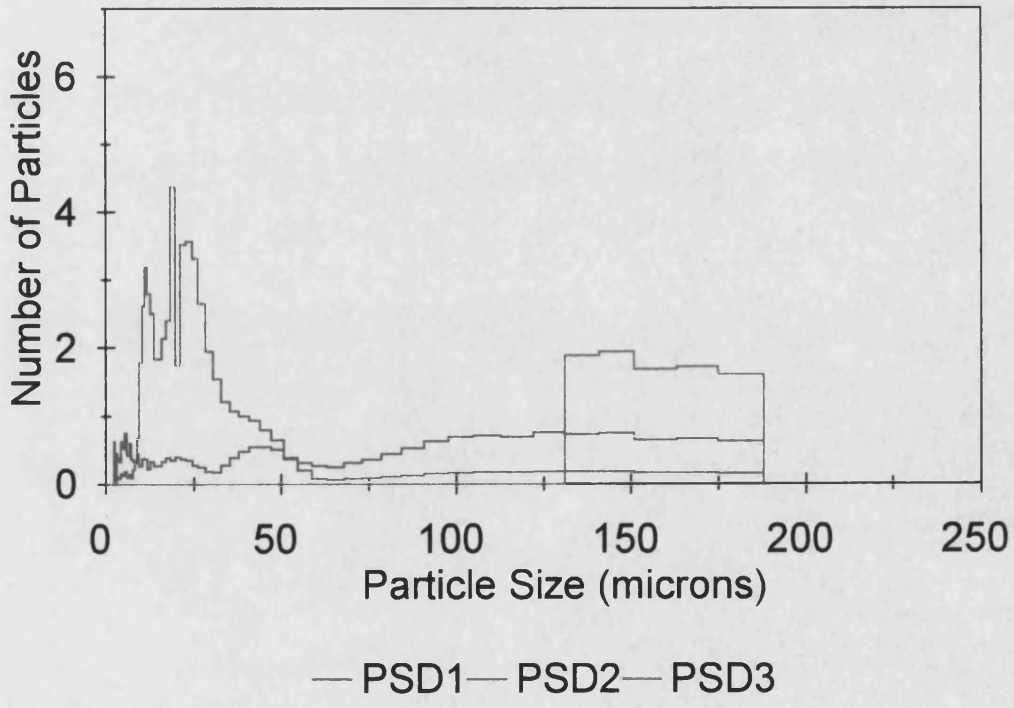

Figure 2.2 Iron powder size distributions

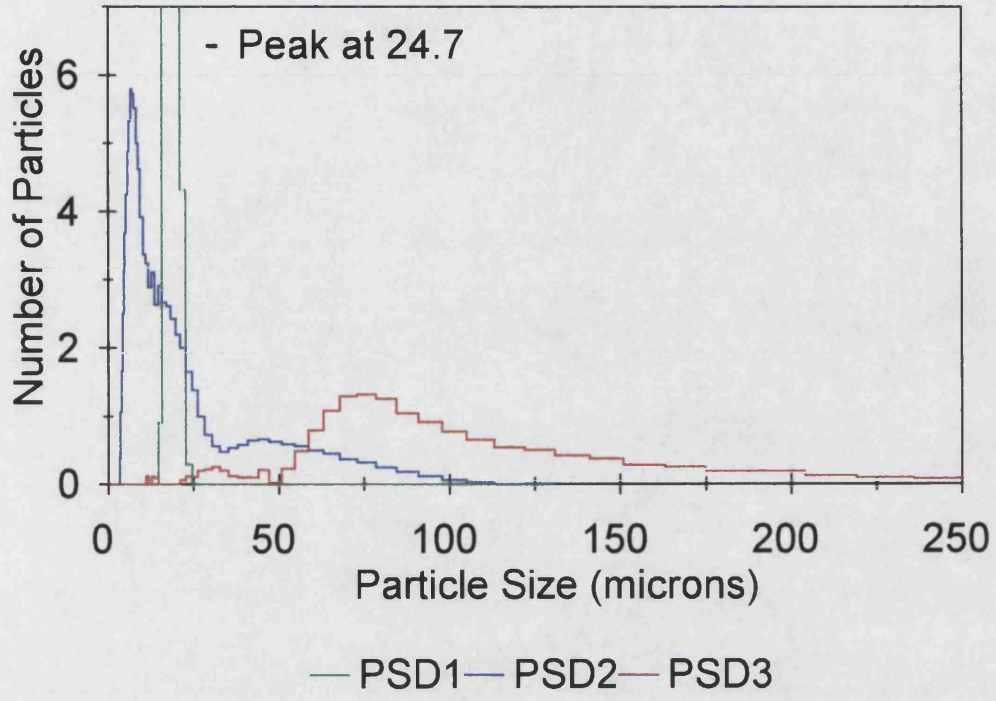

Figure 2.3 Nickel powder size distributions

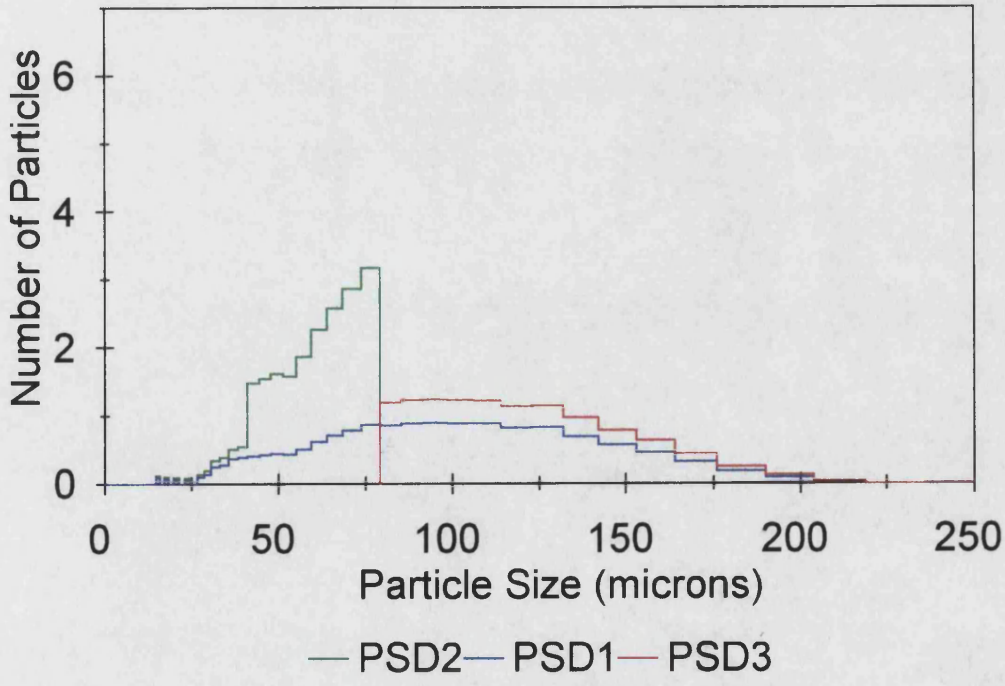

Figure 2.4 Titanium powder size distributions

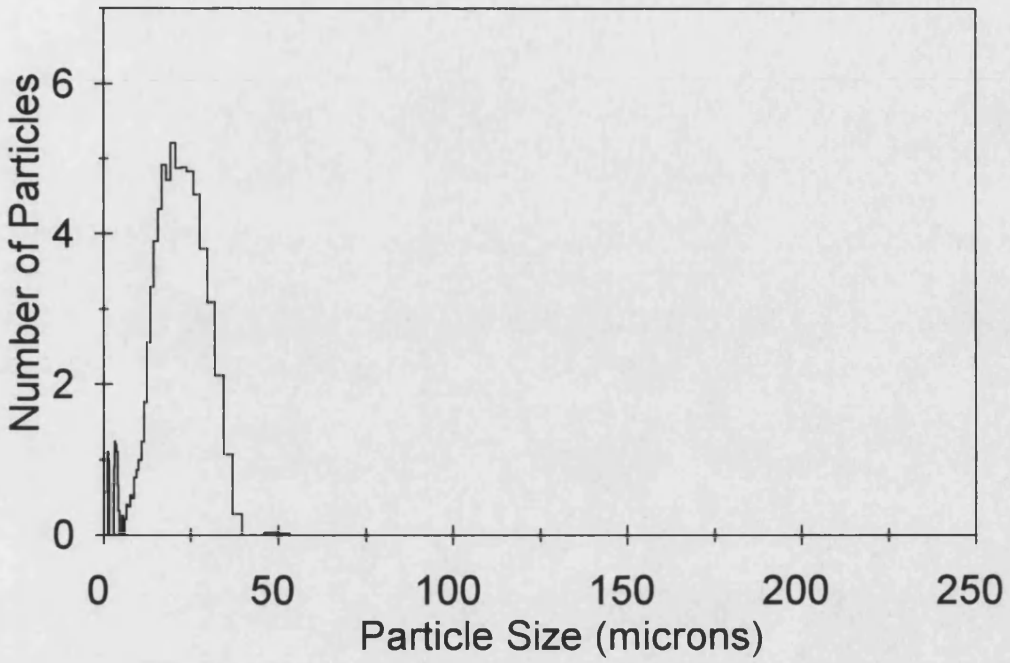

Figure 2.5 Alumina powder size distribution

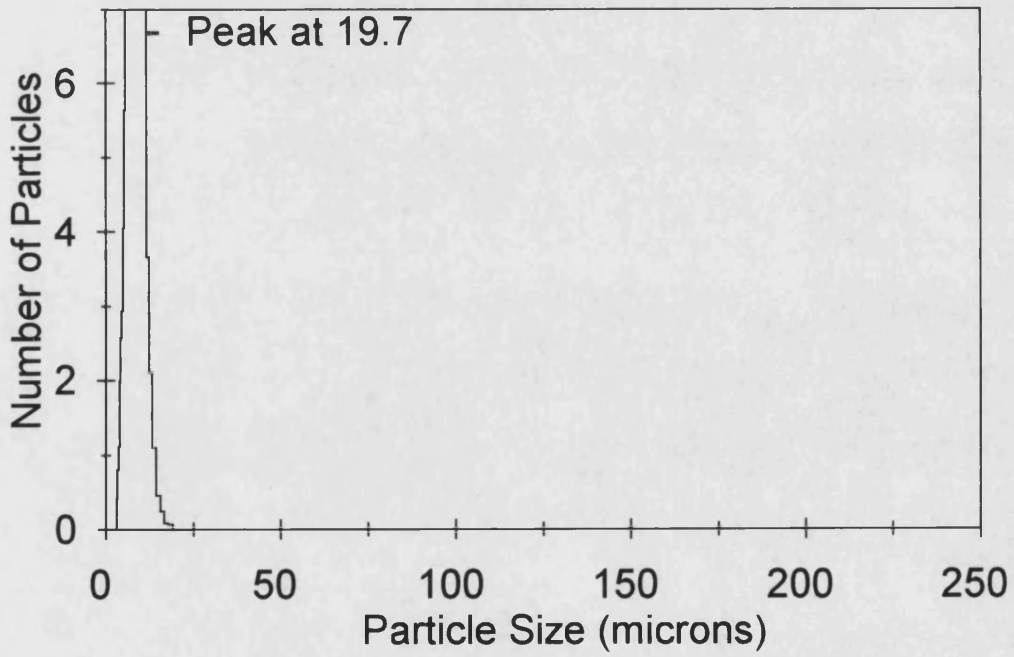

Figure 2.6 Silicon carbide powder size distribution

The large samples produced in Sections 3, 4 and 5 were sectioned on a Buehler Abrasimet 2 abrasive cutter. A variety of 12″ diameter cutting wheels were used, with the type dependent on the material being sectioned. Hard materials required softer adhesives in the cutting wheels to allow the blunted abrasive to break away and reveal fresh, sharp surfaces. Materials cut with blunted abrasive were damaged from overheating. The smaller samples produced in Sections 6, 7, 8 and 9 were sectioned on a Buehler Isomet 2000 precision saw using a 7″ diameter, diamond edged wheel.

Polishing: After sectioning, the samples were mounted in carbon filled conductive phenolic powder using a 25.4mm diameter Buehler mounting press. This mounting medium allowed the samples to be examined in SEMs without the need for the application of a conducting layer of dag to the sample surface. When porous samples were mounted, the pores were subsequently vacuum impregnated with Epothin epoxy resin. This prevented abrasives from being captured in the pores during coarse polishing and becoming released during a later stage of the preparation.

Once the samples were mounted, they were ground down with progressively finer grades of silicon carbide paper to produce a flat surface. A Buehler Metaserv Motopol 12 grinder-polisher machine, utilising various abrasives, was used to prepare the samples for scanning electron microscopy. Each material had its own polishing routine to obtain a flat finish which was free of scratches. A large amount of time was devoted to this work since samples containing two or more phases of different hardness, such as composites, were particularly difficult to polish. The various surfaces, abrasives, wheel speeds, loads and polishing times of each routine are given in Appendix D.

Optical Microscopy: Optical microscopy was carried out on a Zeiss ICM405 Inverted Microscope. The microscope was used during the preparation of the sample surfaces since frequent checks were required during the polishing routines.

Image Analysis: Optimas 6 image analysis software was used in Sections 6 to 9 to measure porosities in the final materials and in Sections 6 and 7 to measure contact lengths between the transition metal and aluminium powders in the green compacts. A programme, listed in Appendix E, was written within this software to measure the

contact lengths. Five porosity or contact length measurements were taken to give mean and standard deviation values for each sample.

2.2.2 Scanning Electron Microscopy

The principle of scanning electron microscopy (SEM) is as follows. A beam of electrons is emitted from an electron gun and accelerated towards the sample surface. On route the beam is demagnified by a series of condenser lenses until the beam has a diameter of 2-10nm. Scan coils are used to move the electron beam across the surface and a detector counts the number of electrons or other forms of radiation emitted. The electron signal is used to form a picture on a cathode-ray tube (CRT) scanning in synchronism with the beam, the brightness of the spot on the screen being related to the electron signal, Figure 2.7.

The secondary electrons emitted from the sample surface are used to produce a topographical image of the sample surface since the yield of electrons is sensitive to the angle of the surface to the detector. Figure 2.8 shows that more electrons are detected from surfaces A and C, than from surface B, which thus appears to be in shadow. Backscattered electrons are used to provide a compositional image of the surface since the number emitted is more sensitive to atomic number. Elements of higher atomic

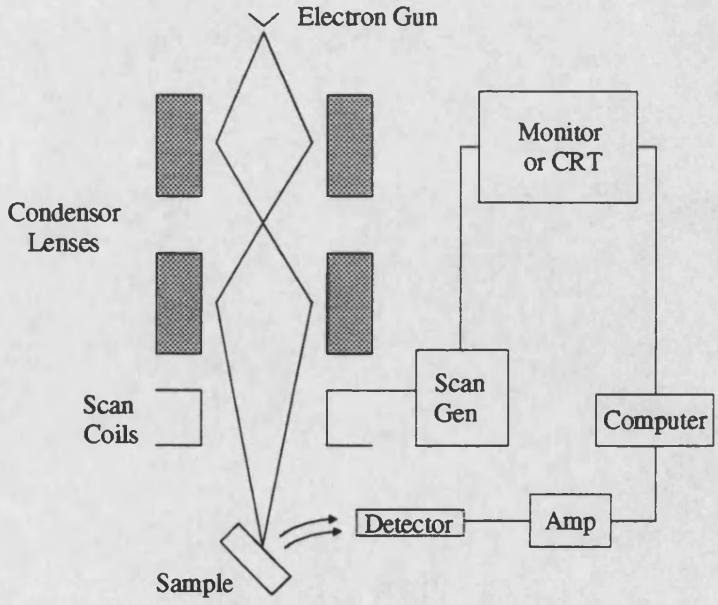

Figure 2.7 Schematic diagram of SEM (after Goodhew and Humphreys[104])

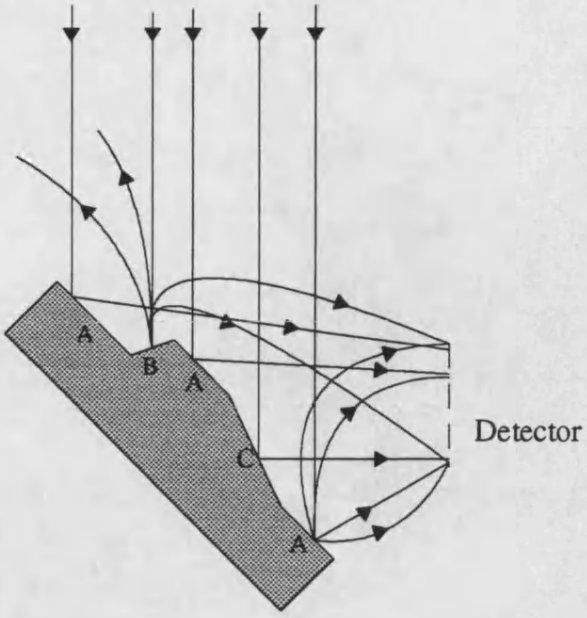

Figure 2.8 Effect of angle of surface to detector[123]

numbers produce more backscattered electrons than those with lower atomic numbers and thus contrast is produced between different compositional regions. X-rays are also produced by the incident electron beam and these are used for the electron probe microanalysis.

The SEM used in this investigation was a JEOL JSM-6310 instrument which used a computer rather than a CRT to display images of the sample. The computer was able to digitally store the scan in memory and was able to display an image of the whole area simultaneously. By averaging several scans of the same area a clearer image was obtained. The stored image could also be transferred directly to other analysis software.

2.2.3 Electron Probe Microanalysis

In electron probe microanalysis (EPMA) the x-ray spectrum generated in the sample by the electron beam is analysed. The spectrum contains x-rays which are characteristic of the elements present and also a background of continuous x-rays, Figure 2.9.

The characteristic x-ray energies and wavelengths are related to the energy states of the atoms excited by the incident electron and can be used to establish which elements

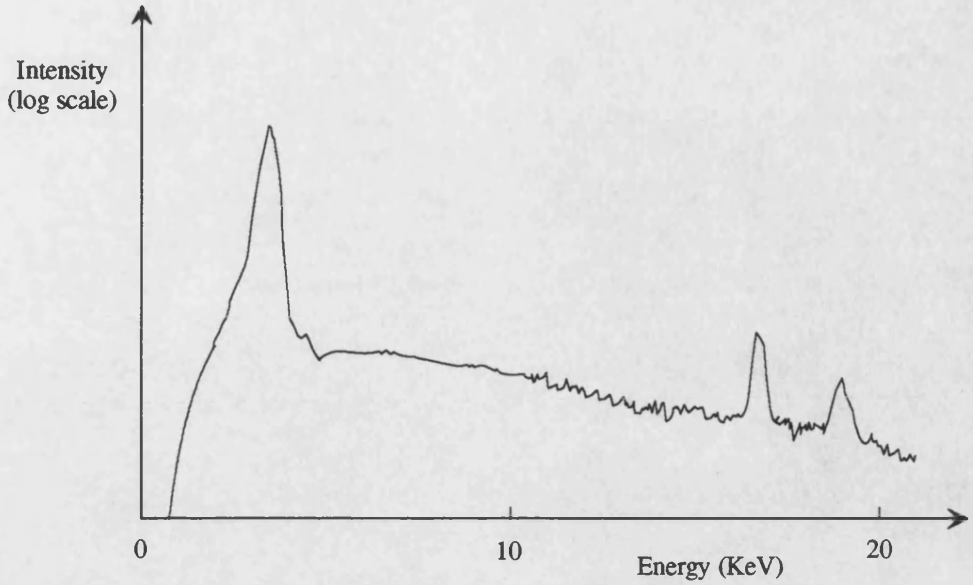

Figure 2.9 X-ray spectrum showing characteristic peaks above background

are present in the sample. The intensity of a particular x-ray will give a measure of the amount of that element present. The energies of the x-rays are used in energy dispersive spectrometry (EDS) and the wavelengths of the x-rays are used in wavelength dispersive spectrometry (WDS).

Energy Dispersive Spectrometry: EDS uses a silicon semiconductor as a detector. The x-rays produce electron-hole pairs, the number of pairs being proportional to the x-ray energy and the current produced. The current produced by each x-ray only lasts a short amount of time and is referred to as a pulse. This is amplified and displayed on a histogram according to the energy of the x-ray, and a computer matches the histogram with standards of all the elements.

Wavelength Dispersive Spectrometry: WDS filters the x-rays so that only those of a certain wavelength reach the detector. The filtering is achieved by diffracting the x-rays with a crystal according to;

$$\lambda = \frac{2d \sin \theta}{n}$$

where λ is wavelength, d is the spacing between the crystal lattice, θ is the angle between the incident x-rays and the crystal planes and n is an integer. By altering θ, x-rays from a specific element may be counted without the detector having to

differentiate between x-rays of different energies. This gives the WDS technique a higher spectral resolution and a greater peak-to-background ratio than EDS. However, only one element can be detected at a time and a scan of all wavelengths for qualitative analysis is time consuming.

For quantitative analysis, standards usually consisting of the appropriate pure elements are used. The ratio of X-ray intensities is measured and a correction is applied to take account of the atomic number effect (Z), absorption (A) and fluorescence (F).

EPMA work was carried out using a JEOL JXA-8600 instrument fitted with four crystal spectrometers and a ZAF analysis programme for quantitative analysis.

2.2.4 X-ray Diffraction

X-ray diffraction (XRD) supplies information about the interplanar spacings of crystals. As in WDS, the x-rays are diffracted by the crystals according to;

$$\lambda = \frac{2d\sin\theta}{n}$$

Previously, the interplanar spacing was known and the wavelength was unknown. In XRD, the wavelength of the x-rays is known and by altering the angle between the incident x-rays and the crystal and noting the reflection intensities, the interplanar spacing may be calculated. When the equation is satisfied, the X-rays interfere constructively. Plots of x-ray intensity against the angle θ are characteristic for a particular crystal.

The x-rays are generated from a line source and the instrument used in this investigation generated copper K_α x-rays. The sample is usually a polycrystalline sample or powder which allows all the lattice planes to be covered since the angle between the x-rays and the sample can only be altered in one dimension. The sample is mounted on a goniometer which carefully controls the angle θ and is linked to the detector which has to be rotated in conjunction with the sample. The x-rays are detected by a xenon gas proportional counter, where they produce electron-ion pairs when they collide with gas atoms and produce a pulse. The pulses are filtered to allow

through only pulses within a specific energy and thus wavelength range and by counting these pulses the intensity of x-rays for an angle θ may be calculated.

In this study, the plots of x-ray intensity against angle θ were compared against a database of plots of known compounds to deduce the phases present in the samples. For clarity, the XRD plots shown in the following sections are schematic representations of the data produced by the diffractometer.

2.2.5 Hardness Testing

Macrohardness: Macrohardness measurements were taken using a Vickers Armstrong hardness machine with a pyramidal diamond indentor. The indentor was pushed into the sample for a given time, by a pre-set load. By measuring the dimensions of the indent and using a chart which allowed different loads to be standardised, a Vickers hardness number (Hv) was obtained.

Microhardness: The Leco M-400 hardness tester with a pyramidal diamond indentor was a smaller version of the Vickers machine. This produced smaller indents which allowed more specific areas of a sample to be measured. Using this apparatus, hardness measurements could be taken of individual phases and between pores, which the larger machine was unable to do.

Section 3

DIFFUSION BETWEEN TRANSITION METALS AND ALUMINIUM

The first series of experiments performed in this investigation was aimed at producing an intermetallic material by solid-state diffusion using a non-reactive synthesis route.

3.1 Materials

The materials used in this experiment were bulk super-pure aluminium in the form of 7.0cm^3 blocks and the iron, nickel and titanium wires as detailed in Section 2.1.

3.2 Experimental Procedures

Separate iron, nickel and titanium-aluminium diffusion couples were produced by infiltrating a preform, consisting of the three transition metals, with molten aluminium. The preform was made by winding the wires in three separate regions around a steel plate. The assembly was placed in a die which had been pre-heated to 400°C. Super-pure aluminium was heated in a crucible above the die to a temperature of 850°C and introduced into the die down a launder, Figure 3.1. A ram was immediately lowered into the die and a pressure of 25MPa was applied to force the metal into the preform.

When the die had cooled to room temperature, the billet was removed and cut into the three transition metal sections. Six diffusion couples were made from each section, which were then heat treated in a furnace for 0, ½, 4, 16, 64 and 256 hours at 640°C. A temperature of 640°C was chosen as it was the highest temperature that could be safely set on the furnace controls without the possibility of melting the aluminium. Each heat treated sample was cut in half and the internal face was prepared for SEM and EPMA examination.

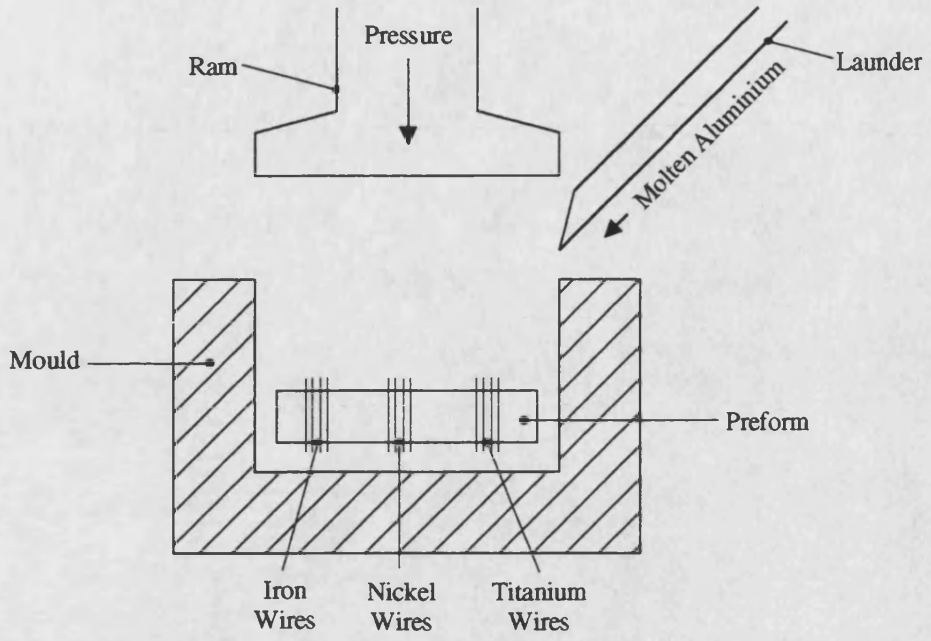

Figure 3.1 Liquid metal infiltration apparatus

3.3 Results

3.3.1 Iron-Aluminium

Examination of the iron-aluminium cast sample showed that there had been some interaction between the wire and the aluminium during production of the diffusion couple. Figures 3.2a-b show that a phase (G) had formed between the aluminium matrix (A) and the iron wire (B) and that there was a dispersion ($G_{(disp)}$) present in the aluminium close to the wires. EPMA data revealed that phase (G) had a composition consistent with the $FeAl_3$ intermetallic phase, whilst phase ($G_{(disp)}$) had a composition of approximately Fe-85at%Al, which corresponded to a solid solution of iron in aluminium. However, since the dispersoids were smaller than the resolution of the EPMA technique, around $1\mu m^3$, some of the surrounding aluminium was also sampled. This enhanced the aluminium content and therefore, the dispersoids were probably $FeAl_3$. The varying size of the dispersoids affected the quantity of aluminium that was sampled and produced large standard deviation values. Appendix A lists the identification letters used in the images alongside the alloys and compounds they denote.

The interface between the aluminium and the $FeAl_3$ appeared to be relatively smooth, whilst the interface between the $FeAl_3$ and the remaining iron wire was very irregular. There were few pores present in this sample.

Heat treatment for 0.5hrs at 640°C resulted in a steady increase in the amount of $FeAl_3$ phase present, Figures 3.3a-b. The intermetallic phase appeared to expand outwards from the wire in an irregular pattern, disrupting the originally smooth aluminium/$FeAl_3$ interface. However, the $FeAl_3$/iron interface became smoother as it moved further into the wires. Pore formation occurred between the aluminium and the $FeAl_3$, but none was observed between the $FeAl_3$ and the iron. The quantity of dispersion decreased.

Further increases in the heat treatment time continued these trends, Figures 3.4a-b. The remaining iron wire was slowly consumed to form $FeAl_3$ and pore formation was concentrated in the aluminium regions between iron wires. No other intermetallic phases were produced.

After 256hrs at 640°C, all the iron had been converted to $FeAl_3$, large pores were present in the $FeAl_3$ region and no dispersed phase remained, Figures 3.5.a-b. The $FeAl_3$ intermetallic was cracked and chipped, which was possibly a consequence of the sample preparation routine.

Time at 640°C (hrs)	Phase	Fe (at%) Mean	Fe (at%) SD	Al (at%) Mean	Al (at%) SD	Element/ Compound
0	A	0.0	0.0	100.0	0.0	Al
	B	99.7	0.4	0.3	0.4	Fe
	G	26.1	0.3	73.9	0.3	$FeAl_3$
	$G_{(disp)}$	16.4	1.7	83.6	1.7	$FeAl_3$
½	A	0.2	0.0	99.8	0.0	Al
	B	99.1	0.0	0.9	0.0	Fe
	G	28.2	0.6	74.8	0.6	$FeAl_3$
	$G_{(disp)}$	19.0	2.1	81.0	2.1	$FeAl_3$
16	A	0.1	0.1	99.9	0.1	Al
	B	99.8	0.0	0.2	0.0	Fe
	G	25.7	0.5	74.3	0.5	$FeAl_3$
256	A	0.1	0.1	99.9	0.1	Al
	B	99.7	0.2	0.3	0.2	Fe
	G	26.2	0.7	73.8	0.7	$FeAl_3$

Table 3.1 EPMA data for Fe-Al diffusion couples (SD-standard deviation)

3.3.2 Nickel-Aluminium

As in the iron-aluminium system, there had been some intermetallic formation during casting of the diffusion couples, Figure 3.6a-b. Two thin layers (M and L) had formed at the interface between the aluminium (A) and nickel (H). EPMA of these two phases identified them as $NiAl_3$ (M) and Ni_2Al_3 (L). The interface between the aluminium and the $NiAl_3$ phase was irregular and outside the original nickel wire region. The interface between the two intermetallic phases was also irregular and followed the line of the original aluminium/nickel interface. The Ni_2Al_3/nickel interface was found to be smooth and within the original nickel region. A dispersion ($M_{(disp)}$) had formed around the wires, Figure 3.6a, and this was approximated to $NiAl_3$, Table 3.2. The dispersoids were again too small to be resolved by EPMA and gave an aluminium rich reading. No pores were discovered in this sample.

After 0.5hrs at 640°C, the intermetallic phases had increased in width, Figures 3.7a-b. The Ni_2Al_3 phase had penetrated a considerable distance towards the centre of the

Time at 640°C (hrs)	Phase	Ni (at%) Mean	Ni (at%) SD	Al (at%) Mean	Al (at%) SD	Element/ Compound
0	A	0.5	0.3	99.5	0.3	Al
	H	99.7	0.0	0.3	0.0	Ni
	L	39.0	1.0	61.0	1.0	Ni_2Al_3
	M	23.4	0.3	76.6	0.3	$NiAl_3$
	$M_{(disp)}$	20.1	3.3	79.9	3.3	$NiAl_3$
½	A	0.7	0.0	99.3	0.0	Al
	H	99.5	0.1	0.5	0.1	Ni
	L	39.2	0.0	60.8	0.0	Ni_2Al_3
	M	26.7	1.3	73.3	1.3	$NiAl_3$
	$M_{(disp)}$	20.2	2.6	79.8	2.6	$NiAl_3$
16	A	1.0	0.1	99.0	0.1	Al
	H	99.3	0.1	0.7	0.1	Ni
	L	39.0	0.8	61.0	0.8	Ni_2Al_3
	M	24.4	0.6	75.6	0.6	$NiAl_3$
	$M_{(disp)}$	23.4	1.9	76.6	1.9	$NiAl_3$
256	A	0.7	0.1	99.3	0.1	Al
	H	99.2	0.1	0.8	0.1	Ni
	L	38.2	0.2	61.8	0.2	Ni_2Al_3
	M	24.5	0.4	75.5	0.4	$NiAl_3$
	$M_{(disp)}$	24.1	0.3	75.9	0.3	$NiAl_3$

Table 3.2 EPMA data for Ni-Al diffusion couples

Time at 640°C (hrs)	Phase	Ni (at%) Mean	SD	Al (at%) Mean	SD	Element/ Compound
16	L	36.9	-	63.1	-	Ni_2Al_3
	L	38.9	-	61.1	-	Ni_2Al_3
	L	39.8	-	60.2	-	Ni_2Al_3
16	M	24.7	-	75.3	-	$NiAl_3$
	M	24.0	-	76.0	-	$NiAl_3$
	M	25.1	-	74.9	-	$NiAl_3$

Table 3.3 EPMA data across $NiAl_3$ and Ni_2Al_3

nickel wires and the interface with the $NiAl_3$ phase had moved outwards, whilst the $NiAl_3$ phase had only slightly increased in width. No changes in the smoothness of the interfaces were observed and as with the aluminium-iron system, there was a decrease in the amount of dispersed phase present. Pores formed between the aluminium/$NiAl_3$ interface and were concentrated in regions originally surrounded by nickel wires, whilst cracks had begun to form along the $NiAl_3/Ni_2Al_3$ interfaces, Figure 3.7b.

With increasing heat treatment times above 0.5hrs, the Ni_2Al_3 phase increased in width more rapidly than the $NiAl_3$ phase, Figures 3.8a-b. Pore sizes increased and the dispersed phase gradually disappeared.

After 256hrs, none of the nickel wire remained, only a structure consisting of Ni_2Al_3 and some $NiAl_3$, Figures 3.9a-b.

No concentration gradient was observed across the $NiAl_3$, but this was not the case for the Ni_2Al_3 where a variation in the nickel content of ~3at% was recorded, with the highest concentration being next to the Ni_2Al_3/nickel interface, Table 3.3.

3.3.3 Titanium-Aluminium

The titanium-aluminium diffusion couples differed from the other two systems after casting. No intermetallic formation or dispersion was observed in the as cast sample, Figures 3.10a-b.

After heat treatment at 640°C for 0.5hrs, a phase (S) had formed between the aluminium (A) and the titanium (N) Figures 3.11a-b. EPMA revealed this to be the $TiAl_3$ intermetallic , Table 3.4. The aluminium/$TiAl_3$ interface was outside the original

Time at 640°C (hrs)	Phase	Ti (at%) Mean	SD	Al (at%) Mean	SD	Element/ Compound
0	A	0.0	0.1	100.0	0.1	Al
	N	100.0	0.1	0.0	0.1	Ti
½	A	0.1	0.1	99.9	0.1	A
	N	99.9	0.1	0.1	0.1	Ti
	S	24.2	1.4	75.8	1.4	$TiAl_3$
16	A	0.1	0.1	99.9	0.1	Al
	N	100.0	0.0	0.0	0.0	Ti
	S	25.8	1.0	74.2	1.0	$TiAl_3$
256	A	0.0	0.0	100.0	0.0	Al
	N	100.0	0.0	0.0	0.0	Ti
	S	25.1	0.3	74.9	0.3	$TiAl_3$

Table 3.4 EPMA data for Ti-Al diffusion couples

regions of the titanium wires and was irregular. The $TiAl_3$/titanium interface was inside the original region of the titanium wire and was comparatively smooth. Pores had formed between the aluminium and the intermetallic phase and were concentrated in the regions surrounded by titanium wires.

The intermetallic phases and pores rapidly increased in size with longer heat treatment times, with the aluminium/$TiAl_3$ phases expanding outwards and the $TiAl_3$/titanium interfaces penetrating further into the wires, Figures 3.12a-b.

After 256hrs at 640°C, a few regions of titanium wire remained. These had become almost entirely surrounded by pores and thus had their supply of aluminium restricted, Figure 3.13a. The aluminium/$TiAl_3$ interface had also become fragmented during this time, Figure 3.13b.

3.4 Discussion

3.4.1 Iron-Aluminium

The presence of a dispersion around the iron wires in the cast sample suggested that the first molten aluminium which came into contact with the wires had dissolved some of the iron. Whilst the aluminium was still passing between the wires, the dissolved iron was transported away. Then the aluminium cooled to below its melting point and

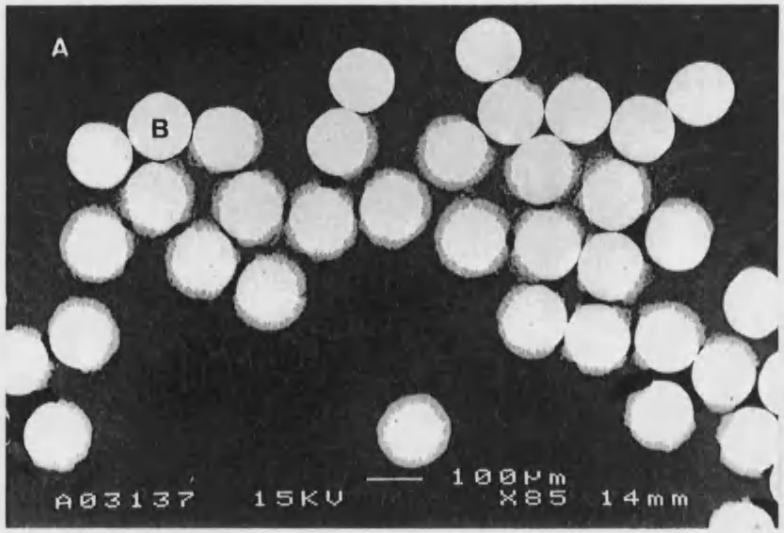

Figure 3.2a Fe-Al diffusion couple. 0hrs at 640°C.
A-Al, B-Fe 100µm

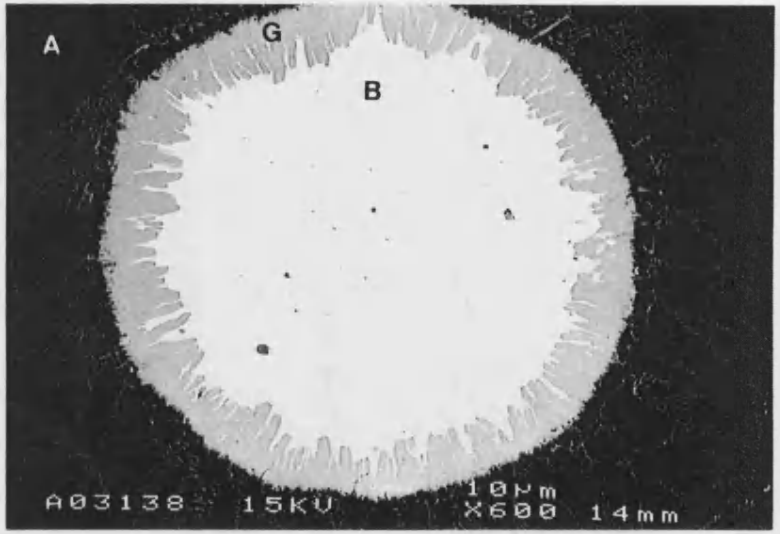

Figure 3.2b Fe-Al diffusion couple. 0hrs at 640°C.
A-Al, B-Fe, G-$FeAl_3$ 10µm

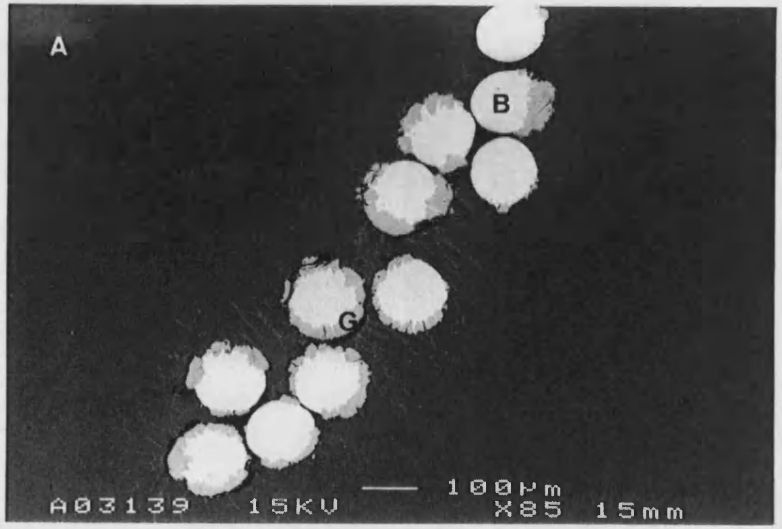

Figure 3.3a Fe-Al diffusion couple. 0.5hrs at 640°C.
A-Al, B-Fe, G-$FeAl_3$ 100µm

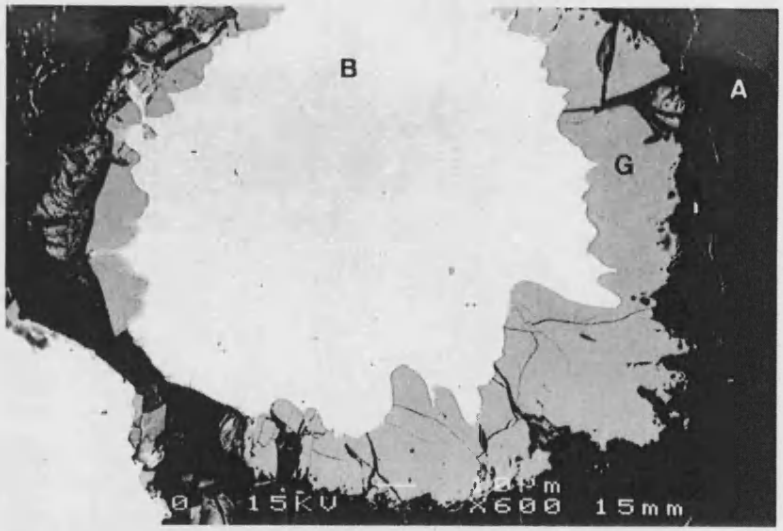

Figure 3.3b Fe-Al diffusion couple. 0.5hrs at 640°C.
A-Al, B-Fe, G-$FeAl_3$ 10µm

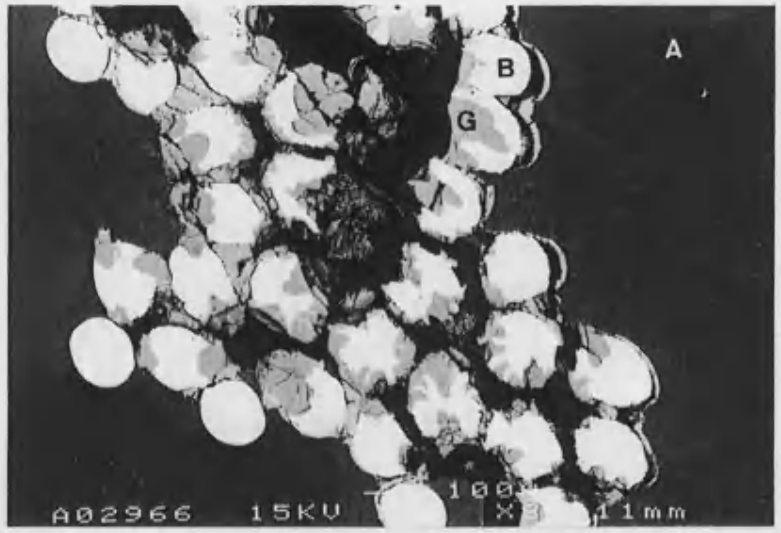

Figure 3.4a Fe-Al diffusion couple. 16hrs at 640°C.
A-Al, B-Fe, G-$FeAl_3$ 100μm

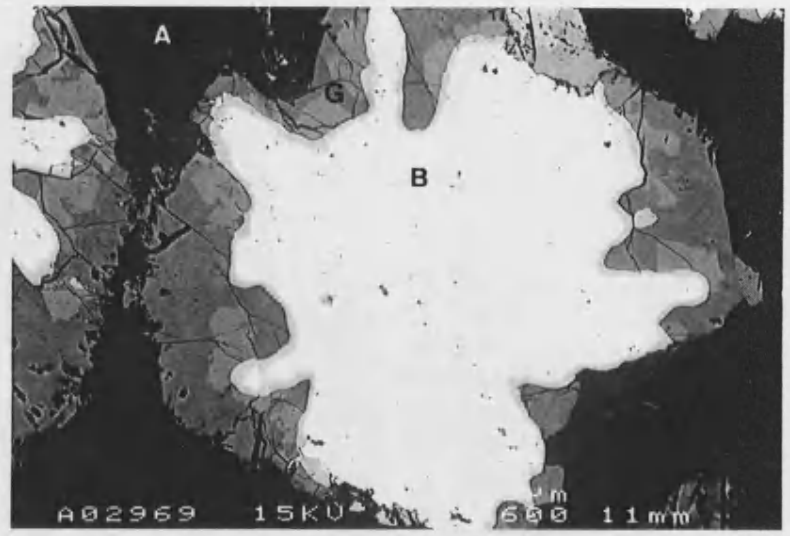

Figure 3.4b Fe-Al diffusion couple. 16hrs at 640°C.
A-Al, B-Fe, G-$FeAl_3$ 10μm

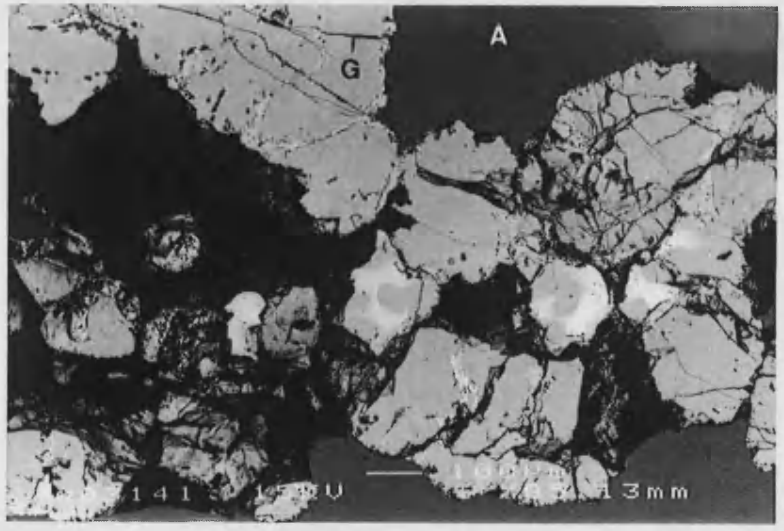

Figure 3.5a Fe-Al diffusion couple. 256hrs at 640°C.
A-Al, G-$FeAl_3$ 100μm

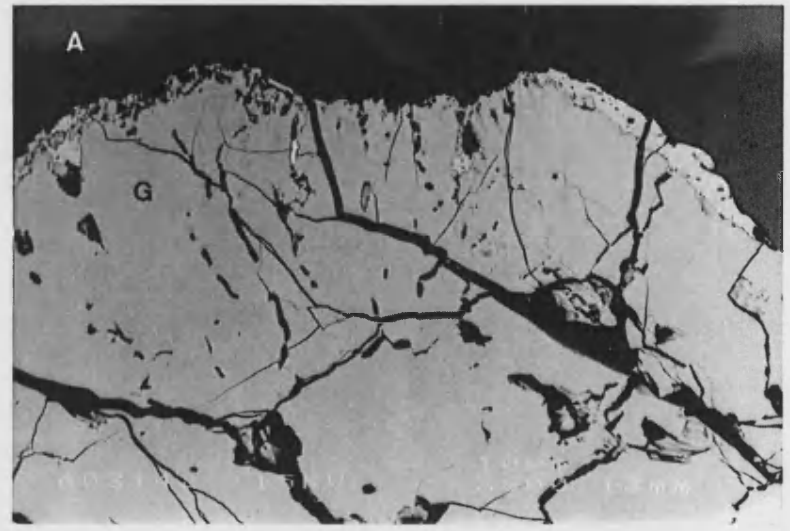

Figure 3.5b Fe-Al diffusion couple. 256hrs at 640°C.
A-Al, G-$FeAl_3$ 10μm

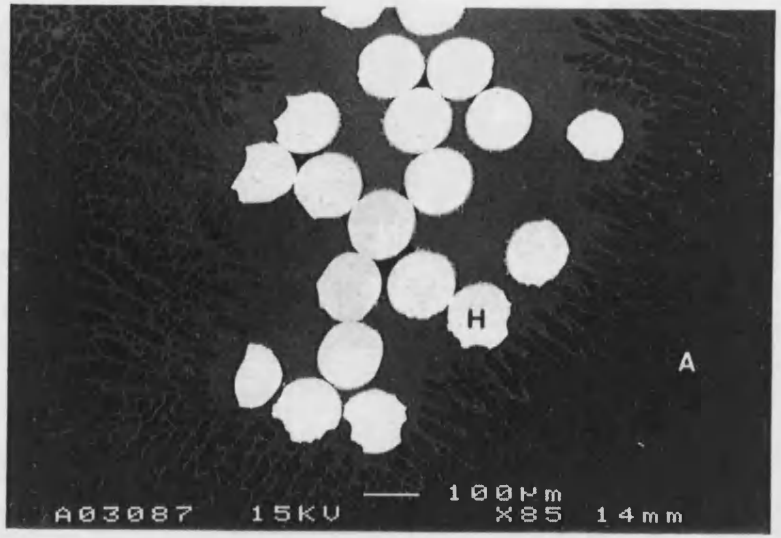

Figure 3.6a Ni-Al diffusion couple. 0hrs at 640°C.
A-Al, H-Ni 100µm

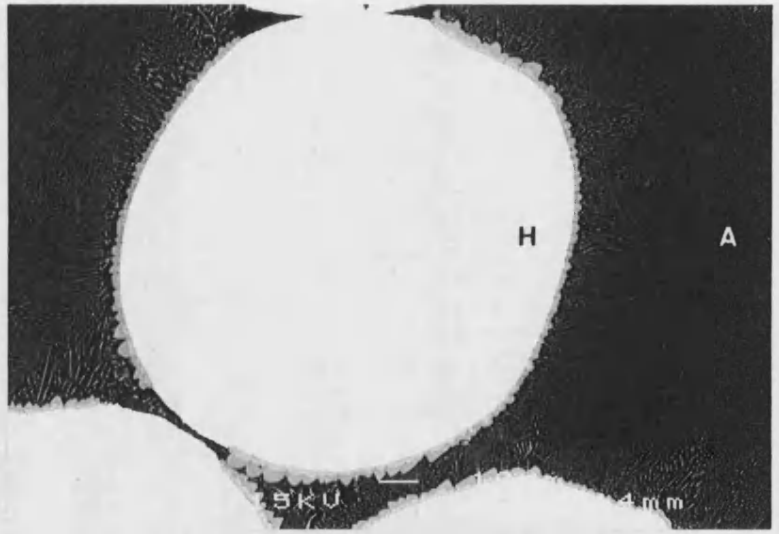

Figure 3.6b Ni-Al diffusion couple. 0hrs at 640°C.
A-Al, H-Ni 10µm

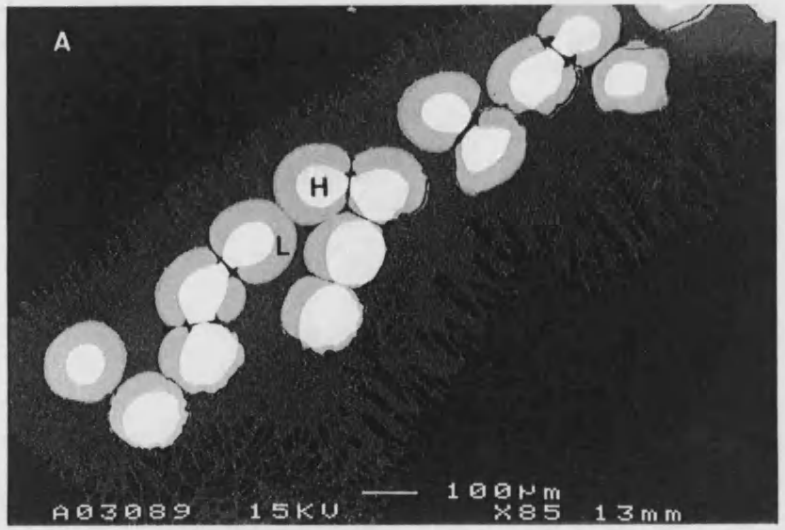

Figure 3.7a Ni-Al diffusion couple. 0.5hrs at 640°C.
A-Al, H-Ni, L-Ni_2Al_3 100µm

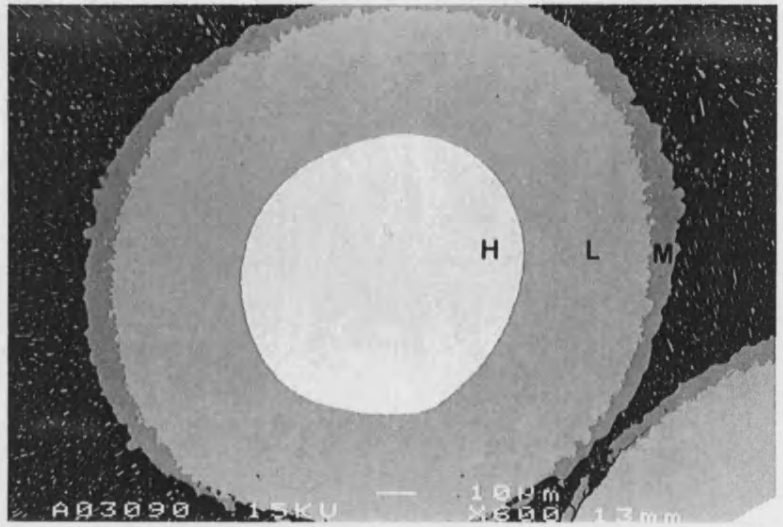

Figure 3.7b Ni-Al diffusion couple. 0.5hrs at 640°C.
H-Ni, L-Ni_2Al_3, M-$NiAl_3$ 10µm

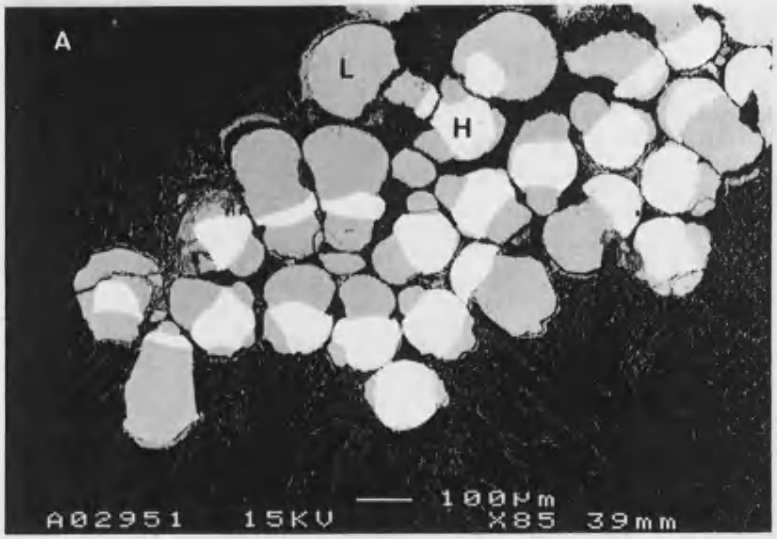

Figure 3.8a Ni-Al diffusion couple. 16hrs at 640°C.
A-Al, H-Ni, L-Ni_2Al_3 100µm

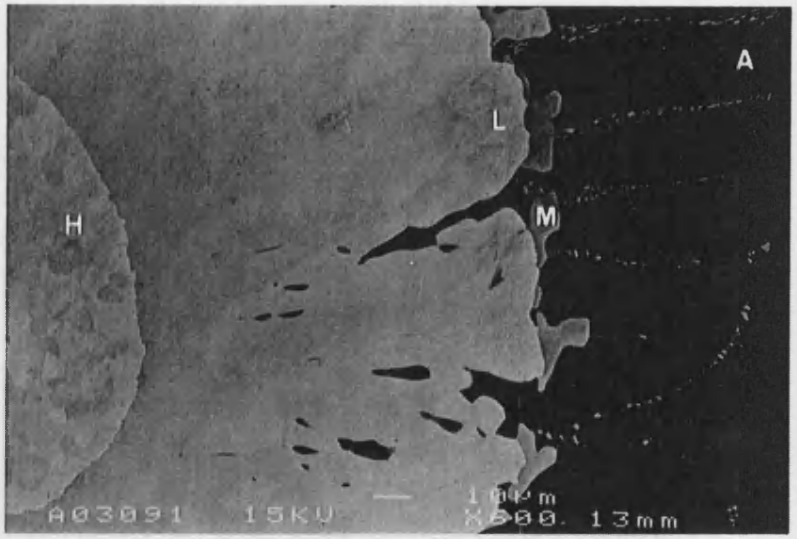

Figure 3.8b Ni-Al diffusion couple. 16hrs at 640°C.
A-Al, H-Ni, L-Ni_2Al_3, M-$NiAl_3$ 10µm

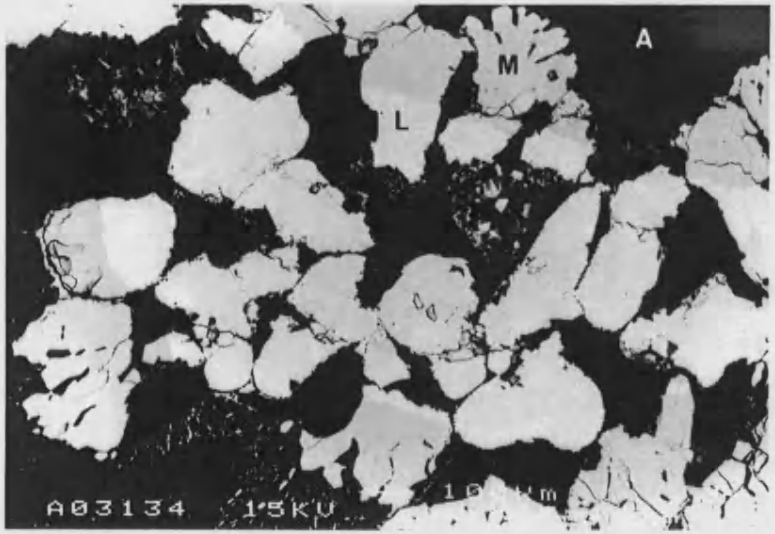

Figure 3.9a Ni-Al diffusion couple. 256hrs at 640°C.
A-Al, L-Ni_2Al_3, M-$NiAl_3$ 100µm

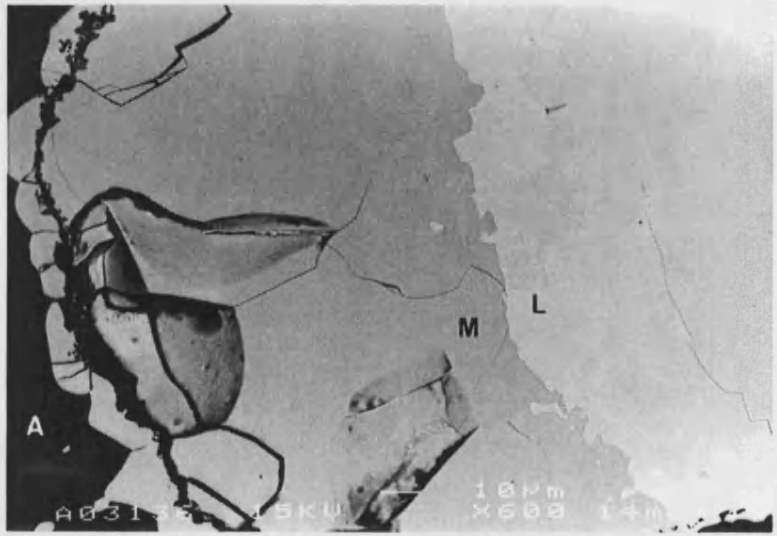

Figure 3.9b Ni-Al diffusion couple. 256hrs at 640°C.
A-Al, L-Ni_2Al_3, M-$NiAl_3$ 10µm

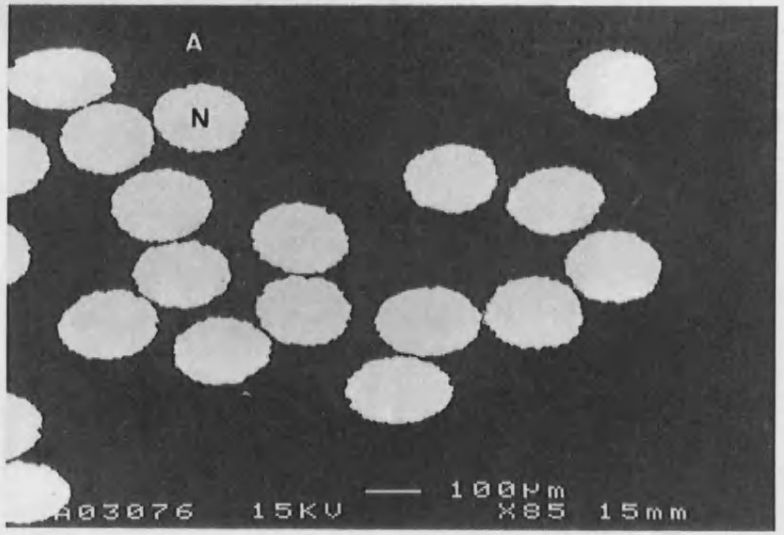

Figure 3.10a Ti-Al diffusion couple. 0hrs at 640°C.
A-Al, N-Ti 100µm

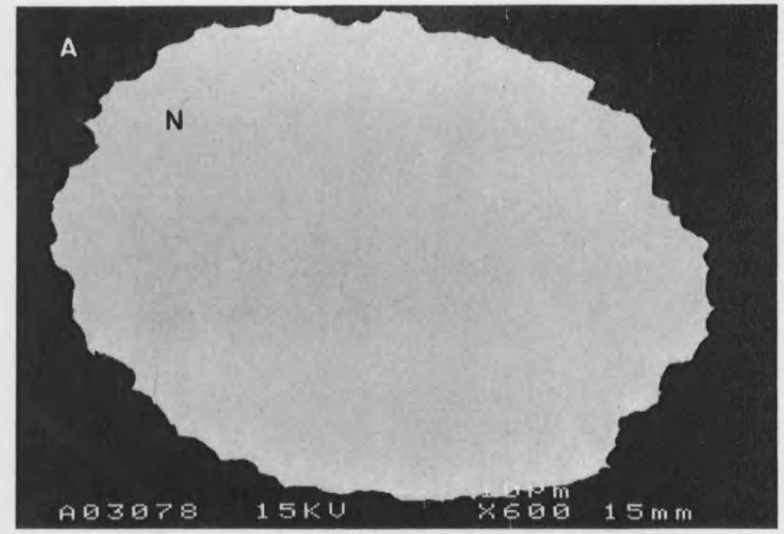

Figure 3.10b Ti-Al diffusion couple. 0hrs at 640°C.
A-Al, N-Ti 10µm

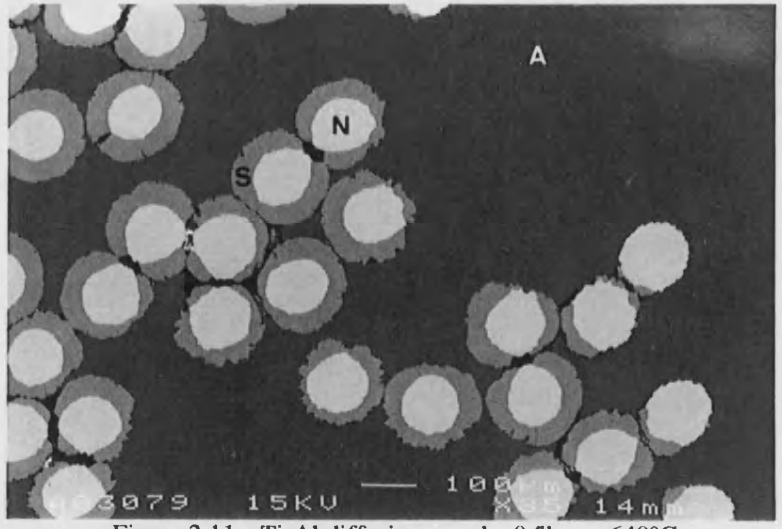

Figure 3.11a Ti-Al diffusion couple. 0.5hrs at 640°C.
A-Al, N-Ti, S-$TiAl_3$ 100µm

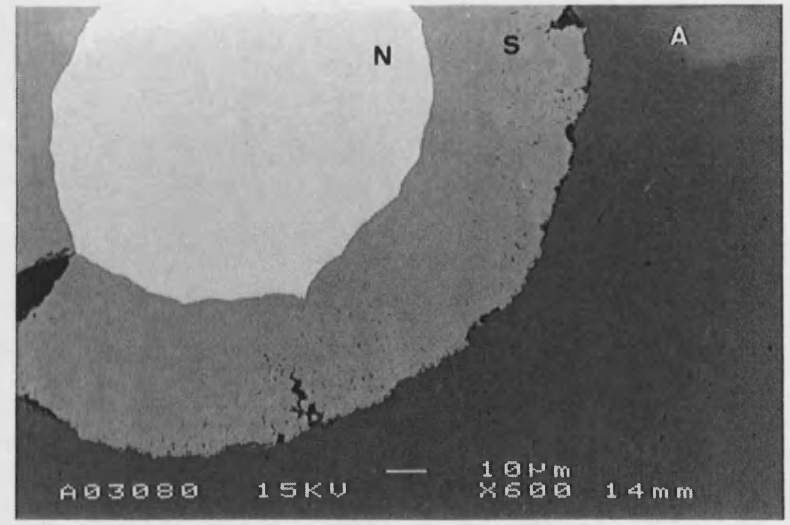

Figure 3.11b Ti-Al diffusion couple. 0.5hrs at 640°C.
A-Al, N-Ti, S-$TiAl_3$ 10µm

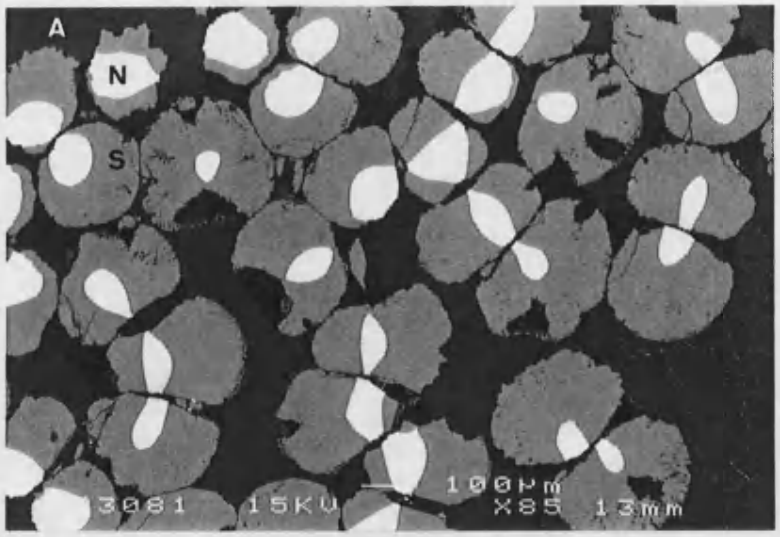

Figure 3.12a Ti-Al diffusion couple. 16hrs at 640°C.
A-Al, N-Ti, S-$TiAl_3$ 100µm

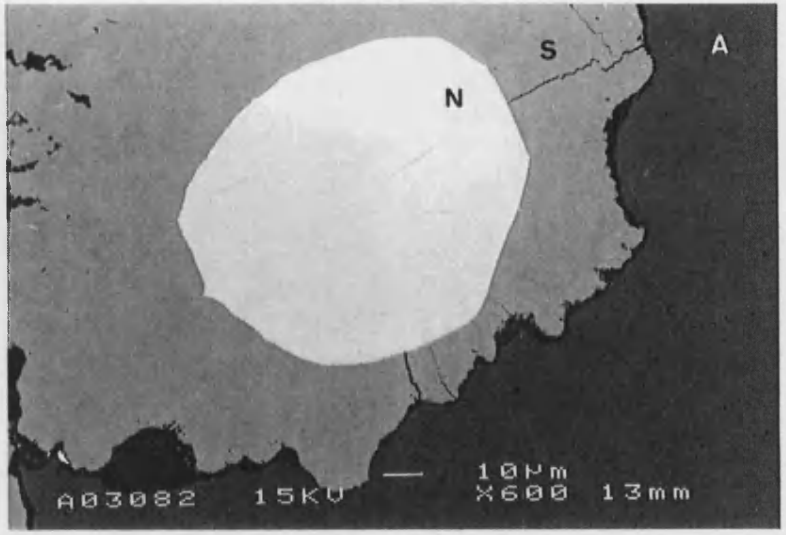

Figure 3.12b Ti-Al diffusion couple. 16hrs at 640°C.
A-Al, N-Ti, S-$TiAl_3$ 10µm

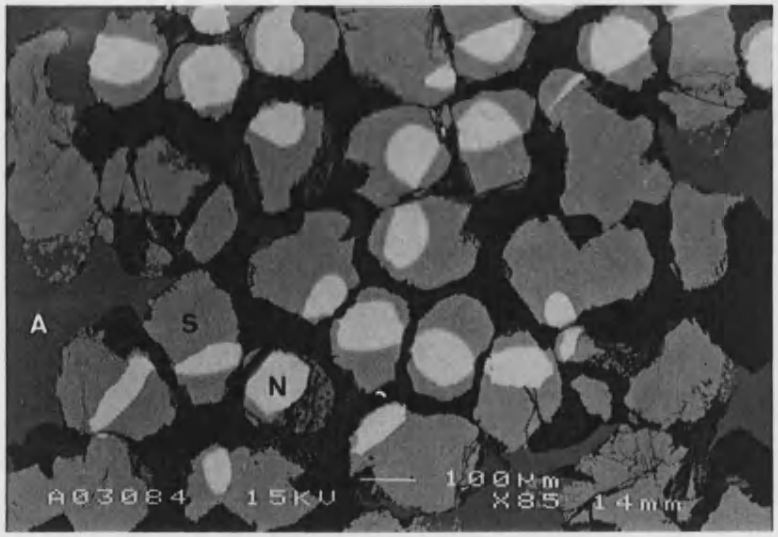

Figure 3.13a Ti-Al diffusion couple. 256hrs at 640°C.
A-Al, N-Ti, S-$TiAl_3$ 100µm

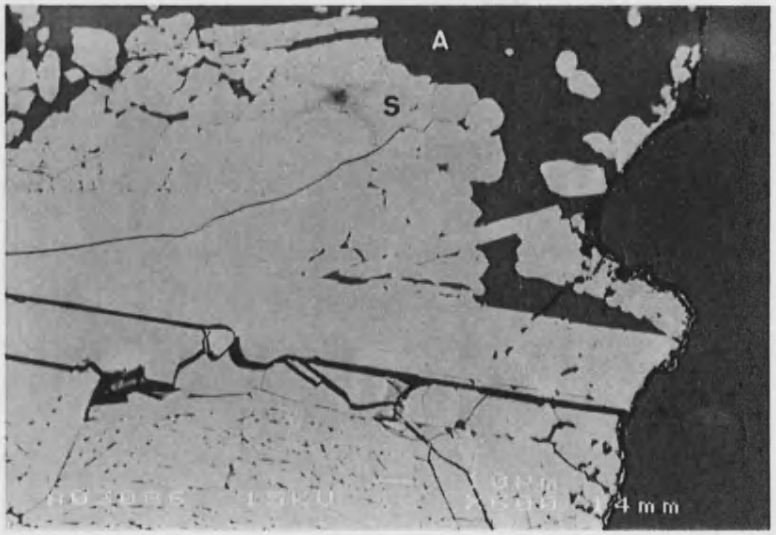

Figure 3.10a Ti-Al diffusion couple. 256hrs at 640°C.
A-Al, S-$TiAl_3$ 10µm

some of the liquid passed through the eutectic point at 655°C, Fe-99.1at%Al, Figure 1.2, producing a eutectic dispersion of $FeAl_3$ in aluminium. The actual composition of the dispersed phases appeared high in aluminium in comparison with the $FeAl_3$ phase boundaries, Table 3.1, but this may be explained by the difficulty in accurately calculating the composition of the small dispersoids. The dispersoids were dissolved back into the aluminium after heat treatment at 640°C.

It also appeared that once the aluminium had ceased moving past the iron wires, temperatures were sufficiently high for a long enough time to form the $FeAl_3$ intermetallic layer by solid-state diffusion. Heat treatments promoted further solid-state diffusion and $FeAl_3$ phase formation.

The major diffusing species through the intermetallic phase was aluminium. This was evidenced by the presence of pores on the aluminium side of the intermetallic. The Kirkendall effect stating that for two inter-diffusing phases, pores will form in the phase from which atoms are most rapidly diffusing[124]. The formation of the $FeAl_3$ intermetallic was constrained by volume considerations. The volume that one mole of $FeAl_3$ occupied was $36.00cm^3$, whilst the volume that one mole of iron occupied was $7.07cm^3$. Hence the intermetallic could not be contained within the original volume of the wire and extended into the aluminium.

The rough $FeAl_3$/iron interface indicated that the growth of the $FeAl_3$ into the iron was controlled by grain boundary diffusion, whilst the smoother aluminium/$FeAl_3$ interface suggested its growth into the aluminium was controlled by volume diffusion. The aluminium/$FeAl_3$ interface became distorted by heat treatments, due to pore formation between the aluminium and the intermetallic and local restrictions in the amount of aluminium available. After 256hrs at 640°C, the rate of formation of $FeAl_3$ had been sufficiently rapid to consume all the iron, but the resulting microstructure was very porous.

As mentioned previously, pore formation was concentrated in regions originally surrounded by iron wires. This was because the large consumption of aluminium from these regions to form $FeAl_3$ resulted in pores, formed by the Kirkendall effect and volume changes. However, the large volume of pores formed could not be solely attributed to these two factors. Calculations show that the formation of $1.00cm^3$ of

$FeAl_3$ would only cause a reduction in volume of $0.03cm^3$. It is therefore contended that the remaining porosity was a result of the loss of the brittle and weakly held intermetallic during preparation of the sample surface.

3.4.2 Nickel-Aluminium

As in the iron-aluminium diffusion couples, a eutectic dispersion was formed around the nickel wires during casting due to the dissolution of nickel by molten aluminium. As the aluminium cooled, it passed through the eutectic point corresponding to Ni-97at%Al at 639.9°C, Figure 1.4. The dispersoids were initially too small for accurate measurement of their composition by EPMA, but after heat treatments they became coarser and allowed more accurate EPMA measurements to be taken, whereupon it was found that the phases fell within the $NiAl_3$ phase range.

Once the aluminium had solidified, thin regions of intermetallic phases formed around the nickel wires during cooling, with compositions corresponding to $NiAl_3$ and Ni_2Al_3. It was reported that the growth of the $NiAl_3$ phase is controlled by both grain boundary and volume diffusion, whilst the growth of the Ni_2Al_3 phase is controlled by volume diffusion[125,126]. In comparison with the iron-aluminium diffusion couple, the intermetallic phases increased in width and the transition metal was consumed at a faster rate. After 256hrs, the nickel had disappeared and the intermetallic phases were mainly Ni_2Al_3 with small regions of $NiAl_3$ around the outer edge. Unlike the $FeAl_3$ phase, these intermetallics were relatively free from cracks.

The jagged interface between the aluminium and the $NiAl_3$ in the as-cast sample became smoother during heat treatment. This suggests that, initially, the nickel was dissolved into the aluminium as it cooled, forming $NiAl_3$ around the wire and giving the jagged interface. This was then smoothed out as aluminium diffused into the $NiAl_3$ during heat treatment. The observation that after heating at 640°C for 16hrs, pores began to form between the two intermetallic phases indicated that aluminium was diffusing faster than nickel into the Ni_2Al_3.

The expansion of intermetallic phases out of the nickel wires was to accommodate the lower density intermetallics, since calculations show that one mole each of $NiAl_3$ and

Ni_2Al_3 occupies a volume of 77.11cm^3, whereas the nickel required to form them only occupies a volume of 19.79cm^3.

The reasonably constant composition of $NiAl_3$ across its width and the increase in the nickel content of the Ni_2Al_3 phase towards the Ni_2Al_3/nickel interface may be explained by studying the nickel-aluminium phase diagram, Figure 1.4, where it can be seen that $NiAl_3$ exists over a very narrow composition in comparison with Ni_2Al_3. A composition gradient is required for diffusion to occur[127], hence the Ni_2Al_3 was able to form a wider phase than the $NiAl_3$ during the heat treatments due to the presence of a steeper concentration gradient.

The formation of large pores between the nickel wires was due to a combination of factors. As mentioned for the iron-aluminium diffusion couples, pores were formed through the Kirkendall effect and through changes in volume. Regions between nickel wires were particularly susceptible to porosity as aluminium was consumed on all sides. Performing the same calculations as before, to form 1.00cm^3 each of $NiAl_3$ and Ni_2Al_3 would result in an increase in porosity of 0.07cm^3. It is also noted that some of the intermetallic compounds were again lost during sample preparation.

3.4.3 Titanium-Aluminium

Unlike the other two systems, the titanium-aluminium diffusion couples did not produce a dispersed phase during casting. There were three reasons for this:

i) The titanium-aluminium phase diagram had no eutectic point at the aluminium end, Figure 1.6.

ii) Titanium did not readily diffuse into aluminium[93,121,128] which restricted the titanium content to a composition within the solid solution of titanium in aluminium.

iii) The thermodynamic stability of the titanium oxides, compared with aluminium oxide, was much greater than the iron and nickel oxides, Figure 3.14.

Thus, iron and nickel oxides were reduced by the aluminium much more quickly than the titanium oxide, which exposed the metals and allowed their rapid dissolution into the aluminium.

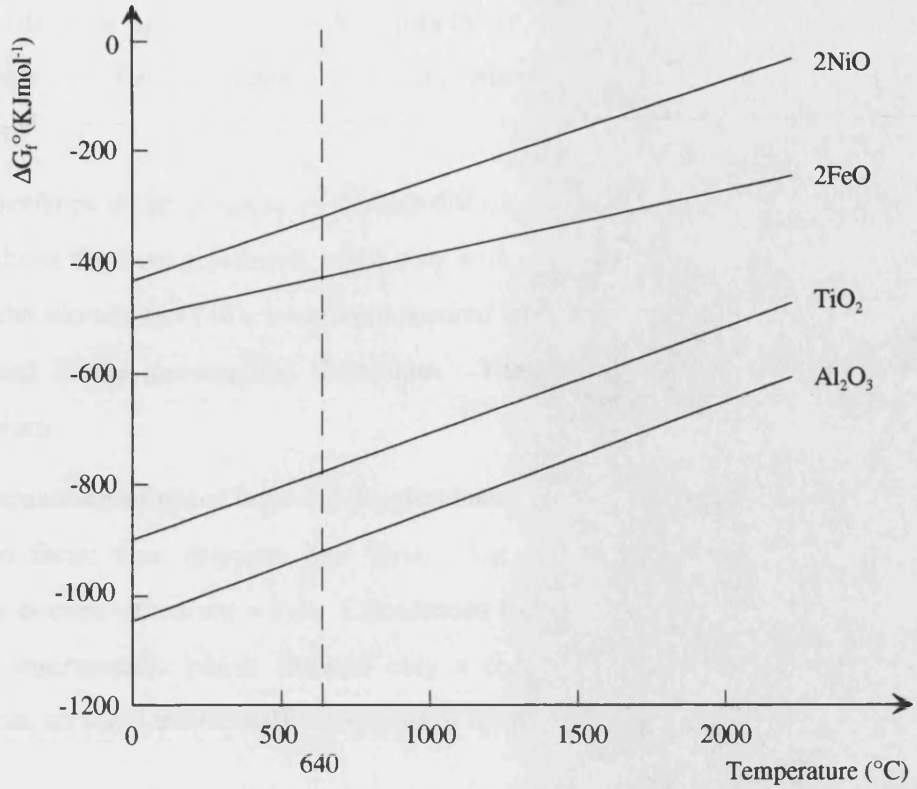

Figure 3.14 Ellingham diagram[101]

The cast sample did not show any intermetallic formation during cooling, which indicated a low rate of diffusion of aluminium into titanium. The $TiAl_3$ intermetallic was formed after the samples were heat treated at 640°C, as noted in other reports[129]. The width of the $TiAl_3$ intermetallic phase region after 0.5hrs and 16hrs was greater than the $FeAl_3$ phase for the same heat treatment times, but narrower than the nickel-aluminium phases. Hence, the diffusion of aluminium through $TiAl_3$ must be more rapid than diffusion of aluminium through titanium. However, there seemed to be another contradiction after heat treating for 256hrs. In both the previous systems, all the transition metal regions had been consumed after 256hrs. This was not the case for the titanium-aluminium system which still contained large regions of titanium. One explanation is that the regions containing titanium were mostly isolated from the aluminium by pore formation which prevented further formation of $TiAl_3$, but it is not clear why this did not occur in the other two systems.

The $TiAl_3$ again expanded outwards from the titanium due to a volume effect. That is one mole of $TiAl_3$ occupied $37.89cm^3$, whereas one mole of titanium occupied $10.64cm^3$.

The interfaces in the titanium-aluminium diffusion couples remained reasonably smooth throughout the heat treatment. The only noticeable difference occurred after 256hrs when the aluminium/$TiAl_3$ interface appeared to fragment and particles of $TiAl_3$ were produced in the surrounding aluminium. The was due to $TiAl_3$ dissolving in the aluminium.

The occurrence of pores between the aluminium and the $TiAl_3$ suggests that aluminium diffuses faster than titanium into $TiAl_3$. Larger pores were again concentrated in regions between titanium wires. Calculations for volume changes on forming $1.00cm^3$ of the intermetallic phase showed only a reduction of $0.06cm^3$ from the original elements, so some intermetallic compounds must have been lost during polishing.

3.4.4 Summary

Intermetallic phases were formed by a process of solid-state diffusion at 640°C. However, the intermetallics all had high aluminium contents (XAl_3 and X_2Al_3) and were not the major structural phases (XAl, X_3Al) of their respective systems. It must be assumed that the XAl and X_3Al phase regions were present in the diffusion couples, between the detected intermetallic phases and the transition metal, but that they were too small to be resolved[124,127,130]. The width of a phase region within a system was dependent on the relative velocities of its two interfaces. The two interfaces did not move with the same velocity and it is conceivable that a situation occurred where one interface closely followed the other, forming an intermetallic phase too thin to resolve. The interface velocities were proportional to the interdiffusion coefficients[131] of the phases either side of it. A high interdiffusion coefficient allowed a phase to grow quickly and this encouraged its interfaces to move rapidly outwards. If this phase bordered on a neighbouring phase with a substantially lower interdiffusion coefficient, then the interface between the two would closely follow the other, more slowly moving interface, of the neighbouring phase.

Intermetallic Phase	Interdiffusion Coefficient at 870°C (m^2/s)
Ni_2Al_3	3.2×10^{-11}
NiAl	4.6×10^{-15}
Ni_3Al	1.5×10^{-15}

Table 3.5 Interdiffusion coefficients[131,132]

Unfortunately, the availability of interdiffusion coefficients at 640°C for all the systems encountered in this study was limited. Table 3.5 details the interdiffusion coefficients for some of the phases in the nickel-aluminium system at 870°C. It can be seen that the coefficient for the Ni_2Al_3 phase is much larger than those for NiAl or Ni_3Al; this is consistent with the greater width of the Ni_2Al_3 phase.

Intermetallic phases were found to form most rapidly in the nickel-aluminium system. However, the time taken to produce these phases through solid-state diffusion was too long to be economically practical and, furthermore, pore formation was also found to be excessive in all the final materials. To solve these problems, a route using liquid-state reactions to reduce process times and pressure to prevent the formation of pores was required. As a first step, a liquid-state reaction was attempted by adding transition metal powders to molten aluminium, the details of which are given in Section 4.

Section 4

MIXING OF TRANSITION METAL POWDERS WITH MOLTEN ALUMINIUM

From the results of the previous set of experiments it was decided to produce intermetallic compounds by liquid-state reactions. This was achieved by adding transition metal powders to molten aluminium.

4.1 Materials

The materials used in this section were bulk super-pure aluminium and the iron, nickel and titanium transition metal powders described in Section 2. PSD2 of each transition metal powder was used.

4.2 Experimental Procedures

The apparatus shown in Figure 4.1 was used to heat 80g of aluminium to 850°C in an alumina crucible. This temperature matched that of the molten aluminium used to

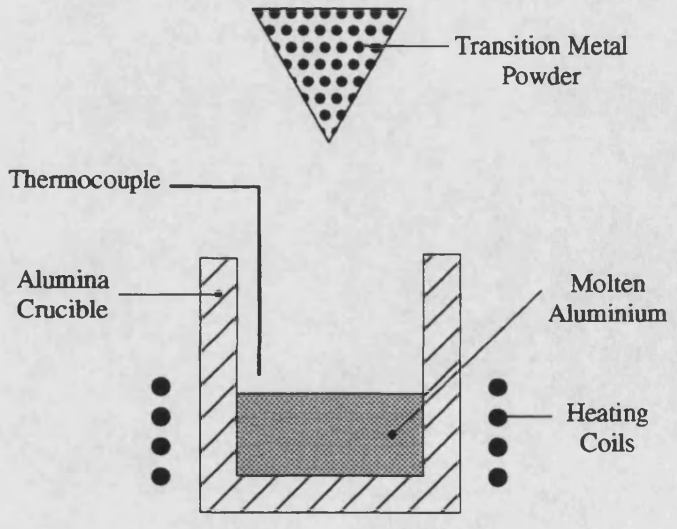

Figure 4.1 Apparatus

prepare the diffusion couples in the previous section. Once the aluminium had been heated to the correct temperature, the heat supply was removed and 15g of one of the transition metal powders, either iron, nickel or titanium was immediately added to the aluminium by pouring it into the top of the crucible. Any temperature increase was measured by a thermocouple placed just above the molten aluminium.

The resulting material was then allowed to cool to room temperature before being sectioned and prepared for SEM and EPMA analysis.

4.3 Results

As the transition metal powders were poured into the molten aluminium, a cloud of glowing particles emerged from the top of the crucible. It was noticed that the molten aluminium was covered in an alumina film, but this did not prevent some of the powder from reacting with it. Table 4.1 lists the temperatures and observations recorded for each system.

After the resulting materials had been cut into samples and polished, it was obvious from optical examination that multiple phases were present in all the samples. Analysis of the samples by SEM and EPMA revealed the presence of the phases detailed in Table 4.2.

4.3.1 Iron-Aluminium

Figures 4.2a-c show the two phase microstructure produced in the iron-aluminium system. Flakes and needles of $FeAl_3$ (C) were distributed in a matrix of a solid solution of iron in aluminium (A), Table 4.2. The regions containing flakes had denser distributions of $FeAl_3$ than those containing needles. The distribution of the regions appeared to be random and the whole sample was free from pores.

System	Maximum Temperature (°C)	Comments
Fe-Al	850	Cloud of glowing particles
Ni-Al	1100	-
Ti-Al	1050	Cloud of glowing particles

Table 4.1 Temperatures and observations

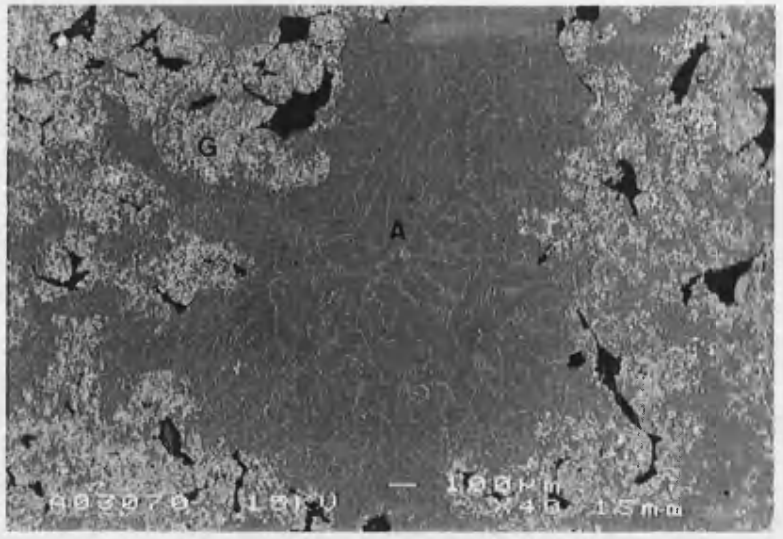

Figure 4.2a Fe powder added to molten Al.
A-Al, G-$FeAl_3$ 100μm

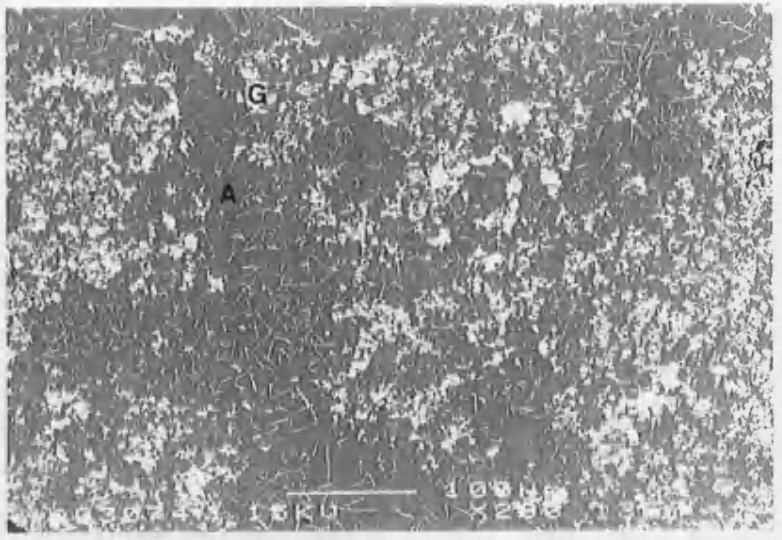

Figure 4.2b Flakes of $FeAl_3$ in Al.
A-Al, G-$FeAl_3$ 100μm

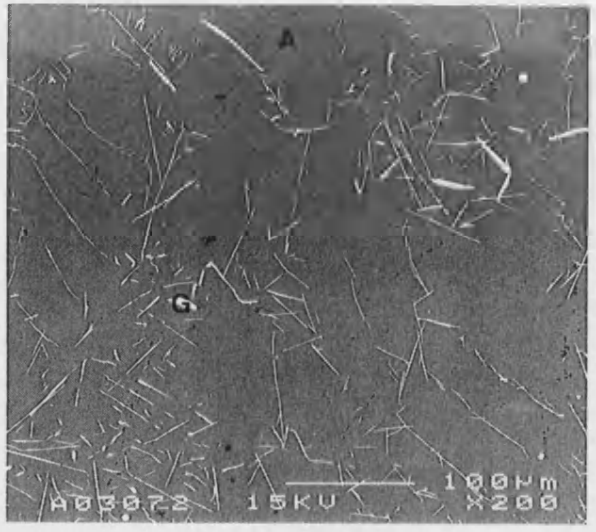

Figure 4.2c Needles of $FeAl_3$ in Al.
Al, G-$FeAl_3$ 100μm

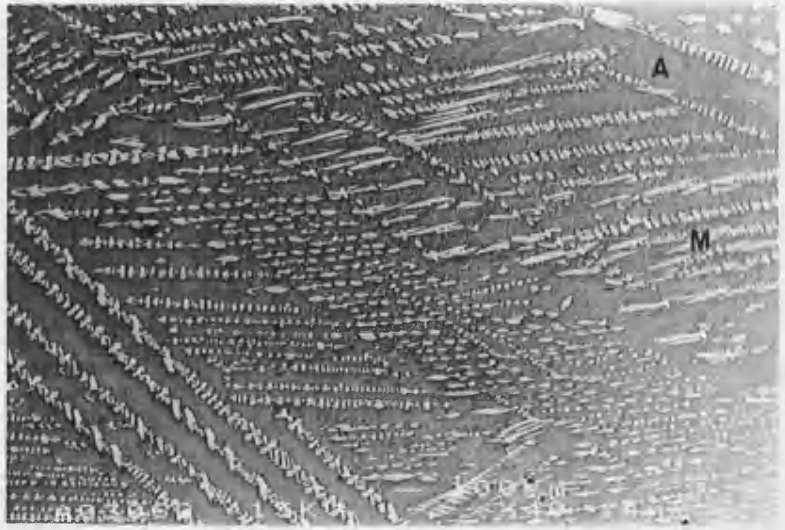

Figure 4.3a Ni powder added to molten Al.
A-Al, M-$NiAl_3$ 100μm

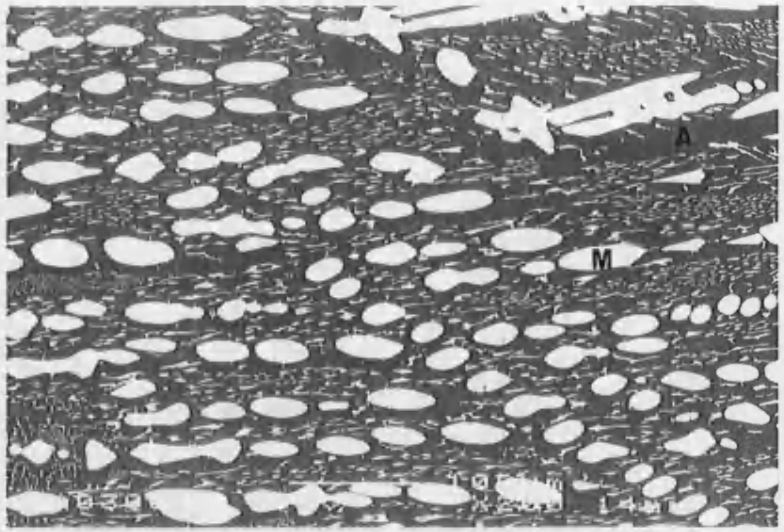

Figure 4.3b Dispersion of $NiAl_3$ in Al.
A-Al, M-$NiAl_3$ 100μm

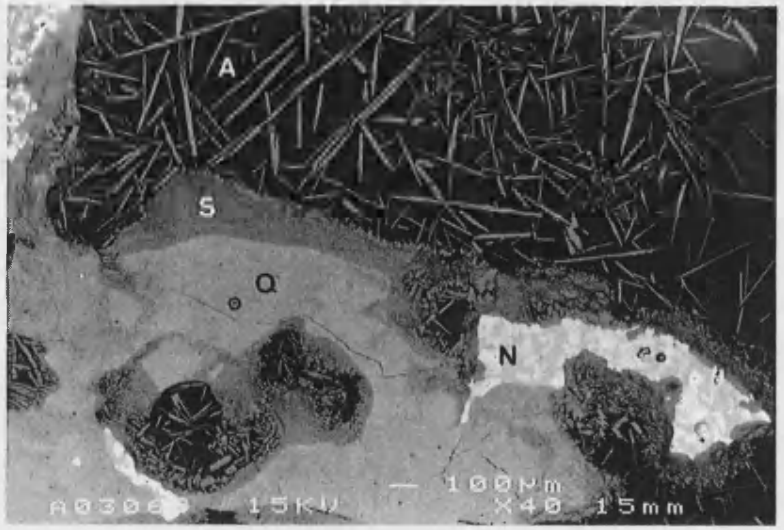

Figure 4.4a Ti rich area in Al.
A-Al, N-Ti rich, Q-TiAl, S-$TiAl_3$ 100μm

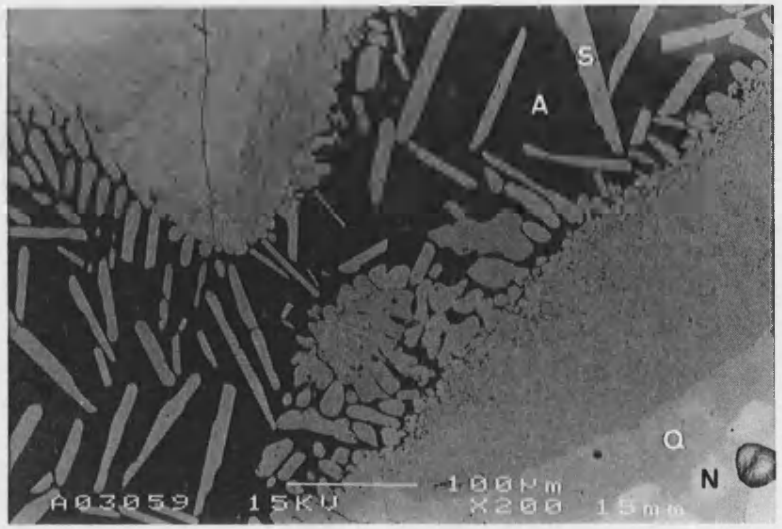

Figure 4.4b Dispersion of $TiAl_3$ in Al.
A-Al, N-Ti rich, Q-TiAl, S-$TiAl_3$ 100μm

System	Phase	X (at%)		Al (at%)		Alloy/ Compound
		Mean	SD	Mean	SD	
Fe-Al	A	0.0	0.0	100.0	0.0	Al
	$C_{(needles)}$	22.2	1.0	77.8	1.0	$FeAl_3$
	$C_{(flakes)}$	23.3	0.5	76.7	0.5	$FeAl_3$
Ni-Al	A	0.3	0.2	99.7	0.2	Al
	M	24.1	0.4	75.9	0.4	$NiAl_3$
Ti-Al	A	0.2	0.5	99.8	0.5	Al
	N	85.0	0.9	15.0	0.9	Ti
	Q	44.7	0.3	55.3	0.3	TiAl
	S	25.0	0.1	75.0	0.1	$TiAl_3$

Table 4.2 EPMA data

4.3.2 Nickel-Aluminium

As in the iron-aluminium system, this sample contained two phases, Figures 4.3a-b. The microstructure consisted of a fine eutectic dispersion of $NiAl_3$ (M) in a solid solution of nickel in aluminium (A), Table 4.2. A temperature rise to 1100°C was measured for this reaction, which produced a fully dense sample.

4.3.3 Titanium-Aluminium

This was the most inhomogeneous material produced, Figures 4.4a-b. A matrix, consisting of a solid solution of titanium in aluminium (A), contained a dispersion of $TiAl_3$ needles (S) and regions consisting of TiAl (Q) and a supersaturated solid solution of aluminium in titanium (N). The reaction produced a temperature rise to 1050°C and a fully dense sample.

4.4 Discussion

Both the iron and titanium systems produced a cloud of glowing particles as the powdered transition metals were added to the molten aluminium. Some of the powder particles, heated in the brief time they were in the crucible, were glowing when they were caught in convection currents and carried upwards. However, this was not noticed for the nickel powder. It can only be assumed that the denser nickel particles, coupled with their small size, prevented them from being caught.

The penetration of the alumina coating by the transition metal powders was dependent on the stability of their oxides in comparison to the alumina. The iron and nickel oxides were more unstable than the titanium oxide, Figure 3.14, and they were quickly reduced. Thus, they interacted with and penetrated the alumina film more rapidly than the titanium.

4.4.1 Iron-Aluminium

A rapid liquid-state reaction occurred between the molten aluminium and the iron powder. The powder that reached the aluminium was dissolved into the melt and formed an aluminium rich solution. By adding 15g of iron to 80g of aluminium, and with uniform mixing of the two elements, a composition of Fe-91.7at%Al was produced. At 850°C this existed as $FeAl_3$+liquid, Figure 1.2, which precipitated flakes of $FeAl_3$ as it cooled to the eutectic temperature. The fraction of the material still liquid just above the eutectic temperature of 655°C produced the eutectic dispersion of needle shaped $FeAl_3$ in a solid solution of iron in aluminium. This resulted in the room temperature microstructure of $FeAl_3$ flakes and needles.

Even though the formation of $FeAl_3$ was exothermic, Table 1.2, no exotherm was recorded by the thermocouple in the crucible. This was due to a combination of two factors. First, the enthalpy of formation of $FeAl_3$ was only weakly exothermic, around a third of the values of $NiAl_3$ and $TiAl_3$, and second, the thermocouple was not actually within the reacting material, thus reducing its sensitivity.

4.4.2 Nickel-Aluminium

By adding 15g of nickel to 80g of aluminium and with complete mixing of the two elements, a composition of Ni-92.1at%Al was produced. This existed as a liquid phase at 850°C, Figure 1.4, which cooled to near 750°C before $NiAl_3$ was precipitated. As in the iron-aluminium system, a large proportion of the material was still liquid just above the eutectic temperature of 639.9°C and this produced a large eutectic dispersion of $NiAl_3$ in a solid solution of nickel in aluminium. The more uniform dispersion of the XAl_3 phase in the nickel-aluminium system was due to the presence

of only a liquid phase to a much lower temperature than in the iron-aluminium system, where $FeAl_3$ flakes were formed as soon as the iron was added to the aluminium.

A temperature rise was recorded by the thermocouple once the two elements had been added together. The enthalpy of formation of $NiAl_3$ was approximately three times that of $FeAl_3$ and thus the temperature rise caused by this reaction was sufficient to be measured by the thermocouple.

4.4.3 Titanium-Aluminium

A composition of Ti-9.6at%Al would have been produced if 15g of titanium and 80g of aluminium were completely mixed. This composition would have formed a much smaller proportion of liquid phase at 850°C than either of the two previous systems. However, at 850°C in the titanium-aluminium phase diagram, Figure 1.6, the addition of even a small amount of titanium to the aluminium precipitated $TiAl_3$. Approximately 36at% of the titanium-aluminium would have been liquid, compared to 78at% for the iron-aluminium and 100at% for the nickel-aluminium compositions. The low proportion of liquid phase hindered the mixing of the titanium and aluminium and coupled with the relatively slow penetration of the alumina film, a very inhomogeneous structure was produced. This formed the regions containing titanium rich phases scattered within regions of $TiAl_3$ needles in a solid solution of titanium in aluminium.

A temperature rise was again recorded by the thermocouple. Despite the lack of mixing, the intermetallic phases formed released sufficient heat to allow the thermocouple to measure a temperature rise.

4.4.4 Summary

Temperature rises were measured in the nickel-aluminium and titanium-aluminium systems as the transition metals reacted with the aluminium. A rapid liquid-state reaction and a large area of reaction between the molten aluminium and the transition metal powders allowed a rapid release of energy as the intermetallic phases quickly formed. This heated the reaction and an exotherm was measured.

Although the same elements were used, a much higher extent of reaction was achieved in this section than in Section 3. Even though the initial aluminium melt temperatures

were the same, the aluminium in Section 3 was quickly solidified when it was introduced into the die. This limited liquid-state reactions in Section 3 to a brief period before there was good contact between the reactants. The dimensions of the transition metals also varied. Wires were used in Section 3 whilst the powders used in Section 4 greatly increased the surface area and thus the area of reaction. The resulting rise in temperature in Section 4 allowed the aluminium to remain molten for a longer time and thus sustained the rapid liquid-state reaction.

Finally, the proportions of reactants varied between the two sections. The transition metals in Section 3 were effectively swamped by the large quantity of aluminium and any energy released by the limited intermetallic formation was quickly conducted away from the intermetallic and dispersed into the aluminium.

The samples in this section were all found to be free from pores, a fact attributed to the presence of the liquid phase. The liquid phase filled pores produced by volume changes and negated the Kirkendall effect which occurred in solid-state diffusion.

Therefore, it was found that the presence of a liquid rapidly formed intermetallic phases and reduced porosity and if the area of reaction was sufficiently large then the reaction became self-sustaining. To achieve this, the reactants had to be heated until a liquid phase formed, the remaining solid reactants had to have a large surface area to volume ratio and the reactants had to be well mixed. Further, the majority of the phases formed in this section were XAl_3 intermetallics. To produce the XAl intermetallics the correct proportions of each constituent element were required. This was difficult to achieve in the above apparatus since some of the transition metal powders were lost to convection currents.

To accomplish the above, two reactive synthesis routes were investigated. In the first route, developed in Sections 5 to 8, powders of the constituent elements were mixed together in the correct proportions and heated until a liquid phase was formed. This being an attempt at a thermal explosion. In the second route, Section 9, the liquid phase of one of the constituents infiltrated a porous preform of the remaining constituents, a reactive liquid metal infiltration route.

Section 5

THERMAL EXPLOSIONS IN LOOSE POWDERS

In order to produce an XAl intermetallic phase, a liquid-state reaction was initiated in a correctly proportioned mixture of the constituent elements.

5.1 Materials

PSD2 titanium powder was mixed with aluminium powder. Details of both powders are given in Section 2.1.

5.2 Experimental Procedures

Titanium and aluminium powders were weighed out in a 50/50at% ratio to give a combined mass of 150g. These powders were mixed by placing them in a ceramic pot containing 250g of assorted alumina balls and sufficient acetone to cover the powder and balls. The pot was sealed, placed on a Berco ball mill and rotated at 30 'Rotary Regavolts'. After four hours, it was opened and the acetone was allowed to evaporate. The powder mixture was separated from the balls by sieving.

50g of the powder mixture was placed in the bottom of an alumina crucible and an alumina mat cover was placed over it, Figure 5.1. The cover prevented reactant

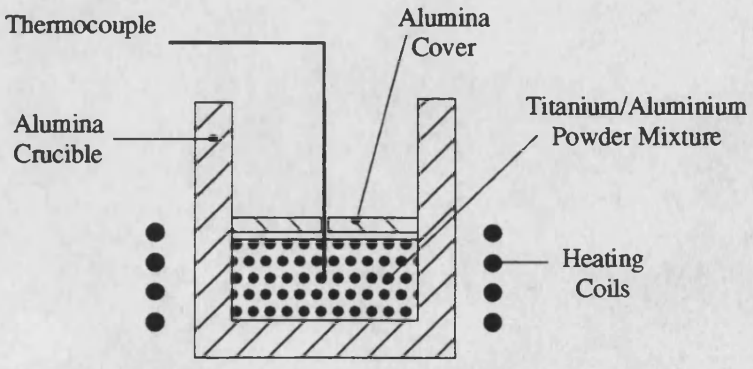

Figure 5.1 Apparatus

particles from being caught in convection currents. A thermocouple was used to monitor temperatures during the experiment and this was placed through the alumina cover and into the powder mixture.

The crucible was heated by the surrounding heating coils until an exotherm was measured by the thermocouple. A sharp temperature rise indicated the onset of such an exothermic reaction. At this point the heating coils were switched off and the crucible was allowed to cool. Both the initiation temperature and the peak temperature of the reaction were noted. The material in the crucible was sectioned and prepared for examination using the routine detailed in Section 2.2.

5.3 Results

5.3.1 Titanium-Aluminium

By monitoring the thermocouple reading by eye, an approximate initiation temperature of 700°C and a peak temperature of 1300°C were recorded. The rise to the peak temperature was very rapid, less than 5 seconds, but this temperature was not maintained and soon decreased.

The majority of the material was found to consist of a highly porous microstructure. Only a small region in the centre, with a porosity of 53.8±9.3%, was sufficiently dense to be polished, Figure 5.2.a. A SEM image of this region revealed an inhomogeneous microstructure, Figure 5.2.b. Light regions (N) and two-phase lamellar regions (P) were dispersed in a darker background phase (Q). EPMA revealed that the light regions were solid solutions of aluminium in titanium, the darker regions had a composition corresponding to TiAl and the lamellar regions had an overall composition of Ti-37at%Al, Table 5.1. The layers in the lamellar regions were

System	Phase	Ti (at%)		Al (at%)		Alloy/ Compound
		Mean	SD	Mean	SD	
Ti-Al	N	98.2	1.3	1. 8	1.3	Ti
	P	63.0	2.8	37.0	2.8	TiAl/Ti_3Al
	Q	48.8	2.6	51.2	2.6	TiAl

Table 5.1 EPMA data

too thin to analyse individually by EPMA, but several sources have reported that they are alternating plates of the darker TiAl and lighter Ti_3Al phases[3,8,15].

5.4 Discussion

5.4.1 Titanium-Aluminium

The TiAl and Ti_3Al intermetallic phases were formed in the centre of the mixture and the rise in temperature recorded by the thermocouple indicated that an exothermic reaction had occurred within the crucible. These results suggested that a thermal explosion had been produced within the powder mixture.

The exothermic reaction was seen to initiate around 700°C, but an error was involved when optically monitoring the thermocouple read-out. The thermocouple temperature was only updated every second on the read-out and as the temperature quickly increased, once the thermal explosion had been initiated, the exact initiation temperature was easily missed. An estimation of the error involved, based on data from subsequent experiments, gave a value of ±50°C. Therefore, the hypothesis that the thermal explosion was initiated when a liquid phase formed[2] was seen to be reasonable. Examination of the titanium-aluminium phase diagram, Figure 1.6, indicated that the lowest temperature at which a liquid phase formed was 660°C, the melting point of aluminium, which was within the error range.

The loose, porous nature of the majority of the final material was a result of the loosely packed reactant powders. A large amount of porosity was present in the powder mixture prior to the thermal explosion and any further increase in porosity due to volume changes in forming the intermetallic phases was insignificant in comparison. The widely spaced powder particles hindered any consolidation by capillary action drawing liquid between them and the crucible walls helped to quench the reaction and quickly solidified any liquid phase formed. The centre of the material, being the furthest away from the quenching effect of the crucible walls, maintained a higher temperature for a longer period of time since there was a lower rate of heat loss. This produced a larger quantity of liquid phase and thus a denser central region. Swelling

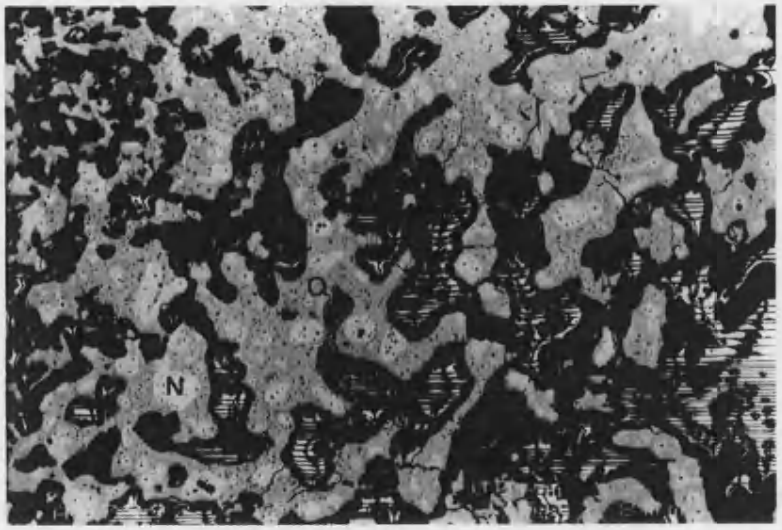

Figure 5.2a Thermal explosion of Ti-Al powder mixture.
N-Ti rich, Q-TiAl 100μm

Figure 5.2b Thermal explosion of Ti-Al powder mixture.
N-Ti rich, P-TiAl/Ti_3Al, Q-TiAl 100μm

of the compact due to the formation of a liquid phase did not occur since the original porosity was easily able to accommodate it.

The duplex microstructure of single-phase TiAl grains and two-phase TiAl/Ti_3Al lamellar grains was consistent with rapidly cooling a Ti-50at%Al composition from 1300°C[7,15,50]. A Ti-50at%Al composition at 1300°C existed in the $\alpha+\gamma$ phase field. Where α is a solid solution of aluminium in titanium and γ is TiAl. Rapid cooling from this temperature did not allow the α phase time to transform to the equilibrium structure of TiAl and it became quenched into the microstructure. As the material was cooled to below 1125°C[8], the α phase transformed into TiAl and Ti_3Al to give the lamellar grains present in the sample.

The light regions of the sample were found to be titanium rich areas and their presence indicated that the reaction had not continued to completion. These were the remnants of large titanium particles in the powder mixture which had not reacted fully before the reactive synthesis was quenched. These titanium rich regions were surrounded by two-phase lamellar regions. This was not surprising as the preferred composition to form lamellar phase is titanium rich Ti-48at%Al[5,15].

5.4.2 Summary

The liquid produced during the thermal explosion increased the rate of intermetallic phase formation through liquid-state reactions and provided some consolidation in the central region of the mixture. This experiment demonstrated that with a good mixing of reactants in the correct atomic ratio, it was possible to form the XAl and the X_3Al intermetallic phases. However, the highly porous mixture of reactants resulted in a low final density and reduced the area of reaction, which quenched the reaction before completion.

Due to the porosity problems, the experiment was not repeated for the iron-aluminium and nickel-aluminium systems. Instead, the set of experiments in Section 6, which reduced porosity in the reactant mixtures, was developed.

Section 6

THERMAL EXPLOSIONS IN POWDER COMPACTS

To increase the density of the reactant powder mixtures, the powders were pressed into compacts. This reduced porosity and broke up the oxide films on the powder surfaces to allow metal to metal contact.

6.1 Materials

The metal powders used in this experiment are detailed in Section 2. All three particle size distributions of each transition metal were used in a series of reactions, but the aluminium particle size distribution was the same throughout.

6.2 Experimental Procedures

6.2.1 Preparing and Heating the Compacts

Powder mixtures comprising of a 50/50at% ratio of transition metal to aluminium were produced using the method described in Section 5. The mixtures were pressed into compacts by placing them in the die shown in Figure 6.1, the walls of which were coated with a PTFE lubricant to prevent the powders from sticking. The mass of the compacted powder mixtures was dependent on the system. Each compact contained 10.79g of aluminium and to retain the correct atomic ratio of reactants, the following masses were required. Iron-aluminium: 33.13g, nickel-aluminium: 34.31g, titanium-aluminium: 30.00g. A pressure of 218MPa was used to uniaxially press the powders and once the resulting compact had been ejected from the die, its mass and dimensions were measured to calculate its porosity. Samples of the green compacts were mounted in a conductive phenolic compound and examined using SEM. An image, 350×350μm, was taken from a region near the centre of each of the green compacts.

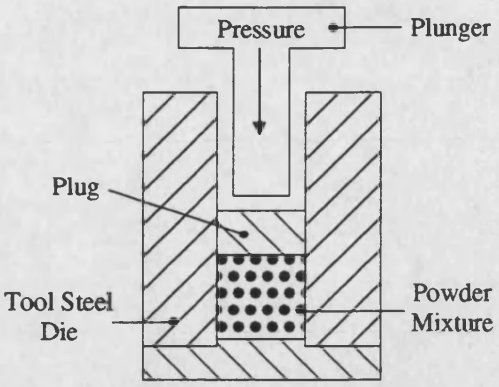

Figure 6.1 Powder press die

These were transferred to a computer running Optimas 6 image analysis software to calculate contact lengths between the transition metals and the aluminium.

To record the time/temperature profiles of the thermal explosions, a thermocouple was inserted into the compacts. A hole 7mm deep and 2mm in diameter was drilled into the centre of the bottom face of each compact and a thermocouple was inserted. The thermocouple wires were protected from the reactants by alumina sleeves and the thermocouple bead was covered in a thin alumina slurry. This was heated at 500°C for 1hr to allow the slurry to dry and form a solid alumina coating. The thermocouple was then linked via an amplifier to a 386SX personal computer running data collection software. This software, listed in Appendix E, monitored the temperature of the

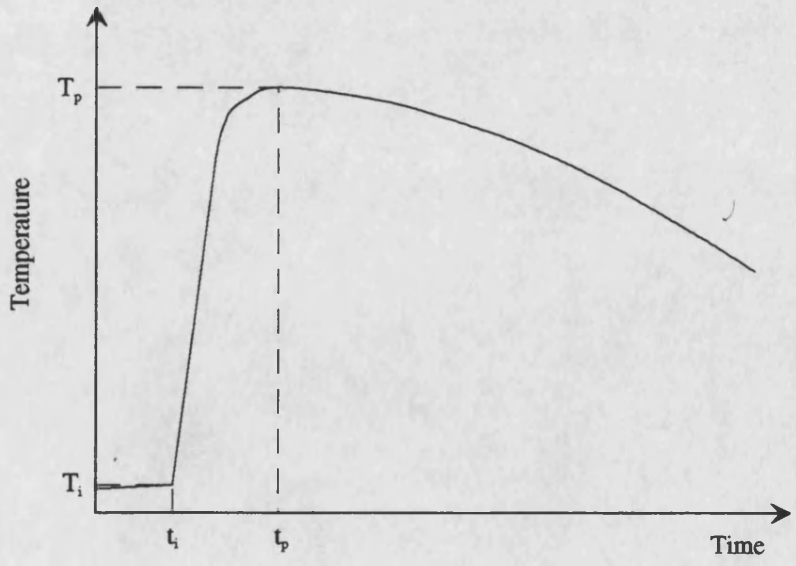

Figure 6.2 Typical time/temperature profile

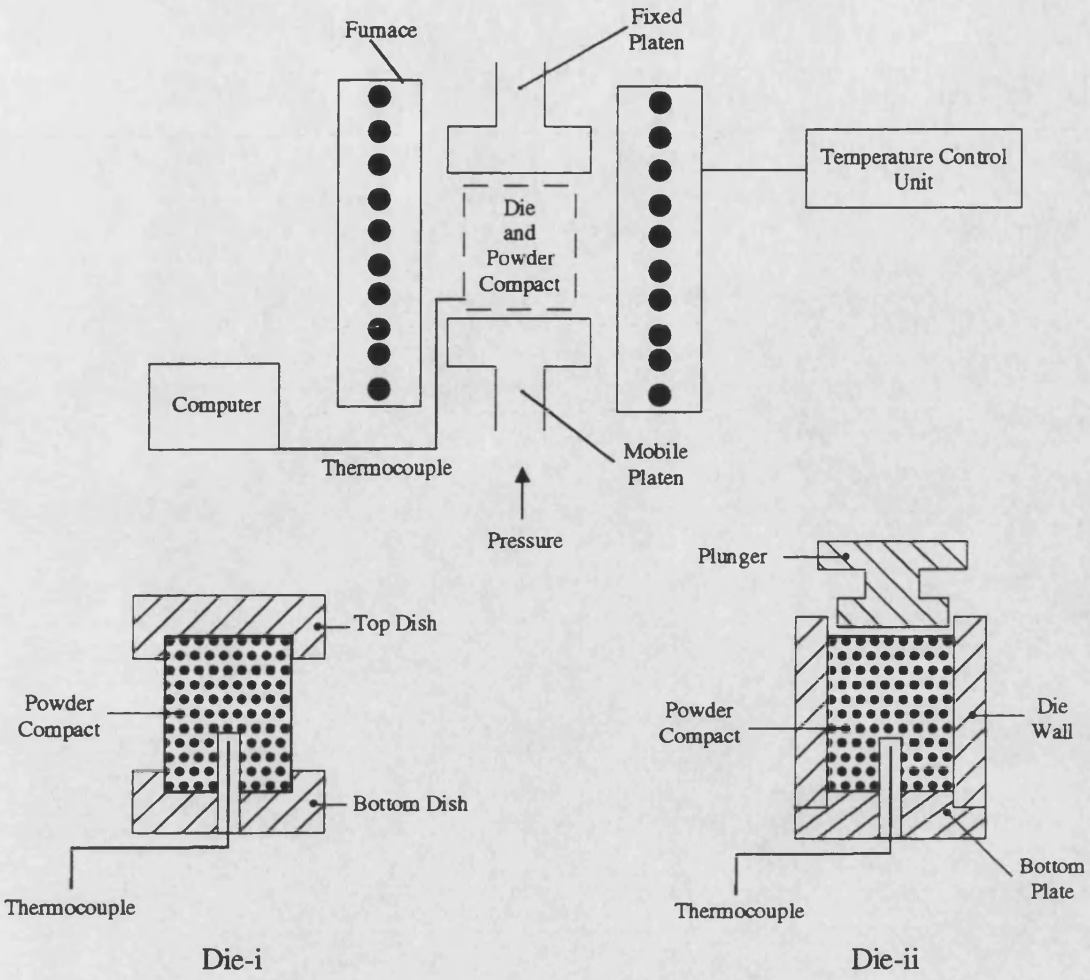

Figure 6.3 Schematic of furnace arrangement and dies

compact until the reaction was initiated and then recorded the time/temperature profile of the reaction. Readings were taken every tenth of a second for five seconds prior to initiation and then every one hundredth of a second for forty seconds after initiation. The criterion for the initiation of the thermal explosion was a temperature increase of 10°C or greater over one second. The data obtained were entered into a spread sheet to produce a time/temperature profile for each thermal explosion.

Figure 6.2 is an example of a typical time/temperature profile. After an initial slow temperature rise, as the furnace heated the reactants, there was a sudden increase as the thermal explosion was initiated at a time t_i and temperature T_i. The temperature

increased rapidly to a peak temperature *Tp* at time *tp* before decreasing slowly. The average rate of temperature rise, $\frac{dT}{dt}$, was calculated from;

$$\frac{dT}{dt} = \frac{(T_p - T_i)}{(t_p - t_i)}$$

The compacts were heated in a Severn Furnaces TF.75.2.3z.N furnace, with a maximum temperature of 1000°C, which was attached to a 1195 Instron testing machine with a 10,000Kgf load cell, Figure 6.3. This allowed the compacts to be heated and pressed simultaneously. The furnace was protected from the thermal explosions by placing the compacts in one of the two dies described below. Argon gas was pumped into the furnace to reduce oxidation of the reactants during the heating cycle.

The rate of temperature rise of the furnace was non-linear, but could be controlled, Figure 6.4. The read-out provided by the data collection software indicated the initiation point of the thermal explosion and the furnace was switched off as soon as

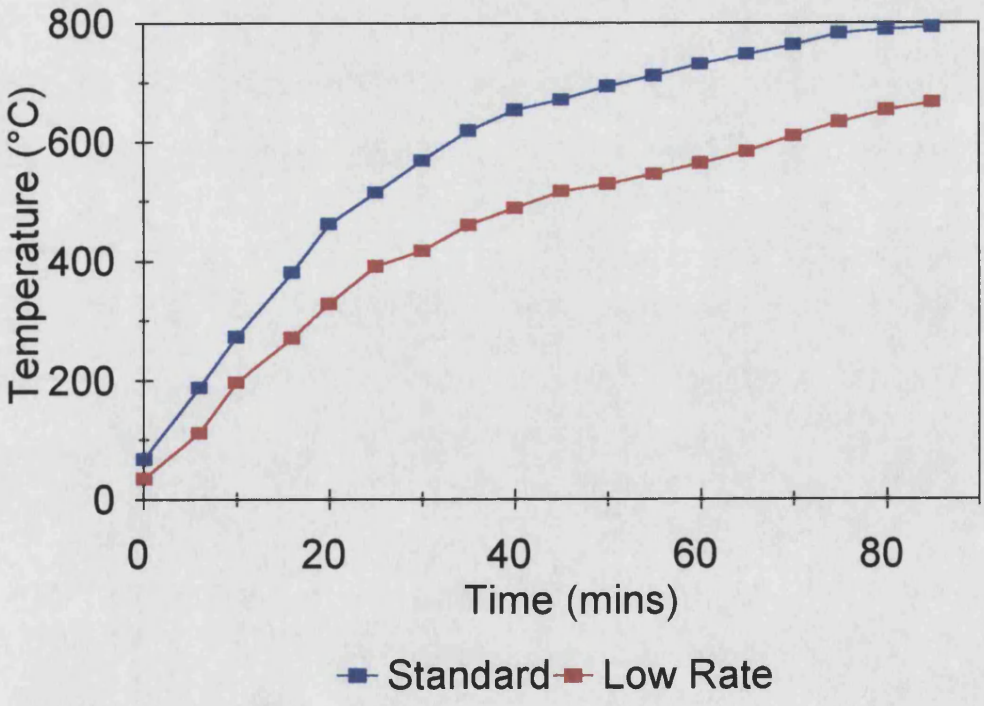

Figure 6.4 Time/temperature profile of furnace

this occurred. Once the furnace had cooled to room temperature, the die was lowered out of the bottom of the furnace.

The reacted compacts and dies were photographed and then the compacts were cut horizontally to reveal a surface perpendicular to and level with the thermocouple tip. Samples of these surfaces were prepared for examination using the routines detailed in Section 2.2. A SEM was first used to obtain images of the surfaces and EPMA and XRD were used to ascertain the composition of the phases present in the samples. Three regions of each sample were examined, the central region, a region midway between the centre and the surface and a region near the surface.

Hardness measurements were taken on both macro and micro scales at five equidistant points from the centre of the sample to the surface. The macrohardness measurements gave an overall hardness value for a particular region since the indents were large enough to cover more than one phase as well as pores. Therefore, by comparing these values with those from homogeneous, low porosity samples, an indication of the homogeneity and porosity of the region could be gained. Microhardness readings were taken in an attempt to find the hardness of individual phases. However, where the phases were too small or porosity was too finely distributed, this proved to be impossible.

The following sub-sections list the variations in processing parameters applied to the thermal explosions. The design of the die, the particle size distributions, the green density, the rate of heating and the pressure applied during the reaction were all altered. To enable easy identification of each compact, the following labelling system was used,

eg. Ti2-i-LD

The green compact was identified by the letters and numbers before the first dash. The chemical symbol for the transition metal was used to identify the system, Fe for Fe-Al, Ni for Ni-Al and Ti for Ti-Al. This was followed by the transition metal particle size distribution, 1/2/3.

After a dash, the type of die was denoted, i/ii.

Finally after another dash, LD denoted a compact with a low green density, LH a low rate of heating and P the application of pressure during the thermal explosion. Alternatively, a description of an adjustment to the thermocouple was inserted, (TU) denoting an uncoated thermocouple and (TS) denoting a thermocouple near the surface of the compact.

6.2.2 Particle Size Distribution

The first series of reactions investigated the effect of particle size distribution on the thermal explosions. PSD1, PSD2 and PSD3 transition metal-aluminium compacts from all the systems were reacted in die-i, Table 6.1. The thermal explosions initiated in the Fe2-i, Ni2-i and Ti2-i green compacts became the standards for their systems, against which all variations in processing parameters were compared.

System	PSD1	PSD2	PSD3
Fe-Al	Fe1-i	Fe2-i	Fe3-i
Ni-Al	Ni1-i	Ni2-i	Ni3-i
Ti-Al	Ti1-i	Ti2-i	Ti3-i

Table 6.1 Variations in the particle size distribution

6.2.3 Die Design

The next series of reactions examined the effect of die design on the thermal explosions. Two different die designs, were used;

System	Die-i	Die-ii
Fe-Al	Fe1-i	Fe1-ii
Fe-Al	Fe2-i	Fe2-ii
Ni-Al	Ni1-i	Ni1-ii
Ni-Al	Ni2-i	Ni2-ii
Ti-Al	Ti1-i	Ti1-ii
Ti-Al	Ti2-i	Ti2-ii

Table 6.2 Variations in the die design

Die-i, illustrated in Figure 6.3, was an open die arrangement which sandwiched the compact between two 'dishes'.

Die-ii, Figure 6.3, was designed to confine the reaction when pressure was applied. The compact was fully contained and a plunger transferred a force from the Instron to the reacting elements.

The dies were machined from tool steel and contained a small hole in the centre of their bases to allow a thermocouple into the compact. The compacts were pressed from mixtures of PSD1 or PSD2 transition metal and aluminium powders. All three transition metal-aluminium systems were reacted in die-i and die-ii, Table 6.2.

6.2.4 Green Density of the Compact

To examine the effect of the green density of the compact on the thermal explosion, the following reactions were performed, Table 6.3. Using PSD2 nickel-aluminium and PSD2 titanium-aluminium powder mixtures only, green compacts were prepared by compacting the powder mixtures using a lower pressure of 150MPa, the standard being 218MPa. The iron-aluminium compact was omitted since previous results from this system had proved disappointing.

System	Compacted Under 218MPa	Compacted Under 150MPa
Fe-Al	-	-
Ni-Al	Ni2-i	Ni2-i-LD
Ti-Al	Ti2-i	Ti2-i-LD

Table 6.3 Variations in the green density of the compact

6.2.5 Rate of Heating of the Compact

The rate of heating of the furnace could be controlled and an investigation into the effect of this on the thermal explosions was carried out. The rate of heating was reduced from the standard to give the profile shown in Figure 6.4. Only nickel-aluminium and titanium-aluminium compacts were heated under this lower rate and compared against the standards, Table 6.4.

System	Standard Rate of Heating	Low Rate of Heating
Fe-Al	-	-
Ni-Al	Ni2-i	Ni2-i-LH
Ti-Al	Ti2-i	Ti2-i-LH

Table 6.4 Variations in the rate of heating

6.2.6 Applying Pressure During the Thermal Explosion

Pressure was applied during the thermal explosions to reduce porosity in the reacted compacts. A pressure of 37MPa was applied by a cross head speed of 20mm per minute as soon as the thermal explosion had initiated and triggered the data collection software. This pressure was maintained for 40 seconds after initiation. To contain the reaction, nickel-aluminium compacts were reacted in die-ii, whilst titanium-aluminium compacts were reacted in die-i. The iron-aluminium system was omitted, Table 6.5.

To allow the rapid application of pressure as soon as the thermal explosion was initiated, a small pressure of less than 1MPa was applied to the dies during the heating cycle. This was applied at a temperature 30°C below the initiation temperature and ensured that there was no gap between the top platen of the Instron and the die. The initiation point of the thermal explosion was also detected by monitoring this small pressure. The formation of a liquid phase to initiate the thermal explosion caused the compact to collapse and this resulted in a drop in pressure.

System	0 MPa	37 MPa
Fe-Al	-	-
Ni-Al	Ni2-ii	Ni2-ii-P
Ti-Al	Ti2-i	Ti2-i-P

Table 6.5 Variations in the pressure applied during the thermal explosion

6.2.7 Thermocouple Effects

Finally, to estimate possible errors introduced by the thermocouples in the time/temperature profiles of the thermal explosions, additional reactions were performed, Table 6.6. To examine the effect of the coating on the temperatures

System	Standard Thermocouple	Uncoated Thermocouple	Surface Thermocouple
Fe-Al	-	-	-
Ni-Al	Ni2-i	Ni2-i-TU	Ni2-i-TS
Ti-Al	Ti2-i	Ti2-i-TU	Ti2-i-TS

Table 6.6 Thermocouple effects

recorded, uncoated thermocouple beads were inserted into compacts. To investigate the effect that the position of the thermocouple had on the temperatures recorded, coated thermocouples were positioned near the surface of the compacts.

6.3 Results

6.3.1 Iron-Aluminium

Green Compact	Fe-Al Contact Length (µm)		Porosity (%)	
	Mean	SD	Mean	SD
Fe1	2055	181	19.8	1.5
Fe2	1634	156	21.3	0.3
Fe3	981	257	19.1	0.2

Table 6.7 Details of Fe-Al green compacts

Compact Fe1-i: Table 6.7 displays the contact length and porosity measurements and Figure 6.5a shows the network of aluminium (A) around the iron particles (B) in the green compact.

Although the cylindrical shape and dimensions of the green compact were retained by the bottom half of the reacted compact, the top half expanded and ruptured the surface, which split and 'peeled' back, Figure 6.6a.

The time/temperature profile recorded for this reaction is plotted in Figures 6.7a-b. An initiation temperature of 579°C was followed by a temperature rise of 17°C/s to a peak temperature of 1062°C, Table 6.8.

Compact	Profile Temperatures			Porosity (%)		Hardness			
	Initiation (°C)	Rate (°C/s)	Peak (°C)	Mean	SD	Macro (Hv) Mean	SD	Micro (Hv) Mean	SD
Particle Size Distribution									
Fe1-i	579	17	1062	51.1	6.6	79.6	4.0	132.6	44.6
Fe2-i	609	14	1054	37.9	6.6	99.5	17.0	279.3	96.1
Fe3-i	605	11	1034	67.9	24.5	60.2	1.0	256.7	22.3
Die Design									
Fe1-i	579	17	1062	51.1	6.6	79.6	4.0	132.6	44.6
Fe1-ii	586	20	1011	26.8	5.3	119.8	4.3	122.3	35.7
Fe2-i	609	14	1054	37.9	6.6	99.5	17.0	279.3	96.1
Fe2-ii	602	22	870	36.3	2.5	102.3	4.2	78.2	24.2

Table 6.8 Details of Fe-Al thermal explosions and reacted compacts

Compact	Phase	Fe (at%) Mean	SD	Al (at%) Mean	SD	Alloy/ Compound
Fe1-i	B	93.7	1.8	6.3	1.8	Fe
	C	72.3	2.1	27.7	2.1	Fe_3Al
	D	49.5	0.2	50.5	0.2	FeAl
	E	34.7	1.0	65.3	1.0	$FeAl_2$
Fe2-i	C	78.8	1.9	21.2	1.9	Fe_3Al
	D	49.2	0.4	50.8	0.4	FeAl
	E	35.5	0.9	64.5	0.9	$FeAl_2$
Fe3-i	B	94.6	1.3	5.4	1.3	Fe
	C	71.8	1.9	28.2	1.9	Fe_3Al
	D	53.8	0.2	46.2	0.2	FeAl
Fe1-ii	B	96.5	3.0	3.5	3.0	Fe
	C	74.3	1.2	25.7	1.2	Fe_3Al
	D	51.5	1.1	48.6	1.1	FeAl
	F	29.2	0.5	70.8	0.5	Fe_2Al_5
Fe2-ii	B	99.9	0.1	0.1	0.1	Fe
	C	69.2	2.4	30.7	2.4	Fe_3Al
	D	50.8	1.7	49.2	1.7	FeAl
	E	33.8	0.1	66.2	0.1	$FeAl_2$
	F	30.0	0.2	70.0	0.2	Fe_2Al_5

Table 6.9 EPMA data for Fe-Al reacted compacts

The reacted compact contained a variety of phases, Table 6.9. The surface regions contained a mixture of iron rich (B), Fe_3Al (C), FeAl (D) and $FeAl_2$ (E) phases, Figure 6.9a. The phases became fewer in number towards the centre, with only the FeAl (D) and $FeAl_2$ (E) phases present near the tip of the thermocouple, Figures 6.9b-c. The XRD plot for this sample contained many peaks from which it was difficult to resolve the individual phases, Figure 6.8a. The sample was highly porous since no consolidation had taken place during the reaction, Table 6.8.

Macrohardness measurements were consistently low since they covered a large amount of porosity, but microhardness measurements were more varied due to the number of phases present in the sample, Table 6.8.

Compact Fe2-i: Table 6.7 displays the contact length and porosity measurements and Figure 6.5b shows the network of aluminium (A) around the iron particles (B) in the green compact.

Although the cylindrical shape and dimensions of the green compact were retained by the bottom half of the reacted compact, the top half expanded and ruptured the surface, which split and 'peeled' back, Figure 6.6a.

This compact produced an initiation temperature of 609°C and a rate of temperature rise of 14°C/s to a peak temperature of 1054°C, as displayed in Figures 6.7a-b and Table 6.8. The initial rate of temperature rise was too slow to trigger the software immediately and gave an inaccurately high initiation temperature shown on the profile at 4s. The gradient of the plot prior to initiation is steeper than the rate of temperature rise of the furnace and therefore, the actual initiation temperature is the one quoted in Table 6.8.

The surface regions of the compact contained FeAl (D) and $FeAl_2$ (E), Figure 6.10a, whilst the central region contained Fe_3Al (C), FeAl (D) and $FeAl_2$ (E), Figure 6.10b. The material in the midway region was dislodged during polishing and left a large hole in the compact. The EPMA and XRD data obtained from the reacted compact are displayed in Table 6.9 and Figure 6.8a respectively. Little consolidation of the compact during the reaction resulted in a large amount of porosity, Table 6.8.

The macrohardness values from the centre and midway regions of the compact were missing since there was insufficient material to take a reading from. Where there was sufficient material to take microhardness measurements, the values reflected the variety of phases in the microstructure, Table 6.8.

Compact Fe3-i: Table 6.7 displays the contact length and porosity measurements and Figure 6.5c shows the network of aluminium (A) around the iron particles (B) in the green compact.

Although the cylindrical shape and dimensions of the green compact were retained by the bottom half of the reacted compact, the top half expanded and ruptured the surface, which split and 'peeled' back, Figure 6.6a.

This compact produced an initiation temperature of 605°C, a rate of temperature rise of 11°C/s and a peak temperature of 1034°C, Figures 6.9b and Table 6.8. The same problems of measuring the initiation temperature, as experienced by Fe2-i, were encountered.

The loose powders in the midway region of this compact were dislodged during polishing, leaving a hole. The other regions of the sample lacked consolidation and were very porous, Table 6.8. The surface and central regions contained iron rich regions (B), Fe_3Al (C) and FeAl (D), Figure 6.11. EPMA and XRD data are displayed in Table 6.9 and Figure 6.8a respectively.

Trends in hardness measurements were similar to those of previous samples, Table 6.8.

Compact Fe1-ii: Table 6.7 displays the contact length and porosity measurements and Figure 6.5a shows the network of aluminium (A) around the iron particles (B) in the green compact.

The die constrained expansion in the radial direction, which was directed longitudinally and pushed the plunger upwards. The top surface of the compact appeared cracked due to this expansion, Figure 6.6b.

Figure 6.7b compares the time/temperature profile of this reaction against those of other compacts. The reaction initiated in the compact at a temperature of 586°C and raised the temperature at a rate of 20°C/s to a peak temperature of 1011°C, Table 6.8.

This sample possessed a more inhomogeneous microstructure then the previous sample. The surface region contained Fe rich cores (B) surrounded by Fe_2Al_5 (F), Figure 6.12a. The midway region contained more iron rich cores (B) surrounded by FeAl (D) and Fe_2Al_5 (F), Figure 6.12b, and the centre region contained iron rich cores (B) surrounded by Fe_3Al (C), FeAl (D) and Fe_2Al_5 (F), Figure 6.12c. Table 6.9 contains the EPMA data and Figure 6.8b shows the XRD plot with the many peaks indicating the presence of a large number of phases. Porosity was high due to a lack of consolidation during the reaction, Table 6.8.

As before, macrohardness measurements were consistent, but were low since they covered a number of pores, whilst microhardness measurements were more varied due to the presence of many phases, Table 6.8.

Compact Fe2-ii: Table 6.7 displays the contact length and porosity measurements and Figure 6.5b shows the network of aluminium (A) around the iron particles (B) in the green compact.

The die constrained expansion in the radial direction, which was directed longitudinally and pushed the plunger upwards. The top surface of the compact appeared cracked due to this expansion, Figure 6.6b.

The time/temperature profile recorded for this reaction is shown in Figure 6.7b. An initiation temperature of 602°C was followed by a temperature rise of 22°C/s to reach a peak temperature of 870°C, Table 6.8.

The microstructure of this sample was similar to that of Fe1-ii. Iron cores (B) were surrounded by a variety of phases, Table 6.9 and Figure 6.8b. Fe_2Al_5 (F) in the surface region, Figure 6.13a, FeAl (D) and Fe_2Al_5 (F) in the midway region, Figure 6.13b, and Fe_3Al (C), FeAl (D) and $FeAl_2$ (E) in the central region, Figure 6.13c. Porosity was again due to a lack of consolidation during the reaction, Table 6.8.

A similar trend in macrohardness and microhardness to the previous iron-aluminium samples was found in this compact, Table 6.8.

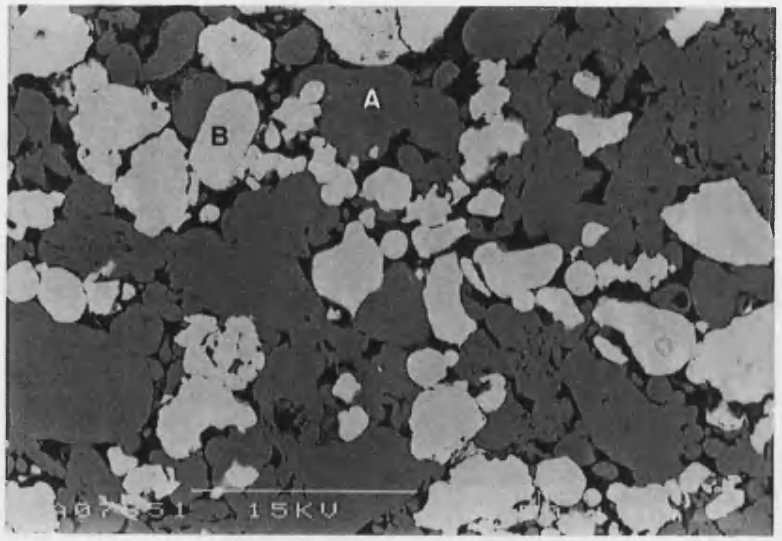

Figure 6.5a Fe1 green compact
A-Al, B-Fe 100μm

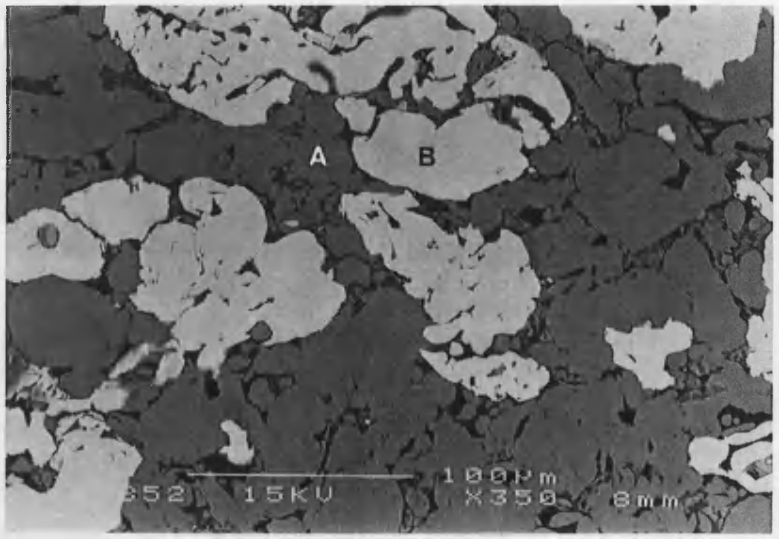

Figure 6.5b Fe2 green compact
A-Al, B-Fe 100μm

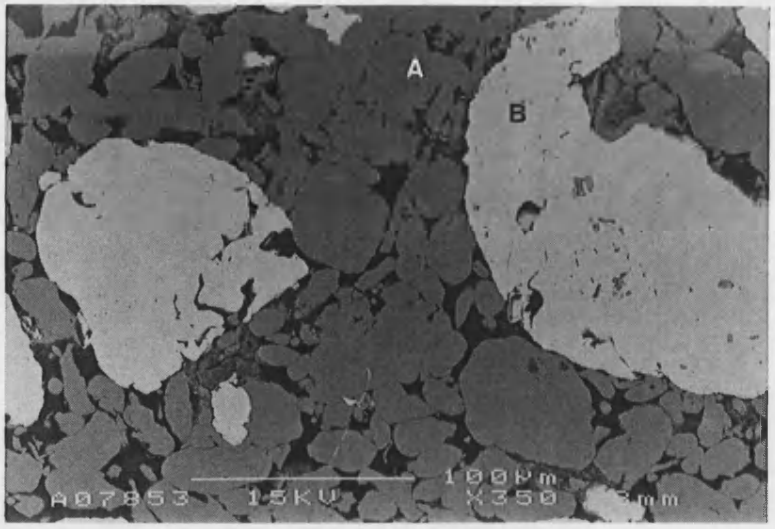

Figure 6.5c Fe3 green compact
A-Al, B-Fe 100μm

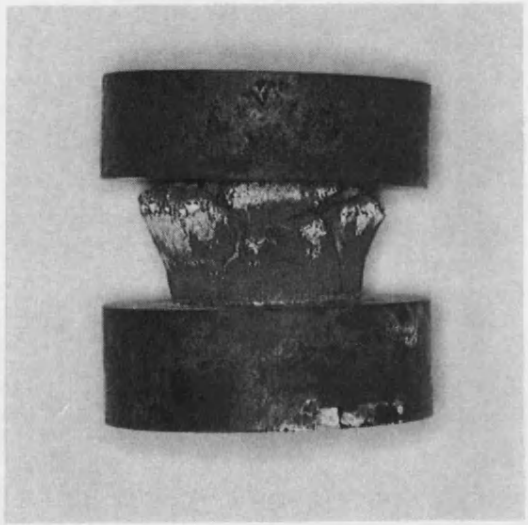

Figure 6.6a Fe-Al compact reacted in die-i 10mm

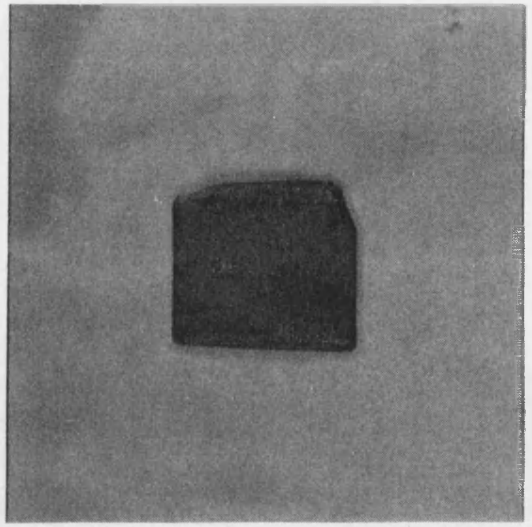

Figure 6.6b Fe-Al compact reacted in die-ii 10mm

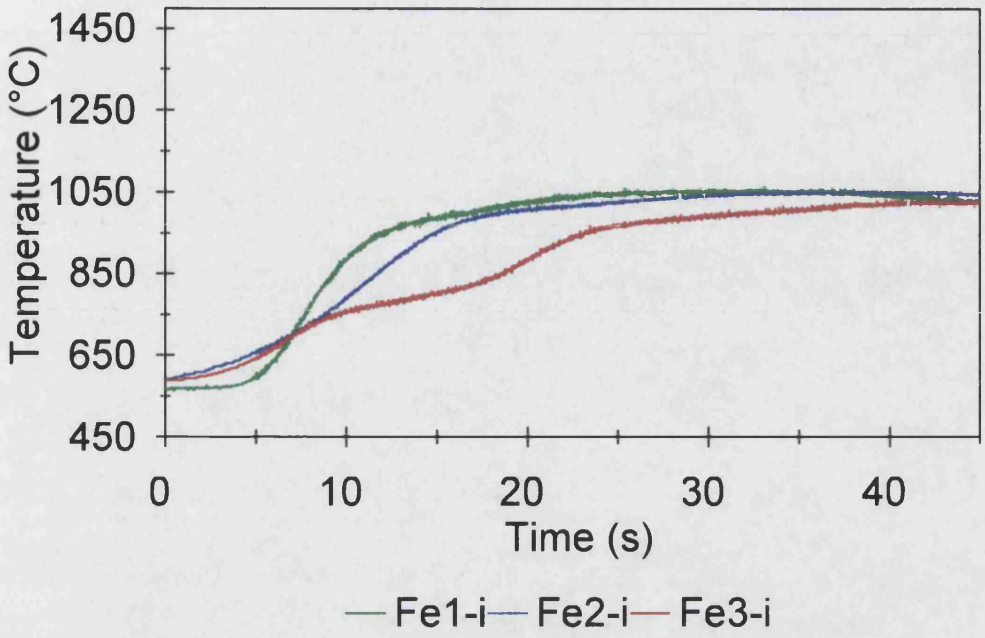

Figure 6.7a Effect of titanium PSD on iron-aluminium time/temperature profiles

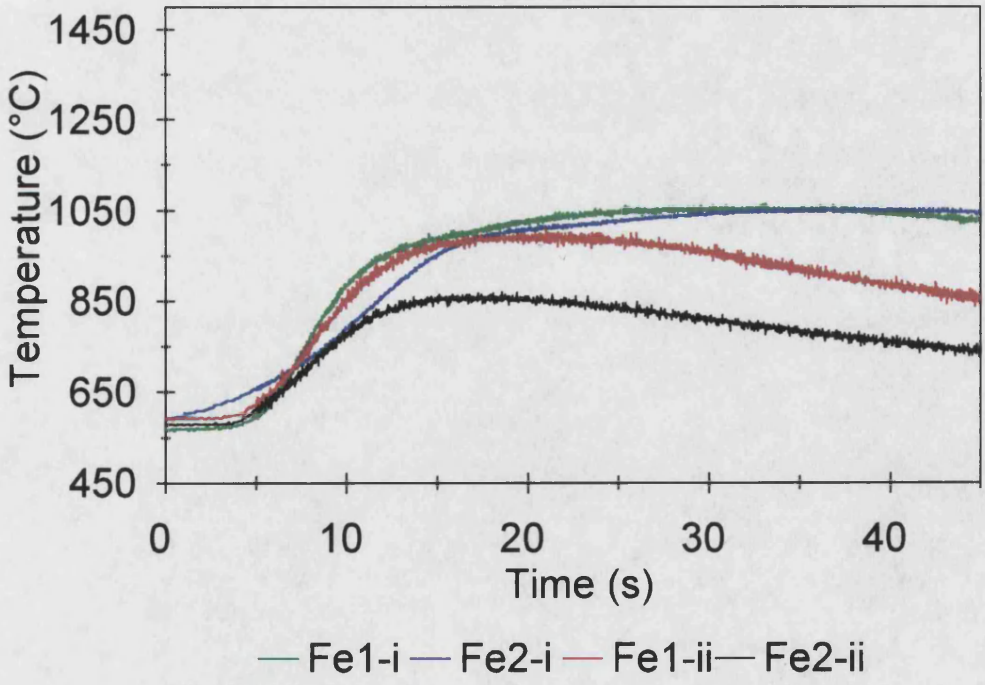

Figure 6.7b Effect of the die.on iron-aluminium time/temperature profiles

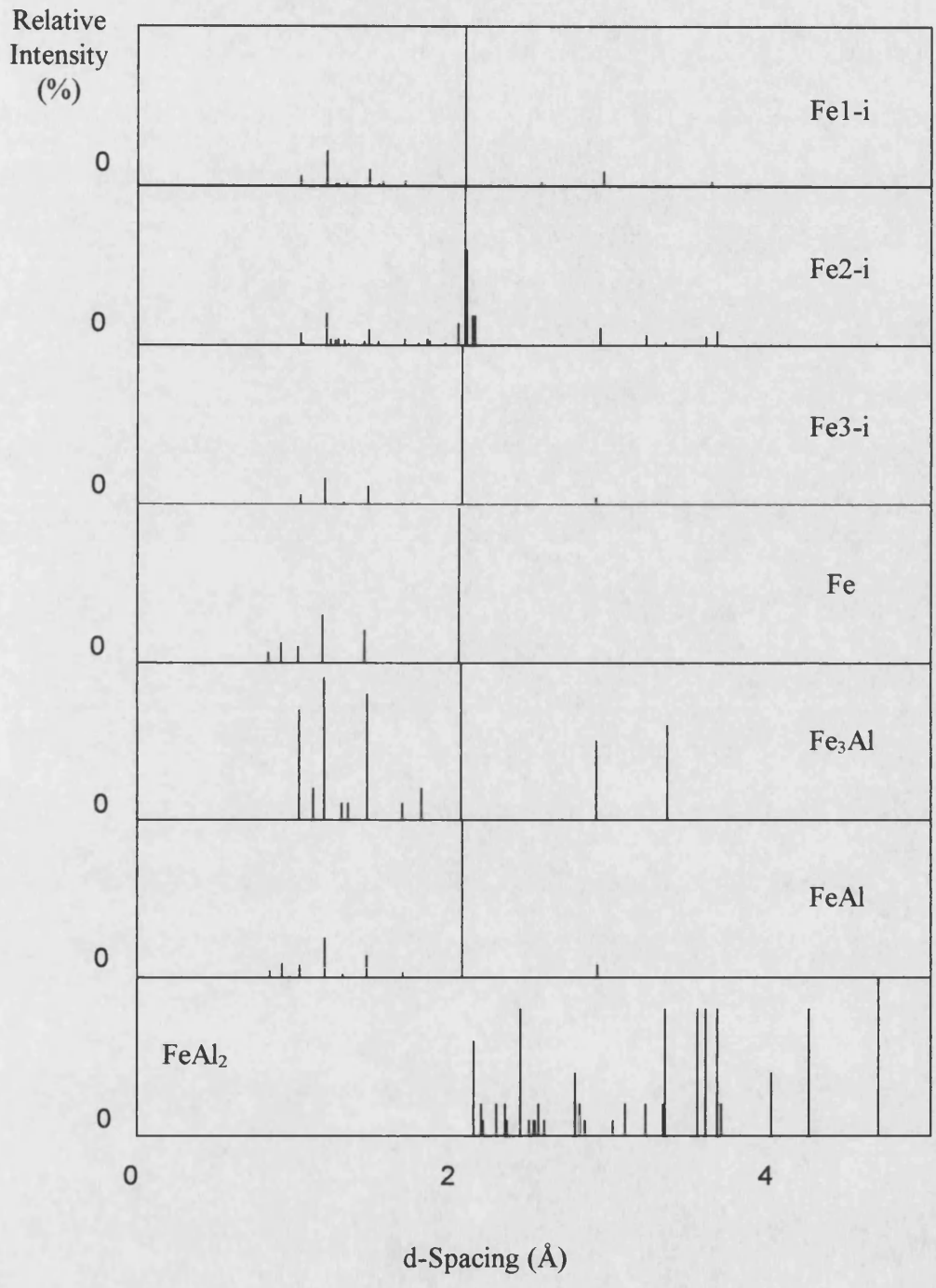

Figure 6.8a XRD plots for iron-aluminium compacts

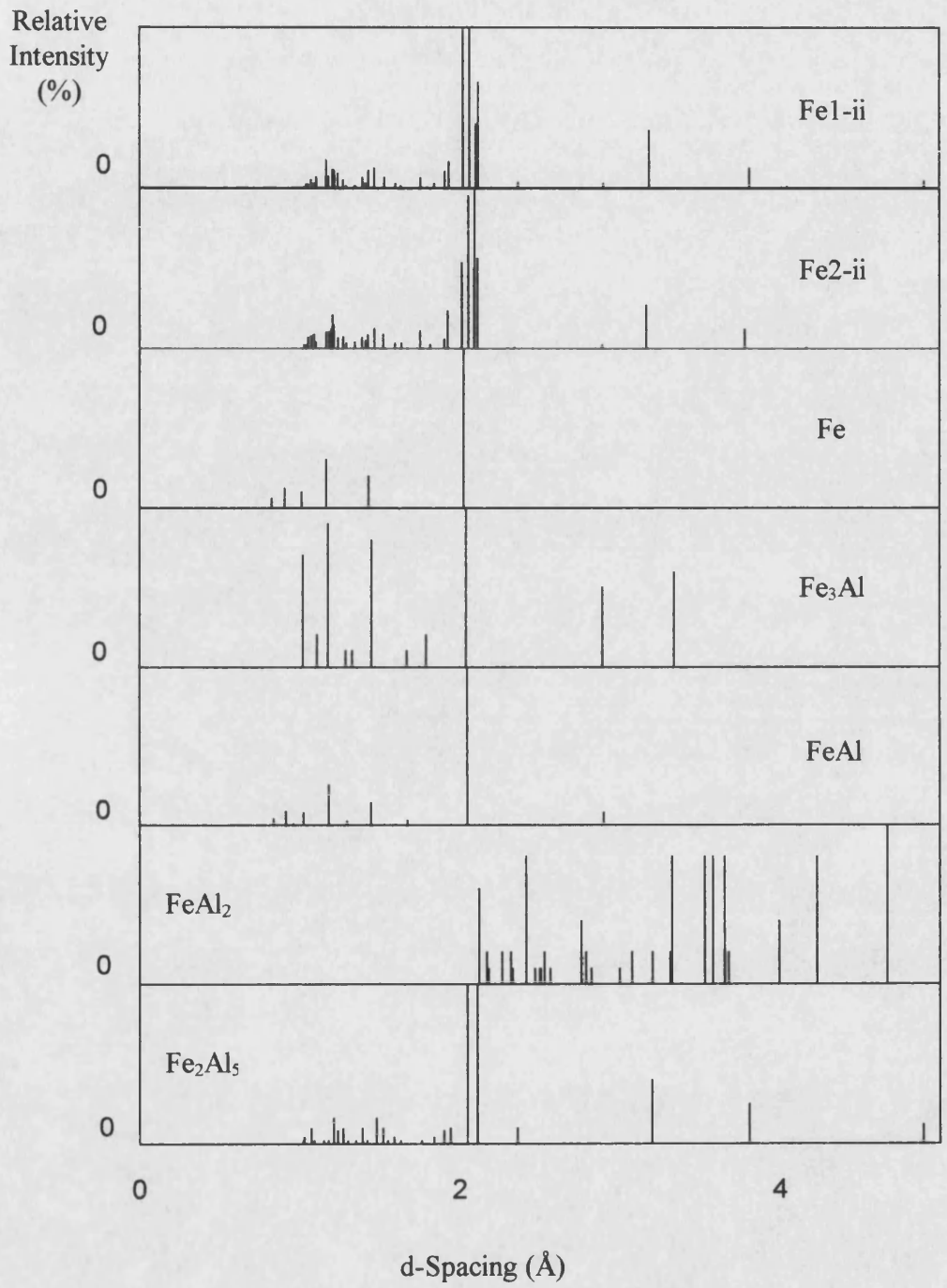

Figure 6.8b XRD plots for iron-aluminium compacts

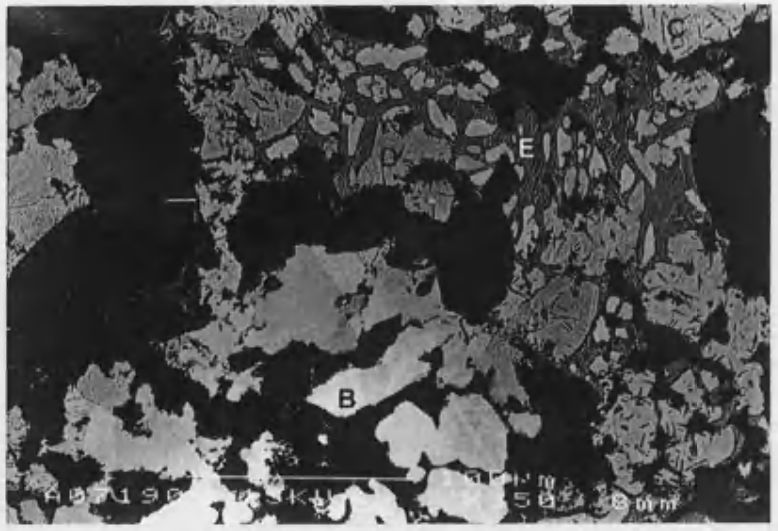

Figure 6.9a Surface region of Fe1-i
B-Fe rich, C-Fe_3Al, D-FeAl, E-$FeAl_2$ 100μm

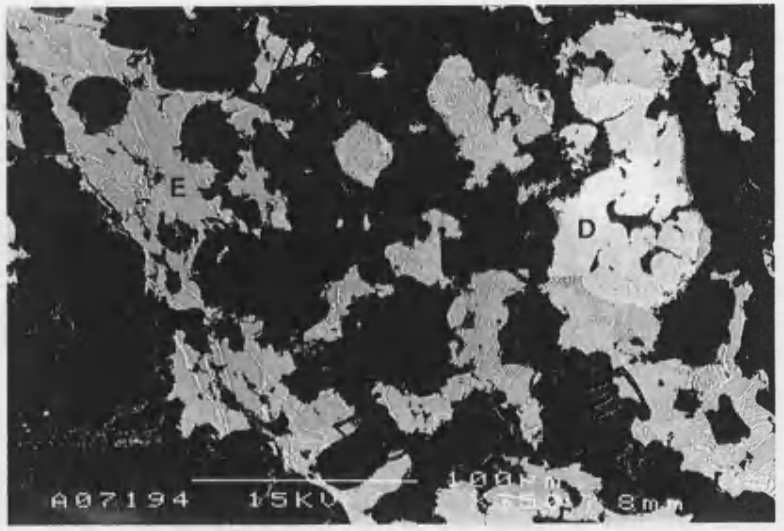

Figure 6.9b Midway region of Fe1-i
D-FeAl, E-$FeAl_2$ 100μm

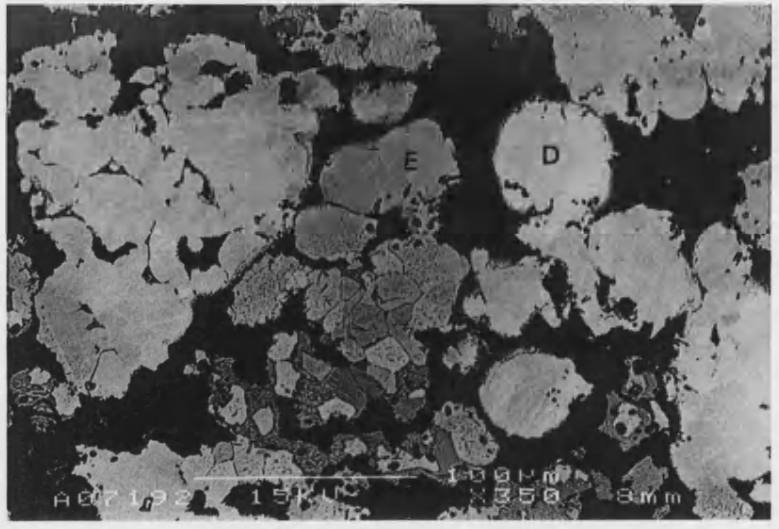

Figure 6.9c Centre region of Fe1-i
D-FeAl, E-$FeAl_2$ 100μm

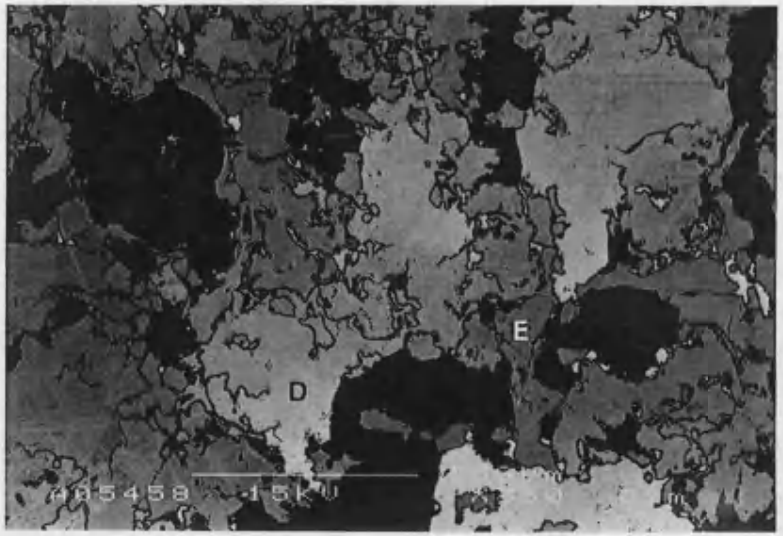

Figure 6.10a Surface region of Fe2-i
D-FeAl, E-$FeAl_2$ 100μm

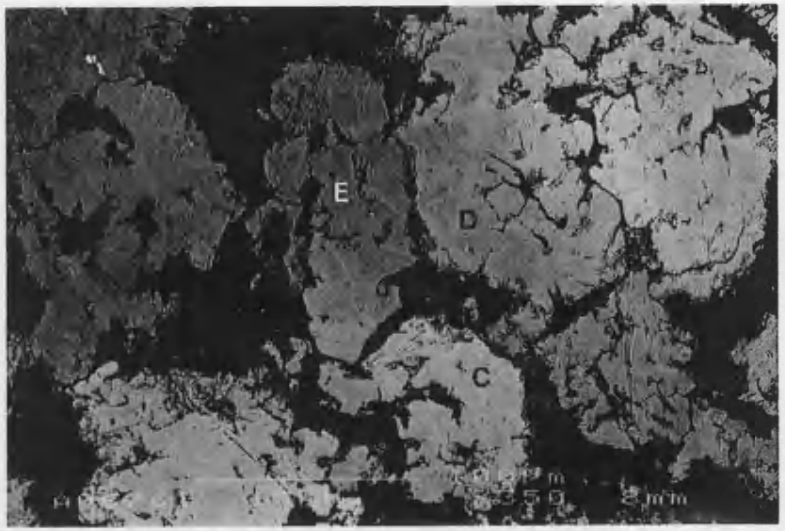

Figure 6.10b Centre region of Fe2-i
C-Fe_3Al, D-FeAl, E-$FeAl_2$ 100μm

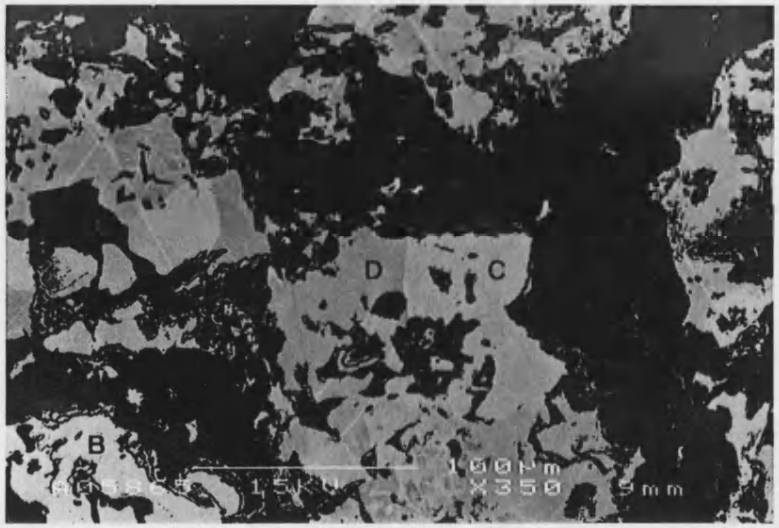

Figure 6.11 Surface and centre regions of Fe3-i
B-Fe rich, C-Fe_3Al, D-FeAl 100μm

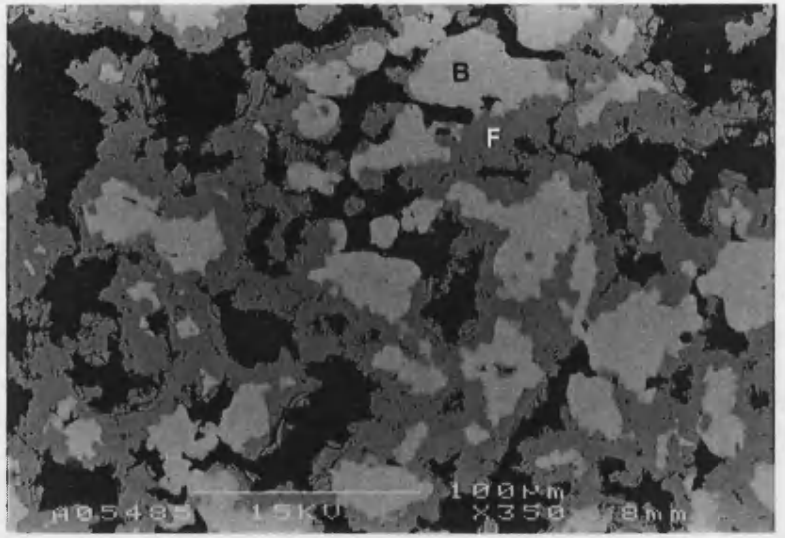

Figure 6.12a Surface region of Fe1-ii
B-Fe rich, F-Fe_2Al_5 100µm

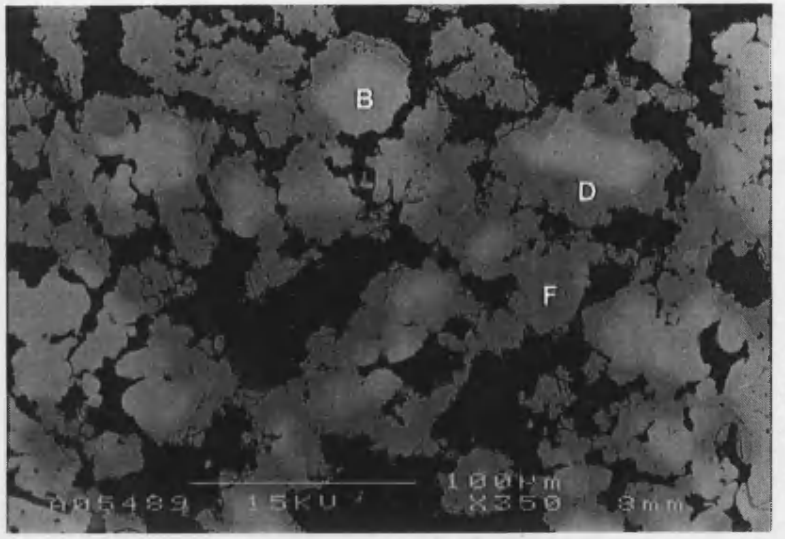

Figure 6.12b Midway region of Fe1-ii
B-Fe rich, D-FeAl, F-Fe_2Al_5 100µm

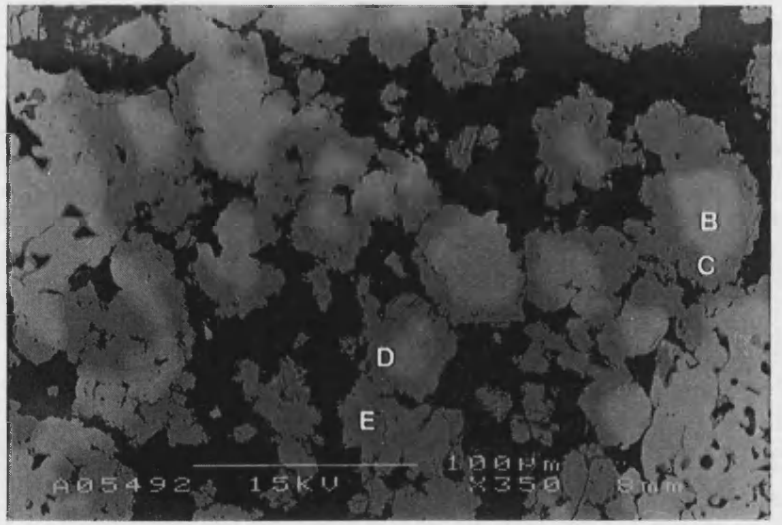

Figure 6.12c Centre region of Fe1-ii
B-Fe rich, C-Fe_3Al, D-FeAl, F-Fe_2Al_5 100µm

Text refers to F Fe_2Al_5
← Label here is E

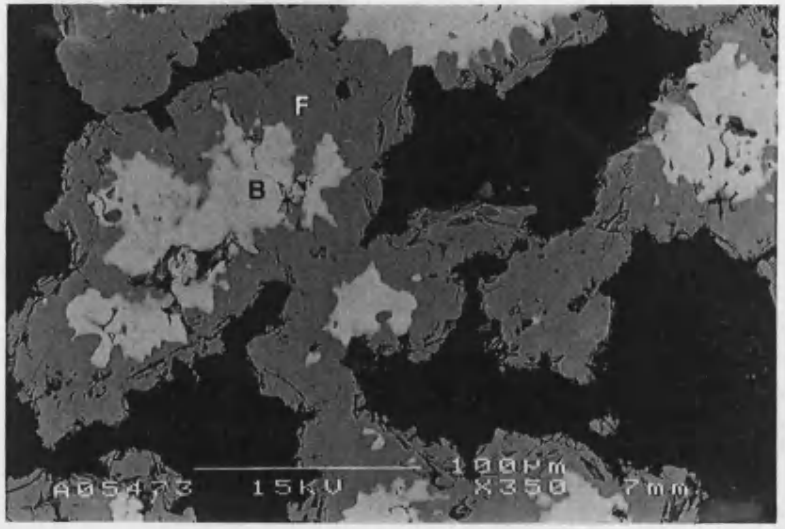

Figure 6.13a Surface region of Fe2-ii
B-Fe rich, F-Fe_2Al_5 100µm

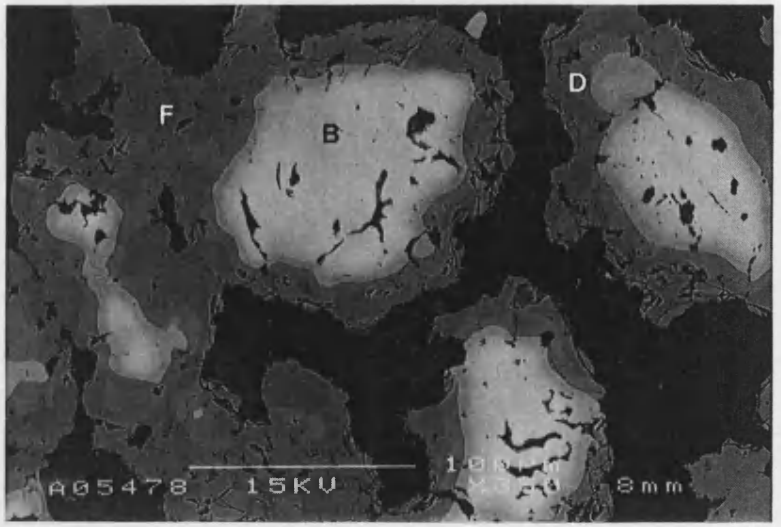

Figure 6.13b Midway region of Fe2-ii
B-Fe rich, D-FeAl, F-Fe_2Al_5 100µm

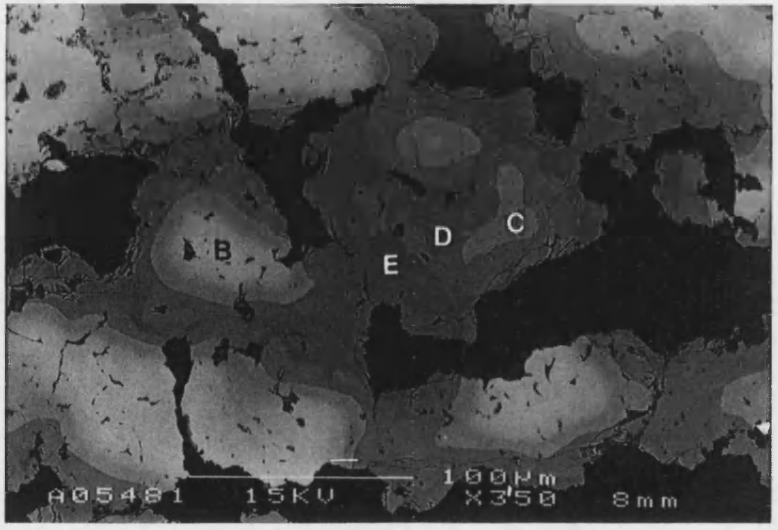

Figure 6.13c Centre region of Fe2-ii
B-Fe rich, C-Fe_3Al, D-FeAl, E-$FeAl_2$ 100µm

6.3.2 Nickel-Aluminium

Green Compact	Ni-Al Contact Length (μm)		Porosity (%)	
	Mean	SD	Mean	SD
Ni1	3357	380	29.8	0.9
Ni2	2978	432	30.3	1.1
Ni3	1030	149	22.2	0.3

Table 6.10 Details of Ni-Al green compacts

Compact	Profile Temperatures			Porosity (%)		Hardness			
	Initiation (°C)	Rate (°C/s)	Peak (°C)	Mean	SD	Macro (Hv) Mean	SD	Micro (Hv) Mean	SD
Particle Size Distribution									
Ni1-i	550	391	1496	10.6	10.6	235.4	54.7	255.8	31.4
Ni2-i	552	400	1464	7.8	9.4	275.6	33.1	273.4	17.1
Ni3-i	655	155	1450	5.3	3.5	279.4	23.6	253.2	47.4
Die Design									
Ni1-i	550	391	1496	10.6	10.6	235.4	54.7	255.8	31.4
Ni1-ii	551	367	1457	33.6	17.6	192.0	36.1	279.8	8.4
Ni2-i	552	400	1464	7.8	9.4	275.6	33.1	273.4	17.1
Ni2-ii	553	193	1464	11.9	11.3	223.0	28.4	262.6	8.8
Green density of the Compact									
Ni2-i	552	400	1464	7.8	9.4	275.6	33.1	273.4	17.1
Ni2-i-LD	529	303	1474	23.1	11.7	233.4	49.3	272.6	19.3
Rate of Heating of the Compact									
Ni2-i	552	400	1464	7.8	9.4	275.6	33.1	273.4	17.1
Ni2-i-LH	533	237	1457	5.8	4.9	268.4	18.3	286.4	14.9
Applying Pressure During the Thermal Explosion									
Ni2-ii	553	193	1464	11.9	11.3	223.0	28.4	262.6	8.8
Ni2-ii-P	571	413	1446	15.3	18.7	207.2	34.8	267.4	17.6

Table 6.11 Details of Ni-Al thermal explosions and reacted compacts

Compact	Phase	Ni (at%)		Al (at%)		Alloy/ Compound
		Mean	SD	Mean	SD	
Ni1-i	K	51.0	0.2	49.0	0.2	NiAl
Ni2-i	K	49.6	0.3	50.4	0.3	NiAl
Ni3-i	K	50.4	0.9	49.6	0.9	NiAl
Ni1-ii	K	50.0	0.6	50.0	0.6	NiAl
Ni2-ii	K	49.9	0.3	50.1	0.3	NiAl
Ni2-i-LD	K	51.1	0.3	48.9	0.3	NiAl
Ni2-i-LH	K	51.3	0.5	48.7	0.5	NiAl
Ni2-ii-P	K	50.5	0.5	49.5	0.5	NiAl

Table 6.12 EPMA data for Ni-Al reacted compacts

Compact Ni1-i: The SEM image of the unreacted powders shows that the small nickel particles (H) had formed a network separating the aluminium particles (A), Figure 6.14a. The nickel-aluminium contact length and the porosity of the green compact are given in Table 6.10.

The compact collapsed during the thermal explosion, allowing material to flow from the die, Figure 6.15a. The surface of the reacted compact was smooth and free from cracks.

The thermal explosion initiated at a temperature of 550°C, and produced a rate of temperature rise of 391°C/s to a peak temperature of 1496°C as detailed in Table 6.11. Figures 6.16b plots the time/temperature profile against those of identical compacts reacted in different die designs, whilst Figure 6.16a plots it against compacts containing different nickel powder size distributions.

Table 6.12 and Figure 6.17a contain the EPMA and XRD data which identified the single phase in the reacted compact as NiAl (K), Figure 6.18 The porosity present in the sample, Table 6.11, originated from two sources. The rounded porosity was due to trapped gases within the reacted compact, whilst the remainder was due to the original porosity in the green compact.

The low porosity, single phase microstructure produced similar macrohardness and microhardness values, Table 6.11.

Compact Ni2-i: The SEM image of the unreacted powders shows that the nickel particles (H) had formed a network separating the aluminium particles (A), Figure 6.14. The nickel-aluminium contact length and the porosity of the green compact are given in Table 6.10.

The compact collapsed during the thermal explosion, allowing material to flow from the die, Figure 6.15. The surface of the reacted compact was smooth and free from cracks.

The thermal explosion had an initiation temperature of 552°C, a rate of temperature rise of 400°C/s and a peak temperature of 1464°C, Figures 6.16-b and Table 6.11.

The SEM image of this sample, Figure 6.19a-b, shows a single phase which was found to be NiAl (K) by EPMA, Table 6.12, and XRD, Figure 6.17a. Both types of porosity were present, with the majority being gas porosity once again, Table 6.11.

Both macrohardness and microhardness measurements were consistently high across the sample, indicating low porosity, homogeneous microstructure, Table 6.11. The microhardness measurements were comparable with those of previous samples containing NiAl.

Compact Ni3-i: The distribution of the nickel (H) and aluminium (A) powders was less uniform than in compacts containing the PSD1 and PSD2 nickel. In this compact, groups of nickel particles were separated by a network of aluminium, Figure 6.14c. The nickel-aluminium contact length and the porosity of the green compact are given in Table 6.10.

The compact collapsed during the thermal explosion, allowing material to flow from the die, Figure 6.15a. The surface of the reacted compact was smooth and free from cracks.

The thermal explosion initiated at a higher temperature of 655°C, but had a slower temperature rise of 155°C/s to a peak temperature of 1450°C, Figure 6.16a and Table 6.11.

A single phase was formed throughout the sample, Figures 6.20a-b and this was found to be NiAl (K) when it was analysed by EPMA, Table 6.12, and XRD Figure 6.17a. On a large scale, the distribution of porosity was even, Table 6.11, but on a finer scale

it was found that regions of well consolidated material existed next to regions containing many fine pores.

Macrohardness values were consistent throughout the sample, but microhardness measurements were more susceptible to the fine pores and were consequently more erratic and gave a lower average hardness than previous samples, Table 6.11.

Compact Ni1-ii: The SEM image of the unreacted powders shows that the small nickel particles (H) had formed a network separating the aluminium particles (A), Figure 6.14a. The nickel-aluminium contact length and the porosity of the green compact are given in Table 6.10.

During the thermal explosion, the reacted compact flowed to fill the diameter of the confining die, Figure 6.15b, and once the reacted compact had been removed from the die, the surface was found to contain a large quantity of gas porosity.

The thermal explosion initiated at 551°C and rose to a peak temperature of 1457°C at a rate of 367°C/s, Figures 6.16a-b and Table 6.11.

The data in Table 6.12 and Figure 6.17b show only the presence of NiAl (K) in the sample, Figure 6.21. Gas porosity was present in the sample and this increased dramatically in quantity towards the surface, as can be seen from the large standard deviation value. Porosity remaining from the original green compact was also present, Table 6.11.

The low macrohardness measurements reflected the high porosity of the sample, but the microhardness measurements taken between the pores gave a more accurate value of the hardness of the NiAl phase, Table 6.11.

Compact Ni2-ii: The SEM image of the unreacted powders shows that the nickel particles (H) had formed a network separating the aluminium particles (A), Figure 6.14b. The nickel-aluminium contact length and the porosity of the green compact are given in Table 6.10.

During the thermal explosion, the reacted compact flowed to fill the diameter of the confining die, Figure 6.15b, and once the reacted compact had been removed from the die, the surface was found to contain a large quantity of gas porosity.

The thermal explosion initiated at a temperature of 553°C, and this was followed by a rate of temperature rise of 193°C/s to a peak temperature of 1464°C, Figures 6.16b and Table 6.11.

Figure 6.22 shows a single phase structure identified by EPMA, Table 6.12, and XRD, Figure 6.17b, as NiAl (K). Porosity was derived from gas pores, whose number increased towards the outer surface, and a lack of consolidation of the green compact during the thermal explosion, Table 6.11.

The low macrohardness values were a result of the high porosity, whilst microhardness values were of the correct magnitude for NiAl, Table 6.11.

Compact Ni2-i-LD: The green compact was found to have a porosity of 36.8%, before it collapsed during the thermal explosion, allowing material to flow from the die, Figure 6.15a. The surface of the reacted compact was smooth and free from cracks.

The thermal explosion initiated at a lower temperature of 529°C, had a rate of temperature rise of 303°C/s and a peak temperature of 1474°C, Figure 6.16c and Table 6.11.

Figures 6.23 shows a single phase of NiAl (K), which was identified by EPMA, Table 6.12 and XRD, Figure 6.17c. The porosity of the reacted compact was higher than in the standard sample and was mostly derived from a lack of consolidation of the compact during the reaction, Table 6.11.

Finally, macrohardness readings confirmed the high porosity and microhardness readings confirmed the presence of NiAl, Table 6.11.

Compact Ni2-i-LH: The SEM image of the unreacted powders shows that the nickel particles (H) had formed a network separating the aluminium particles (A), Figure 6.14b. The nickel-aluminium contact length and the porosity of the green compact are given in Table 6.10.

The compact collapsed during the thermal explosion, allowing material to flow from the die, Figure 6.15a. The surface of the reacted compact was smooth and free from cracks.

The thermal explosion had an initiation temperature of 533°C, a rate of temperature rise of 237°C/s and a peak temperature of 1457°C, Figure 6.16d and Table 6.11.

There was no noticeable difference in porosity, Figure 6.24 and Table 6.11, phases formed, Table 6.12 and Figure 6.17c, or hardness values, Table 6.11, between this sample and the standard.

Compact Ni2-ii-P: The SEM image of the unreacted powders shows that the nickel particles (H) had formed a network separating the aluminium particles (A), Figure 6.14b. The nickel-aluminium contact length and the porosity of the green compact are given in Table 6.10.

As pressure was applied to the compact during the thermal explosion, some of the material was forced between the plunger and the die wall. When the die cooled and contracted, the plunger became wedged in the die and first had to be levered out before the reacted compact could be removed. The compact had the same diameter as the die and the surface appeared to contain gas pores , Figure 6.15c.

The thermal explosion was characterised by an initiation temperature of 571°C, a rate of temperature rise of 311°C/s and a peak temperature of 1446°C, Figure 6.16e and Table 6.11.

The NiAl (K) microstructure, Table 6.12 and Figure 6.17c, contained only a small amount of porosity in the central and midway regions, but a large amount of gas porosity in the surface regions, Figure 6.25 and Table 6.11. The hardness measurements confirmed this microstructure, Table 6.15.

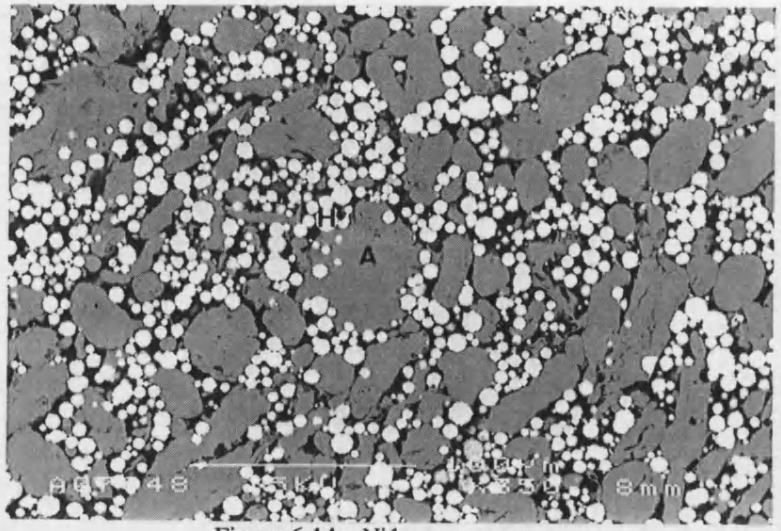

Figure 6.14a Ni1 green compact
A-Al, H-Ni 100μm

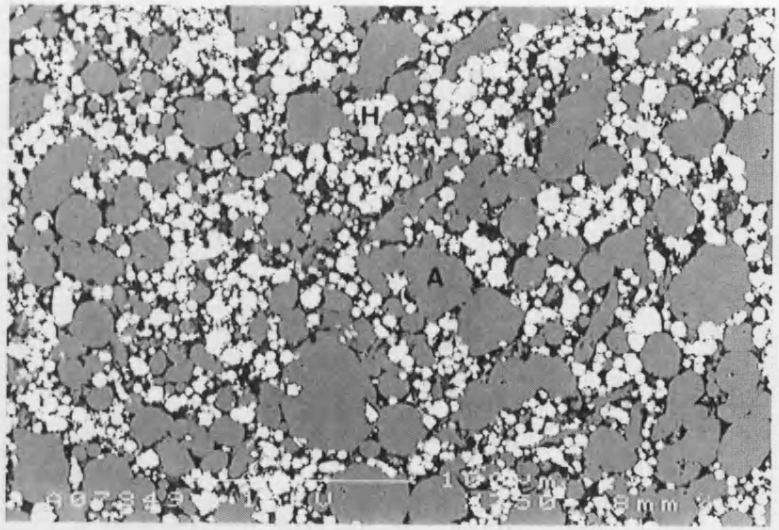

Figure 6.14b Ni2 green compact
A-Al, H-Ni 100μm

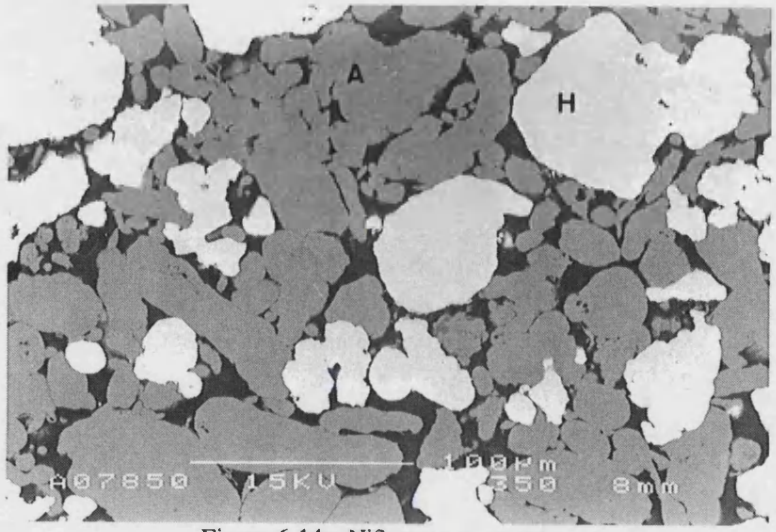

Figure 6.14c Ni3 green compact
A-Al, H-Ni 100μm

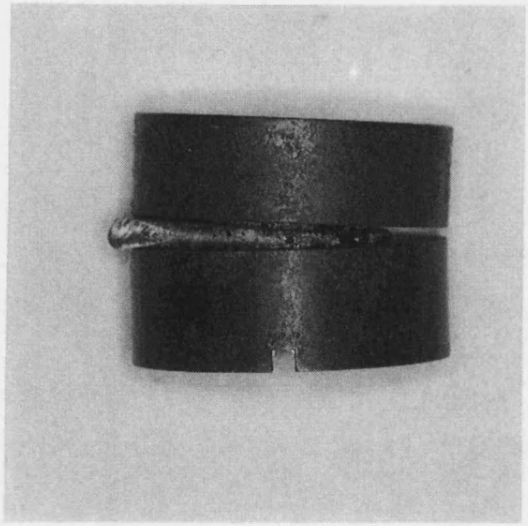

Figure 6.15a Ni-Al compact reacted in die-i 10mm

Figure 6.15b Ni-Al compact reacted in die-ii 10mm

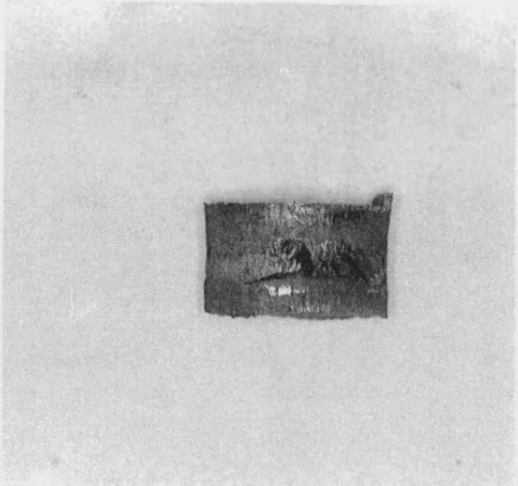

Figure 6.15c Ni-Al compact reacted in die-ii under pressure 10mm

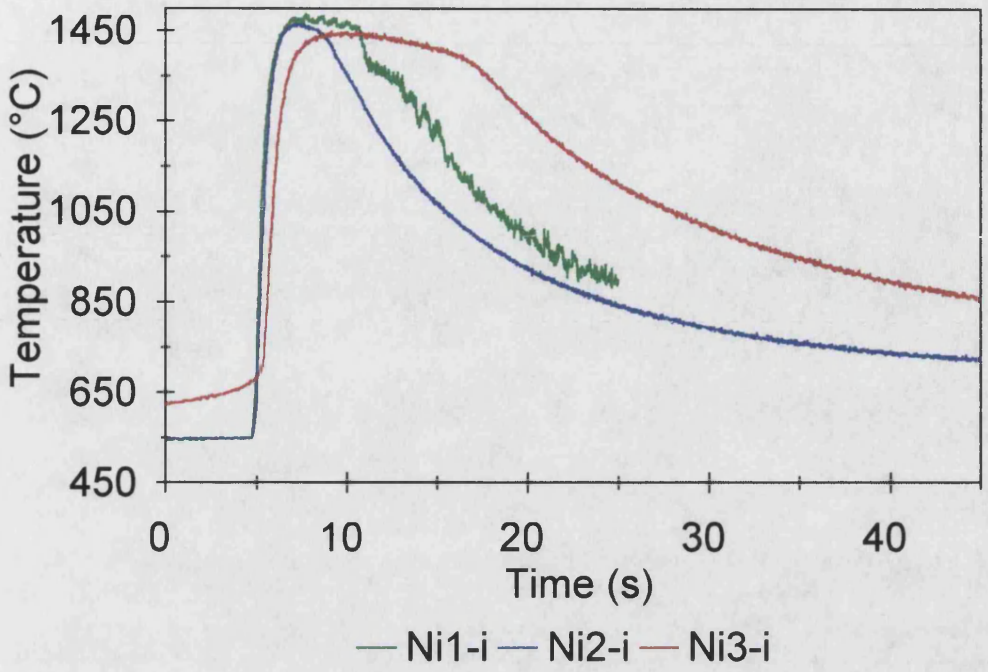

Figure 6.16a Effect of nickel PSD on nickel-aluminium time/temperature profiles

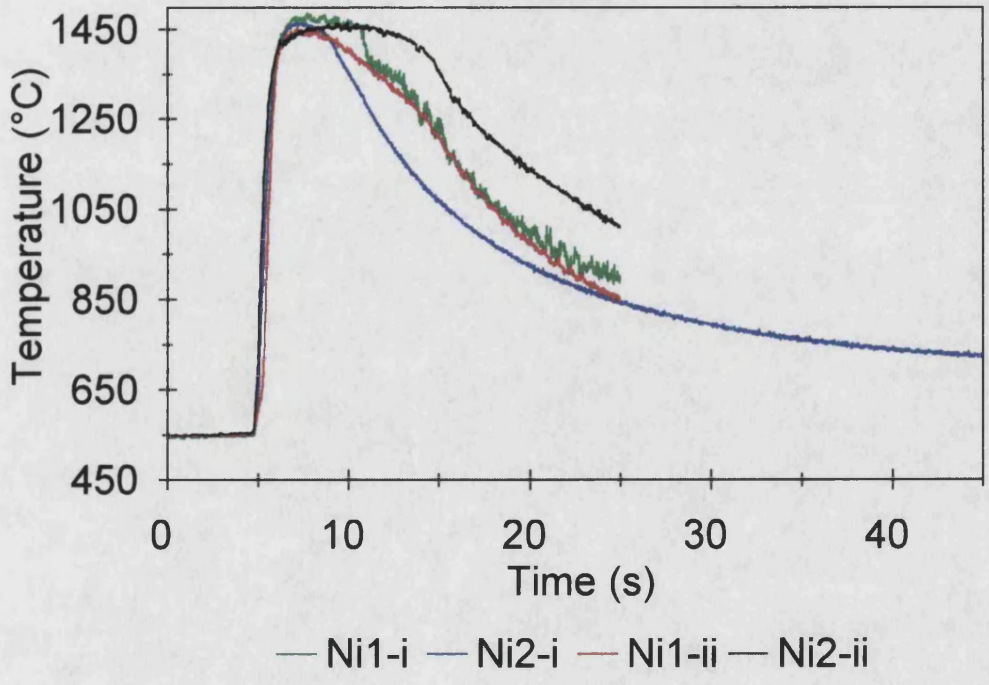

Figure 6.16b Effect of die on nickel-aluminium time/temperature profiles

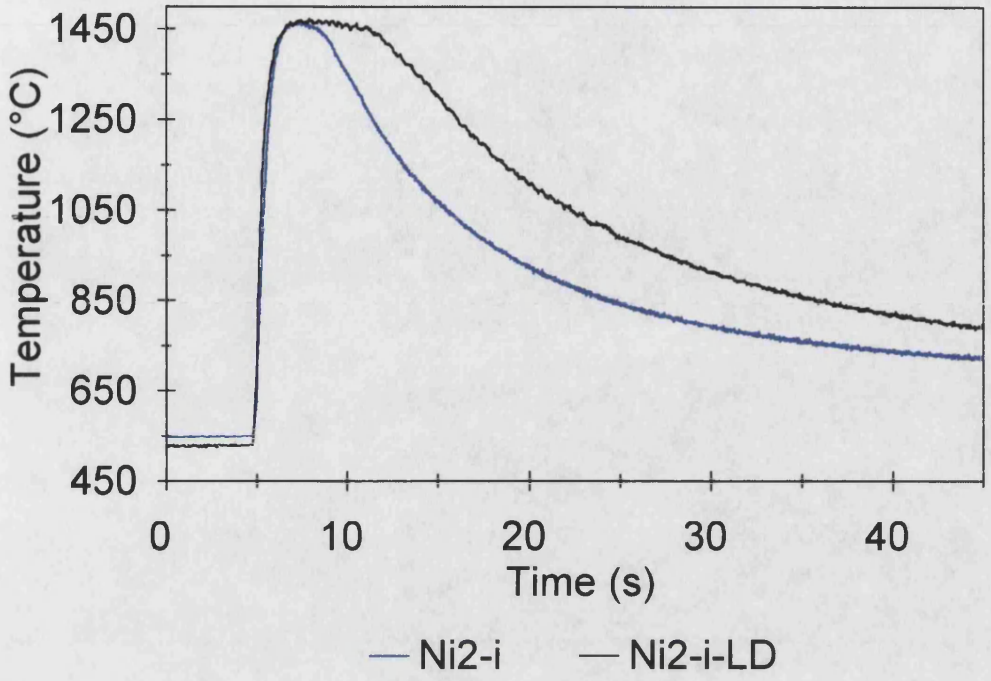

Figure 6.16c Effect of green density on nickel-aluminium time/temperature profiles

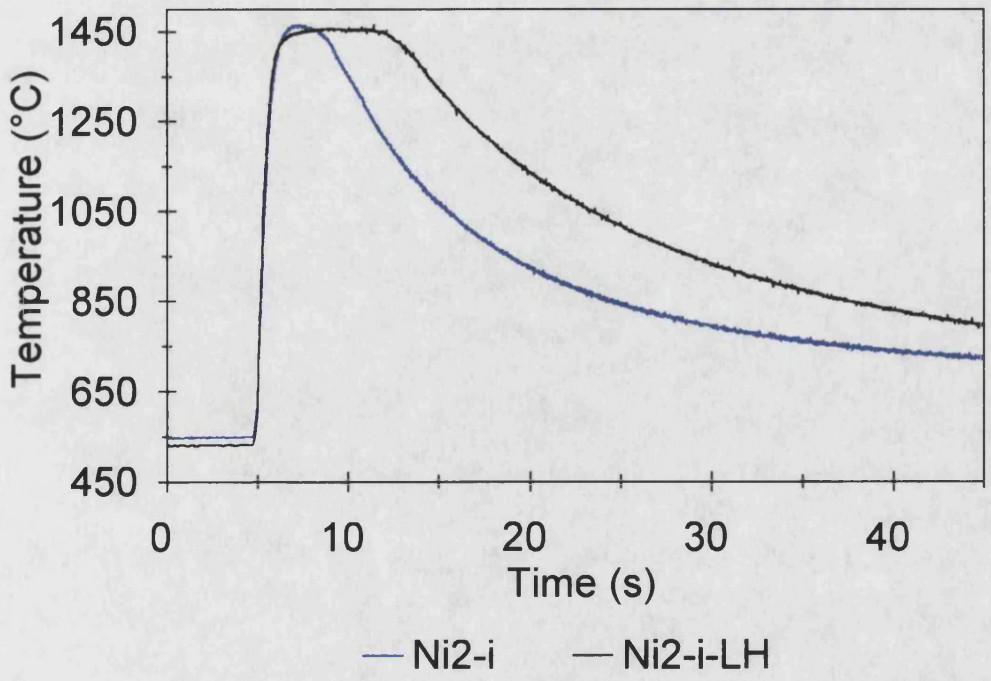

Figure 6.16d Effect of heating rate on nickel-aluminium time/temperature profiles

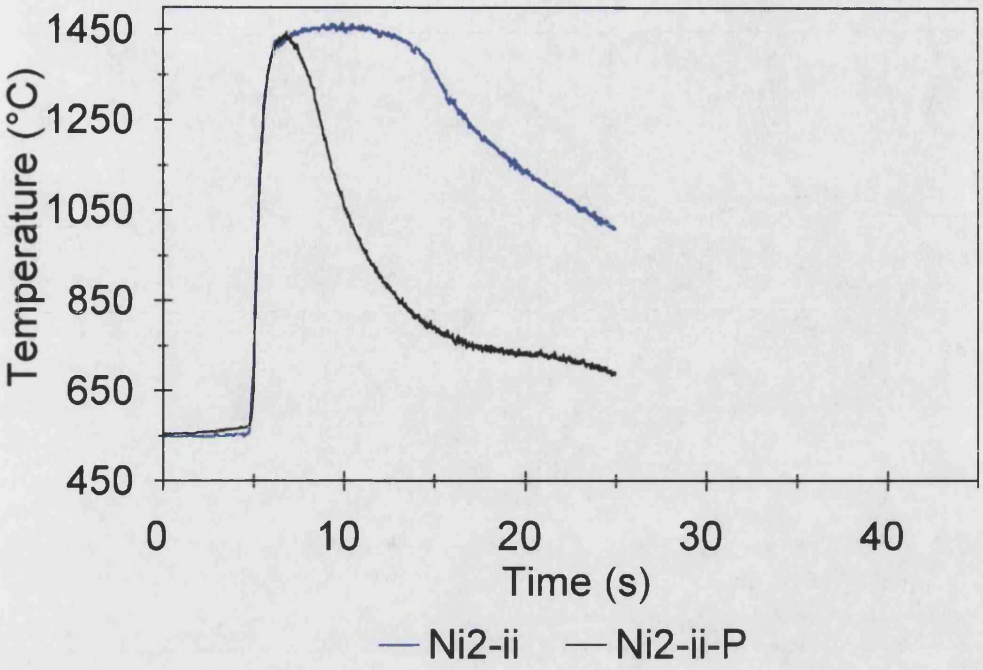

Figure 6.16e Effect of pressure on nickel-aluminium time/temperature profiles

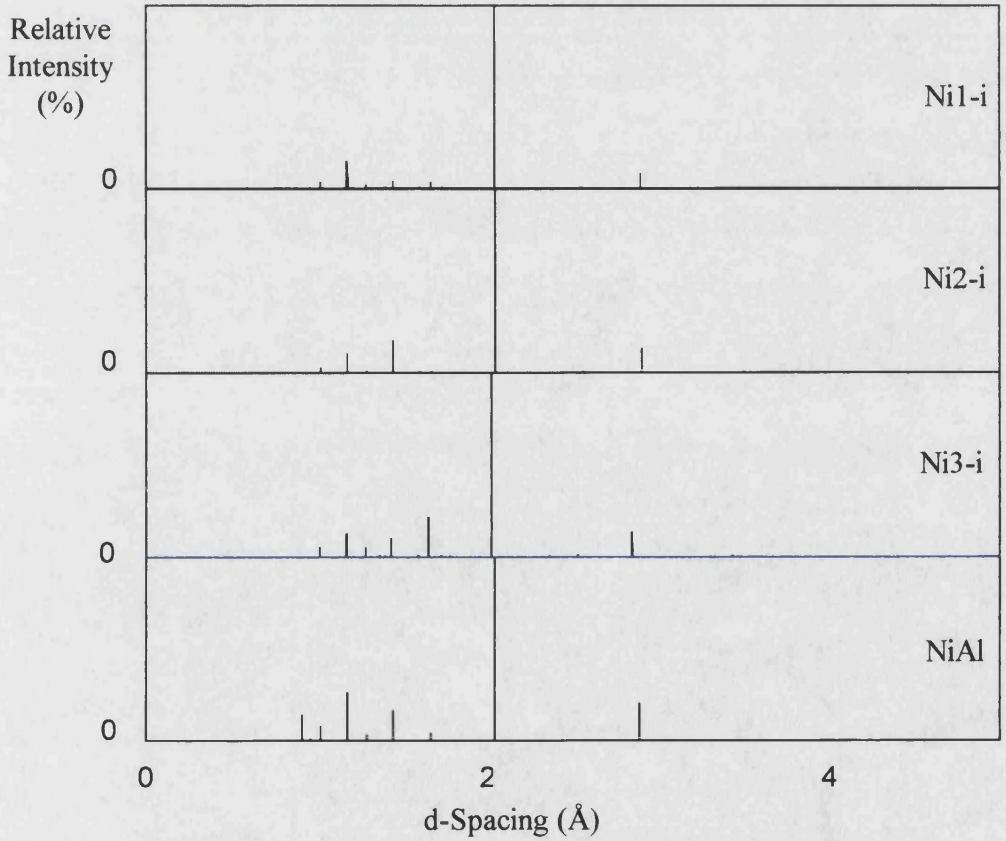

Figure 6.17a XRD plots for nickel-aluminium compacts

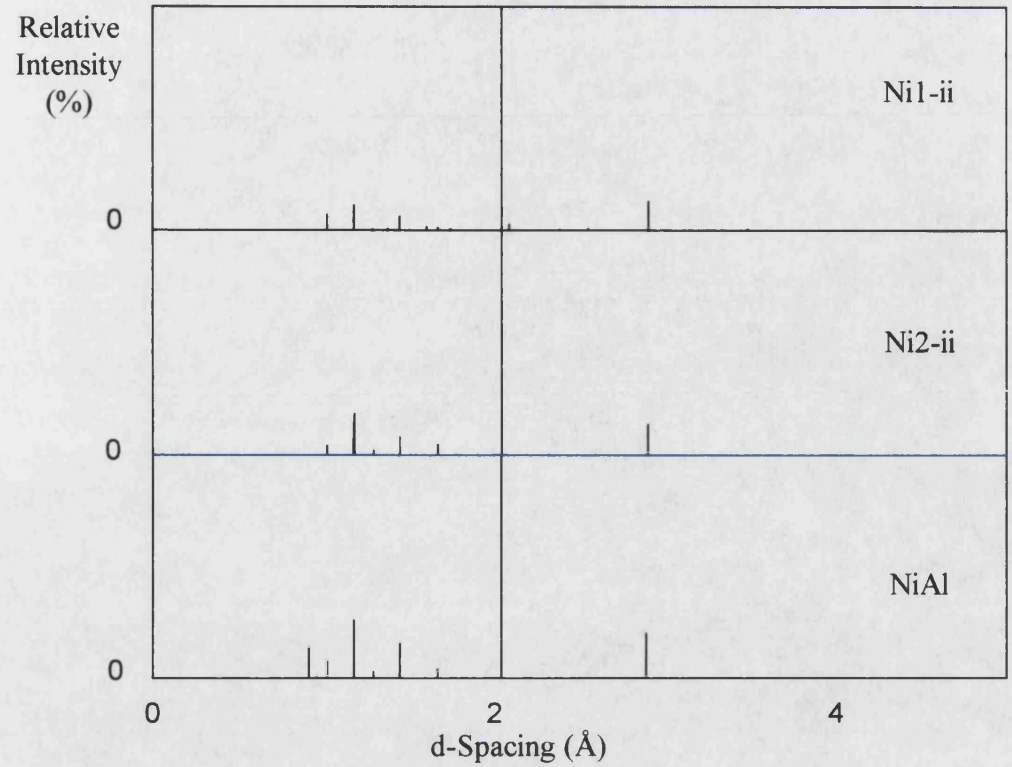

Figure 6.17b XRD plots for nickel-aluminium compacts

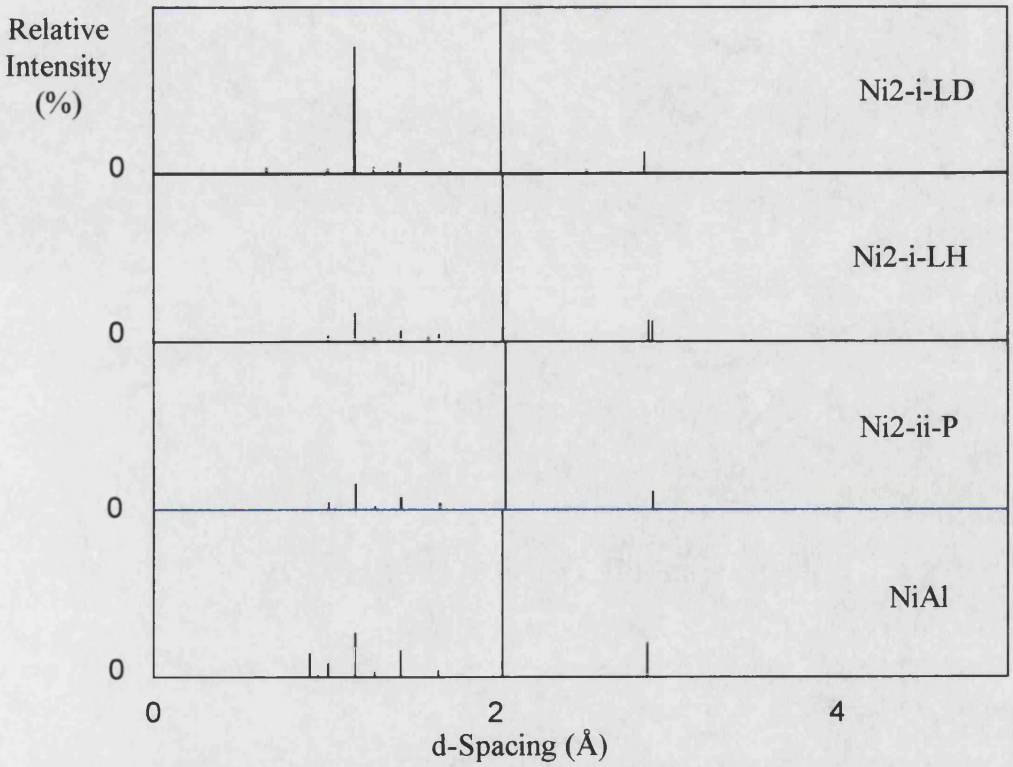

Figure 6.17c XRD plots for nickel-aluminium compacts

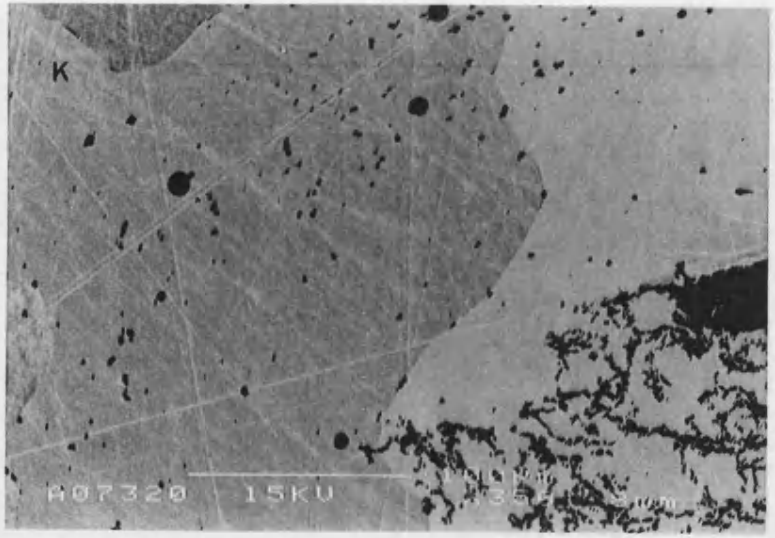

Figure 6.18 Microstructure of Ni1-i
K-NiAl 100μm

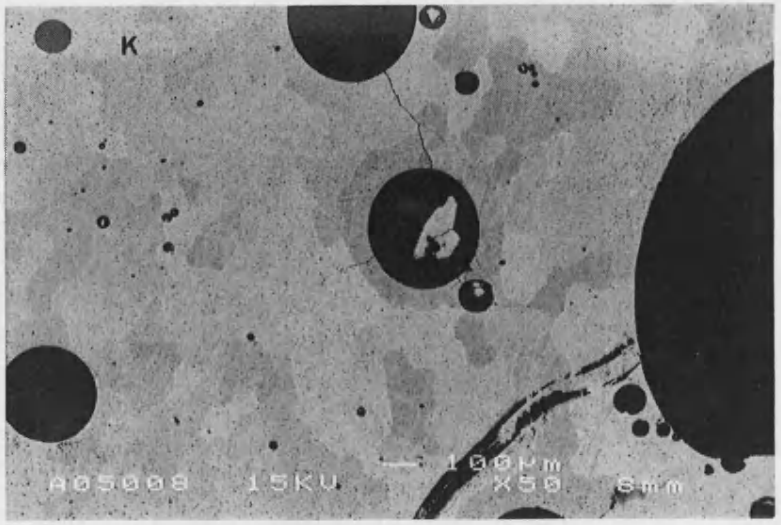

Figure 6.19a Microstructure of Ni2-i
K-NiAl 100μm

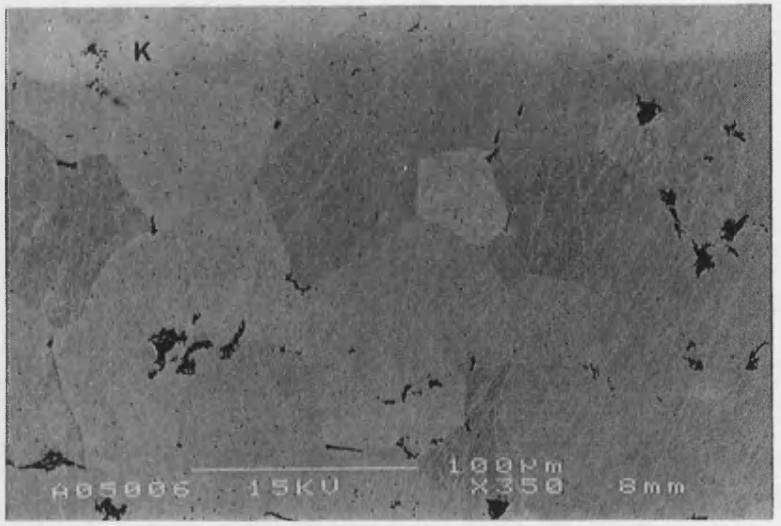

Figure 6.19b Microstructure of Ni2-i
K-NiAl 100μm

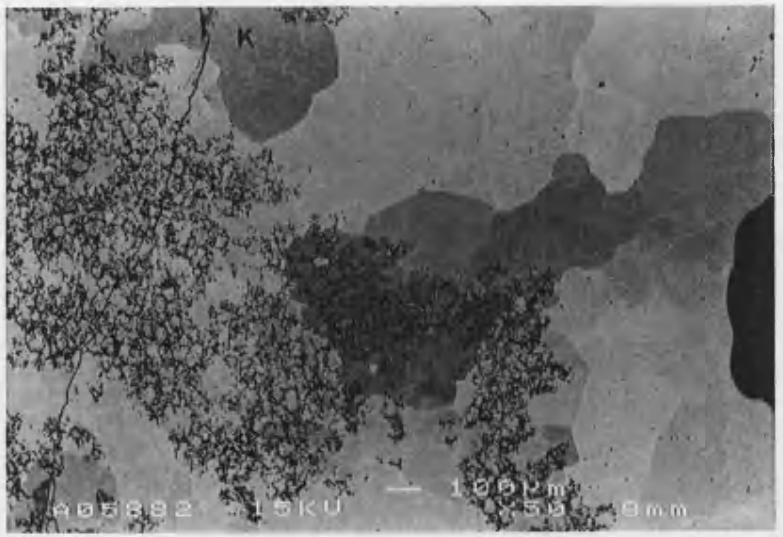

Figure 6.20a Microstructure of Ni3-i
K-NiAl 100µm

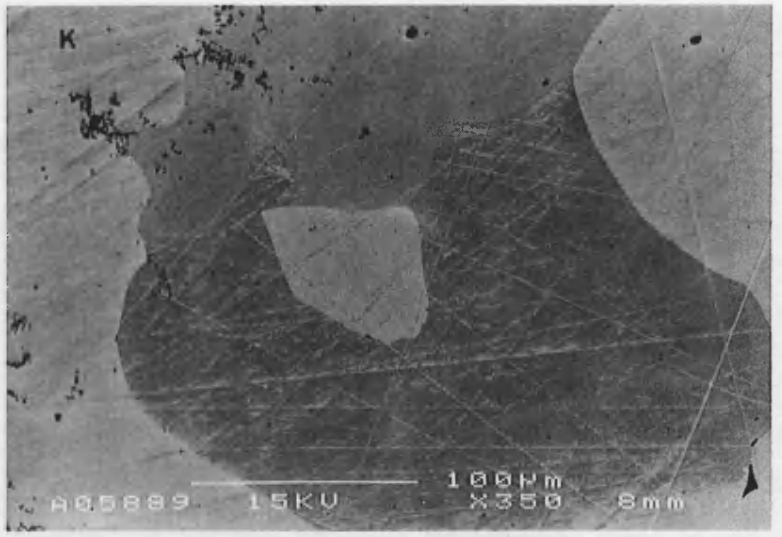

Figure 6.20b Microstructure of Ni3-i
K-NiAl 100µm

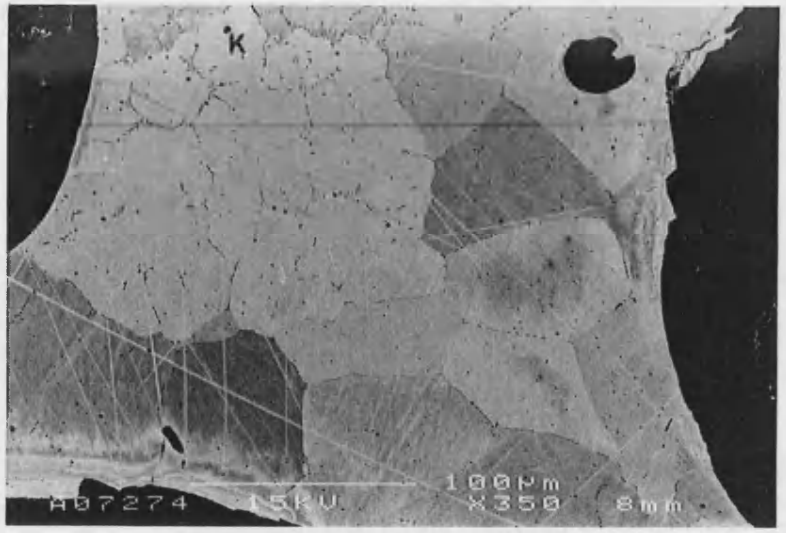

Figure 6.21 Microstructure of Ni1-ii
K-NiAl 100µm

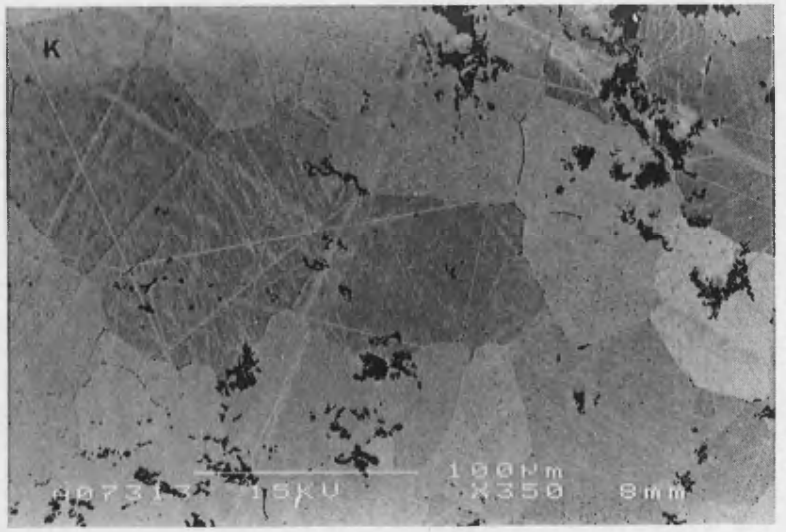

Figure 6.22 Microstructure of Ni2-ii
K-NiAl 100µm

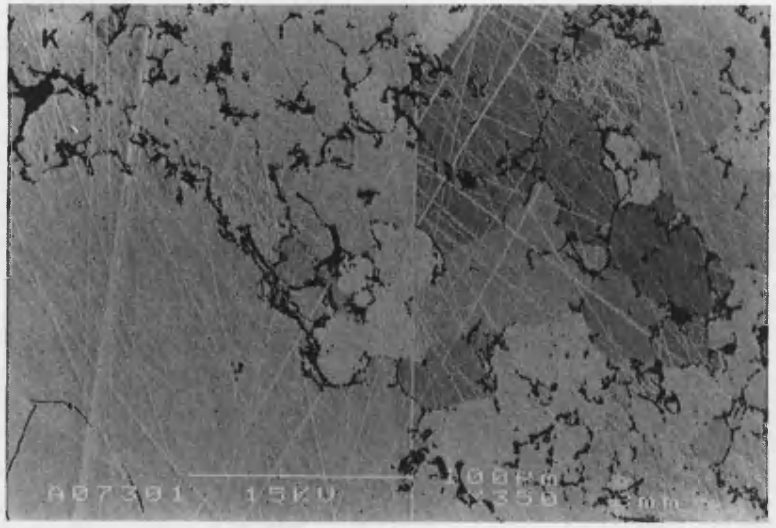

Figure 6.23 Microstructure of Ni2-i-LD
K-NiAl 100µm

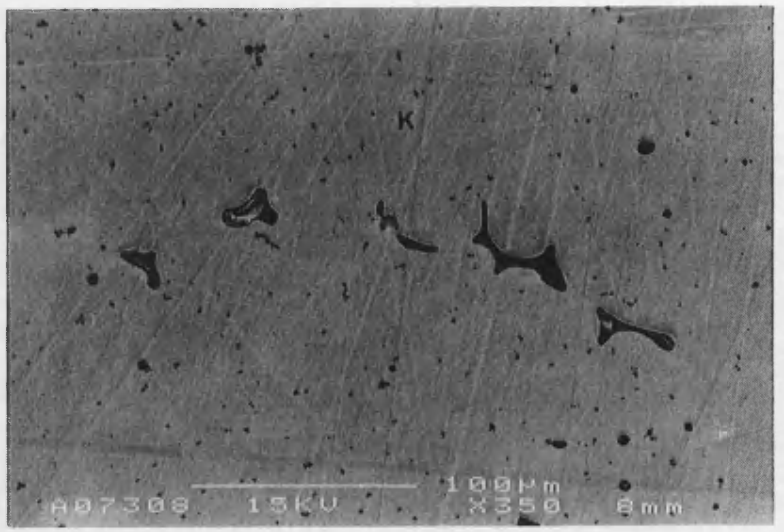

Figure 6.24 Microstructure of Ni2-i-LH
K-NiAl 100µm

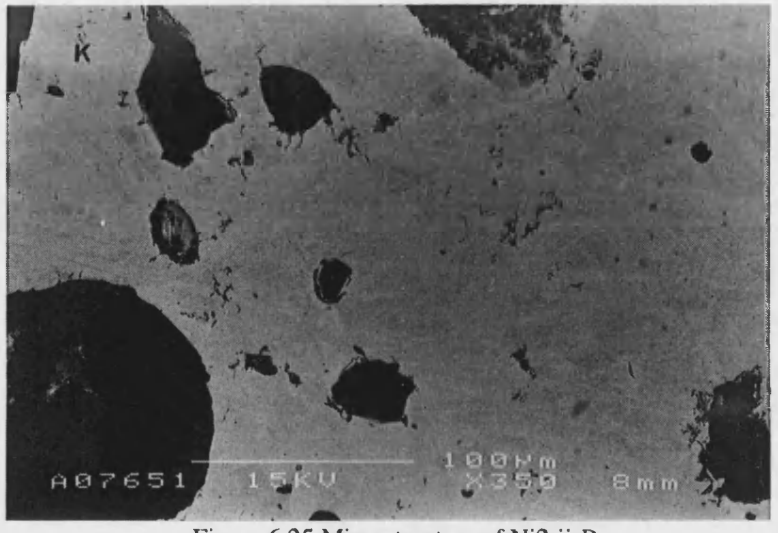

Figure 6.25 Microstructure of Ni2-ii-P
K-NiAl 100µm

6.3.3 Titanium-Aluminium

Green Compact	Ti-Al Contact Length (μm)		Porosity (%)	
	Mean	SD	Mean	SD
Ti1	1615	346	27.4	0.9
Ti2	1128	235	27.0	1.4
Ti3	870	240	26.8	0.6

Table 6.13 Details of Ti-Al green compacts

Compact	Profile Temperatures			Porosity (%)		Hardness			
	Initiation (°C)	Rate (°C/s)	Peak (°C)	Mean	SD	Macro (Hv) Mean	SD	Micro (Hv) Mean	SD
Particle Size Distribution									
Ti1-i	622	78	1313	25.1	10.8	295.8	27.5	421.4	33.6
Ti2-i	642	72	1316	19.7	7.5	226.2	67.3	453.8	52.5
Ti3-i	638	41	1283	20.7	5.1	195.0	61.6	455.8	29.2
Die Design									
Ti1-i	622	78	1313	25.1	10.8	295.8	27.5	421.4	33.6
Ti1-ii	702	9	882	18.9	9.2	117.8	46.7	308.4	93.4
Ti2-i	642	72	1316	19.7	7.5	226.2	67.3	453.8	52.5
Ti2-ii	-	-	-	8.4	2.9	67.8	7.4	136.1	24.6
Green density of the Compact									
Ti2-i	642	72	1316	19.7	7.5	226.2	67.3	453.8	52.5
Ti2-i-LD	579	66	1256	33.6	12.1	180.7	71.5	367.8	92.7
Rate of Heating of the Compact									
Ti2-i	642	72	1316	19.7	7.5	226.2	67.3	453.8	52.5
Ti2-i-LH	590	57	1327	18.2	7.8	204.8	82.8	441.6	59.8
Applying Pressure During the Thermal Explosion									
Ti2-i	642	72	1316	19.7	7.5	226.2	67.3	453.8	52.5
Ti2-i-P	607	-	-	5.6	2.5	316.8	40.2	333.8	33.6

Table 6.14 Details of Ti-Al thermal explosions and reacted compacts

Compact	Phase	Ti (at%)		Al (at%)		Alloy/ Compound
		Mean	SD	Mean	SD	
Ti1-i	P	53.9	1.0	46.1	1.0	$TiAl/Ti_3Al$
	Q	48.3	1.6	51.7	1.6	TiAl
Ti2-i	N	94.8	2.0	5.2	2.0	Ti
	P	54.8	1.5	45.2	1.5	$TiAl/Ti_3Al$
	Q	45.6	3.6	54.4	3.6	TiAl
Ti3-i	N	94.8	1.4	5.2	1.4	Ti
	P	55.6	0.9	44.4	0.9	$TiAl/Ti_3Al$
	Q	45.1	0.6	54.9	0.6	TiAl
Ti1-ii	N	99.1	0.9	0.9	0.9	Ti
	P	53.6	0.9	46.4	0.9	$TiAl/Ti_3Al$
	Q	48.4	0.9	51.6	0.9	TiAl
	R	34.0	0.3	66.0	0.3	$TiAl_2$
	S	24.7	0.1	75.3	0.1	$TiAl_3$
Ti2-ii	N	99.0	1.6	1.0	1.6	Ti
	S	25.0	0.4	75.0	0.4	$TiAl_3$
Ti2-i-LD	N	96.7	2.6	3.4	2.6	Ti
	P	54.7	1.1	45.3	1.1	$TiAl/Ti_3Al$
	Q	44.9	0.2	55.1	0.2	TiAl
Ti2-i-LH	N	97.4	2.1	2.6	2.1	Ti
	P	54.9	0.9	45.1	0.9	$TiAl/Ti_3Al$
	Q	45.1	0.6	54.9	0.6	TiAl
Ti2-i-P	N	99.9	0.0	0.1	0.0	Ti
	S	26.6	0.8	73.4	0.8	$TiAl_3$

Table 6.15 EPMA data for Ti-Al reacted compacts

Compact Ti1-i: The SEM image of the unreacted compact showed that the aluminium (A) had formed a connected network around groups of titanium particles (N), Figure 6.26a. Details of the titanium-aluminium contact length and the porosity of the green compact are given in Table 6.13.

Figure 6.27a is a photograph of the reacted compact which shows that the top of the compact had expanded upwards during the thermal explosion and that the weight of the top dish had pulled it to one side and ruptured the surface. The surface of the compact was found to be rough and solid.

This compact produced a thermal explosion which initiated at 622°C, and rose to a peak temperature of 1313°C at a rate of 78°C/s, Table 6.14. The time/temperature

profile for this thermal explosion is plotted against those of identical compacts reacted in different die designs in Figures 6.28a and against compacts containing different titanium powder size distributions in Figure 6.28b.

Figure 6.30a shows that a multiphase microstructure, consisting of grains of TiAl (Q) interspersed with lamellar regions (P), was formed in this sample. The layers of the lamellar regions were too thin to resolve individually, but previous work[3,8,15] has identified them as alternating plates of TiAl (Q) and Ti_3Al (O), Figure 6.30b. The EPMA data which was obtained from the sample is displayed in Table 6.15 and the XRD plot which identifies the presence of TiAl and Ti_3Al is shown in Figure 6.29a.

The porosity found in the sample was mostly porosity remaining from the green compact, though there were a few small gas pores present. Porosity levels were greatest at the surface of the compact and decreased towards the centre, Table 6.14.

The high microhardness measurements taken between the pores indicated the formation of hard intermetallic phases, whilst the lower macrohardness measurements, which included pores, indicated the porous nature of the material, Table 6.14.

Compact Ti2-i: Figure 6.26b is a SEM image of the unreacted compact containing the PSD2 titanium powder. The aluminium particles (A) had formed a connected network between the titanium particles (N) to give the contact length and porosity displayed in Table 6.13.

Figure 6.27a is a photograph of the reacted compact which shows that the top of the compact had expanded upwards during the thermal explosion and that the weight of the top dish had pulled it to one side and ruptured the surface. The surface of the compact was found to be rough and solid.

This compact was heated to a temperature of 642°C to initiate a thermal explosion which raised the temperature to a peak of 1316°C at a rate of 72°C/s, Figures 6.28a-b and Table 6.14.

The majority of the sample microstructure contained TiAl (Q) and lamellar regions of $TiAl/Ti_3Al$ (P), but there were also a few titanium rich cores (N), Figure 6.31. The EPMA and XRD data are displayed in Table 6.15 and Figure 6.29a respectively. A

few gas pores were found in the sample, but most of the porosity was derived from a lack of consolidation of the sample during the thermal explosion, Table 6.14.

Macrohardness measurements were varied and dependent on porosity, whilst microhardness values were high and indicated the formation of hard intermetallic phases, Table 6.14.

Compact Ti3-i: Once again, the aluminium (A) had formed a connected network around the titanium particles (N), Figure 6.26c, and this gave the titanium-aluminium interfacial length and green porosity detailed in Table 6.13.

Figure 6.27a is a photograph of the reacted compact which shows that the top of the compact had expanded upwards during the thermal explosion and that the weight of the top dish had pulled it to one side and ruptured the surface. The surface of the compact was found to be rough and solid.

This compact produced a thermal explosion with an initiation temperature of 638°C, a rate of temperature rise of 41°C/s and a peak temperature of 1283°C, Figure 6.28a and Table 6.14.

The whole of the sample contained titanium rich regions (N), TiAl/Ti_3Al lamellae (P) and TiAl (Q), Figure 6.32. EPMA data are presented in Table 6.15 and the XRD plot showed peaks for TiAl and Ti_3Al, Figure 6.29a.

Porosity levels were similar to those of the other compacts reacted in die-i, Table 6.14, and microhardness measurements were also comparable to other TiAl and TiAl/Ti_3Al containing samples.

Compact Ti1-ii: The SEM image of the unreacted compact showed that the aluminium had formed a connected network around groups of titanium particles, Figure 6.26a. Details of the titanium-aluminium contact length and the porosity of the green compact are given in Table 6.13.

Die-ii directed the expansion of the compact upwards during the thermal explosion to give the shape shown in, Figure 6.27b. The surface of the reacted compact, which was in contact with the die wall during the reaction, was found to be loose and powdery.

The thermal explosion ignited in this compact had an initiation temperature of 702°C, a slow rate of temperature rise of 9°C/s and a peak temperature of 882°C, Figures 6.28b and Table 6.14.

The central region of the reacted compact contained TiAl (Q) and $TiAl/Ti_3Al$ (P) layers, Figure 6.33a, but there was a gradual change in the phases formed towards the surface. The midway region consisted of titanium rich cores (N) surrounded by TiAl (Q), $TiAl_2$ (R) and $TiAl_3$ (S), Figure 6.33b, and the surface region consisted of titanium rich cores (N) surrounded by $TiAl_3$ (S) only, Figure 6.33c. EPMA data from these regions were used to identify the phases, Table 6.15, but XRD plots contained too many peaks to successfully resolve the individual phases Figure 6.29b.

The sample contained a large amount of porosity, which increased from the centre to the surface, since there had been little consolidation of the reacting compact during the thermal explosion and the porosity in the green compact had remained, Table 6.15.

The large standard deviation of the hardness measurements reflected the changes in porosity and phases across the sample, Table 6.14. This was particularly noticeable for the microhardness measurements which were taken from a variety of phases with widely differing hardness values.

Compact Ti2-ii: Figure 6.26b is a SEM image of the unreacted compact containing the PSD2 titanium powder. The aluminium particles had formed a connected network between the titanium particles to give the contact length and porosity displayed in Table 6.13.

Die-ii directed the expansion of the compact upwards during the thermal explosion to give the shape shown in, Figure 6.27b. The surface of the reacted compact, which was in contact with the die wall during the reaction, was found to be loose and powdery.

The compact was heated in the furnace to a temperature of 725°C, but no thermal explosion was detected by the data collection software. Either, no thermal explosion was initiated or the rate of temperature rise was too slow to trigger the software.

When the sample was examined using EPMA, Table 6.15, and XRD, Figure 6.29b it was found to contain titanium rich regions (N) surrounded by a matrix of $TiAl_3$ (S), Figure 6.34. The compact also contained a large amount of porosity which had been

present in the green compact and both macrohardness and microhardness values were low, Table 6.14.

Compact Ti2-i-LD: The lower pressure produced a green compact with a porosity of 32.8%. Figure 6.27a is a photograph of the reacted compact which shows that the top of the compact had expanded upwards during the thermal explosion and that the weight of the top dish had pulled it to one side and ruptured the surface. The surface of the compact was found to be rough and solid.

The time/temperature profile of the thermal explosion showed an initiation temperature of 579°C, a rate of temperature rise of 66°C/s and a peak temperature of 1256°C, Figure 6.28c and Table 6.14.

The same phases as those in the standard sample were formed, with titanium rich cores (N), TiAl/Ti_3Al lamellar regions (P) and TiAl (Q) all present, Figure 6.35. The EPMA and XRD data obtained from this sample are displayed in Table 6.15 and Figure 6.29c respectively. The sample was more porous than the standard and all the porosity derived from a lack of consolidation of the green compact. Hardness measurements reflected the highly porous nature of the sample, Table 6.14.

Compact Ti2-i-LH: Figure 6.26b is a SEM image of the unreacted compact containing the PSD2 titanium powder. The aluminium particles had formed a connected network between the titanium particles to give the contact length and porosity displayed in Table 6.13.

Figure 6.27a is a photograph of the reacted compact which shows that the top of the compact had expanded upwards during the thermal explosion and that the weight of the top dish had pulled it to one side and ruptured the surface. The surface of the compact was found to be rough and solid.

The lower heating rate produced a thermal explosion in the compact which initiated at a temperature of 590°C, and rose to a peak temperature of 1327°C at a rate of 57°C/s, Figure 6.28d and Table 6.15.

The usual microstructure of titanium rich cores (N), TiAl/Ti_3Al lamellar regions (P) and TiAl (Q), for a compact reacted in die-i, was formed, Figure 6.36. The EPMA

data are included in Table 6.15 and the XRD plot showed peaks for TiAl and Ti_3Al, Figure 6.29c.

Gas pores and a lack of consolidation of the green compact again accounted for the porosity, Table 6.14, and hardness values were comparable to the standard sample.

Compact Ti2-i-P: Figure 6.26b is a SEM image of the unreacted compact containing the PSD2 titanium powder. The aluminium particles had formed a connected network between the titanium particles to give the contact length and porosity displayed in Table 6.13.

The pressure applied during the thermal explosion squashed the compact and forced the top to expand radially, Figure 6.27c. Since the reacting compact had been firmly pushed into the two dishes of die-i, it became wedged as the die cooled and the die had to be sectioned to remove it.

An initiation temperature of 607°C was measured by the thermocouple, but the wires of the thermocouple became separated when pressure was applied to the die and no further readings were taken.

EPMA data, Table 6.15, revealed that the application of pressure had quenched the thermal explosion and formed a microstructure of titanium rich cores (N) surrounded by $TiAl_3$ (S), Figure 6.37. This was supported by the XRD plot in Figure 6.29c.

The pressure applied during the thermal explosion succeeded in closing some of the porosity present in the green compact, Table 6.14. The macrohardness values reflected the lower porosity levels and the low microhardness levels indicated that the reaction had not continued to completion, Table 6.14.

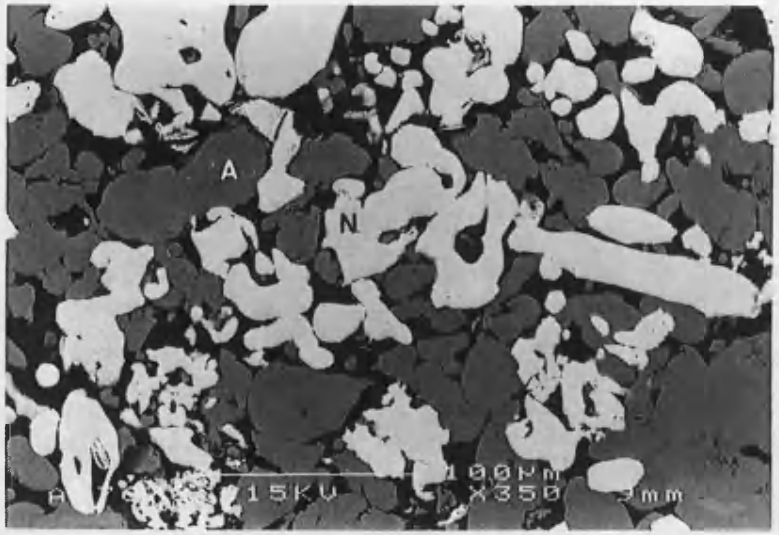

Figure 6.26a Ti1 green compact
A-Al, N-Ti 100μm

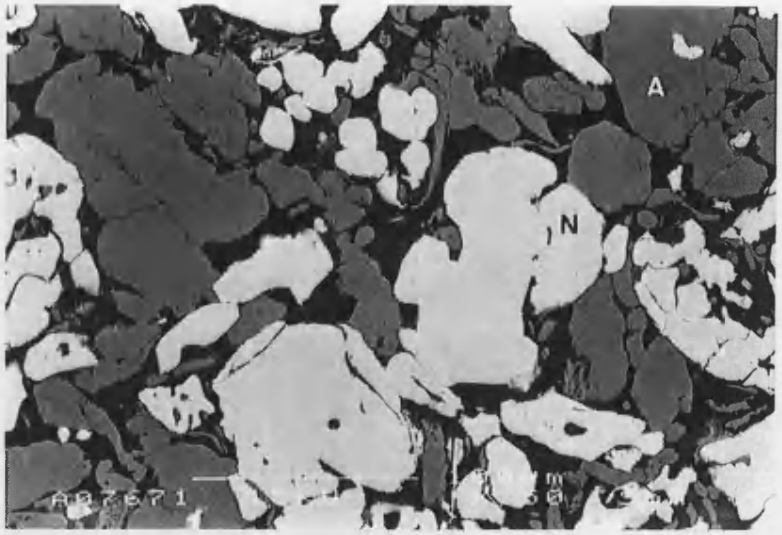

Figure 6.26b Ti2 green compact
A-Al, N-Ti 100μm

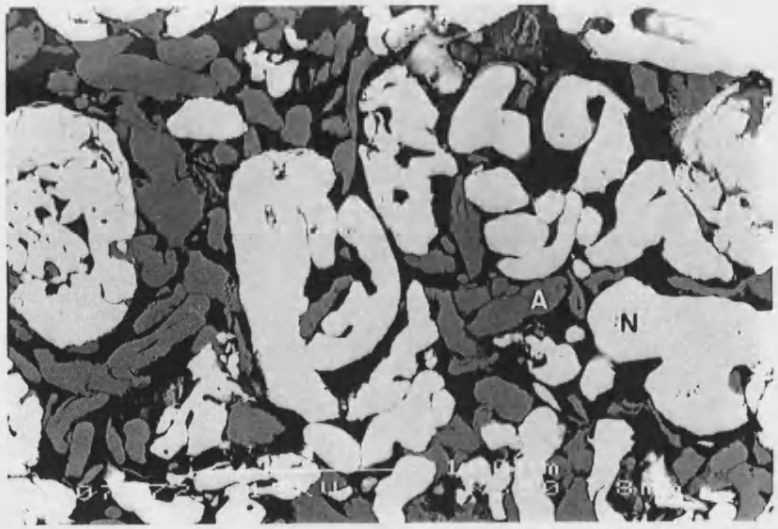

Figure 6.26c Ti3 green compact
A-Al, N-Ti 100μm

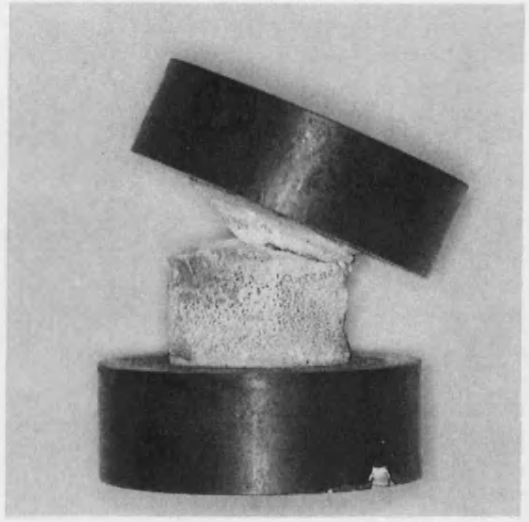

Figure 6.27a Ti-Al compact reacted in die-i 10mm

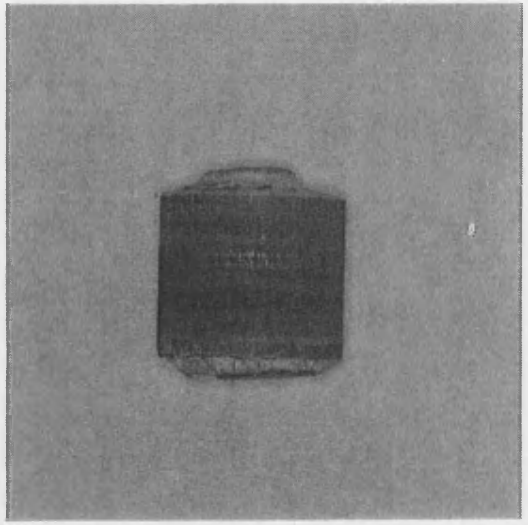

Figure 6.27b Ti-Al compact reacted in die-ii 10mm

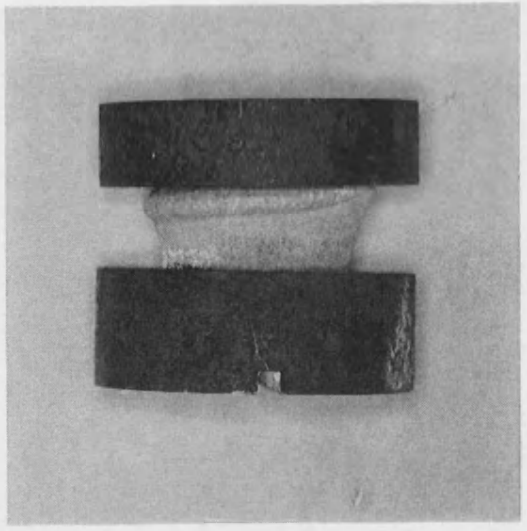

Figure 6.27c Ti-Al compact reacted in die-i under pressure 10mm

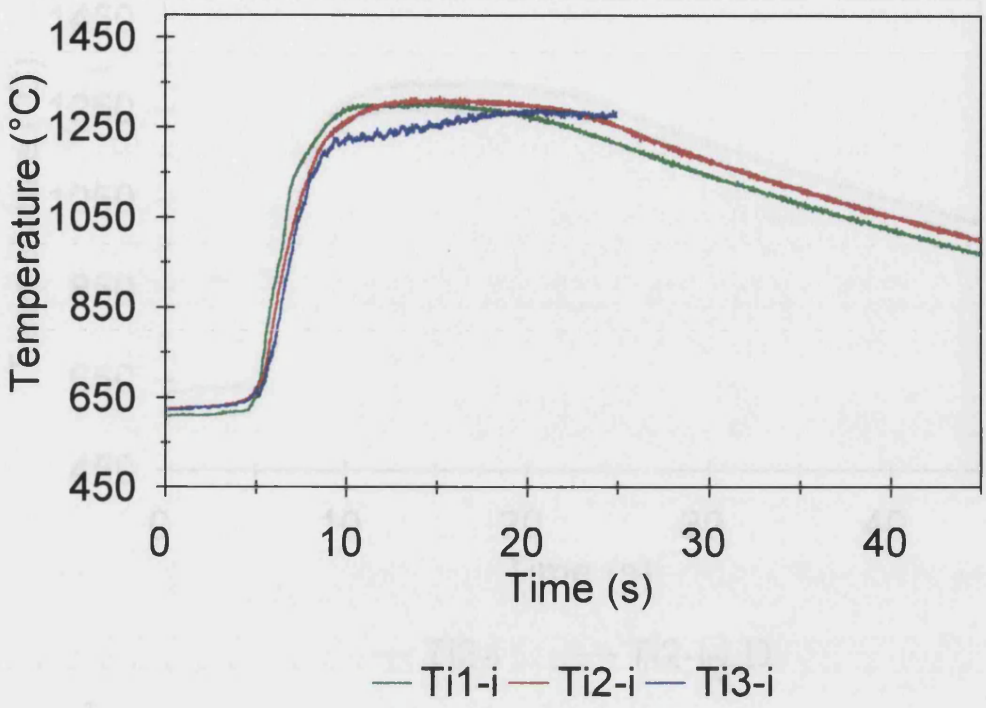

Figure 6.18a Effect of titanium PSD on titanium-aluminium time/temperature profiles

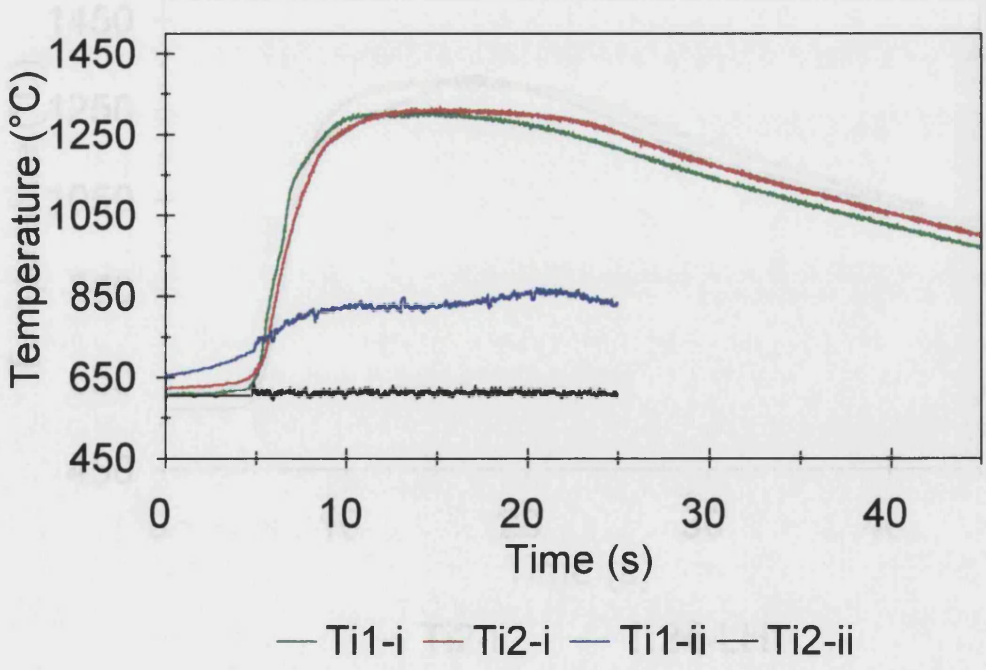

Figure 6.18b Effect of the die on titanium-aluminium time/temperature profiles

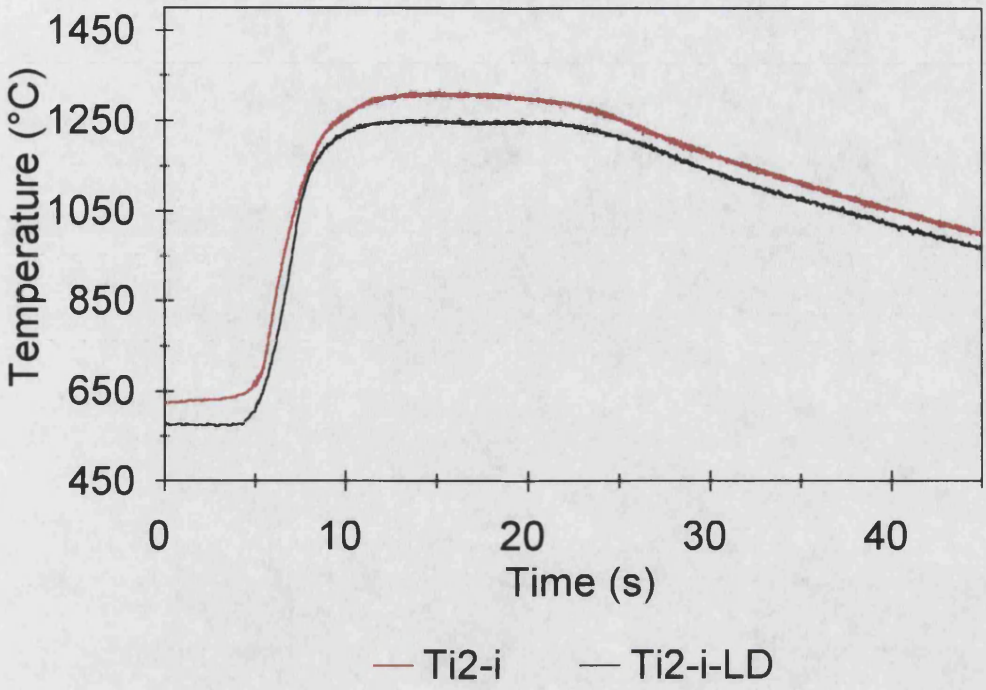

Figure 6.18c Effect of green density on titanium-aluminium time/temperature profiles

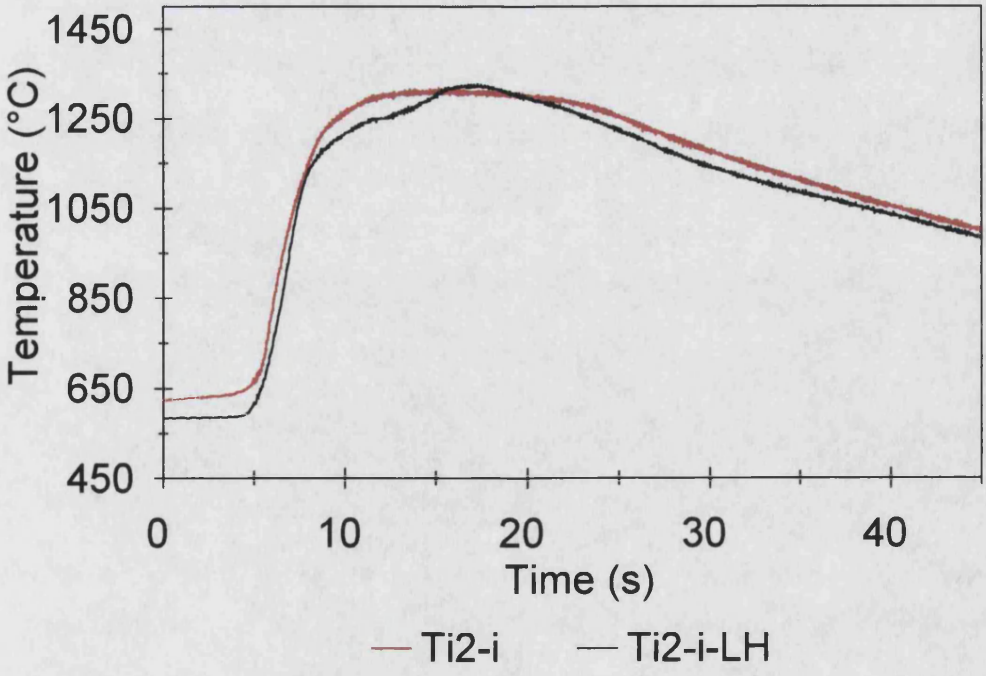

Figure 6.18d Effect of heating rate on titanium-aluminium time/temperature profiles

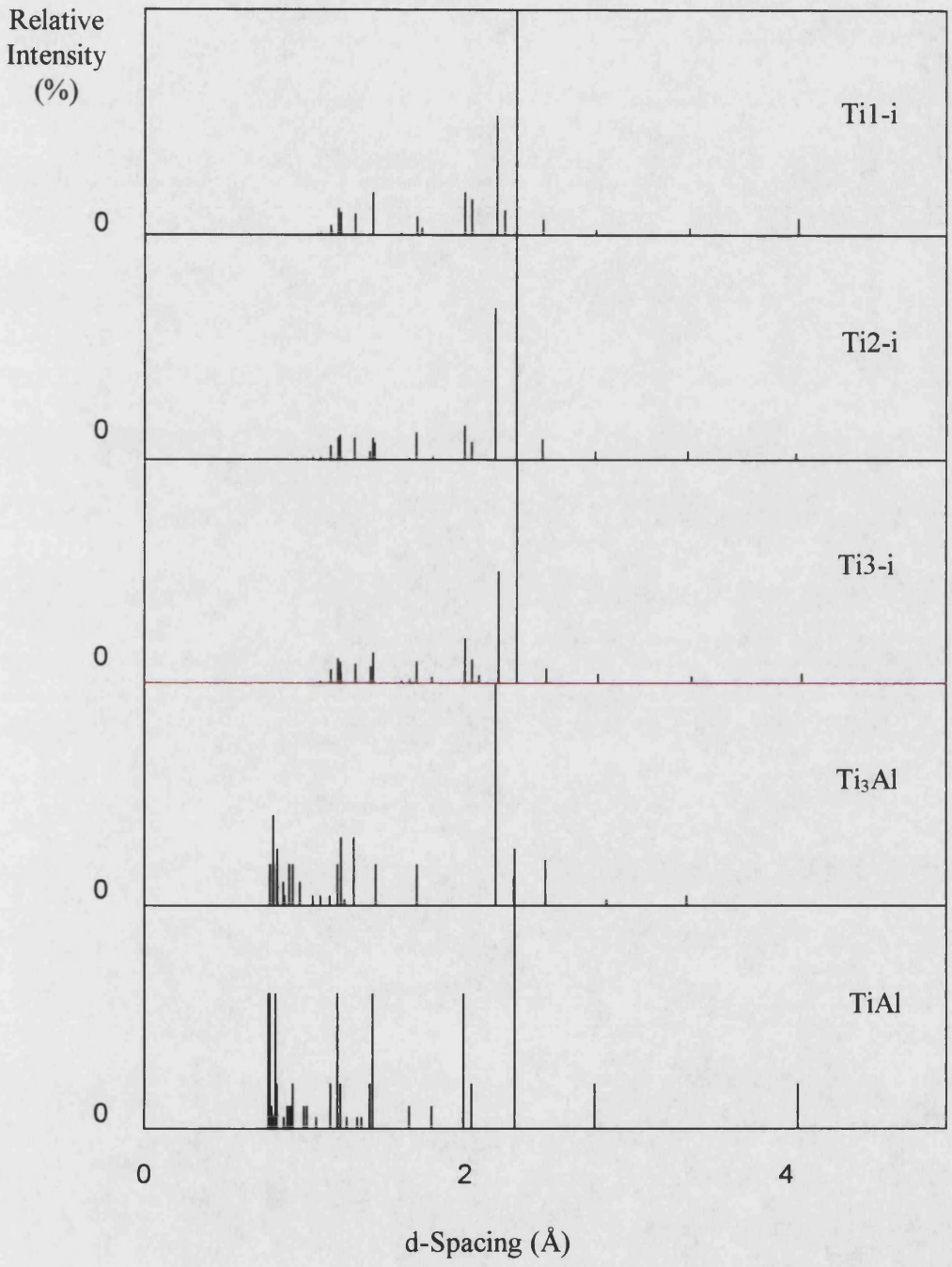

Figure 6.29a XRD plots for titanium-aluminium compacts

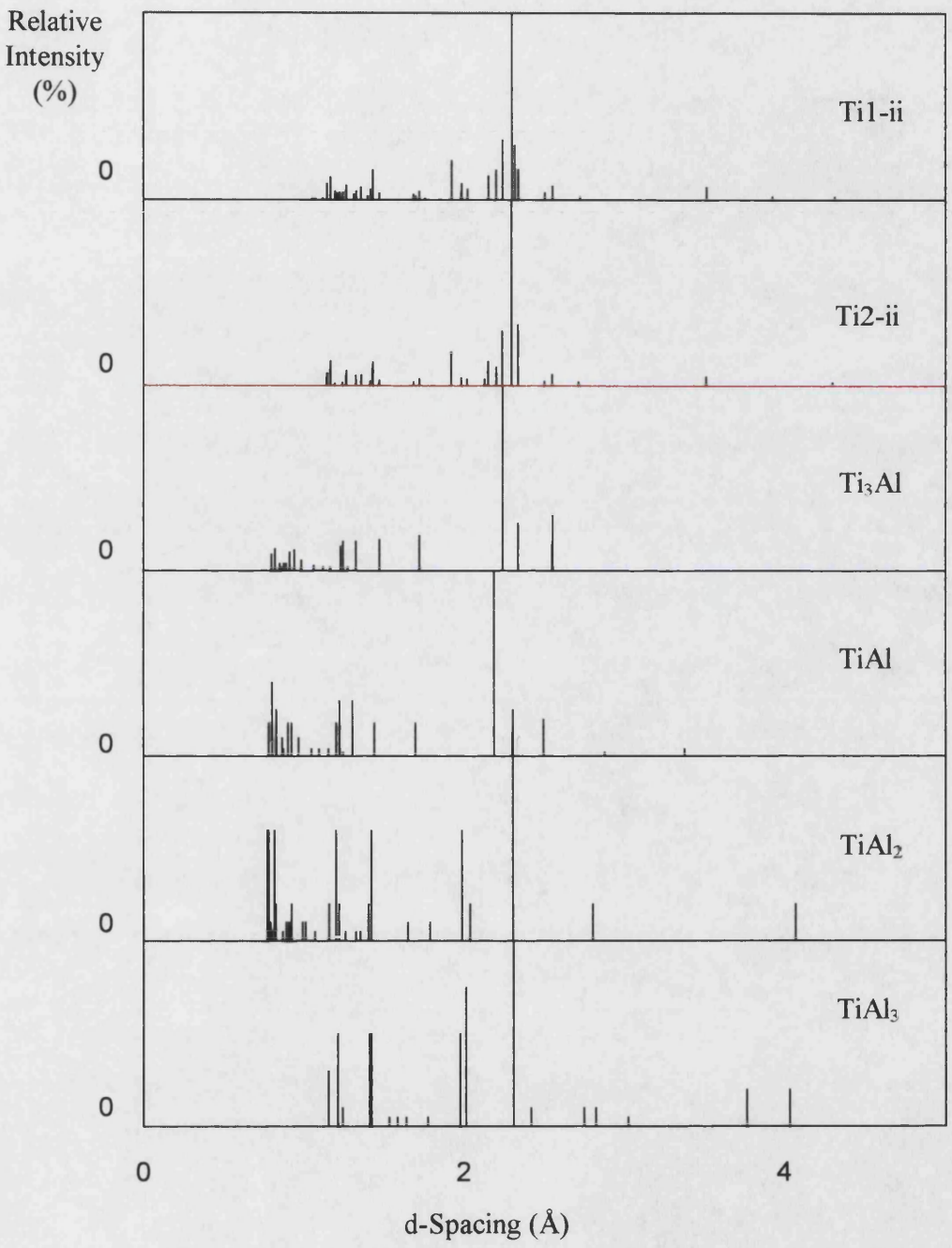

Figure 6.29b XRD plots for titanium-aluminium compacts

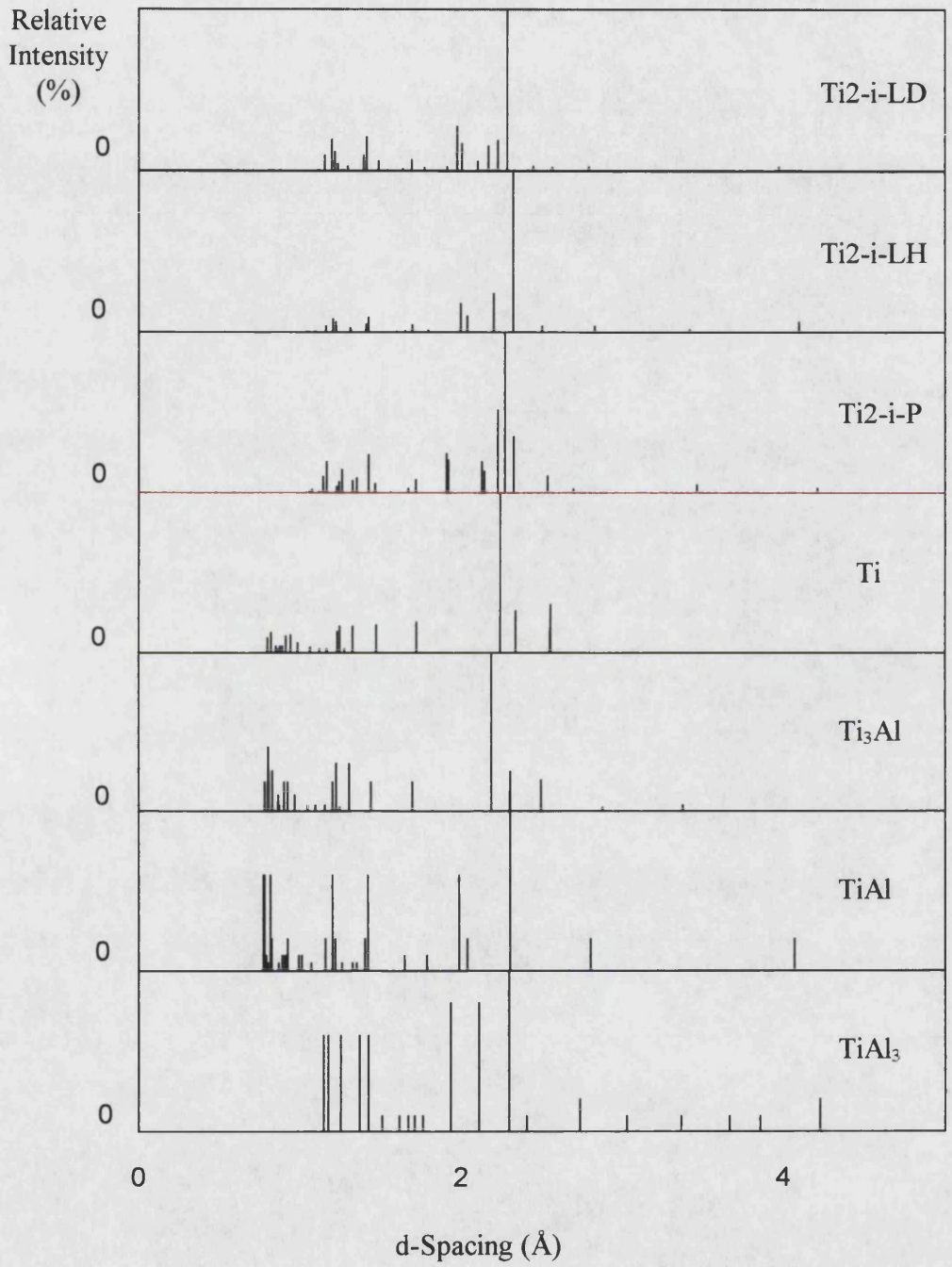

Figure 6.29c XRD plots for titanium-aluminium compacts

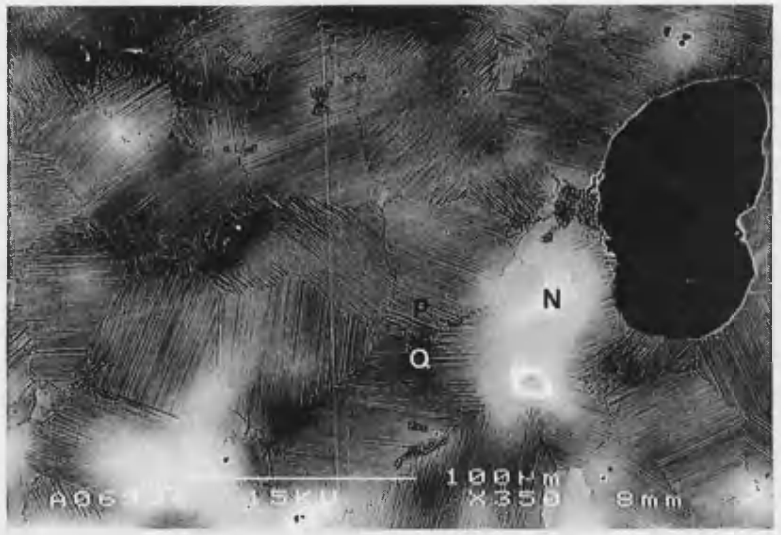

Figure 6.30a Microstructure of Ti1-i
N-Ti rich,P-TiAl/Ti_3Al, Q-TiAl 100µm

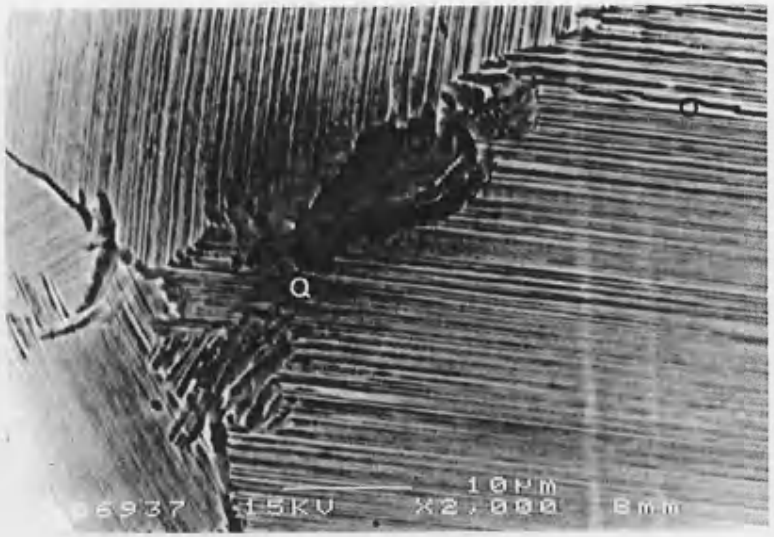

Figure 6.30b Lamellar region
O-Ti_3Al, Q-TiAl 100µm

Figure 6.31 Microstructure of Ti2-i
N-Ti rich, P-TiAl/Ti_3Al, Q-TiAl 100µm

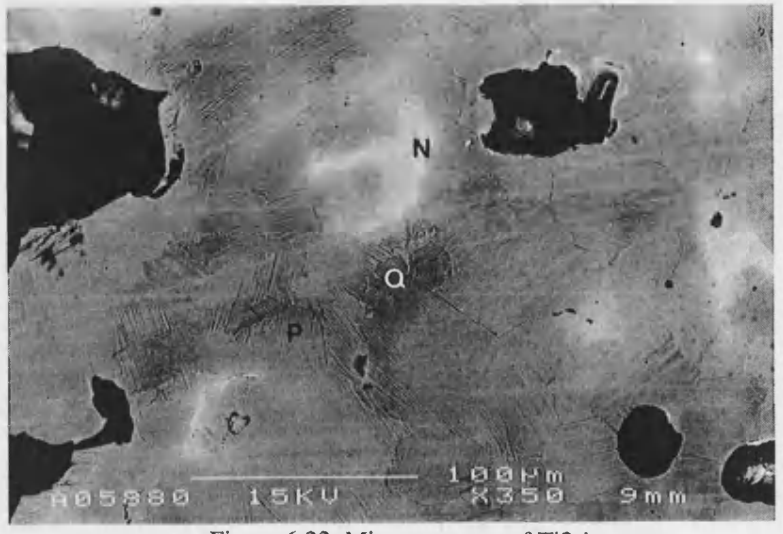

Figure 6.32 Microstructure of Ti3-i
N-Ti rich, P-TiAl/Ti_3Al, Q-TiAl 100µm

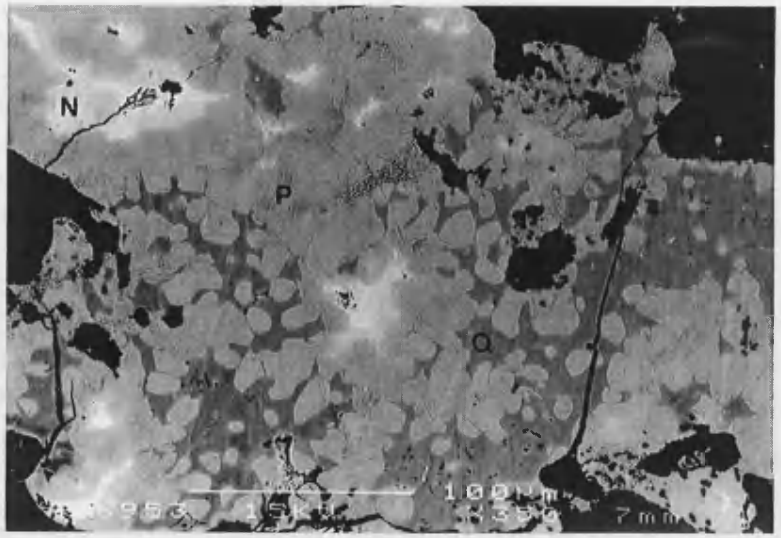

Figure 6.33a Centre region of Ti1-ii
N-TiAl, P-TiAl/Ti_3Al, Q-TiAl 100μm

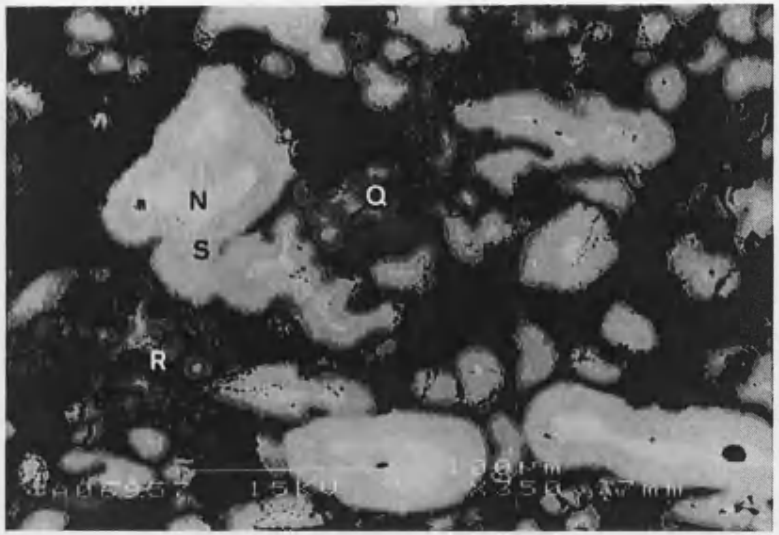

Figure 6.33b Midway region of Ti1-ii
N-Ti rich, Q-TiAl, R-$TiAl_2$, S-$TiAl_3$ 100μm

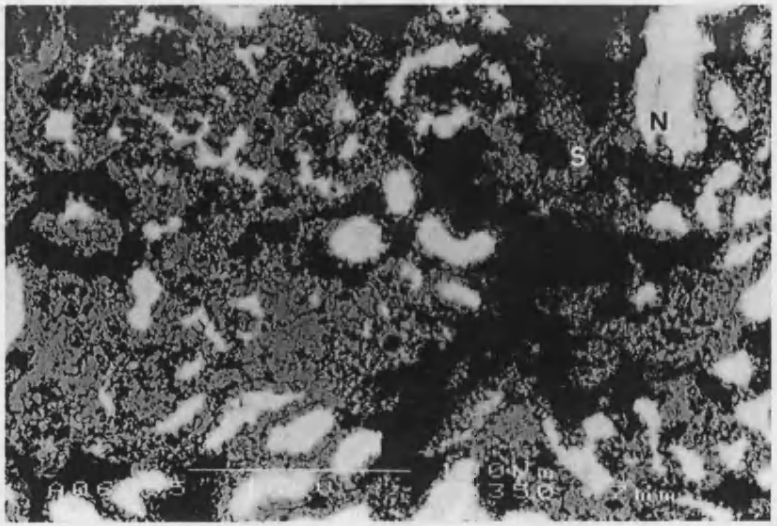

Figure 6.33c Surface region of Ti1-ii
N-Ti rich, S-$TiAl_3$ 100μm

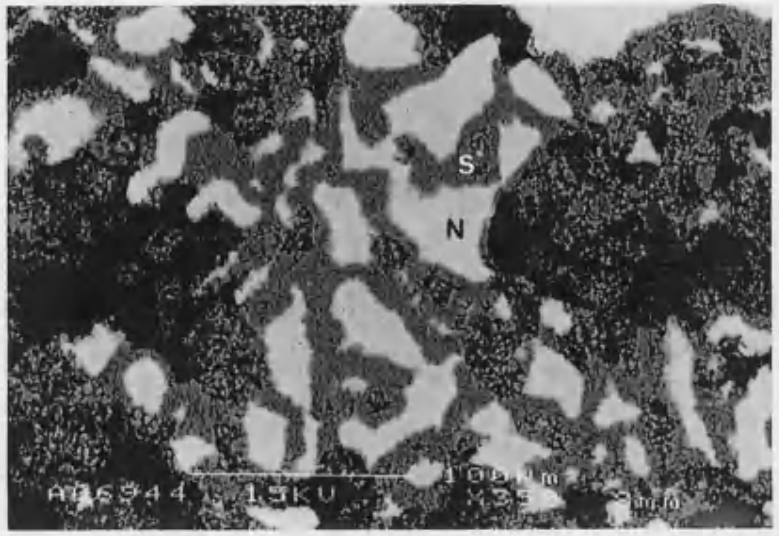

Figure 6.34 Microstructure of Ti2-ii
N-Ti rich, S-$TiAl_3$ 100μm

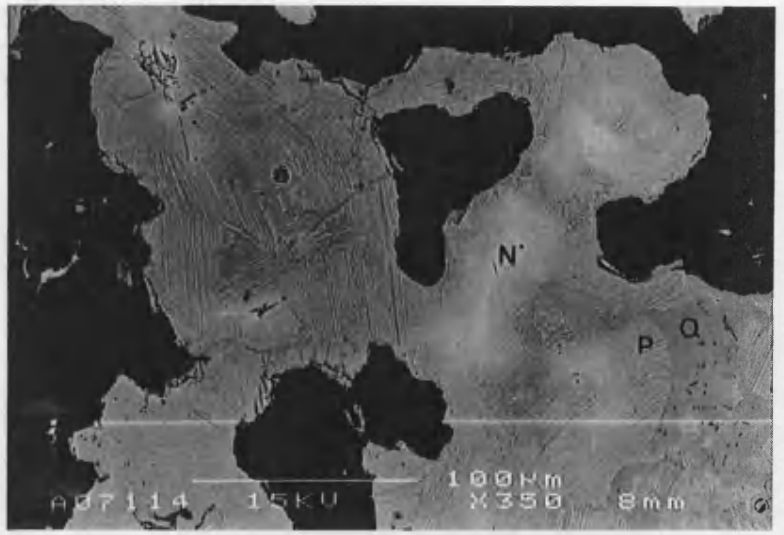

Figure 6.35 Microstructure of Ti2-i-LD
N-Ti rich, P-TiAl/Ti_3Al, Q-TiAl 100μm

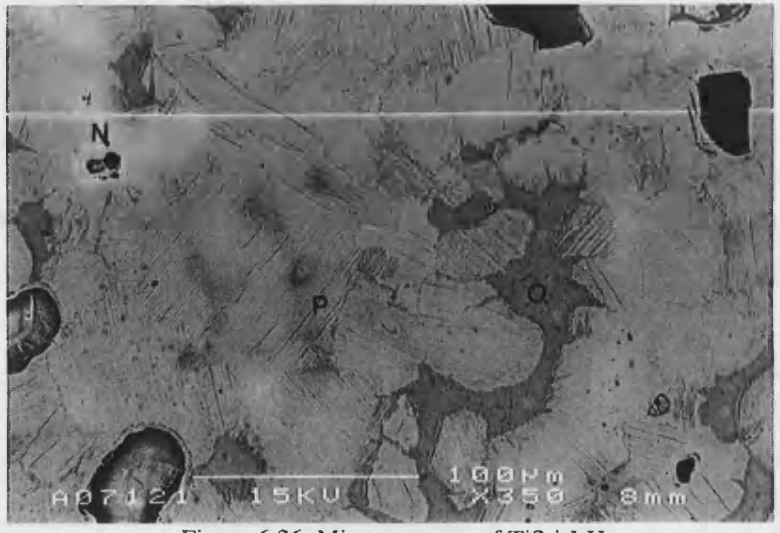

Figure 6.36 Microstructure of Ti2-i-LH
N-Ti rich, P-TiAl/Ti_3Al, Q-TiAl 100μm

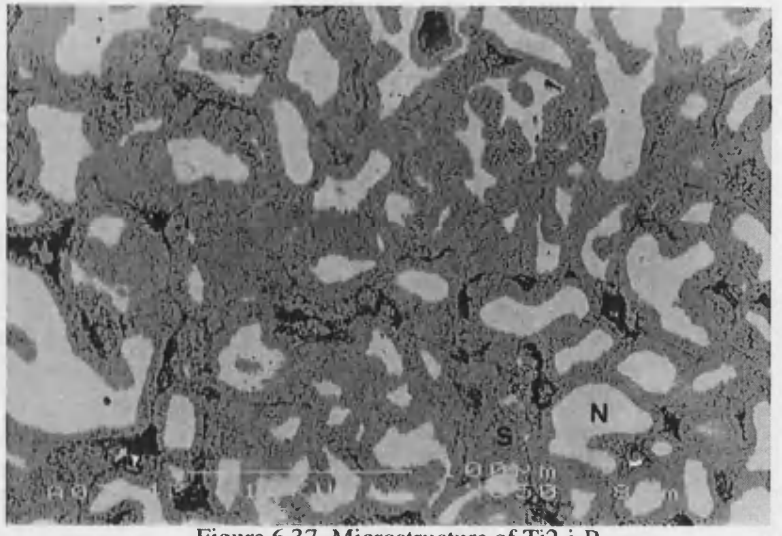

Figure 6.37 Microstructure of Ti2-i-P
N-Ti rich, S-$TiAl_3$ 100μm

6.3.4 Thermocouple Effects

Compact	Profile Temperatures		
	Initiation (°C)	Rate (°C/s)	Peak (°C)
Uncoated Thermocouple			
Ni2-i	552	400	1464
Ni2-i-(TU)	546	-	-
Ti2-i	642	72	1316
Ti2-i-(TU)	636	72	1341
Thermocouple at Compact Surface			
Ni2-i	552	400	1464
Ni2-i-(TS)	543	199	1457
Ti2-i	642	72	1316
Ti2-i-(TS)	632	67	1280

Table 6.16 Thermocouple effects on the time/temperature profiles

Compact Ni2-i-(TU): The thermocouple was only able to record an initiation temperature of 541°C before the bead was dissolved by the reactants and the thermocouple junction was broken, Table 6.16.

Compact Ni2-i-(TS): When the thermocouple was positioned near the surface of the green compact, an initiation temperature of 533°C was recorded, followed by a temperature rise of 199°C/s to a peak temperature of 1457°C, Table 6.16.

Compact Ti2-i-(TU): Even though the thermocouple was not protected from the reactants, the bead survived the thermal explosion to give an initiation temperature of 636°C, followed by a temperature rise of 72°C/s and a peak temperature of 1341°C, Table 6.16.

Compact Ti2-i-(TS): The thermocouple placed at the surface of the reacting compact produced a time/temperature profile with an initiation temperature of 602°C, a rate of temperature rise of 67°C/s and a peak temperature of 1280°C, Table 6.16.

6.4 Discussion

6.4.1 Comparison of Systems

A comparison of the systems was made by studying the standard samples, X2-i. The rapid rise in temperature shown by the time/temperature profiles indicated that a thermal explosion had been initiated in all three compacts. However, it was evident from both the shape of the reacted compacts and their microstructures, that the extent of reaction varied.

The Green Compact: In Table 6.17 it can be seen that the interfacial contact length between the transition metals and the aluminium was longest in the Ni2 green compact and shortest in Ti2. The nickel particles were much smaller than either the iron or titanium, which gave Ni2 a potentially larger reaction area. However, a large amount of porosity remained between the small nickel particles and this formed the least dense green compact. Only the iron and titanium-aluminium systems formed a connected network of aluminium, the nickel-aluminium system formed a connected network of nickel instead, and this suggested that the flow of liquid phase around Ni2 would be restricted during the reaction[71,77,94].

Figs 6.5 6.14 6.25

Shape of the Reacted Compacts: The nickel-aluminium compact collapsed during the thermal explosion since a large fraction of the compact became liquid during the reaction[88]. The iron and titanium-aluminium compacts expanded slightly and this indicated that a smaller fraction of the these compacts had become liquid[70,92,93]. The surfaces of the reacted compacts also reflected the volume of liquid phases formed, with the smooth surface of the nickel-aluminium compact suggesting that it had been solidified from a liquid.

Green Compact	Ti-Al Contact Length (μm)		Porosity (%)	
	Mean	SD	Mean	SD
Fe2	1634	156	21.3	0.3
Ni2	2978	432	30.3	1.1
Ti2	1128	235	27.0	1.4

Table 6.17 Details of Green Compacts

These results fit the thermodynamic calculations in Section 1.4, which predicted that the nickel-aluminium system would produce a larger volume fraction of liquid during the thermal explosion, Figure 1.13.

Time/Temperature Profiles: From Figure 6.38 and Table 6.18 it can be seen that the iron-aluminium system produced the slowest rate of temperature rise and the lowest peak temperature, whilst the nickel-aluminium system produced a rapid rise in temperature to the highest peak value. The titanium-aluminium system produced intermediate values.

It was assumed that a thermal explosion was initiated when a liquid phase was formed in the compact, Section 1.4. An examination of the phase diagrams revealed that the lowest temperatures that a liquid phase formed in the iron and nickel-aluminium systems were the eutectic temperatures of 655°C and 639.9°C respectively. The lowest temperature that a liquid phase formed in the titanium-aluminium system was 660.1°C, the melting point of aluminium. Although the initiation temperatures and the liquid formation temperatures were in the order of, nickel-aluminium lowest and iron-aluminium highest, the values did not correspond, Figures 1.2, 1.4 and 1.6.

To check that this discrepancy was not a thermocouple error, the reactions were repeated with different thermocouple arrangements. The coatings did not affect temperature measurements since uncoated thermocouples gave very similar reaction temperatures to the coated thermocouples, Table 6.16. The position of the thermocouple in the compact was another possible source of error. It was thought that if the overall thermal conductivity of the compact was low, a temperature gradient may have existed between the surface of the compact and its centre. The thermal explosion would have been initiated at the surface, and the thermocouple at the centre would have measured a lower temperature than the actual initiation temperature. However, thermocouples placed near to the compact surfaces measured the same initiation temperatures as those at the centres, Table 6.16.

Therefore, the low initiation temperatures were attributed to solid-state diffusion prior to initiation of the thermal explosion[70]. The results from Section 3 showed that high aluminium content intermetallics were formed by solid-state diffusion at 640°C. The

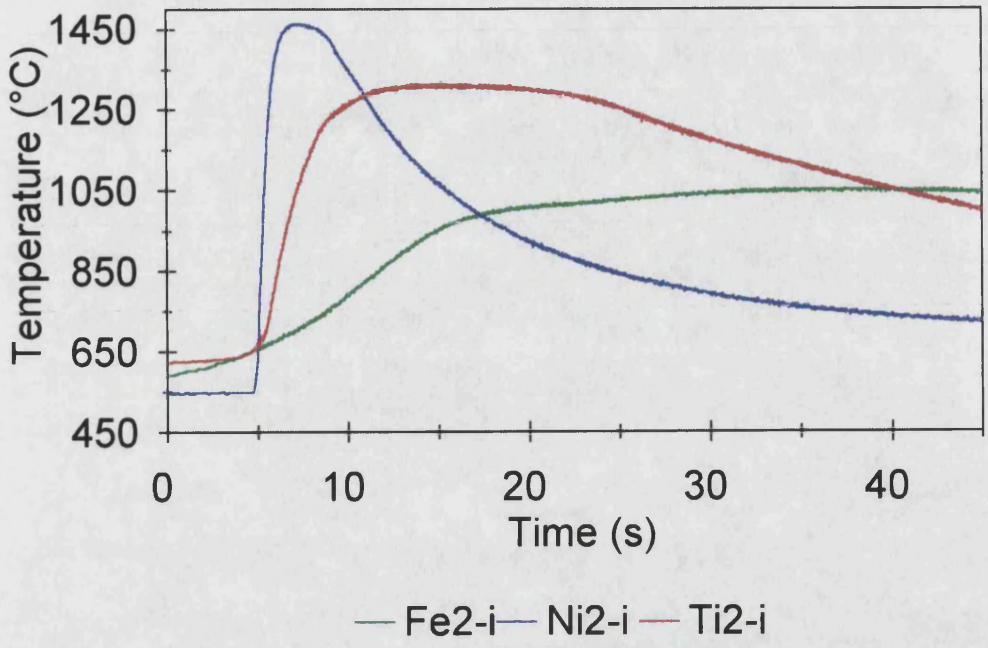

Figure 6.38 Comparison of time/temperature profiles of standard samples

Compact	Profile Temperatures			Porosity (%)		Hardness			
	Initiation (°C)	Rate (°C/s)	Peak (°C)	Mean	SD	Macro (Hv) Mean	SD	Micro (Hv) Mean	SD
Fe2-i	609	14	1054	37.9	6.6	99.5	17.0	279.3	96.1
Ni2-i	552	400	1464	7.8	9.4	275.6	33.1	273.4	17.1
Ti2-i	642	72	1316	19.7	7.5	226.2	67.3	453.8	52.5

Table 6.18 Details of the standard compacts

formation of these intermetallics was exothermic, Table 1.2. If the energy released by their formation was sufficiently rapid to heat the surrounding material to a temperature high enough to form a local liquid phase, then the thermal explosion would appear to initiate at a lower compact temperature.

The results from Section 3 showed that the formation of intermetallics by solid-state diffusion was more rapid in the iron and nickel-aluminium systems than in the titanium-aluminium system. As the compacts were heated, more energy was released at a faster rate in the iron and nickel compacts and the thermal explosions initiated at lower compact temperatures. In the nickel-aluminium system, the longer interfacial contact length in the green compact, which allowed a greater amount of solid-state diffusion to take place, and the larger enthalpies of formation of the intermetallics released more energy, more rapidly to give the lowest initiation temperature of the three systems.

A rapid rate of temperature rise required a high rate of energy release. This in turn needed a large negative enthalpy of formation for all intermediate and final phases formed and a large area of reaction. The nickel-aluminium system, which produced the highest rate of temperature rise, fitted both these criteria. The formation of NiAl was the most exothermic reaction, Table 1.2, and the reacting compact formed the largest area of reaction. The large area of reaction was due to a combination of the small nickel particles, which provided a large surface area to volume ratio, and the formation of a large proportion of liquid to cover these particles. By studying the aluminium rich ends of the phase diagrams of the three systems, it was seen that a wider range of compositions existed as a liquid to lower temperatures in the nickel-aluminium system. These compositions corresponded to the transient, aluminium rich liquid phase which formed after initiation and spread around the compact to increase the area of reaction.

The lack of a connected aluminium network in Ni2, Figure 6.14b, appeared to have little effect on the rate of temperature rise. Although the nickel particles separated the aluminium, they provided little hindrance to the spread of the liquid phase since they were small and easily consumed.

The titanium-aluminium system produced a slower rate of temperature rise, Table 6.18. The enthalpy of formation of TiAl was less exothermic and the area of reaction

was smaller since the titanium particles were larger and a smaller proportion of transient liquid phase was formed after initiation.

Even though the phase diagram showed that the iron-aluminium system formed a slightly larger proportion of transient liquid phase after initiation than the titanium-aluminium system, Figures 1.2 and 1.6, and the iron particles were comparable in size to the titanium particles, it produced the slowest rate of temperature rise. This was attributed to the less exothermic enthalpy of formation of the XAl intermetallic and the formation of aluminium rich intermetallic phases prior to initiation, Table 1.2. As discussed in Section 1.4, the formation of the latter released energy slowly, left less aluminium to form a liquid phase and acted as diffusion barriers, all of which reduced the rate of temperature rise. In the discussion of initiation temperatures above it was explained that greater quantities of these intermetallics were produced in the iron-aluminium system.

In Section 1.4 it was explained that the peak temperature was dependent on the rate of heat accumulation compared to the rate of heat loss. The standard reactions were carried out in identical surroundings, thus the rate of heat loss was considered to be approximately constant between the systems. The rate of heat accumulation was controlled by the rate of temperature rise and therefore it was not surprising to find that the nickel-aluminium system produced the highest peak temperature and the iron-aluminium system the lowest.

The thermocouple at the surface of the titanium-aluminium compact measured a lower peak temperature than the one at its centre because heat from the surface was quickly absorbed by the surroundings. No reduction was noticed in the nickel-aluminium compact because the compact collapsed during the thermal explosion and enveloped the thermocouple.

Microstructures: By examining the microstructures of the reacted compacts it became clear that the nickel-aluminium system had undergone the highest extent of reaction and the iron-aluminium system the lowest.

The single NiAl phase that was produced throughout the reacted nickel-aluminium compact, Figure 6.19a-b, indicated that the thermal explosion had continued to completion. The rate of heat accumulation, in comparison to the rate of heat loss, had

been rapid enough to attain a high temperature for a sufficiently long time to convert all the reactants to NiAl. In fact, the peak temperature was high enough to melt the reactants and any intermediate phases. This caused the compact to collapse, but allowed NiAl to be formed rapidly from a liquid phase.

The final porosity of the reacted nickel-aluminium compact was the lowest of the three systems, Table 6.18, and was a combination of gas porosity and some porosity remaining from the green compact. Most of the porosity present in the green compact was eradicated as the compact collapsed and the liquid phase filled the pores. However, gases evolved from oxides and hydroxides on the surfaces of the reactant particles became trapped in the liquid when it solidified.

The titanium-aluminium compact produced a near complete reaction. The duplex microstructure of TiAl and TiAl/Ti_3Al lamellar regions, Figure 6.31, was consistent with rapidly cooling a Ti-50at%Al composition from 1316°C[7,15,51]. However, the presence of a few titanium rich regions implied that the rate of heat accumulation had not been rapid enough to allow the reaction to fully progress to completion. The peak temperature of 1316°C was not high enough to melt either the titanium or any intermediate $TiAl_3$ formed during the reaction and this hindered the rate of formation of TiAl.

The quantity of porosity present was greater than in the nickel-aluminium sample and was derived from porosity in the green compact. Not enough liquid had been formed during the reaction to allow the compact to collapse and fill these pores. Instead, the compact relied on capillary action to draw liquid into the pores and consolidate the sample, and this had only provided a small decrease in porosity.

The reaction in the iron-aluminium compact did not progress to completion. A multiphase microstructure of Fe_3Al, FeAl and Fe_2Al was produced, not the single FeAl phase formed by a complete reaction, Figure 6.10a-b. The rate of heat accumulation was too slow to produce a full reaction since it only produced a peak temperature of 1054°C. This was below the melting points of iron and all possible intermediate phases, and meant that only $FeAl_3$ could be precipitated from a liquid. All the other intermetallics had to be formed by a slow solid-state diffusion route.

A Fe-38.5at%Al compact, using 45μm diameter iron particles, produced a two-step reaction, but this was found to be only a single step when smaller particles were used[13,89,170]. It was surmised that this two-step process was due to the solid-state formation of unspecified diffusion barriers prior to initiation, which were only overcome by temperatures above 900°C. From the results of this investigation it can be assumed that the diffusion barriers were high aluminium content iron aluminides. These were not overcome in this investigation since the iron particles used were larger than 45μm and the trend suggested an increase in diffusion barrier thickness with increased iron particle size.

There was a large amount of porosity remaining from the green compact, which the small amount of liquid, formed during the reaction, was unable to fill. The porosity measurements from the reacted compact appeared to show an increase in porosity, but this was an inaccurately high value. The reacted compact was poorly consolidated and material was lost during the preparation of the sample surface, which contributed to the high porosity measurements.

Hardness Measurements: For a particular sample, a comparison of the macrohardness values with the microhardness values, taken between pores, gave an indication of the porosity. The lower macrohardness values in the iron and titanium-aluminium systems pointed to a high porosity and the equal macro and microhardness values in the nickel-aluminium system indicated a lower porosity, Table 6.18.

Whether a sample consisted of single or multiple phases was indicated by examining the standard deviations of the microhardness measurements. A small standard deviation, produced by the nickel-aluminium system, implied that the sample was homogeneous and probably consisted of only one phase, whilst a large standard deviation implied the presence of multiple phases.

6.4.3 Effect of Particle Size Distribution

The Green Compact: The contact length between the transition metals and the aluminium was longest in PSD1 and shortest in PSD3 for each of the three systems. The greater quantity of small particles in PSD1 increased the surface area to volume ratio and formed a longer contact length. A connected network of aluminium was

formed in all the compacts in the iron and titanium-aluminium systems, Figures 6.5a-c and 6.26a-c. However, a connected aluminium network was only formed in the Ni3 green compact, the other two compacts in this system contained a large proportion of small nickel particles and formed a connected network of nickel around the aluminium.

Altering the PSD had no significant effect on porosity in the iron and titanium-aluminium systems, since the smaller aluminium particles were easily squashed and forced into the gaps between the transition metals during production. When small nickel particles were used, they filled the spaces between the aluminium, but the hard nickel was not easily squashed. This left gaps between the nickel particles which increased porosity.

Shape of the Reacted Compacts: For a particular system, there was no noticeable difference in the shape of the reacted compacts as the PSD was altered. All the nickel-aluminium compacts collapsed during the thermal explosion and all the iron and titanium-aluminium compacts expanded slightly.

Time/Temperature Profiles: All three systems showed an increase in initiation temperature with increasing quantities of large particles from PSD1 to PSD3, Tables 6.8, 6.11 and 6.14. This was explained by the transition metal-aluminium contact lengths in the green compacts. The longer contact lengths in PSD1 allowed a greater amount of solid-state diffusion to take place before initiation and this released energy rapidly and initiated the thermal explosion at a lower compact temperature. As the contact lengths were decreased in PSD2 and PSD3, energy was released more slowly and the thermal explosion was initiated at a higher temperature.

In the nickel-aluminium system there was a large increase in initiation temperature when PSD3 nickel was used. This was due to the much shorter contact length in this compact and the high solid-state diffusion rate which made this system particularly sensitive to changes. The reaction appeared to initiate at a temperature lower than 655°C, but the initial rate of temperature rise was too low to trigger the data collection software. The titanium-aluminium system showed less of a change in initiation temperature as solid-state diffusion was only slow and the difference in contact lengths between the compacts was less pronounced.

By reducing the surface area to volume ratio of the transition metal powders, the possible area of reaction was reduced and this caused an overall decrease in the rate of heat accumulation and thus the rate of temperature rise in all three systems. Once again, the greatest difference was noted in the nickel-aluminium system. As this system produced the greatest quantity of liquid, then a large proportion of the nickel was covered to form a large surface area of reaction. Therefore, a decrease in the surface area of the transition metal, produced a more marked reduction in the area of reaction than in a system forming a smaller proportion of liquid.

The peak temperatures were dependent on the rate of heat accumulation and all the systems exhibited a decrease in peak temperature with increasing proportions of large particles from PSD1 to PSD3.

Work performed on the thermal explosion synthesis of Ni_3Al[77] supported this discussion. An increase in the quantity of $NiAl_3$ and Ni_2Al_3, formed prior to initiation, was noticed when the nickel particle size was decreased. In addition, the peak temperature was also found to decrease as the nickel size increased.

Microstructures: All the nickel-aluminium compacts produced a single NiAl phase, Table 6.12. The peak temperatures were all in excess of, or comparable to, the melting points of the reactants and intermediate phases and NiAl was rapidly formed from a liquid. Therefore, the variation in the size of the nickel particles was not great enough to lower the rate of heat accumulation sufficiently to reduce the extent of reaction.

The porosity found in these samples was a combination of gas porosity and porosity remaining from the green compact. The slightly higher porosity in Ni1-i was attributed to a larger amount of gas evolution from the particle surfaces and a higher porosity in the green compact.

Altering the iron PSD did not change the phases formed, Table 6.9. A number of phases, ranging from near pure iron to $FeAl_2$, were detected in all the compacts and this indicated that the reaction had not continued to completion. The rate of heat accumulation had not been sufficiently modified by the various PSDs to change the phases formed, as was seen in the small difference in peak temperatures.

The porosity in the green compacts was not filled by the small amount of liquid produced during the thermal explosions and appeared to increase. Once again, this was due to the loss of poorly consolidated material during sample preparation, which gave inaccurately large porosity measurements.

The titanium-aluminium system was the only one to show a variation in microstructure, Table 6.15. Compact Ti1-i, which contained the largest proportion of small particles in the green compact, produced a complete reaction to form a duplex microstructure of TiAl and TiAl/Ti_3Al phases. However, the reactions in the other two compacts did not continue to completion and left titanium rich regions in the samples. These regions were the remains of the largest titanium particles which had not been fully consumed when the reaction was quenched. There were no titanium rich regions in sample Ti1-i since the faster rate of heat accumulation produced a higher extent of reaction and the maximum titanium particle size was limited to 75μm.

The porosity in the titanium-aluminium samples was mostly a remainder of the porosity in the green compacts, though there were also a few gas pores present. The liquid had produced some consolidation in the compacts to decrease porosity levels, but gas evolution may have caused the higher porosity in compact Ti1-i.

Hardness Measurements: The varied microhardness values in the iron and titanium-aluminium compacts reflected the multiphase microstructures, whilst the lower macrohardness values reflected the high porosities. The similar hardness values for the nickel-aluminium compacts signified a single phase, low porosity microstructure.

6.4.4 Effect of Die Design

Shape of the Reacted Compacts: The compacts reacted in die-ii were constrained by the die walls. A large proportion of the nickel-aluminium compacts were molten during the thermal explosion and this caused them to collapse and fill the bottom of their dies. The other two systems formed smaller proportions of liquid and expanded.

Time/Temperature Profiles: By performing the thermal explosions in die-ii, the time/temperature profiles of all the systems were altered. The walls drew heat away from the reacting compacts and increased the rate of heat loss, which decreased the

rates of temperature rise and the peak temperatures of nearly all the compacts, Figures 6.7b, 6.16b and 6.18b.

The rate of heat loss was not decreased sufficiently in the nickel-aluminium system to significantly reduce the peak temperatures. Further, enough liquid was still produced to allow the compact to collapse. In comparison, die-ii drew enough heat way from the titanium-aluminium system to drastically reduce the rates of temperature rise and the peak temperatures. In fact, the rate of temperature rise in sample Ti2-ii was too low to trigger the temperature measuring software.

The iron-aluminium system appeared to produce an anomaly in this trend. The peak temperatures were reduced in die-ii, but the rates of temperature rise increased. This increase was a result of calculating the average rates of temperature rise. The peak temperatures in die-i were reached after an initial rapid rise in temperature, followed by a slow increase, to give a low average value, Figure 6.7b. In die-ii, the peak temperatures occurred during or just after the rapid rise in temperature, since the slow increase was prevented by the greater rate of heat loss and this gave higher average values.

Microstructures: Die-ii did not have a significant effect on the nickel-aluminium thermal explosion and a single NiAl phase was formed once again. However, the amount of gas porosity present near the surface of the samples was increased. The die walls rapidly solidified the surface and trapped the gases which were attempting to escape the liquid phase.

The thermal explosions in the iron-aluminium compacts were quenched by die-ii and underwent a lower extent of reaction. The surface regions of the compacts experienced the greatest increase in the rate of heat loss and formed a partially reacted microstructure of iron surrounded by Fe_2Al_5. The extent of reaction increased towards the centre of the compact, where rate of heat loss was the lowest, to form microstructures containing Fe_3Al and FeAl, Figures 6.12a-c and 6.13a-c.

The presence of a few titanium rich regions showed that the Ti2-i compact only verged on a complete reaction. The increased rate of heat loss in die-ii quenched the reaction to form a final microstructure of titanium rich cores surrounded by $TiAl_3$, Figures 6.33b-c. This microstructure was consistent with one reported for a partial reaction in

the titanium-aluminium system[50]. By using PSD1 titanium to increase the rate of heat accumulation, a near complete reaction was produced in the centre of the compact. The extent of reaction gradually decreased towards the surface as the die walls increased the rate of heat loss.

The final porosities of iron and titanium-aluminium compacts were lower when reacted in die-ii because the die walls restricted swelling.

Hardness Measurements: The increased porosity in the nickel-aluminium compacts reacted in die-ii reduced macrohardness values, but microhardness values remained the same as the same phase was formed. In the iron-aluminium compacts in die-ii, macrohardness values were increased because of the lower porosity, but the lower extent of reaction produced softer phases and reduced microhardness values. Although there was less porosity, the greatly reduced extent of reaction in the titanium-aluminium compacts reduced both macro and microhardness values.

6.4.4 Effect of Green Density of the Compact

The Green Compact: The green density of the compacts was reduced by decreasing the pressure applied during their production.

Shape of the Reacted Compacts: There was no noticeable difference in the shapes of the reacted compacts when compared to the standards. This indicated that compact Ni2-i-LD produced a large proportion of liquid during the thermal explosion.

Time/Temperature Profiles: The initiation temperatures in the low density compacts were lower than the standard initiation temperatures, Tables 6.11 and 6.14. This was not the expected result. It was thought that the lower density would reduce the amount of solid-state diffusion prior to initiation and would thus increase the initiation temperatures. From these results, it must be assumed that the lower density reduced the rate of heat loss from the compact during the heating cycle. This allowed the local build-up of heat to initiate the reaction at a lower compact temperature.

The lower density green compacts hindered the spread of the liquid phase by capillary action and reduced the areas of reaction. This produced lower rates of heat accumulation, which lowered the rates of temperature rise. The drop in rate in

compact Ti2-i-LD produced a slight fall in the peak temperature, but the rate in compact Ni2-i-LD was still sufficiently rapid to produce the same peak temperature.

Microstructures: The reduction in green density was not great enough in either system to alter the extent of reaction. However, the extra porosity in the green compacts was not filled by the liquid and the final porosity was increased. This was consistent with the results from previous investigations into green density[25,94].

Hardness Measurements: The macrohardness measurements taken from both systems were reduced by the increased porosity.

6.4.5 Effect of Rate of Heating of the Compact

Shape of the Reacted Compacts: There was no noticeable difference in the shapes of the reacted compacts when compared to the standards. This indicated that compact Ni2-i-LH produced a large proportion of liquid during the thermal explosion.

Time/Temperature Profiles: By reducing the rate of heating, there was more time available for solid-state diffusion as the compact was heated. This allowed more energy to be released and initiated the thermal explosions in compacts Ni2-i-LH and Ti2-i-LH at lower compact temperatures than the standards, Table 6.11 and 6.14. This effect was also noted in a previous investigation into the reactive synthesis of nickel aluminides[77].

In Section 1.4, it was suggested that the solid-state formation of high aluminium content intermetallics reduced the rate of heat accumulation by acting as diffusion barriers and consuming aluminium. This was found to be true for both Ni2-i-LH and Ti2-i-LH. By consuming the aluminium which would otherwise have formed the initial liquid phase, the area of reaction was reduced.

The peak temperatures in both systems remained the same. This was surprising for the titanium-aluminium system where the reduced rate of heat accumulation should have reduced the peak temperature.

Microstructure: It has been reported, that a slower rate of heating altered the microstructure of the final material[70,89]. The rate of heat accumulation was not

sufficiently reduced from the standard in either system to produce any change in microstructure.

Hardness Measurements: The reduced rate did not produce any alterations in hardness measurements.

6.4.6 Effect of Applying Pressure During the Thermal Explosion

Shape of the Reacted Compacts: Compact Ni2-ii-P was reacted under pressure in die-ii and again formed a large proportion of liquid phase and collapsed to fill the bottom of the die. Compact Ti2-i-P was reacted in die-i and withstood the pressure, though the top of the die was forced radially outwards, indicating that a smaller proportion of liquid was formed, Figure 6.27c.

Time/Temperature Profiles: The initiation temperatures of both systems were decreased by the small pressure applied prior to initiation, Tabels 6.11 and 6.14. In Ti2-i-P, the pressure increased the area of contact between the compact and the dishes, whilst in Ni2-ii-P, the pressure increased the area of contact between the compact and the walls of die-ii. This increased the rate of heat loss from both the compacts and delayed the initiation of the thermal explosions.

During the thermal explosion in Ni2-ii-P, the pressure forced the nickel and liquid together and increased the surface area of reaction, which increased the rate of heat accumulation. Although there was an increase in the average rate of temperature rise, this was greatly exaggerated. Without pressure, the reaction experienced a final slow rate of increase to the peak temperature, which greatly reduced the average rate. But when pressure was applied, the reaction was quenched before the slower rate was reached. This did not have an effect on the peak temperatures which were largely dependent on the initial rapid rise in temperature.

The application of pressure quenched the reaction by increasing the area of contact between the die and the compact[35]. This increased the rate of heat loss from the reaction, which was shown in the rapid drop in temperature once the majority of reactants had been consumed in raising the temperature to its peak.

Unfortunately, no temperature profile was recorded for compact Ti2-i-P because the thermocouple was crushed. This was a further indication of the small amount of liquid produced in this reaction. In the nickel-aluminium reaction the liquid flowed around the thermocouple when pressure was applied, but in the titanium-aluminium reaction, the larger proportion of solid phases transferred the pressure to the thermocouple.

Microstructures: Although the reaction was rapidly quenched after the peak temperature had been reached in compact Ni2-ii-P, the NiAl phase had already been formed. The only difference in the microstructures was a change in the amount and distribution of porosity. Pressure closed the pores in the centre of the compact, but the surface regions were rapidly quenched and trapped the gases evolved during the reaction.

An examination of the microstructure of compact Ti2-i-P revealed an incomplete reaction, Figure 6.37. A microstructure of titanium cores surrounded by $TiAl_3$, similar to the one produced by compact Ti2-ii, was formed. As the reaction of Ti2-ii was quenched, it was assumed that Ti2-i-P was also quenched. The titanium-aluminium system was sensitive to any increase in the rate of heat loss, and by applying pressure, the contact area between the compact and the die was increased and the rate was increased sufficiently to quench the reaction. The porosity in the green compact of Ti2-i-P was closed by the pressure during the brief reaction.

Hardness Measurements: In compact Ni2-ii-P, the macrohardness measurements were highest in the centre and lowest in the highly porous surface regions. The microhardness measurements indicated the formation of NiAl throughout. The lower porosity in compact Ti2-i-P gave a higher macrohardness value, whilst the lower extent of reaction lowered the microhardness measurements.

6.4.7 Reaction Routes

In Section 1.4 a general reaction route was described for reactive synthesis reactions. By using this route as a basis and applying knowledge gained from this section and from other authors, it was possible to determine reaction routes for the three transition metal-aluminium systems. In this section, the reactions in the partially reacted compacts did not continue to completion and the intermediate phases, from which the

final phases were formed, were retained. The routes were only approximate, as partial reactions were quenched by changes in the rates of heat accumulation and heat loss and this may have altered the reaction routes slightly.

Iron-Aluminium: An aluminium rich liquid formed and spread around the iron particles[128]. This dissolved the iron and precipitated out $FeAl_3$, which was an exothermic process. If the rate of heat accumulation was rapid enough to raise the temperature of the compact above the melting point of $FeAl_3$ (1150°C), then the liquid phase quickly dissolved more iron and precipitated FeAl. If the FeAl formed around the remaining iron, and providing that the temperature of the reaction did not exceed the melting point of FeAl (1250°C), then the only way the remaining iron could be converted to FeAl was through solid-state diffusion. Solid-state diffusion of aluminium into iron had already occurred during the reaction to form the iron rich phases.

The rates of heat accumulation in this section were not sufficiently rapid to raise the temperature above the melting point of $FeAl_3$. All the intermetallic phases found in the final microstructures were therefore formed by solid-state diffusion. This released energy slowly and explained the long reaction times shown in the time/temperature profiles.

Nickel-Aluminium: Difficulties were encountered in determining a reaction route from the compacts in this section, as they all produced a full reaction and no intermediate phases remained, Figures 6.18-6.25. However, a reaction performed in Section 8 was quenched to give a partial reaction and a microstructure consisting of nickel cores surrounded by Ni_2Al_3. By combining this result with reports on reactive synthesis in the nickel-aluminium system[23,74], the following reaction route was proposed.

The thermal explosion was initiated by the formation of an aluminium rich liquid phase which consumed all the aluminium and spread around the nickel particles[88]. This liquid dissolved nickel and precipitated $NiAl_3$. The formation of $NiAl_3$ was exothermic and produced a rate of heat accumulation rapid enough to raise the temperature above its melting point (854°C). This allowed more nickel to be dissolved by the liquid, which precipitated Ni_2Al_3[23,74,77] and raised the temperature of the reaction further. The Ni_2Al_3 decomposed into NiAl + liquid at its melting point (1133°C) and NiAl was precipitated

from the liquid. The formation of Ni_2Al_3 may have been by-passed if the rate of heat accumulation was rapid enough to raise the temperature of the compact above 1133°C before the liquid had dissolved enough nickel to precipitate the phase.

Not all the initial diffusion was nickel into aluminium, there was also diffusion of aluminium into nickel to form nickel rich phases. However, the temperature exceeded the melting points of the nickel and nickel rich phases to form more liquid from which NiAl was precipitated. All the reactants were consumed rapidly by liquid-state reactions which released energy quickly and produced a high peak temperature and short reaction time.

The microstructure of the partially reacted compact detailed in Section 8 was formed when the reaction was quenched during the formation of Ni_2Al_3. The formation of $NiAl_3$ had produced a rate of heat accumulation sufficiently rapid to raise the temperature of the compact above 854°C. But this rate was not great enough to sustain the reaction beyond the formation of Ni_2Al_3. The presence of nickel rich cores indicated that the Ni_2Al_3 had formed from a liquid surrounding the remains of the nickel particles.

Titanium-Aluminium: The reactive synthesis was initiated by the formation of an aluminium rich liquid. This rapidly precipitated $TiAl_3$ around the titanium particles, since the solubility of titanium in the liquid was low[50]. The exothermic formation of $TiAl_3$ raised the temperature of the compact, but the rate of heat accumulation was not sufficient to raise the temperature above its melting point (1340°C). Although, the temperature of the compact only just reached the melting point of $TiAl_3$, this was maintained for several seconds. This indicated that a proportion of the $TiAl_3$ was converted to a liquid from which TiAl was precipitated.

If the remaining titanium-rich regions were surrounded by TiAl, then the only way that further TiAl could be formed was by solid-state diffusion. Raising the temperature to 1340°C by-passed the Ti_3Al phase field and allowed some solid-state diffusion to produce a composition in the α-titanium + TiAl phase field. This transformed to TiAl and TiAl/Ti_3Al lamellar regions when the compact cooled. The remaining solid $TiAl_3$

underwent some solid-state diffusion to form a phase which decomposed into $TiAl_2$ and $TiAl_3$ when cooled to room temperature.

If the rate of heat accumulation was too low to raise the temperature to the melting point of $TiAl_3$, then only solid-state diffusion with the titanium cores could occur. This lowered the rate of heat accumulation and quenched the reaction to form the microstructures found in compacts Ti2-ii and Ti2-i-P.

6.4.8 Summary

An investigation into the thermal explosion mode of reactive synthesis revealed that the reactions were initiated by the formation of intermetallic phases through solid-state diffusion. The rate of formation, which was dependent on the green density and the rate of heating, influenced the initiation temperature.

The extent of reaction was determined by the rates of heat accumulation and heat loss during the reaction. The rate of heat accumulation was dependent on the system, the dimensions of the reactants, the green density, the rate of heating and the application of pressure. The rate of heat loss was dependent on the surroundings and the application of pressure.

The porosity in the reacted compacts was reduced by increasing the density of the green compact and by applying pressure to the reaction. It was also reduced by forming a large proportion of liquid phase during the reaction.

The nickel-aluminium system produced a complete reaction to form NiAl in all of its compacts. The titanium-aluminium system only produced a fully reacted, duplex TiAl and $TiAl/Ti_3Al$ microstructure when the fastest rate of heat accumulation was generated. The rate of heat accumulation was not sufficiently rapid in any of the iron-aluminium compacts to produce a complete reaction.

By combining the results of this investigation with work of other authors, reaction routes were determined for all three systems. To produce intermetallic matrix composites, it was decided to initiate thermal explosions in compacts containing reinforcement particles. Section 7 investigated the effect that these particles had on the time/temperature profiles of the thermal explosions and on the microstructures formed.

Section 7

THERMAL EXPLOSIONS IN POWDER COMPACTS CONTAINING REINFORCING PARTICLES

To produce intermetallic matrix composites by a thermal explosion route, reactions were initiated in compacts formed from metal powders mixed with alumina or silicon carbide particles. The nickel and titanium-aluminium systems were used to provide the matrices of the composites. The iron-aluminium system was omitted since none of these compacts had produced a complete reaction in the previous section.

7.1 Materials

The metal powders used in this set of experiments were the aluminium powder and the PSD2 nickel and titanium powders. Details of the alumina and silicon carbide reinforcements are given in Section 2.

7.2 Experimental Procedures

7.2.1 Preparing and Heating the Compacts

The alumina or silicon carbide particles were added in 5 and 10 weight percent (wt%) proportions to the transition metal and aluminium powders prior to mixing. These proportions were chosen to match those commonly used in industry[102]. After the powders had been mixed in a Berco ball mill, detailed in Section 5, the mixtures were divided into 34.31g portions for the nickel-aluminium-reinforcement systems and 30.00g portions for the titanium-aluminium-reinforcement systems. These portions matched the masses of the corresponding unreinforced compacts in the previous section. The mixtures were compacted under a pressure of 218MPa in the same apparatus used in Section 6, Figure 6.1.

A sample of each of the compacts was mounted and prepared for examination in the SEM, using the routines detailed in Section 2.

The remainder of the preparation of the compacts was identical to those in Section 6. They were weighed and measured to calculate their porosities and a coated thermocouple was inserted into the centre of the bottom face of the compacts to obtain time/temperature profiles. The furnace and temperature recording equipment from Section 6 was used, Figure 6.3. All the reactions were initiated in die-i, since this had the smallest quenching effect on the reactions and allowed the shapes of the reacted compacts to be viewed. The standard heating rate was used and no pressure was applied during the thermal explosion, which allowed direct comparisons to made with the standard reactions in Section 6.

The reacted compacts were photographed after removal from the furnace and then sectioned and prepared for analysis using SEM, EPMA and XRD techniques.

The notation used in Section 6 was adapted to identify the reinforced compacts,

eg. Ti2A5-i

The additional letters and numbers added to the description of the green compact denotes the type, A for alumina and S for silicon carbide, and weight percent of reinforcement.

7.2.2 The Addition of Alumina

Reactions were initiated in compacts containing 0, 5 and 10 weight percent proportions of alumina in the nickel and titanium-aluminium systems, Table 7.1.

Matrix System	Alumina wt%		
	0	5	10
Ni-Al	Ni2-i	Ni2A5-i	Ni2A10-i
Ti-Al	Ti2-i	Ti2A5-i	Ti2A10-i

Table 7.1 Variations in the addition of alumina

7.2.3 The Addition of Silicon Carbide

Reactions were initiated in compacts containing 0, 5 and 10 weight percent proportions of silicon carbide in the nickel and titanium-aluminium systems, Table 7.2.

Matrix System	Silicon Carbide wt% 0	5	10
Ni-Al	Ni2-i	Ni2S5-i	Ni2S10-i
Ti-Al	Ti2-i	Ti2S5-i	Ti2S10-i

Table 7.2 Variations in the addition of silicon carbide

7.2.4 Thermocouple effects

To examine the effect that the position of the thermocouple had on the temperatures recorded, additional thermal explosions were performed. Reactions were initiated in the Ti2A10-i-(TS) and Ti2S10-i-(TS) compacts, where the thermocouple was placed at the surface, Table 7.3.

Reinforcement	Thermocouple Position Centre	Surface
None	Ti2-i	Ti2-i-(TS)
Alumina	Ti2A10-i	Ti2A10-i-(TS)
Silicon Carbide	Ti2S10-i	Ti2S10-1-(TS)

Table 7.3 Variations in the thermocouple position

7.3 Results

7.3.1 The Addition of Alumina

Compact Ni2A5-i: Figure 7.1a shows the distribution of alumina particles in the green compact. The alumina (V) was evenly distributed between the aluminium particles (A) and disrupted the network of nickel (H). The addition of alumina resulted in a green compact with a porosity of 31.0%, Table 7.4.

Green Compact	Porosity (%) Mean	SD
Nickel-Aluminium-Alumina		
Ni2	30.3	1.1
Ni2A5	31.0	2.3
Ni2A10	30.9	0.3
Titanium-Aluminium-Alumina		
Ti2	27.0	1.4
Ti2A5	26.7	0.9
Ti2A10	25.2	2.1

Table 7.4 Porosities of the green compacts containing alumina

The addition of 5wt% alumina to the nickel-aluminium system reduced the degree of collapse of the reacted compact in comparison with the unreinforced sample, Figure 7.2a. Indicating that a smaller proportion of liquid had been produced.

The time/temperature profile was altered by adding 5wt% alumina, Figure 7.3. The initiation temperature was slightly reduced to 542°C, the rate of temperature rise was reduced to 291°C/s, but the maximum temperature of 1466°C was approximately the same as the unreinforced sample, Table 7.5.

EPMA, Table 7.6, and XRD, Figure 7.4, found a single matrix phase of NiAl (K) throughout the sample. The alumina (V) had remained inert during the reaction, but its distribution was found to be segregated. The centre and surface regions of the compact were reinforced by alumina particles, Figure 7.5a, but the midway regions contained no alumina, Figure 7.5b.

Agglomerations of around five or six alumina particles were found in the alumina containing regions, Figure 7.5a. These had not allowed the NiAl to penetrate into them and gave rise to porosity. Further porosity from trapped gases was also found to be present and this resulted in an increase from the centre outwards, due to the large gas pores found at the outer edge, Table 7.5.

Macrohardness measurements varied across the sample since the indents covered the matrix, reinforcement and porosity. Microhardness measurements, taken from the

matrix, were comparatively constant and were approximately equal to those of the unreinforced sample, Table 7.5.

Compact Ni2A10-i: The green compact consisted of a mixture of nickel (H) and alumina (V) particles distributed between the larger aluminium particles (A), Figure 7.1b. A few agglomerations of alumina were present and these disrupted the network of nickel. The porosity was unaffected by the addition of more alumina, Table 7.4.

By adding 10wt% of alumina to the nickel-aluminium system, the reacted sample retained the approximate dimensions of the green compact, Figure 7.2b.

The initiation temperature, 522°C, and the rate of temperature, 183°C/s, were further reduced and the peak temperature fell to 1448°C, Figure 7.3 and Table 7.5.

The matrix was found to be NiAl (K) by EPMA and XRD techniques, Table 7.3 and, Figure 7.4. The alumina (V) had remained inert during the thermal explosion and there was a gradual increase in the amount of alumina from the centre outwards, Figures 7.6a-b. There were fewer gas pores, but was present due to the large number of agglomerations of alumina particles which had not been penetrated by the NiAl.

Macrohardness measurements were lower than those of the Ni2A5-i sample, but there was no change in microhardness measurements from the matrix phase, Table 7.5.

Compact Ti2A5-i: The alumina (V) particles were well distributed throughout the titanium (N) and aluminium (A) mixture, Figure 7.7a. There were no signs of any alumina agglomerations, but the alumina did disrupt the network of aluminium. The porosity of 26.7% was the same as in the unreinforced green compact, Table 7.4.

By adding 5wt% alumina, the reacted compact maintained its green compact shape to a greater extent than the unreinforced compact. Figure 7.8a shows that there was less swelling of the top of the compact during the reaction since less liquid was formed.

The time/temperature profile, Figure 7.9, shows that the thermal explosion reaction in Ti2A5-i was initiated at a temperature of 595°C and this increased at an average rate of 48°C/s to a peak temperature of 1296°C, Table 7.2.

The matrix of the reacted sample, as revealed by EPMA data in Table 7.6, consisted of a mixture of TiAl (Q) and TiAl/Ti_3Al (P) grains with a few titanium rich regions (N),

Figure 7.11. XRD data indicated the presence of TiAl, Ti_3Al phases and the alumina, which had remained inert during the thermal explosion and was found distributed throughout the sample.

The amount of porosity in the sample was far greater than that in the unreinforced sample, Table 7.4, and was mostly due to a lack of consolidation of the matrix. The pores in the sample were all found to be edged with alumina particles.

The macrohardness of the sample varied across its thickness, but the average value was lower than that of the unreinforced sample, Table 7.5. Microhardness measurements from the matrix were also reduced, but were more constant through the thickness of the sample.

Compact Ti2A10-i: The alumina (V) particles were well distributed in the titanium (N) and aluminium (A), Figure 7.7b. No agglomerations were seen, but the alumina did disrupt the network of aluminium around the titanium.

The shape of the reacted compact closely resembled that of the green compact, as no expansion of the top had occurred, Figure 7.8b.

Referring to Figure 7.9 and Table 7.5 showed that the time/temperature profile had been further altered. There was a further reduction in initiation temperature to 582°C, the rate of temperature rise to 42°C/s and the peak temperature to 1265°C.

There was no difference in the matrix formed in compact Ti2A10-i when compared with those of compacts Ti2A5-i and Ti2-i, Table 7.6 and Figure 7.10. TiAl (Q) and TiAl/Ti_3Al (P) regions were interspersed with a few titanium rich regions (N), Figure 7.12. The distribution of alumina was constant through the thickness of the sample. The amount of porosity was greater than in the samples containing less alumina and was due to a lack of consolidation of the matrix, Table 7.5. Once again, the alumina particles were found ringing the pores.

Macrohardness measurements were lower than those of compact Ti2A5-i, but microhardness measurements were comparable, Table 7.5.

Compact	Profile Temperatures			Porosity (%)		Hardness			
	Initiation (°C)	Rate (°C/s)	Peak (°C)	Mean	SD	Macro (Hv) Mean	SD	Micro (Hv) Mean	SD
Nickel-Aluminium-Alumina									
Ni2-i	552	400	1464	7.8	9.4	275.6	33.1	273.4	17.1
Ni2A5-i	542	291	1466	10.1	12.0	246.4	66.3	270.2	10.4
Ni2A10-i	522	183	1448	6.4	4.1	196.5	34.7	291.5	19.8
Titanium-Aluminium-Alumina									
Ti2-i	642	72	1316	19.7	7.5	226.2	67.3	453.8	52.5
Ti2A5-i	595	48	1296	39.6	6.6	162.0	49.0	368.0	28.2
Ti2A10-i	582	42	1265	42.9	2.9	115.1	37.7	360.4	25.5

Table 7.5 Details of Ni-Al-Al_2O_3 and Ti-Al-Al_2O_3 thermal explosions and reacted compacts

Compact	Phase	Ni (at%) Mean	SD	Al (at%) Mean	SD	O (at%) Mean	SD	Alloy/ Compound
Ni2-i	K	49.6	0.3	50.4	0.3	-	-	NiAl
Ni2A5-i	K	50.3	1.0	49.4	0.1	0.3	0.2	NiAl
	V	0.5	0.2	40.0	0.1	59.5	0.1	Al_2O_3
Ni2A10-i	K	50.1	0.2	49.8	0.2	0.1	0.1	NiAl
	V	0.3	0.1	39.9	0.3	60.1	0.4	Al_2O_3
Compact	**Phase**	**Ni (at%) Mean**	**SD**	**Al (at%) Mean**	**SD**	**O (at%) Mean**	**SD**	**Alloy/ Compound**
Ti2-i	N	94.8	2.0	5.2	2.0	-	-	Ti
	P	54.8	1.5	45.2	1.5	-	-	TiAl/Ti_3Al
	Q	45.6	3.6	54.4	3.6	-	-	TiAl
Ti2A5-i	N	93.7	5.3	5.8	5.3	0.6	0.5	Ti
	P	53.2	0.8	46.7	0.8	0.1	0.1	TiAl/Ti_3Al
	Q	46.1	0.7	53.6	0.7	0.4	0.3	TiAl
	V	0.5	0.1	39.7	0.1	59.8	0.0	Al_2O_3
Ti2A10-i	N	89.2	8.7	10.0	8.7	0.9	0.8	Ti
	P	53.2	2.2	46.6	2.2	0.2	0.3	TiAl/Ti_3Al
	Q	48.7	1.8	50.7	1.8	0.6	0.3	TiAl
	V	0.1	0.0	39.6	0.1	60.3	0.1	Al_2O_3

Table 7.6 EPMA data for Ni-Al-Al_2O_3 and Ti-Al-Al_2O_3 reacted compacts

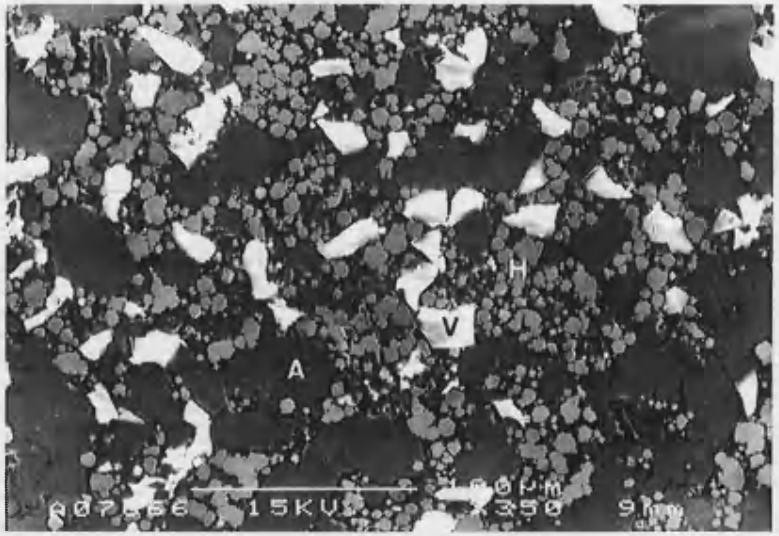

Figure 7.1a Ni2A5 green compact
A-Al, H-Ni, V-Al_2O_3 100μm

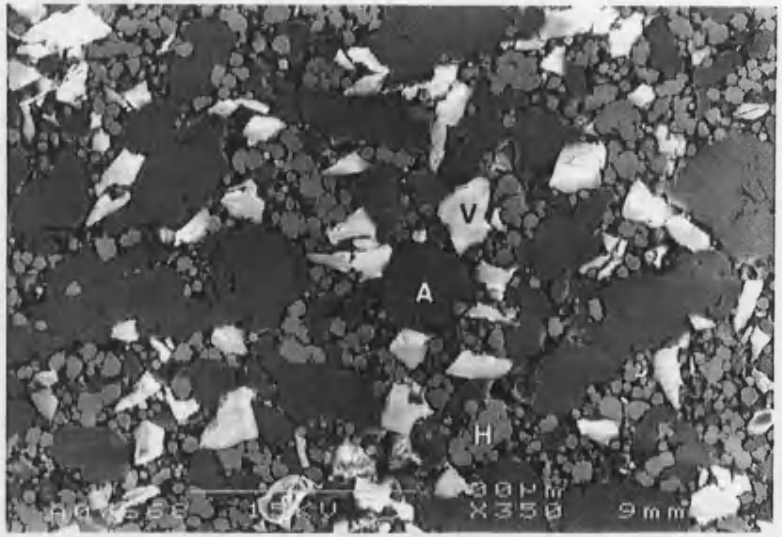

Figure 7.1b Ni2A10 green compact
A-Al, H-Ni, V-Al_2O_3 100μm

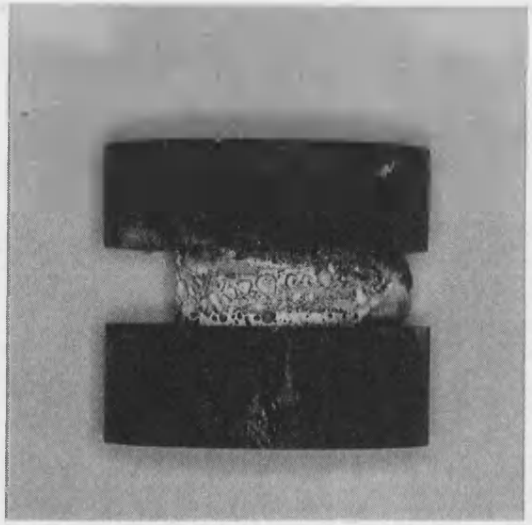

Figure 7.2a Ni2A5 compact reacted in die-i 10mm

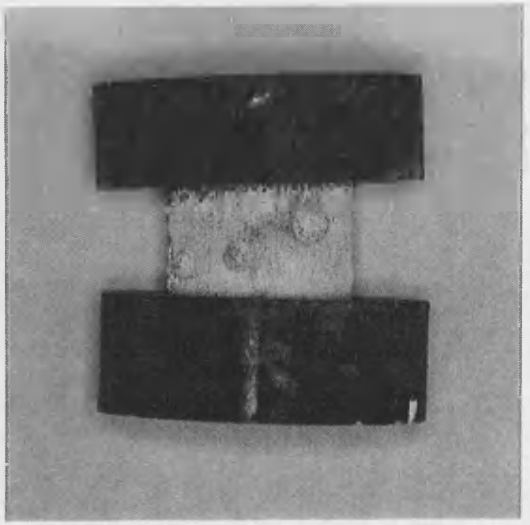

Figure 7.2b Ni2A10 compact reacted in die-i 10mm

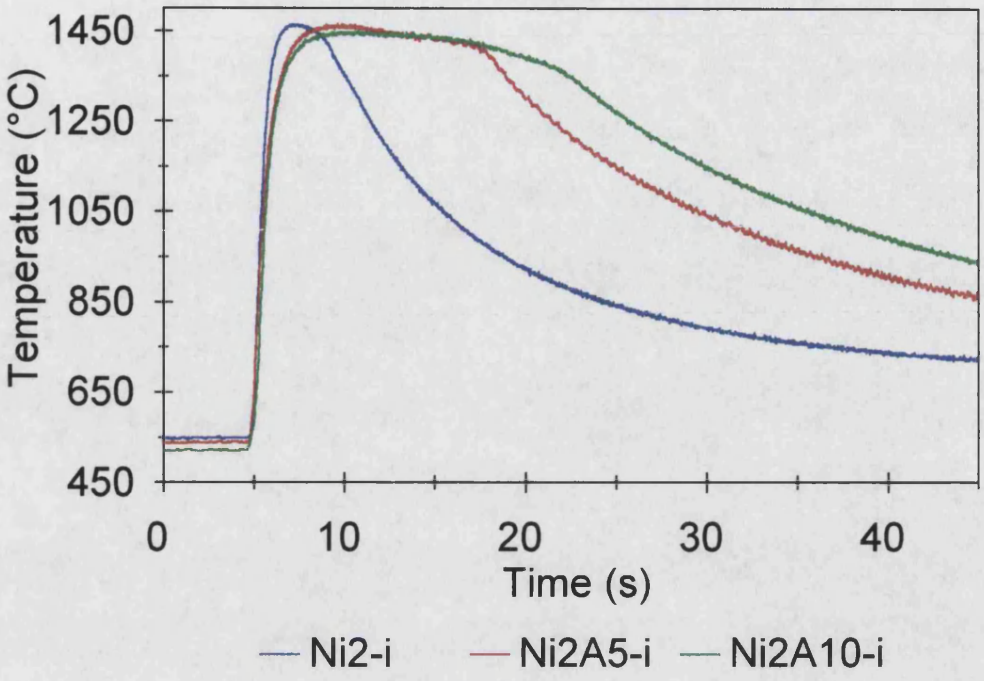

Figure 7.3 Effect of alumina additions on nickel-aluminium time/temperature profile

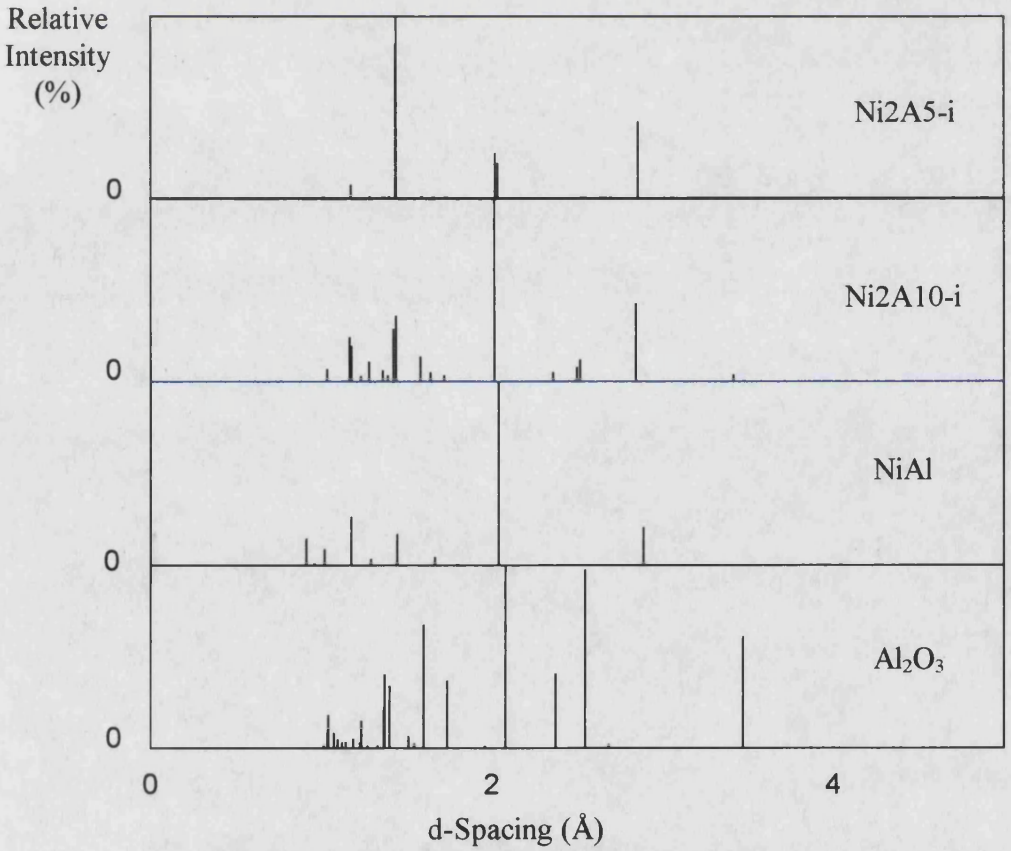

Figure 7.4 XRD plots for Ni2A5-i and Ni2A10-i

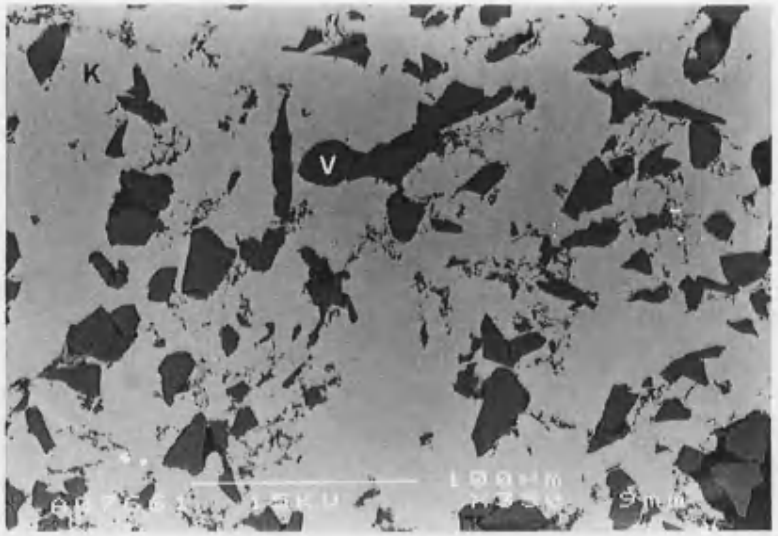

Figure 7.5a Centre and surface regions of Ni2A5-i
K-NiAl, V-Al_2O_3 100μm

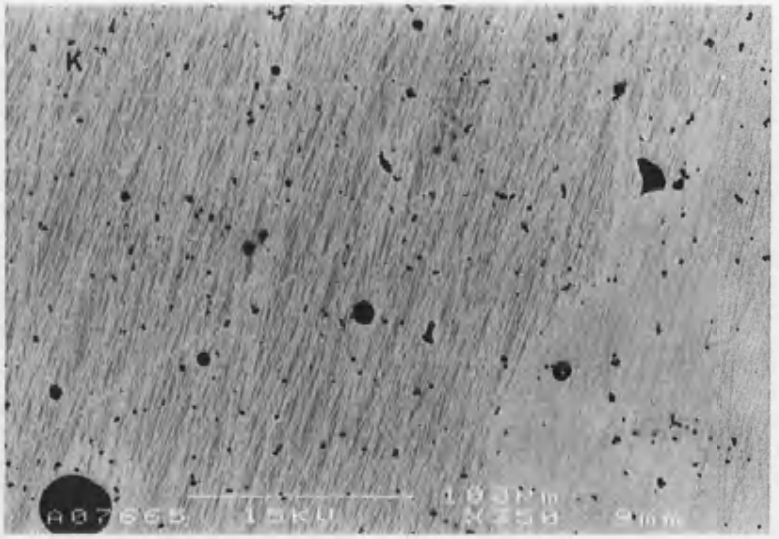

Figure 7.5b Midway region of Ni2A5-i
K-NiAl 100μm

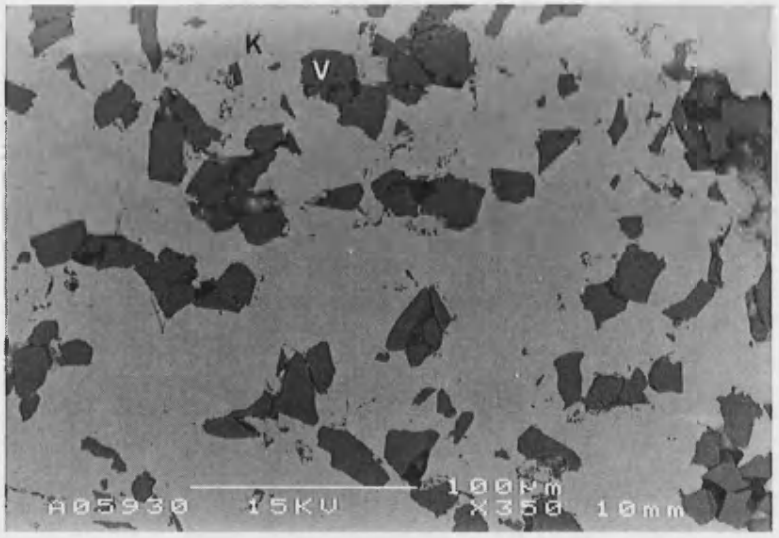

Figure 7.6a Centre region of Ni2A10-i
K-NiAl, V-Al_2O_3 100μm

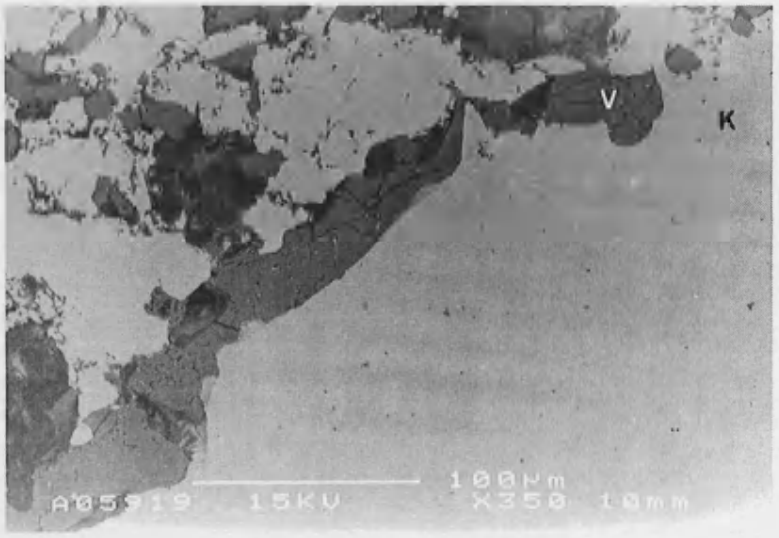

Figure 7.6b Surface region of Ni2A5-i
K-NiAl, V-Al_2O_3 100μm

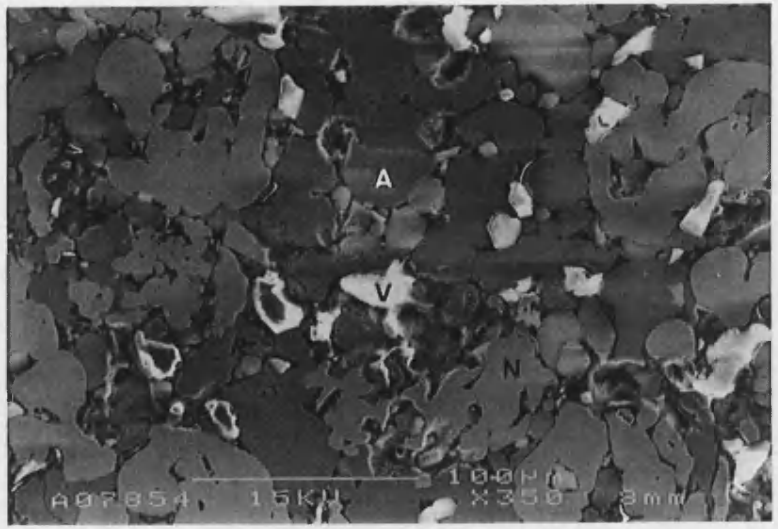

Figure 7.7a Ti2A5 green compact
A-Al, N-Ti, V-Al_2O_3 100µm

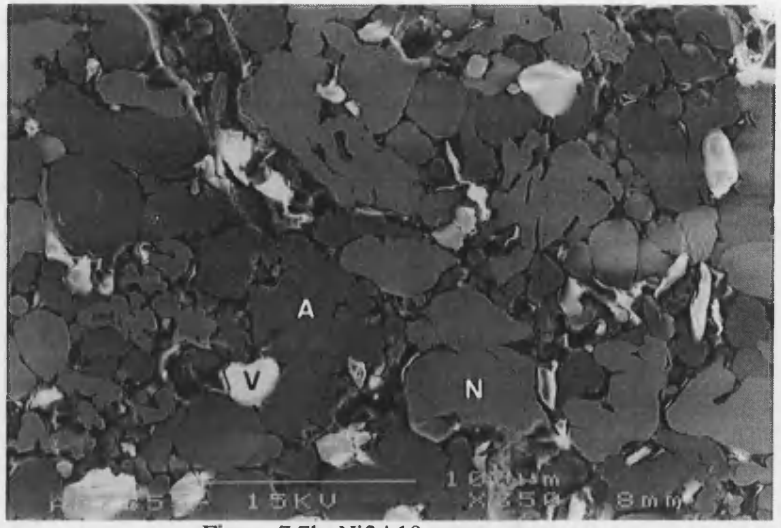

Figure 7.7b Ni2A10 green compact
A-Al, N-Ti, V-Al_2O_3 100µm

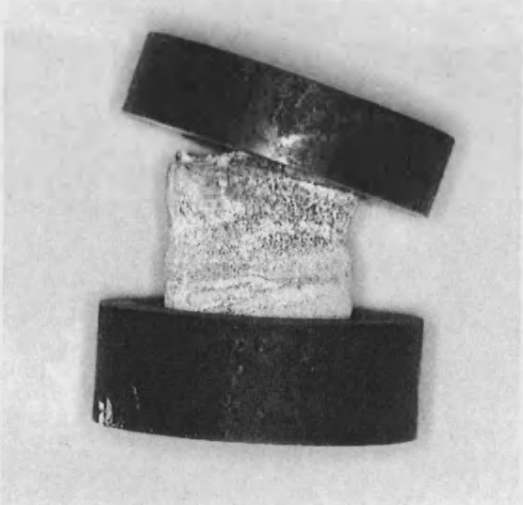

Figure 7.8a Ti2A5 compact reacted in die-i 10mm

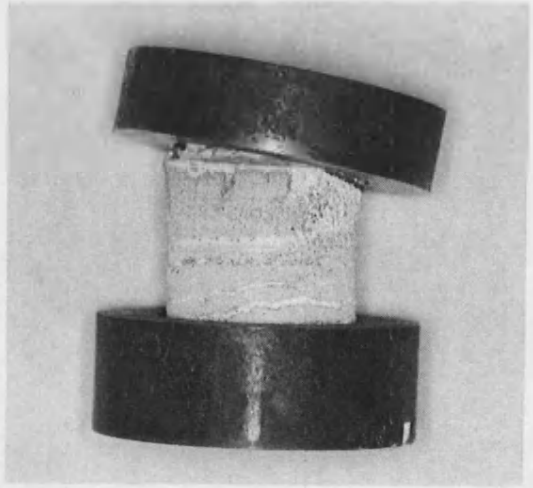

Figure 7.8b Ti2A10 compact reacted in die-i 10mm

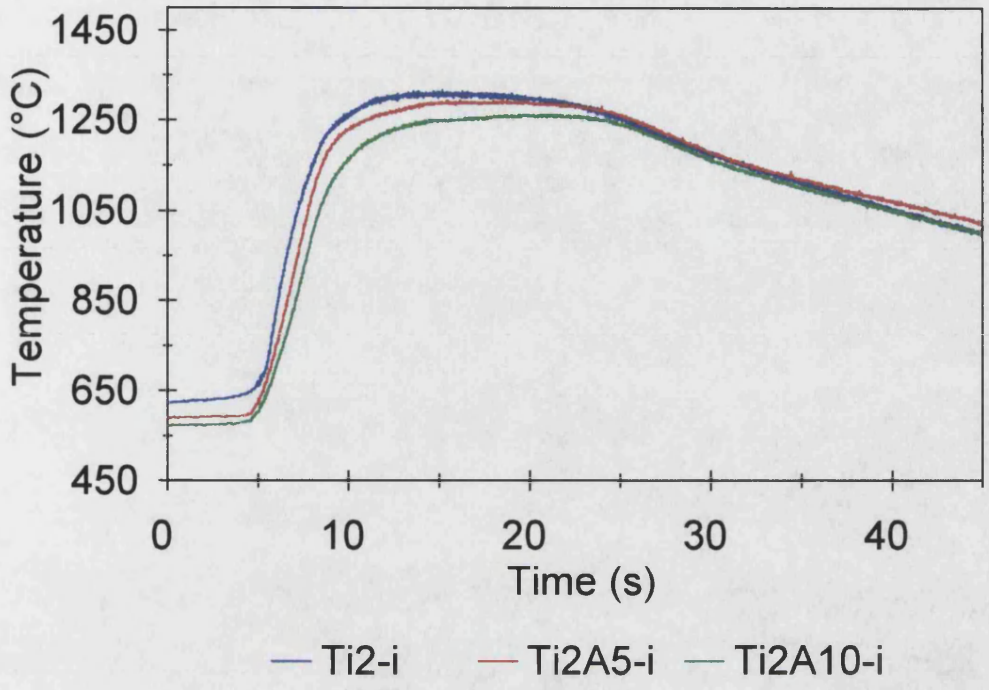

Figure 7.9 Effect of alumina additions on titanium-aluminium time/temperature profile

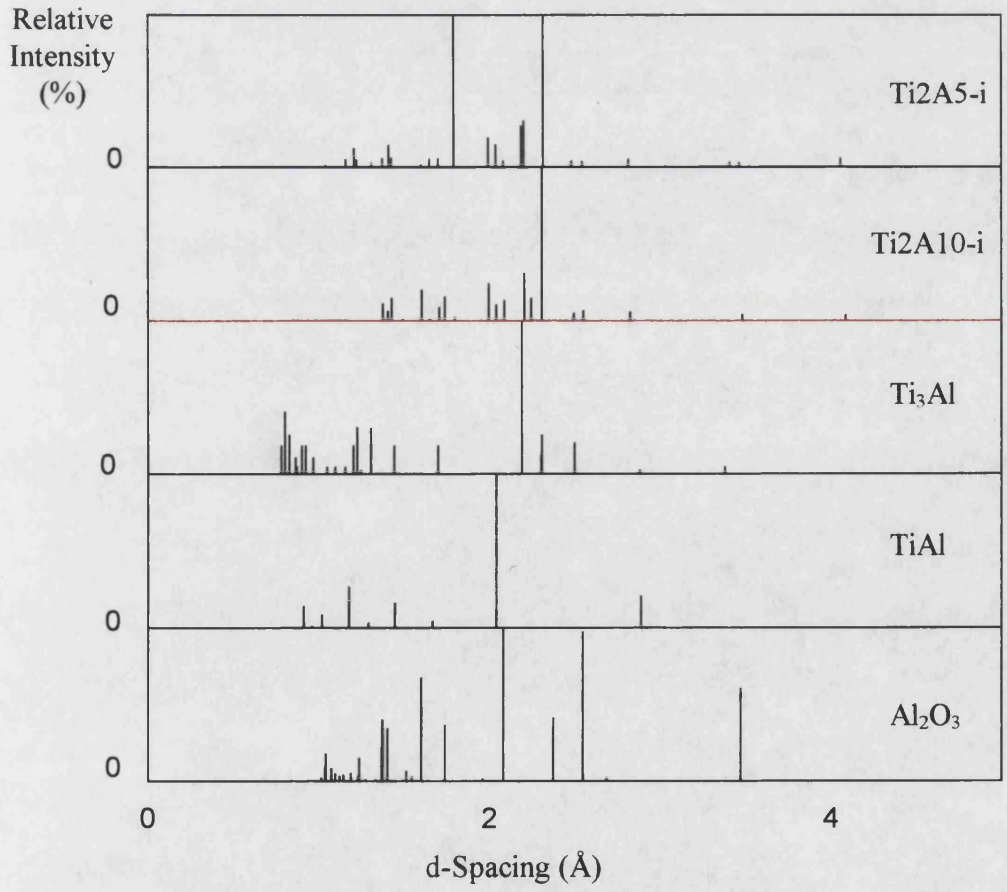

Figure 7.10 XRD plots for Ti2A5-i and Ti2A10-i

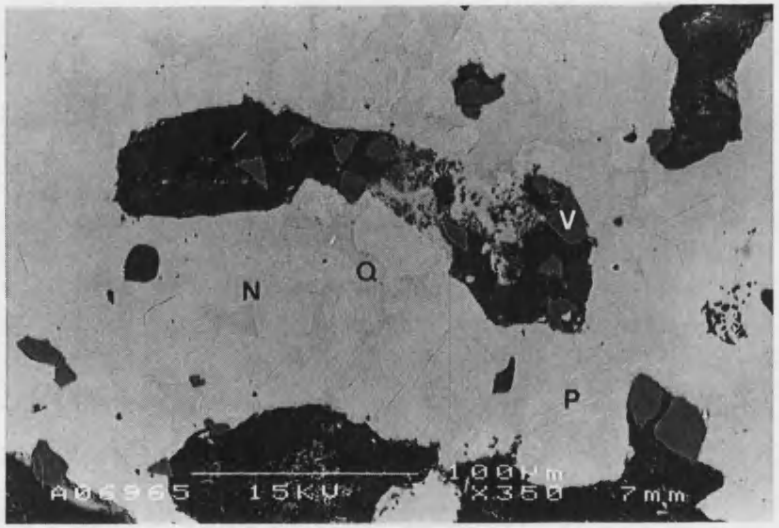

Figure 7.11 Microstructure of Ti2A5-i
N-Ti rich, P-TiAl/Ti_3Al, Q-TiAl, V-Al_2O_3 100μm

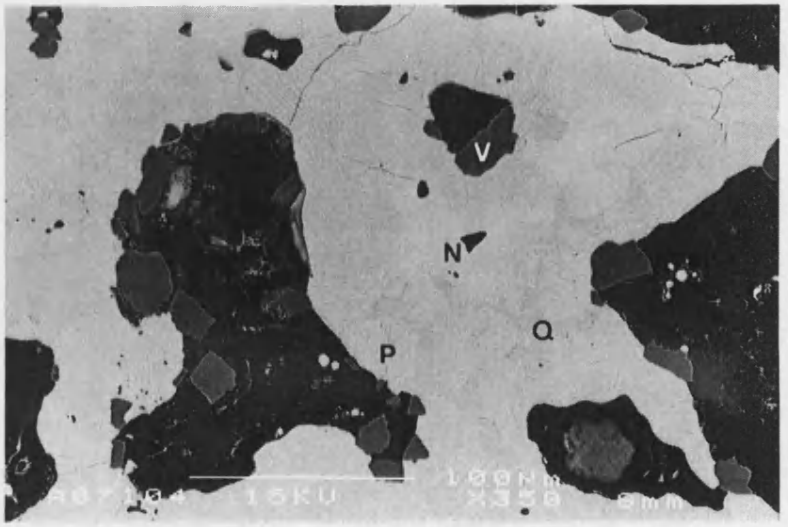

Figure 7.12 Microstructure of Ti2A10-i
N-Ti rich, P-TiAl/Ti_3Al, Q-TiAl, V-Al_2O_3 100μm

7.3.2 The Addition of Silicon Carbide

Green Compact	Porosity (%) Mean	SD
Nickel-Aluminium-Silicon Carbide		
Ni2	30.3	1.1
Ni2S5	31.4	2.3
Ni2S10	35.6	1.4
Titanium-Aluminium-Silicon Carbide		
Ti2	27.0	1.4
Ti2S5	25.3	1.0
Ti2S10	28.0	0.6

Table 7.7 Porosities of the green compacts containing silicon carbide

Compact Ni2S5-i: Figure 7.13a shows the distribution of the silicon carbide particles in the green compact. A mixture of silicon carbide (W) and nickel particles (H) was distributed between the aluminium particles (A), though some silicon carbide particles were dislodged during polishing and became embedded in the aluminium. The addition of silicon carbide did not greatly alter the porosity of the green compact, Table 7.7.

The addition of silicon carbide to the nickel-aluminium compacts allowed greater shape retention during the thermal explosion and formed small beads of extruded material on the surface, Figure 7.14a. This indicated that a much smaller proportion of the compact was liquid during the thermal explosion when compared to the unreinforced sample.

By adding 5wt% silicon carbide to the nickel-aluminium system, the time/temperature profile of the thermal explosion was altered, Figure 7.15. The initiation temperature fell to 490°C, the rate of temperature rise dropped to 329°C/s and the peak temperature was reduced to 1410°C, Table 7.8.

After examining the compact it became obvious that the silicon carbide had interacted with the nickel and aluminium during the thermal explosion, as no silicon carbide particles could be found, Figures 7.17. A matrix phase (K) identified as NiAl was

formed and this contained small amounts of silicon and trace amounts of carbon, Table 7.9. The XRD plots still showed peaks for NiAl, which indicated that the structure had not been greatly distorted by the inclusion of other elements, Figure 7.16. Small oblongs of a dark phase (X) were found distributed around the pores in the NiAl and these were identified as being carbon rich. An accurate composition could not be measured since the width of these phases was approximately 1μm and thus at the resolution limit of the probe. With the additional difficulty of trying to detect the light elements of carbon and silicon at the same time as the heavier nickel, there was some unavoidable sampling of the surrounding phase.

The majority of the sample contained pores arising from a lack of consolidation of the porosity in the green compact, which gave a much higher average porosity than Ni2-i, Table 7.8. The exceptions were the extruded beads of material which contained no porosity.

Macrohardness measurements were lower than those of the unreinforced compact, but microhardness measurements, taken between the pores, revealed a definite increase in the hardness of the material, Table 7.8.

Compact Ni2S10-i: The green compact consisted of a mixture of nickel (I) and silicon carbide (W) distributed between the aluminium particles (A), Figure 7.13b. The porosity of the green compact was increased slightly by the silicon carbide particles increasing the porosity in the nickel network, Table 7.7.

The shape of the reacted compact was almost identical to that of the green compact and there were fewer small beads of extruded material on the sample surface, Figure 7.14b.

The time/temperature profile shown in Figure 7.15 shows that compact Ni2S10-i produced a profile with an initiation temperature of 485°C, a rate of temperature rise of 271°C/s and a maximum temperature of 1352°C, Table 7.8.

The matrix was similar to that of compact Ni2S5-i. No silicon carbide particles could be found and the matrix phase (K) formed was an NiAl compound containing silicon and small amounts of carbon, Table 7.9 and Figure 7.16. Dark carbon rich phases (X) were again found around the edges of pores, Figure 7.18.

The porosity in the green compact was not filled during the reaction and this resulted in a greater amount of porosity than in compact Ni2S5-i, Table 7.8.

Macrohardness measurements, which reflected the porosity of the sample, were lower than compact Ni2S5-i, but microhardness values were approximately the same, Table 7.8.

Compact Ti2S5-i: In the green compact, the aluminium (A) formed a connected network around the titanium (N) and the silicon carbide particles (W) were found between the metal particles, Figure 7.19a. As with the nickel-aluminium-silicon carbide green compacts, silicon carbide particles were imbedded in the metal powders during the polishing routine. No change in porosity was measured, Table 7.7.

A dramatic change in the shape of the compact occurred during the thermal explosion. There was a massive radial expansion of the compact and bubbles were formed on the surface, Figure 7.20a. This suggested that the silicon carbide had reacted with the metals and formed a large amount of a gaseous phase which had forced the compact to expand as it tried to escape.

The initiation temperature was decreased to 612°C, but the rate of temperature rise and the peak temperature were increased to 123°C/s and 1329°C respectively, Figure 7.21 and Table 7.8.

All the silicon carbide particles reacted with the metals and formed a variety of phases, Figure 7.23. A background phase of aluminium rich TiAl (Q) contained small quantities of silicon and carbon, Table 7.9. Three further phases were dispersed in this, but it was difficult to identify their exact compositions since their sizes were at the resolving limit of the EPMA equipment and some of the surrounding phases were also sampled. In addition, there were too many peaks in the XRD plots to isolate the phases present, Figure 7.22. However, an approximation of their compositions was made with the data available and from reports published by other authors[51,72,73].

The first phase was a dark aluminium rich phase (A) containing small amounts of titanium and silicon. The second was a lighter phase (U) which mostly consisted of titanium and silicon, but also contained smaller amounts of aluminium and carbon. As the aluminium and carbon levels varied with silicon carbide content, and the titanium

and silicon levels remained constant, a basic structure corresponding to Ti_5Si_3 was derived. The lightest phase (T) contained titanium, aluminium and carbon only and gave a composition corresponding to Ti_2AlC, which has been reported to exist as the compound $Ti_4Al_2C_2$[72]. The density of these three phases in the background phase increased towards the outer edge of the sample.

The sectioned sample was found to be highly porous, with large gas pores separated by thin regions of consolidated material. This resulted in problems when the samples were mounted, as the pressure applied crushed the sample and closed some of the porosity to give inaccurately low porosity measurements, Table 7.8.

Even though the amount of porosity was greatly increased by the addition of 5wt% silicon carbide, the macrohardness measurements were also increased, which suggested a large increase in the hardness of the phases formed, Table 7.8. Microhardness measurements confirmed this and were found to increase towards the outer edge of the sample where the density of phases in TiAl was greatest.

Compact Ti2S10-i: The silicon carbide particles were distributed along the interfaces of the metal particles, Figure 7.19b, and produced no change in the density of the green compact, Table 7.7.

The reacted sample had expanded further in a radial direction than compact Ti2S5-i and the surface was once again covered in bubbled material, Figure 7.20b.

The thermal explosion reaction initiated at 574°C and the temperature increased at a rate of 201°C/s to a peak temperature of 1345°C, Figure 7.21 and Table 7.8.

The reacted sample was found to contain the same four phases as compact Ti2S5-i, Table 7.9 and Figure 7.22. The background phase of TiAl (Q) had become depleted in titanium, whilst the aluminium rich phase (A) had decreased in quantity. The particle density of Ti_5Si_3 (U) and $Ti_4Al_2C_2$ (T) had increased due to the greater quantity of silicon and carbon available, Figure 7.24. The aluminium required to form these two phases may have come from the titanium rich phases, which explained its decrease, and the greater proportion of titanium required to form these phases was obtained from the TiAl, hence the change in its composition. The particle density of the phases increased towards the outer edge of the sample.

The greater expansion of the compact indicated that there more gas was evolved by the sample. This was found to be the case when it was sectioned and large gas pores were found throughout the sample. However, mounting techniques compacted the sample and measured porosity levels were inaccurately low, Table 7.8.

Macrohardness measurements were difficult to take since it was hard to find sufficiently large areas of material between the large pores. The macrohardness measurements taken were all low and decreased towards the edge of the sample where the porosity increased, Table 7.8. Microhardness measurements were more representative of the phases formed and were higher than those taken from compact Ti2S5-i.

Compact	Profile Temperatures			Porosity (%)		Hardness			
	Initiation (°C)	Rate (°C/s)	Peak (°C)	Mean	SD	Macro (Hv) Mean	SD	Micro (Hv) Mean	SD
Nickel-Aluminium-Silicon Carbide									
Ni2-i	552	400	1464	7.8	9.4	275.6	33.1	273.4	17.1
Ni2S5-i	490	329	1410	49.5	13.7	257.3	93.1	328.7	93.9
Ni2S10-i	485	271	1352	50.4	6.3	162.8	27.5	321.2	68.3
Titanium-Aluminium-Silicon Carbide									
Ti2-i	642	72	1316	19.7	7.5	226.2	67.3	453.8	52.5
Ti2S5-i	612	123	1329	35.0	12.0	307.8	27.8	513.4	29.1
Ti2S10-i	574	201	1345	49.1	10.4	154.5	52.3	602.8	36.9

Table 7.8 Details of Ni-Al-SiC and Ti-Al-SiC thermal explosions and reacted compacts

Compact	Phase	Ni (at%) Mean	SD	Al (at%) Mean	SD	Si (at%) Mean	SD	C (at%) Mean	SD	Alloy/ Compound
Ni2-i	K	49.6	0.3	50.4	0.3	-	-	-	-	NiAl
Ni2S5-i	K	47.2	0.9	48.5	1.3	4.0	0.7	0.3	0.3	NiAl
	X	0.8	0.4	1.3	1.1	0.9	0.5	97.0	1.9	C
Ni2S10-i	K	47.9	1.1	46.0	1.5	5.0	1.0	1.1	0.4	NiAl
	X	0.5	0.3	4.2	4.3	1.2	1.7	94.2	5.6	C
Compact	**Phase**	**Ti (at%) Mean**	**SD**	**Al (at%) Mean**	**SD**	**Si (at%) Mean**	**SD**	**C (at%) Mean**	**SD**	**Alloy/ Compound**
Ti2-i	N	94.8	2.0	5.2	2.0	-	-	-	-	Ti
	P	54.8	1.5	45.2	1.5	-	-	-	-	$TiAl/Ti_3Al$
	Q	45.6	3.6	54.4	3.6	-	-	-	-	TiAl
Ti2S5-i	A	1.4	1.1	97.3	1.7	1.3	1.6	0.0	0.0	Al
	Q	43.8	1.7	55.0	1.7	1.0	1.1	0.2	0.2	TiAl
	T	51.0	1.7	24.9	0.3	0.0	0.0	24.1	1.9	$Ti_4Al_2C_2$
	U	57.2	0.9	7.5	0.4	32.8	1.5	2.5	0.2	Ti_5Si_3
Ti2S10-i	A	3.8	1.8	95.9	2.0	0.2	0.4	0.0	0.0	Al
	Q	37.1	1.8	60.1	3.0	1.4	0.1	1.4	1.2	TiAl
	T	46.5	3.4	25.4	3.7	2.7	3.8	25.5	6.0	$Ti_4Al_2C_2$
	U	56.8	4.4	4.7	0.7	32.2	4.1	6.2	0.9	Ti_5Si_3

Table 7.9 EPMA data for Ni-Al-SiC and Ti-Al-SiC reacted compacts

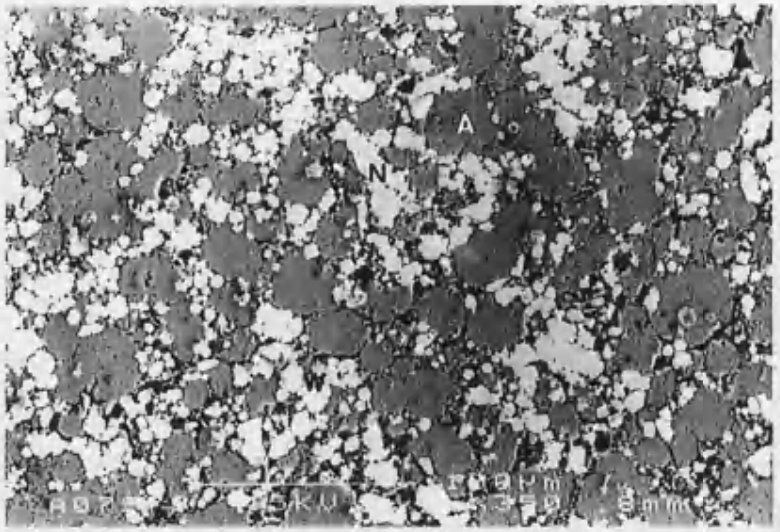

Figure 7.13a Ni2S5 green compact
A-Al, H-Ni, W-SiC 100μm

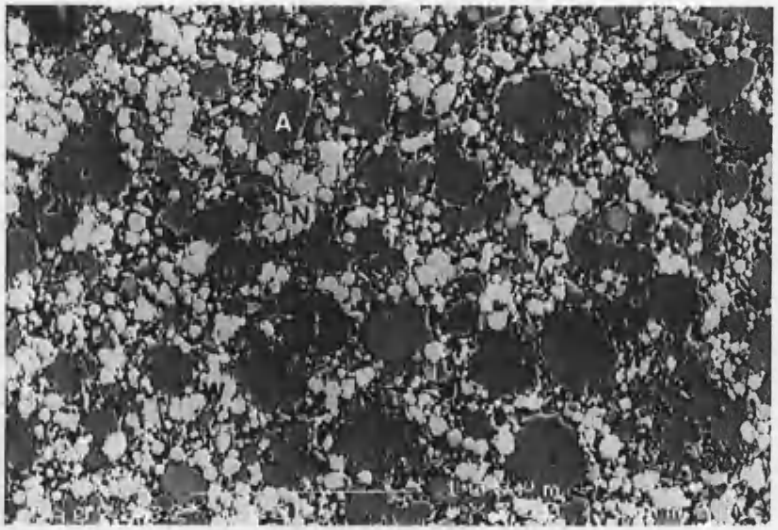

Figure 7.13b Ni2S10 green compact
A-Al, H-Ni, W-SiC 100μm

Figure 7.14a Ni2S5 compact reacted in die-i 10mm

Figure 7.14b Ni2S10 compact reacted in die-i 10mm

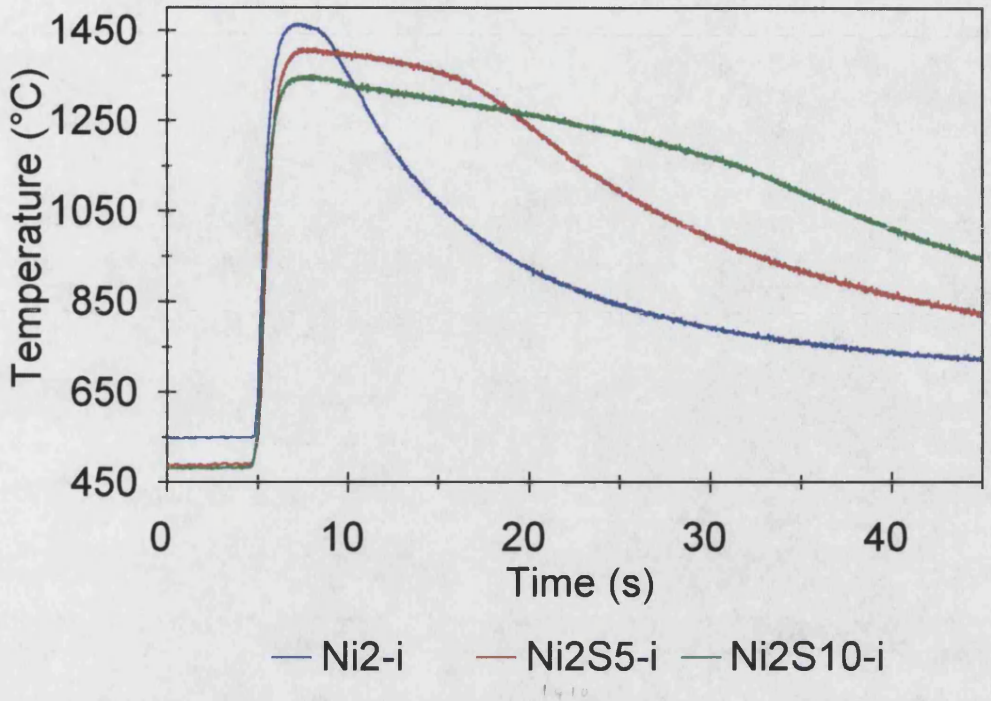

Figure 7.15 Effect of silicon carbide additions on nickel-aluminium time/temperature profile

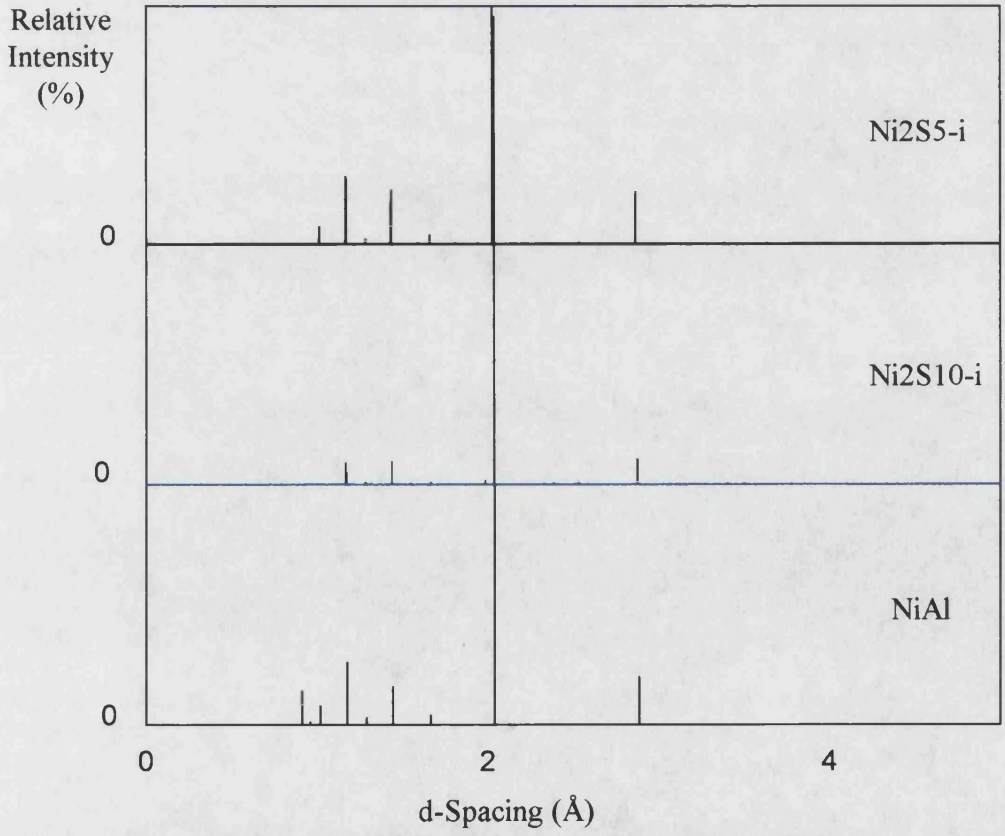

Figure 7.16 XRD plots for Ni2S5-i and Ni2S10-i

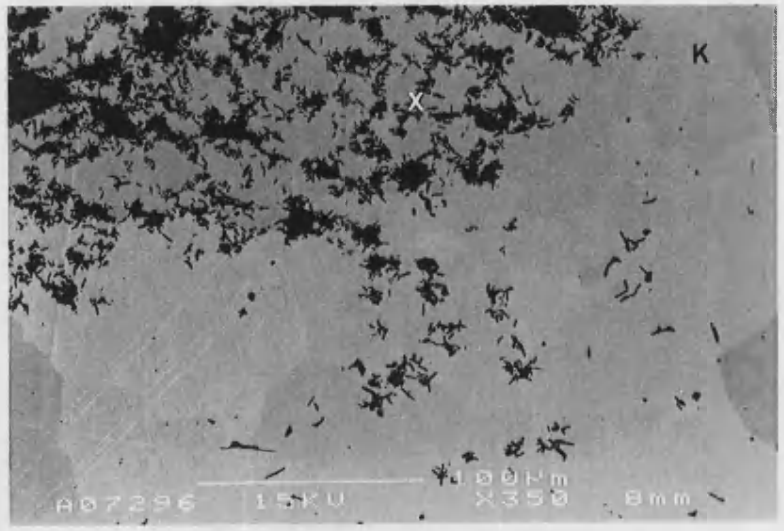

Figure 7.17 Microstructure of Ni2S5-i
K-NiAl, X-carbon 100μm

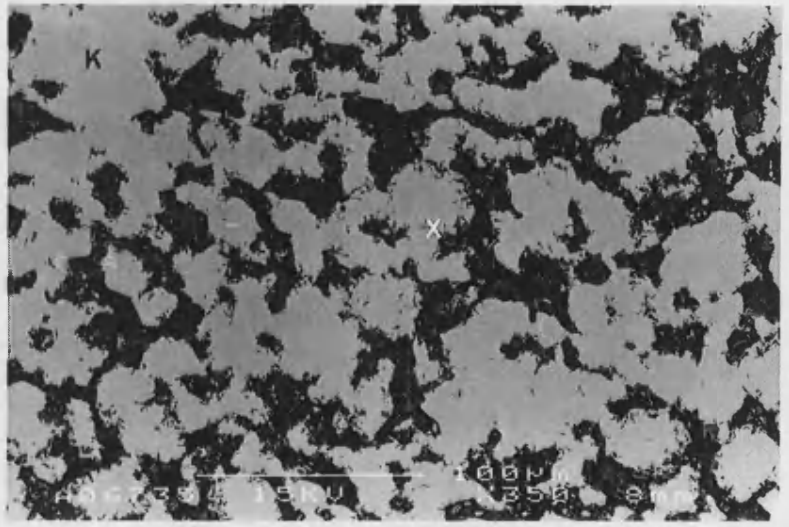

Figure 7.18 Microstructure of Ni2S10-i
K-NiAl, X-carbon 100μm

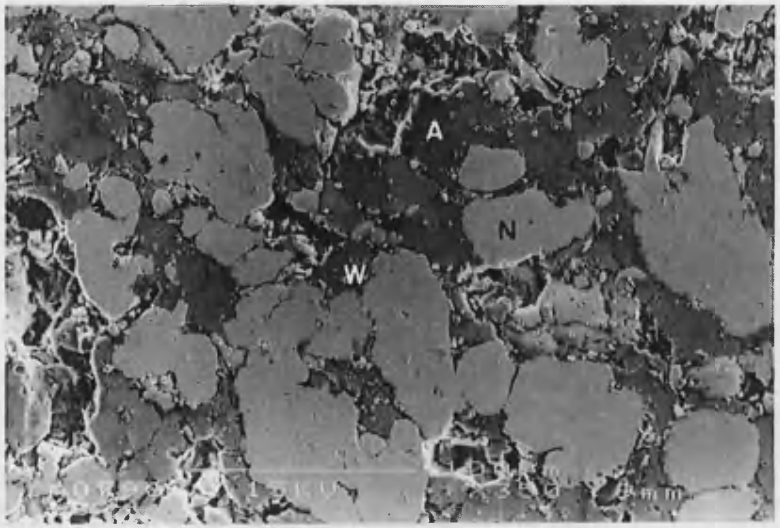

Figure 7.19a Ti2S5 green compact
A-Al, N-Ti, W-SiC 100μm

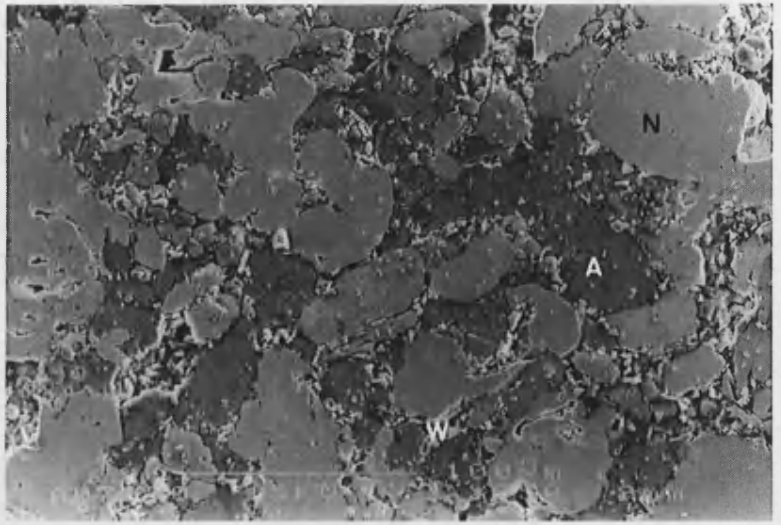

Figure 7.19b Ti2S10 green compact
A-Al, N-Ti, W-SiC 100μm

Figure 7.20a Ti2S5 compact reacted in die-i 10mm

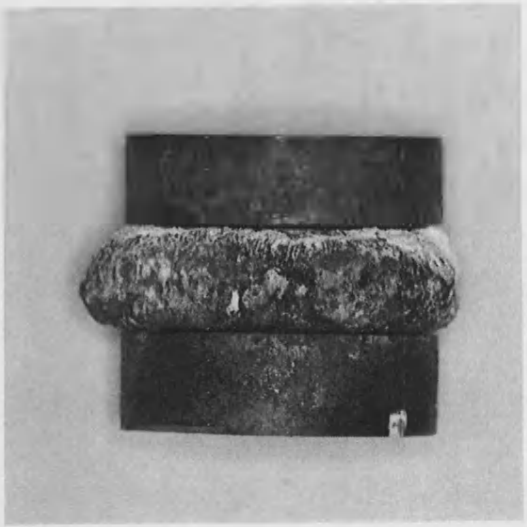

Figure 7.20b Ti2S10 compact reacted in die-i 10mm

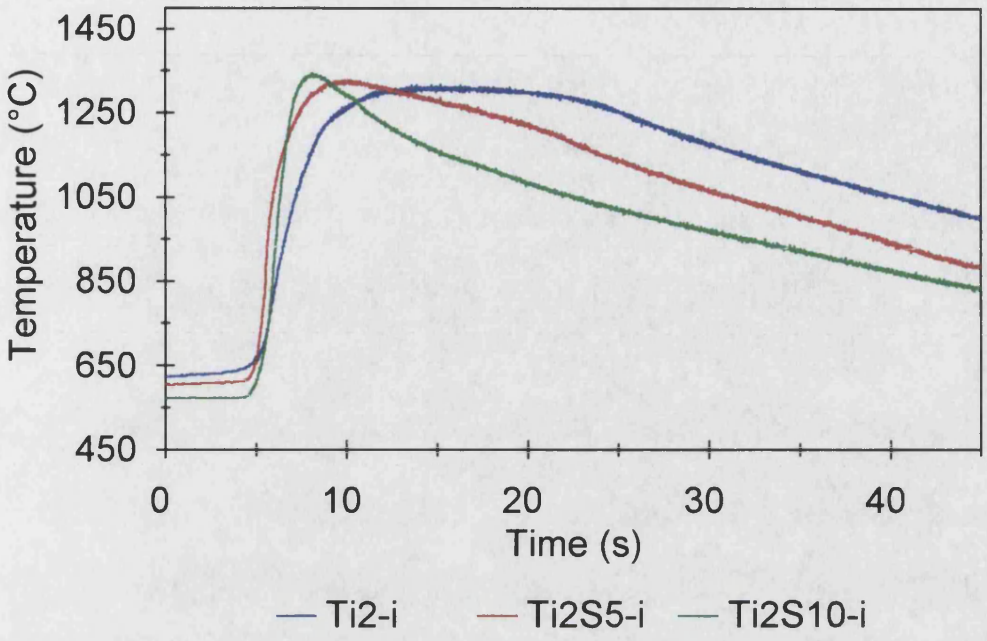

Figure 7.21 Effect of silicon carbide additions on titanium-aluminium time/temperature profile

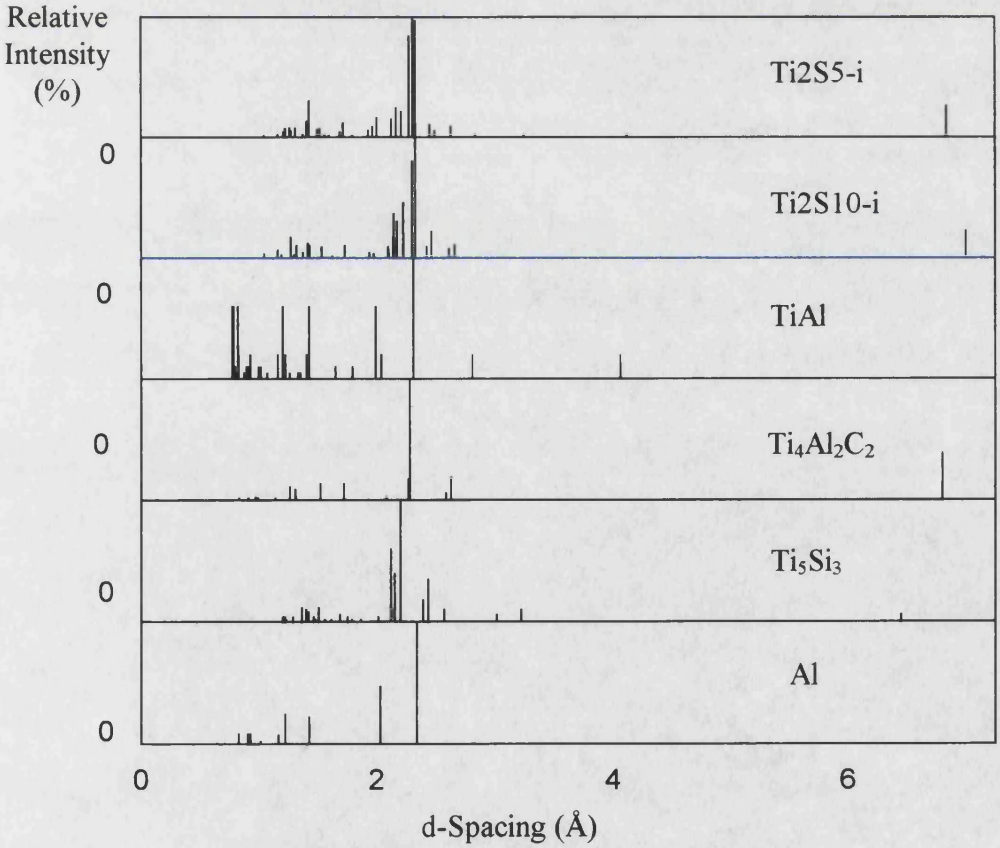

Figure 7.22 XRD plots for Ti2S5-i and Ti2S10-i

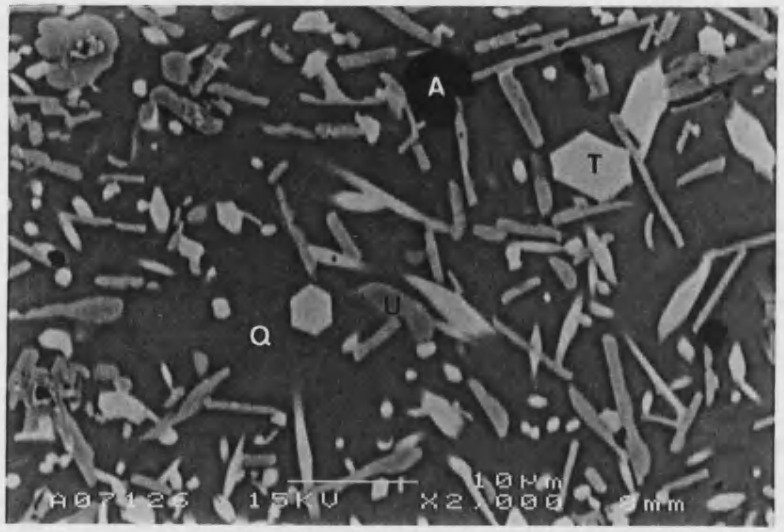

Figure 7.23 Microstructure of Ti2S5-i
A-Al, Q-TiAl, T-$Ti_4Al_2C_2$, U-Ti_5Si_3 100μm

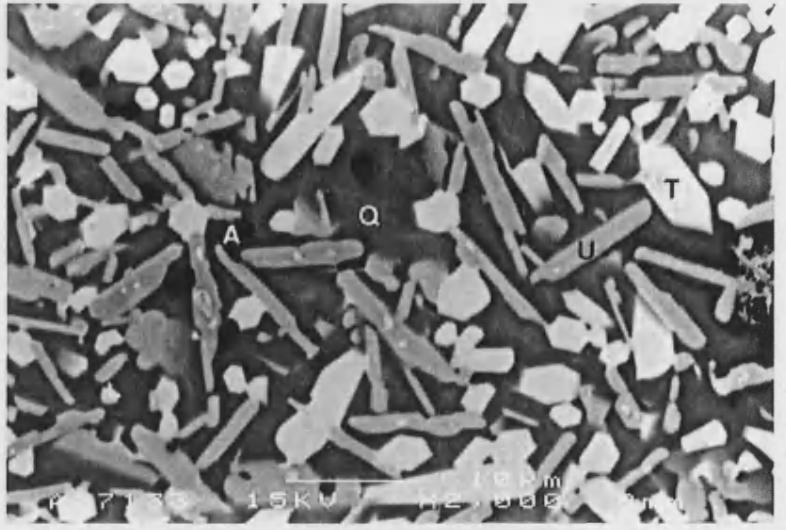

Figure 7.24 Microstructure of Ti2S10-i
A-Al, Q-TiAl, T-$Ti_4Al_2C_2$, U-Ti_5Si_3 100μm

7.3.3 Thermocouple Effects

The thermocouple was moved to the outside of the compacts to investigate whether its position had any marked effect on the temperatures measured during the thermal explosions. The reactions in the titanium-aluminium system reinforced with 10wt% alumina and 10wt% silicon carbide were repeated. From Table 7.10 it can be seen that the compact containing alumina produced a higher initiation temperature, a similar rate of temperature rise and a similar peak temperature when the thermocouple was at the surface. The compact containing silicon carbide also had a higher initiation temperature and a similar rate of temperature rise, but produced an increased peak temperature when the thermocouple was at the surface.

Compact	Profile Temperatures		
	Initiation (°C)	Rate (°C/s)	Peak (°C)
No Reinforcement			
Ti2-i	642	72	1316
Ti2-i-(TS)	636	67	1280
Alumina			
Ti2A10-i	582	42	1265
Ti2A10-i-(TS)	615	44	1277
Silicon Carbide			
Ti2S10-i	574	201	1345
Ti2S10-i-(TS)	621	193	1394

Table 7.10 Effect of thermocouple positions on the time/temperature profiles

7.4 Discussion

7.4.1 The Addition of Alumina

The Green Compacts: The alumina was evenly distributed throughout all the green compacts, apart from Ni2S5 where a few agglomerations were found. It disrupted the network of nickel in the nickel-aluminium compacts and the network of aluminium in

the titanium-aluminium compacts. It also reduced the area of contact between the transition metals and the aluminium.

Shape of the Reacted Compacts: The presence of the alumina in the compacts allowed greater shape retention during the thermal explosions. The alumina decreased the proportion of liquid formed, which reduced collapse in the nickel-aluminium compacts and reduced swelling in the titanium-aluminium compacts.

Time/Temperature Profiles: A study of the time/temperature profiles revealed that adding larger amounts of alumina progressively reduced the initiation temperatures in both systems. This was contrary to the expected trend. Since the alumina remained inert to the reaction, it was thought that it would have absorbed some of the heat generated by the solid-state formation of the high aluminium content intermetallics. Also its presence would have reduced the contact area between the metals and thus reduced the rate of intermetallic formation. Therefore the initiation of the thermal explosion would have been delayed until the compact had reached a higher temperature.

The drop in initiation temperature was partly attributed to the thermal conductivity of the compact. By placing the thermocouple at the surface of compact Ti2A10-i, the measured initiation temperature was raised from 582 to 615°C, Table 7.10. However, placing the thermocouple at the surface of the unreinforced compact produced very little change. Therefore, the alumina decreased the thermal conductivity of the compact and introduced a temperature gradient from the surface to the centre. It did this by disrupting metal to metal contact and introducing more interfaces into the compact[175]. The thermal explosion was initiated at the hotter surface whilst the thermocouple gave the temperature at the cooler centre.

However, the initiation temperature measured at the surface of compact Ti2A10-i was still lower than that of the unreinforced compact. The lower thermal conductivity of the compact reduced the rate of heat loss during heating and this may have accounted for the lower initiation temperature. This effect was also noted for the low green density compacts in Section 6.

The rate of temperature rise of both systems was reduced by the addition of alumina. By remaining inert during the reaction, the alumina reduced the rate of heat accumulation. It did this by diluting the reactants and acting as a heat sink, which drew heat away from the reacting elements. This decreased the amount of liquid formed and reduced the area of reaction. The smaller proportions of liquid phase were also noticed in the shapes of the reacted compacts. The alumina further reduced the area of reaction by restricting the flow of liquid around the compact[94].

The peak temperature was dependent on the rate of heat accumulation and the rate of heat loss. The rate of heat accumulation was decreased by the smaller area of reaction, whilst the alumina particles within the reacting compact had an increasing effect on the rate of heat loss. This produced a progressive reduction in peak temperature with increasing alumina content in the titanium-aluminium compacts, an effect which has also been reported by other authors[73]. For the nickel-aluminium compacts the reduction in peak temperature was less perceptible since the rate of heat accumulation was not reduced sufficiently to produce an effect.

The surface of the unreinforced compact reached a lower peak temperature than the centre. In the compact containing 10wt% alumina there was no difference, as the lower thermal conductivity of the compact reduced the rate of heat loss from the regions near the surface.

Microstructures: The Ellingham Diagram in Figure 3.14 shows that alumina is stable in contact with nickel and titanium within the range of temperatures encountered in the thermal explosion. An inspection of the microstructures found this to be true for the reactions initiated in this investigation. This was supported by reports of previous work into the introduction of alumina to both these systems[73,115,72].

As predicted by the time/temperature profiles, the matrix phases formed by both systems remained largely unchanged by additions of up to 10wt% alumina. All the reactions in the nickel-aluminium compacts continued to completion to form NiAl and all the reactions in the titanium-aluminium compacts produced similar mixtures of titanium rich, TiAl/Ti_3Al and TiAl regions. Larger amounts of alumina were needed to alter the matrix phases formed.

The only differences in the microstructures of the nickel-aluminium compacts were the distribution of alumina and the type and quantity of porosity. The liquid that formed in compact Ni2A5-i carried the alumina particles with it as it flowed and produced a segregated distribution of alumina. In compact Ni2A10-i a smaller amount of liquid phase was formed. This was unable to move the alumina to such a degree and only produced a slight increase in the fraction of alumina towards the surface.

In compact Ni2A5-i a large amount of gas porosity was found in the surface regions of the sample. The gases originated from oxides and hydroxides on the surfaces of the reactant particles and these became trapped when the matrix solidified. The time/temperature profile of compact Ni2A10-i showed that its lower thermal conductivity allowed it to remain at a higher temperature for a longer time and allowed more of the gas porosity to escape from the sample. Further porosity was introduced by agglomerations of alumina particles. These quenched and solidified the surrounding liquid, which prevented infiltration by the matrix and left pores between the particles. As the alumina content increased, so did the number of pores.

No segregation of alumina occurred in the titanium-aluminium compacts since insufficient liquid was formed to move the reinforcement. The alumina easily quenched and solidified the small amount of liquid phase formed and this prevented the matrix from infiltrating between the particles. This can be seen in the SEM images of the sample which show pores edged with alumina particles, Figures 7.11 and 7.12. This resulted in greater porosities and the loss of loosely held alumina from within the porous regions during sample preparation.

Hardness Measurements: The addition of alumina decreased the macrohardness values obtained from both systems, which reflected the increase in porosity. Microhardness measurements more accurately estimated the hardness of the matrix phases. All three samples in the nickel-aluminium system had similar microhardness values which indicated a similar matrix phase. However, there was a drop in microhardness in the reinforced titanium-aluminium samples. This change was attributed more to the increased porosity rather than a change in matrix phases, since it was impossible to make hardness indents between the pores.

7.4.2 The Addition of Silicon Carbide

The Green Compacts: The silicon carbide was found mixed into the network of nickel particles around the larger aluminium particles. This produced an increase in porosity of the network and the compact as a whole. In the titanium-aluminium compact, the silicon carbide was found along the interfaces between the metal reactants and produced no change in the amount of porosity.

Shape of the Reacted Compacts: The addition of silicon carbide to the nickel-aluminium compacts allowed them to retain their dimensions during the thermal explosion. The flow of material was restricted to the formation of a few beads on the surface and these decreased in number when the silicon carbide content was increased. It was apparent that the silicon carbide had somehow decreased the proportion of liquid formed in the thermal explosion.

The titanium-aluminium-silicon carbide compacts were almost unrecognisable once they emerged from the furnace. A massive radial expansion had occurred and the surface had bubbled. It appeared that a reaction involving the silicon carbide had evolved a large amount of gas during the reaction and this had inflated the compact. There was an increase in the proportion of liquid formed as the compact was able to deform to contain the gas porosity without rupturing.

Time/Temperature Profiles: The lack of silicon carbide in the reacted compacts implied that it had a reacted with the metals. A study of the literature revealed that it reacted exothermically with nickel to form nickel silicides and carbon[51,94]:

$$2Ni + SiC \rightarrow Ni_2Si + C$$

$$3Ni + 2SiC \rightarrow Ni_3Si_2 + 2C.$$

This reaction only occurred when NiAl started to form[23] and therefore had no effect on the initiation temperature. The same reasons for the reduction of the initiation temperature by the addition of alumina applied to the reduction of the initiation temperature by the addition of silicon carbide. The silicon carbide particles were smaller than the alumina and this introduced more interfaces into the compact to produce a lower thermal conductivity. This resulted in a greater drop in the initiation temperature.

A reaction between the silicon carbide and the metals also occurred in the titanium-aluminium-silicon carbide compacts. No literature was available to indicate that the thermal explosion was initiated by a reaction with the silicon carbide. The thermocouple at the surface of the Ti2S10-i compact also showed that there was a temperature gradient in the compact and the initiation temperature was only a few degrees lower than that of the unreinforced compact. By taking the lower heat loss from the compact into account, then the silicon carbide was probably inert to the reactants at the initiation temperature.

The rate of temperature rise was reduced by the silicon carbide in the nickel-aluminium compacts, Table 7.8. Immediately after the thermal explosion was initiated, the silicon carbide acted in the same way as the alumina to reduce the rate of heat accumulation. Once the temperature had increased, then the silicon carbide reacted with the nickel to form silicides and carbon. The peak temperature occurred around this point, since the silicide forming reactions were less exothermic than the formation of NiAl, Table 7.11. This quickly reduced the rate of heat accumulation and allowed the temperature of the compact to fall. This accounts for the discrepancy in the average rates of temperature rise for the alumina and silicon carbide containing systems. Even though the average rates were slower in the alumina containing systems, the peak temperatures were higher. This was due to a gradual drop in the rate of heat accumulation to give a low average rate of temperature rise. In the silicon carbide system, the rate of heat accumulation fell sharply, which gave a lower peak temperature, but a higher average rate of temperature rise. The slow conversion of the silicides into NiAl containing silicon released energy to give a slow fall in compact temperature.

The rate of temperature rise was increased in compacts Ti2S5-i and Ti2S10-i by the metals reacting with the silicon carbide. The exact mechanism by which the phases were formed and the rate of heat accumulation was altered is unclear. However, it can be deduced that the presence of the silicon carbide helped to increase the surface area of reaction. The silicon carbide particles had a large surface area to volume ratio and may have reacted to form a larger proportion of liquid phase. The rate of heat accumulation was altered by the increased area of reaction and the differing enthalpies of formation of the new phases. The peak temperatures were increased by the faster rates of heat accumulation.

Compound	ΔH^{o}_{f} (KJmol^{-1})
NiAl	-119
Ni_2Si	-76
Ni_3Si_2	-98
Al_2O_3	-1677
SiC	-67

Table 7.11 Enthalpies of formation

By placing the thermocouple at the surface of the compact, the rate of temperature rise remained the same and the peak temperature increased. The rate of heat loss was not increased at the surface thermocouple, as the compact expanded outwards during the reaction and enveloped it. This expansion may have also pulled the reacting material away from the thermocouple at the centre, which then recorded a low peak temperature.

Microstructures: The alumina is thermodynamically more stable than the silicon carbide[126], Table 7.11, and this was proved by the microstructures of the reacted compacts. It was reported that the SiC decomposed at 1000°C and the silicon reacted with the nickel to form nickel silicides[23,117]. The silicides subsequently reacted with the aluminium to form a matrix of NiAl containing small amounts of silicon and carbon. The majority of the carbon atoms gathered together due to interfacial energy considerations and formed the small oblong phases around the pores.

The pores were formed from the regions containing silicon carbide when it decomposed and this produced the distribution of carbon around them. Up to this point, liquid had been unable to penetrate between the silicon carbide particles, which had been acting as heat sinks, and this had hindered consolidation in the compact. Since only a small proportion of liquid had been formed, the distribution of silicon carbide had not been greatly altered and the pores marked out the original network of nickel and silicon carbide.

The silicon carbide reacted with the titanium-aluminium compacts to produce the variety of phases detailed previously. As the material between the pores was well

consolidated and the compacts were allowed to expand so massively, this indicated that a substantial amount of liquid was formed during the reaction. It was proposed that the inclusion of silicon and carbon into the TiAl produced an aluminium rich composition with a lower melting point, and together with the higher peak temperature, this resulted in an increase in the amount of liquid. The liquid containing more silicon and carbon would have had a lower melting point and would have been able to flow further before solidifying. This would also precipitate a greater density of phases when the compact cooled. This was found to be the case for the material at the surface of compact Ti2S10-i.

It was evident from the overall shape of the reacted compacts and the rounded shape of the porosity that a large amount of gas was evolved during the thermal explosion. This produced bubbles in the liquid phase which were trapped when the compact solidified.

Hardness Measurements: The increased porosity in the nickel-aluminium-silicon carbide compacts decreased the macrohardness values and the inclusion of silicon and carbon into the NiAl produced a slight increase in the hardness on the matrix.

The macrohardness values from the titanium-aluminium-silicon carbide compacts were reduced by the high porosity. But the inclusion of silicon and carbon into the TiAl and the formation of phases within this produced large increases in microhardness measurements.

7.4.3 Summary

The addition of alumina and silicon carbide particles to the transition metal-aluminium systems had markedly different effects. The alumina remained inert during the reactions and diluted the thermal explosions, altering the temperature profiles. However, the changes to the profiles were not significant enough to alter the final phases formed in the compacts. The most significant effect of adding up to 10wt% alumina was to increase the porosity in the reacted compacts.

The silicon carbide reacted with the metals during the thermal explosions. This reduced the amount of liquid formed in the nickel-aluminium compacts, formed a microstructure of NiAl and carbon and increased the porosity. In the titanium-

aluminium system the silicon carbide increased the amount of liquid, formed a variety of phases and produced a large amount of gas porosity.

The introduction of fibre reinforcements by this route presented, however, new problems, in particular the fracture of fibres during mixing with the reactants. As a consequence, an alternative method, described in Section 8, was investigated in order to avoid the problem.

Section 8

INFILTRATION OF FIBRE PREFORMS WITH LIQUID FORMED BY A THERMAL EXPLOSION

This experiment introduced continuous fibres into an intermetallic matrix. A molten intermetallic phase was produced by a thermal explosion route and this was forced into a preform of continuous fibres in a similar manner to liquid metal infiltration.

8.1 Materials

Nickel aluminide was formed by initiating a thermal explosion in PSD2 nickel and aluminium powders. The reinforcing fibres were the carbon and alumina fibres detailed in Section 2.1.

8.2 Experimental Procedures

The nickel-aluminium system was used to provide the matrix phase since the reactions in Section 6 had shown that this system produced the largest proportion of liquid phase during the thermal explosion. This was essential to avoid fracturing the fibres as the matrix was forced into the preform.

The thermal explosion and liquid metal infiltration steps were both carried out in die-ii, Figure 8.1. Nickel-aluminium powder compacts, with a mass of 15g, were produced by the same method as used in Section 6. The compact placed in the bottom of the die had a 3mm deep hole drilled into its centre to allow a thermocouple to be inserted to measure its temperature. This hole was shallow as the compact was thin and only the initiation temperature of the thermal explosion was required. A 1g layer of the loose nickel-aluminium powder mixture was placed over the top of the compact and then a layer of randomly orientated carbon or alumina fibres, lying parallel to the die base, was placed on top of this. 0.1g of carbon fibres or a smaller volume of alumina fibres,

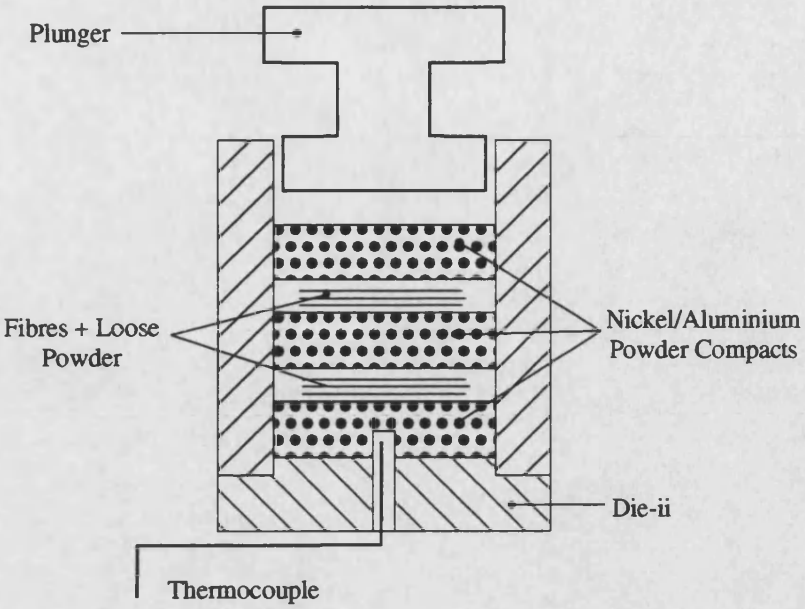

Figure 8.1 Arrangement of reactants in die-ii

0.05g, were used. This arrangement of layers was repeated before a final 15g nickel-aluminium compact was placed into the top of the die. The plunger was then inserted and a light pressure of 25MPa was applied to push the layers together.

An alumina coated thermocouple was inserted through the die base and into the bottom compact and then the die and its contents were placed in the furnace used in Section 6. These were heated under the standard heating rate and the initiation of the thermal explosion was monitored using the thermocouple and the application of a light pressure prior to initiation.

A soon as the thermal reaction was initiated, a uniaxial pressure was applied to the die to force the liquid phase into the preform. A pressure of 77MPa was applied to the die containing the carbon fibres and a pressure of 97MPa to the die containing the alumina fibres.

The die was lowered out of the furnace 45 seconds after the thermal explosion was initiated and allowed to cool. The compact was sectioned down its axis to ensure that the fibre containing regions were intersected. SEM, EPMA and XRD techniques were used to provide images of the microstructures and to identify the phases present.

8.3 Results

Compact	Phase	Ni (at%)		Al (at%)		C (at%)		Alloy/
		Mean	SD	Mean	SD	Mean	SD	Compound
Ni2-ii +	K	50.7	0.2	49.3	0.4	0.7	0.4	NiAl
C	X	1.8	0.8	2.9	1.7	95.3	2.4	C
Compact	**Phase**	**Ni (at%)**		**Al (at%)**		**O (at%)**		**Alloy/**
		Mean	**SD**	**Mean**	**SD**	**Mean**	**SD**	**Compound**
Ni2-ii +	H	96.6	3.8	3.1	3.6	0.3	0.2	Ni
Al_2O_3	L	42.4	0.7	57.6	0.7	0.1	0.0	Ni_2Al_3
	V	0.2	0.0	38.9	1.2	59.9	0.9	Al_2O_3

Table 8.1 EPMA data for Ni-Al + C and Ni-Al + Al_2O_3

8.3.1 Nickel-Aluminium + Carbon Fibres

A SEM image of the sectioned sample showed that the thermal explosion had formed a single uniform matrix phase (K), Figures 8.3a-b. EPMA and XRD revealed this phase to be NiAl, Table 8.1 and Figure 8.2a, and that no reaction had taken place between this and the carbon reinforcement (X). However, the matrix did not infiltrate between the fibres. The fibres appeared to have been pressed together in two separate layers within the compact. Gas pores were located in the matrix away from the reinforcement, giving the unreinforced regions a porosity of 5.9% (SD 2.5%). Macrohardness measurements from these regions were 253Hv (SD 19Hv) and microhardness measurements were 264Hv (SD 15Hv).

8.3.2 Nickel-Aluminium + Alumina Fibres

SEM images of this sample revealed the presence of multiple phases in the matrix, Figure 8.4a. These were identified as nickel rich regions (H) surrounded by Ni_2Al_3 (L), Table 8.1 and Figure 8.2b. As with the nickel-aluminium-alumina composites produced in Section 7, no reaction was detected between the alumina reinforcement (V) and the matrix. The fibre preforms were infiltrated by the matrix phases, Figure 8.4b, and this formed two separate reinforced layers within the compact. Few pores were found near the fibres, but gas pores and a lack of consolidation of the matrix increased levels to 22.8% (SD 2.7%) in the unreinforced regions. Further, there was

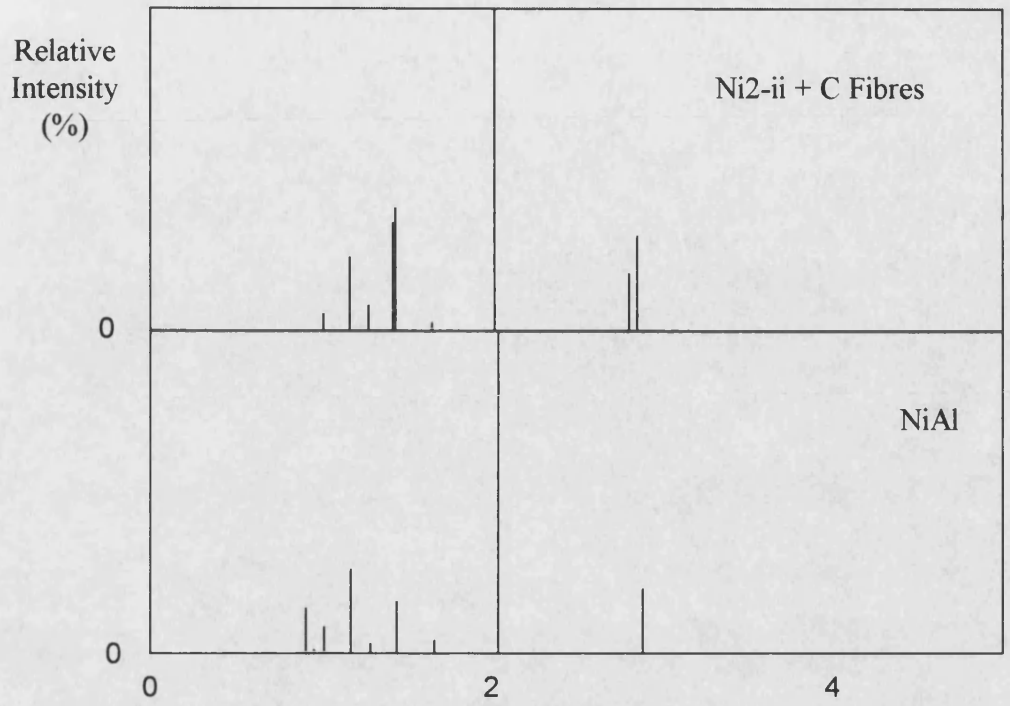

Figure 8.2a XRD plots for Ni2-ii + C fibres

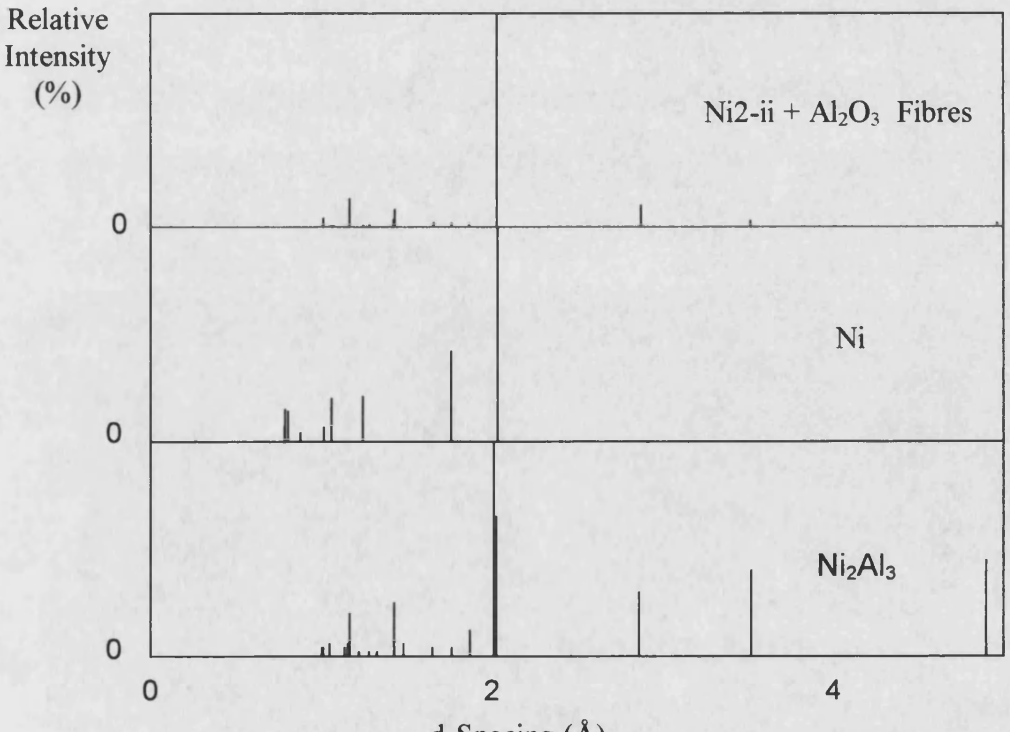

Figure 8.2b XRD plots for Ni2-ii + alumina fibres

Figure 8.3a Microstructure of Ni-Al + C
K-NiAl, X-carbon 100μm

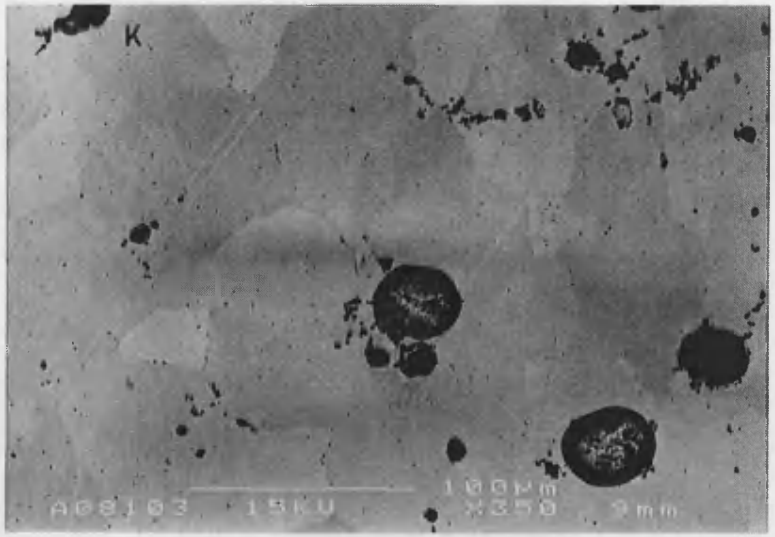

Figure 8.3b Microstructure of Ni-Al + C
K-NiAl 100μm

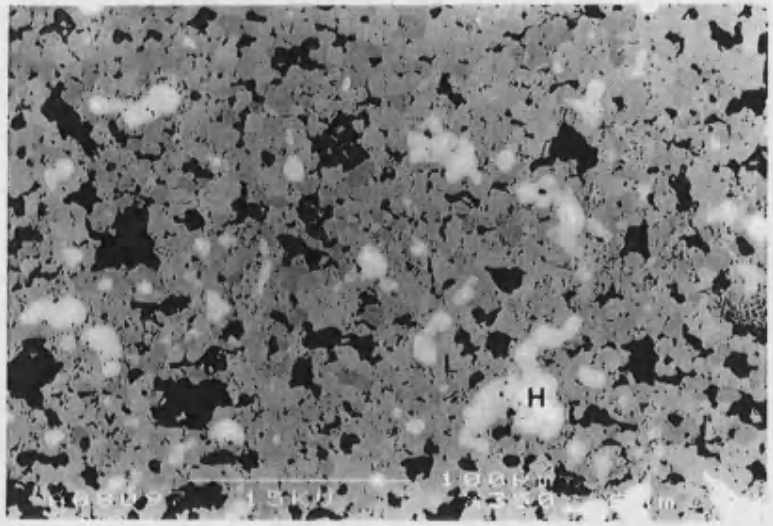

Figure 8.4a Microstructure of Ni-Al + Al_2O_3
H-Ni, L-Ni_2Al_3 100μm

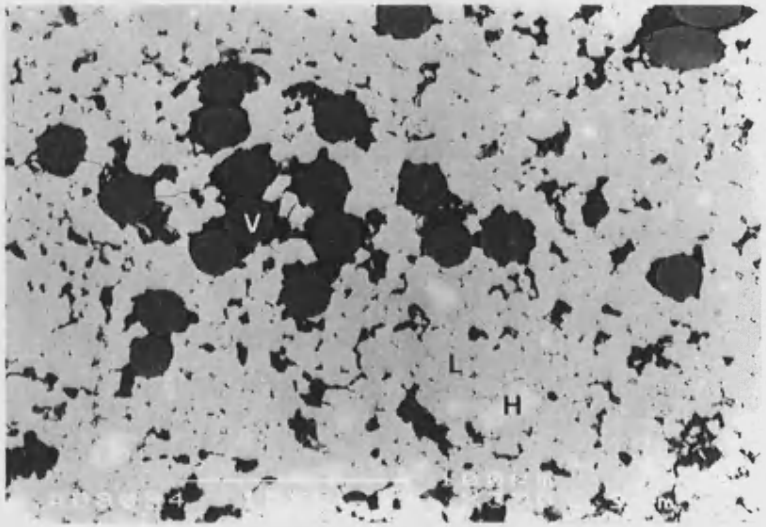

Figure 8.4b Microstructure of Ni-Al + Al_2O_3
H-Ni, L-Ni_2Al_3, V-Al_2O_3 100μm

an increase in the proportion of nickel rich areas in the unreinforced regions. Macrohardness measurements in the unreinforced areas were 301Hv (SD 39Hv) and microhardness measurements were 361Hv (SD 47Hv).

8.4 Discussion

8.4.1 Nickel-Aluminium + Carbon Fibres

According to the results from Section 6, using die-ii and applying pressure during the thermal explosion increased the rate of heat loss from the reaction. However, even though the pressure was increased to 77MPa in this reaction, the rate of heat loss was not increased sufficiently to reduce the extent of reaction and a NiAl matrix was formed by the thermal explosion. Unfortunately, this did not infiltrate the preform of carbon fibres for several reasons. The lower heating rate reduced the proportion of liquid formed by the compacts and increased its viscosity. This resulted in the pressure being too low to force the liquid between the fibres. Further, the fibres did not react with the matrix and therefore they acted as heat sinks, which drew heat away from the liquid and solidified it. This prevented the preform from being infiltrated and the pressure applied to the compact simply compressed the fibres.

The majority of the porosity present in the unreinforced regions was gas porosity formed when the liquid solidified. Porosity levels were lower than those of the corresponding compacts reacted under lower pressures in Section 6 and it was assumed that the greater pressure closed the pores. The microhardness measurements indicated the formation of NiAl and the similar macrohardness measurements reflected the low porosity of the sample.

8.4.2 Nickel-Aluminium + Alumina Fibres

To improve the infiltration of the fibre preforms by the matrix, two changes were made to the previous reaction. Fewer, less densely packed fibres were incorporated into the compact and a higher pressure of 96.8MPa was applied during the reaction. These changes were successful in infiltrating the preform, but the thermal explosion did not continue to completion and a multiphase matrix was formed.

The microstructure of nickel rich cores surrounded by Ni_2Al_3 suggested that a liquid phase was formed around the nickel. This started to consume the nickel and raised the temperature above the melting point of $NiAl_3$. It then precipitated Ni_2Al_3, but the rate of heat loss from the compact was increased by the application of pressure, and the temperature of the reaction did not exceed its melting point. A layer of Ni_2Al_3 was formed around the remaining nickel and solid-state diffusion through this to form NiAl was too slow to sustain the reaction and it was quenched. This quenching effect did not occur in the previous reaction since the lower pressure allowed the temperature to exceed the melting point of Ni_2Al_3 and NiAl was formed by rapid liquid-state reactions.

Even though the alumina fibres had remained inert during the reaction[105,115] and acted as heat sinks, they were ruled out as the cause of the quenching. The preforms had been infiltrated by the matrix and the extent of reaction appeared to be greater around the fibres than in the unreinforced regions. The lower green density of the loose reactant powders around the fibres reduced the thermal conductivity in this region and allowed the reaction to proceed further to completion before it was quenched.

Only a few gas pores were found next to the fibres, but in the unreinforced regions, porosity derived from a lack of consolidation of the matrix was also present. This lack of consolidation indicated a lower extent of reaction in the unreinforced regions.

The microhardness measurements taken from the unreinforced regions were unexpectedly high. This indicated that the combination of nickel rich cores and Ni_2Al_3 formed a harder structure than NiAl. The lower macrohardness measurements highlighted the high porosity in these regions.

8.4.3 Summary

The nickel-aluminium compacts sandwiching the carbon fibre preform formed a NiAl matrix, but failed to infiltrate the preform. This was attributed to an increase in the viscosity of the liquid phase, which prevented the pressure from forcing it between the fibres. The carbon fibres also acted as heat sinks and rapidly solidified the liquid around them. To overcome these problems, a lower density alumina fibre preform was used and the pressure was increased. This preform was found to be infiltrated by the matrix, but the increased pressure reduced the extent of reaction.

To form a continuously reinforced intermetallic matrix composite by this method required careful control of several parameters. A system which produced a large proportion of liquid during the thermal explosion was essential. To force this into a fibre preform a balance was needed between the fraction of reinforcement required and the maximum pressure that could be applied without quenching the matrix forming reaction.

Section 9

REACTIVE INFILTRATION OF NICKEL/ALUMINA PREFORMS WITH MOLTEN ALUMINIUM

An alternative to forming an intermetallic matrix composite by a thermal explosion route was to use reactive liquid metal infiltration. By forcing molten aluminium into a porous preform of nickel and alumina particles, a reactive synthesis reaction was initiated.

9.1 Materials

PSD1 and PSD2 nickels were used to produce the porous nickel preforms and alumina was used as the reinforcement. Super-pure aluminium was used to infiltrate the preform during the liquid-metal infiltration. Details of all are given in Section 2.

9.2 Experimental Procedures

Of the three systems investigated in this report, the nickel-aluminium system produced the largest proportion of liquid phase and the highest extent of reaction. It was on these criteria that it was selected for use in this section since it was known that the surrounding die would increase the rate of heat loss.

9.2.1 Fabrication of Porous Preforms

The first obstacle overcome was one of producing a preform with the correct amount of porosity to allow sufficient aluminium to infiltrate and form NiAl. The preform was required to maintain this porosity during the time it was heated in the die and as pressure was applied to force the molten aluminium into it.

Porous preforms were produced by lightly compacting 30g of nickel powder under a uniaxial pressure in the same die which was used produce powder compacts in Section

powders from adhering to the die walls. The preforms were then sintered under vacuum in an Astro Industries 1000-2560 FP furnace to impart some mechanical strength to them and to prevent them from shrinking as they were heated in the liquid metal infiltration die. Powder sizes, compaction pressures, sintering times and sintering temperatures were all varied in an attempt to produce a sintered preform with the correct porosity, Table 9.1. Porosities were calculated from mass/volume measurements.

It was found necessary to include particles of alumina reinforcement into the preforms to achieve the required porosities. The alumina particles were mixed with nickel powders using the same procedure for powder mixing detailed in Section 6 and then 30g of the mixture was lightly compacted and sintered as before.

Once a preform with the correct porosity had been produced, the ends were ground off to remove any densely packed outer layers. Samples of the preforms were mounted and prepared for examination in a SEM.

9.2.2 Reactive Liquid Metal Infiltration

The reactive liquid metal infiltration was carried out in the die detailed in Figure 9.1. The die was machined form silver steel to improve its oxidation resistance, as it was hoped it would be reused. The preform was placed at the bottom of the die and covered with a thin alumina mat. A block of aluminium, of the correct mass to react with the preform and form NiAl, was placed on top of this, and finally a silver steel plug sealed the die. The alumina mat separated the preform and the aluminium and prevented any interaction during the heating cycle. The die and its contents were heated in the furnace used in Section 6, Figure 9.1, until the aluminium reached a temperature of 700°C. The plug was then pushed down into the die by the plunger, which applied a pressure of 149MPa to force the molten aluminium through the alumina mat and into the preform. The pressure was maintained for 20 seconds after which the die was removed from the furnace and allowed to cool.

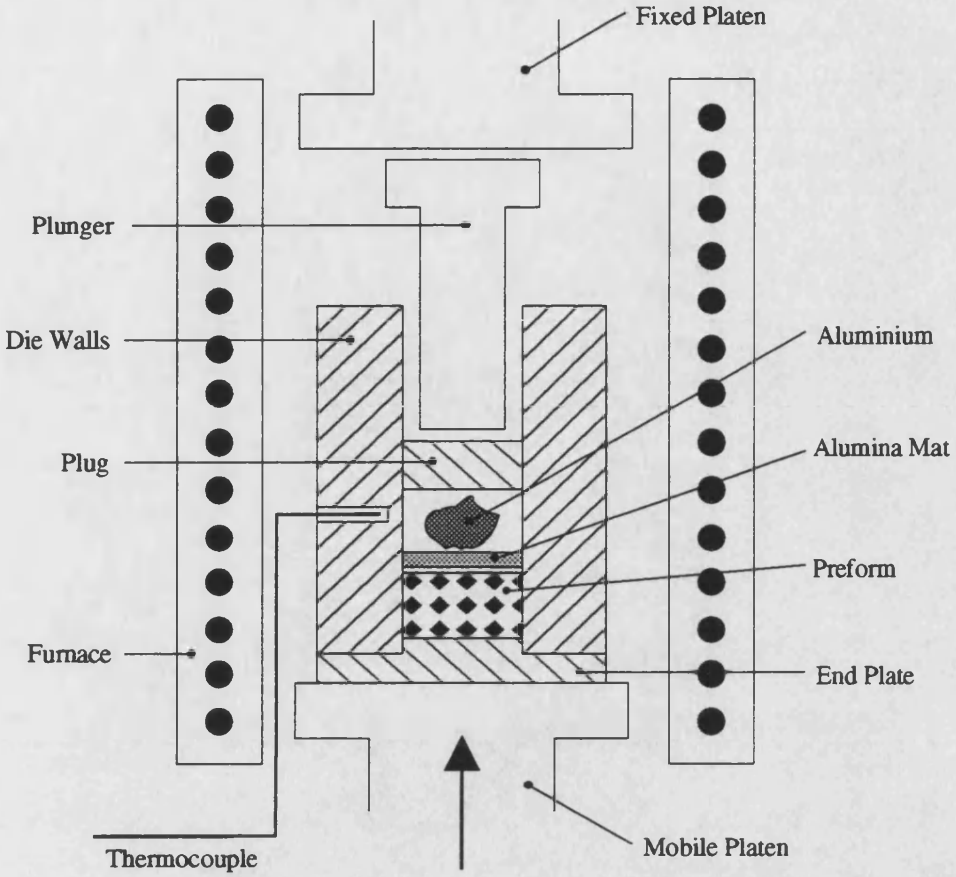

Figure 9.1 Liquid metal infiltration apparatus

A pressure of 149MPa was chosen to provide a pressure high enough to force the aluminium into the preform. However, Section 8 had shown that the increased rate of heat loss from the reaction this produced quenched the thermal explosions initiated in nickel-aluminium compacts. In this case, it was thought that the presence of the alumina would reduce the rate of heat loss, as demonstrated in Section 7, and that this would compensate for the pressure.

A thermocouple could not be placed in the die to indicate when the aluminium had reached 700°C. To solve this problem, a calibration run was carried out without the plug and the plunger. Instead, a coated thermocouple was lowered into the die to measure the temperature of the aluminium and a cover was place over the top of the die. The readings from this thermocouple and a further thermocouple located in the die wall next to the aluminium were recorded as the die was heated to provide two calibration plots, Figure 9.2. Therefore, during the actual infiltration run, the

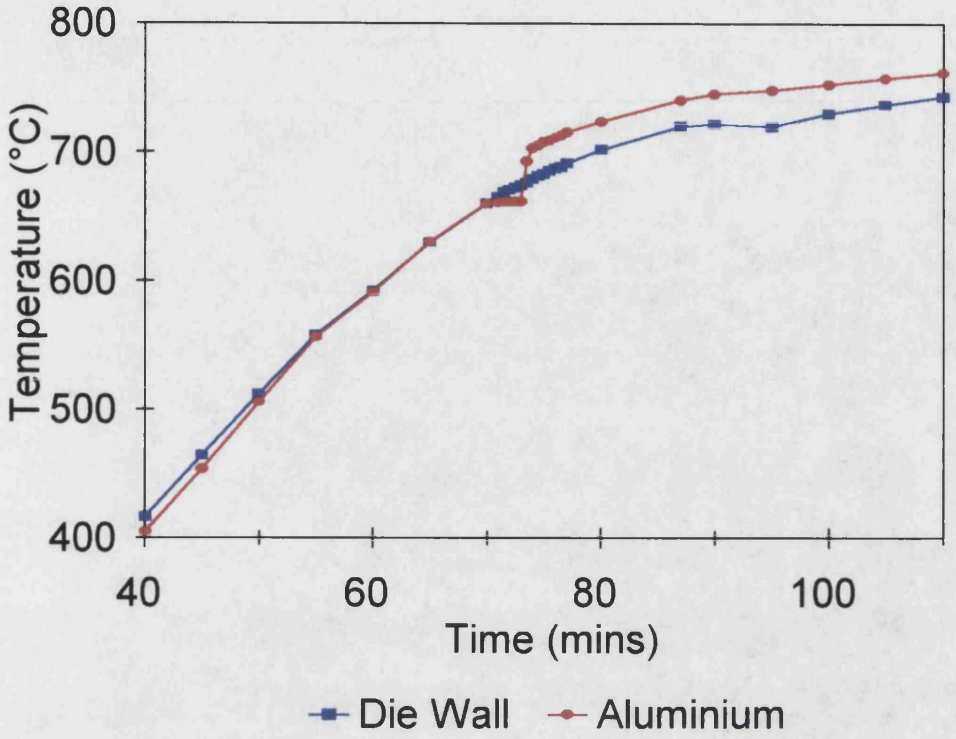

Figure 9.2 Die and aluminium time/temperature plots

temperature of the aluminium could be ascertained from the thermocouple in the die wall.

Once the reacted compact had been recovered from the die, it was prepared for examination by SEM and EPMA.

9.3 Results

9.3.1 Porous Preforms

To allow sufficient aluminium to infiltrate to form NiAl, a porosity of 60% was required in the nickel preforms. Table 9.1 contains details of the effect that powder sizes, compaction pressures, sintering times and sintering temperatures had on the final porosity.

The initial attempt at producing a porous preform used the PSD1 nickel powder, a compaction pressure of 203MPa and sintering temperature of 900°C for one hour. This resulted in preform P1 which had a porosity of only 20%, less than a third of the

Compact	Composition	Powders	Compaction Pressure (MPa)	Sintering Temp. (°C)	Sintering Time (hours)	Porosity (%)
P1	Ni	PSD1 Ni	165	900	1	20
P2	Ni	PSD2 Ni	165	900	1	24
P3	Ni	PSD2 Ni	46	900	1	34
P4	Ni	PSD2 Ni	43	700	1	44
P5	Ni	PSD2 Ni	43	700	½	51
P6	Ni	PSD2 Ni	18	700	½	62
P7	Ni + Al_2O_3	PSD2 Ni + Al_2O_3	41	700	½	52

Table 9.1 Details of porous preforms

required amount. Using larger nickel particles and reducing compaction pressures, sintering times and sintering temperatures increased the porosity. The porosity was increased to 62% in P6 by using PSD2 nickel, a compaction pressure of 43MPa and a sintering temperature of 700°C for half an hour, Figure 9.3. However, this preform was only lightly compacted and sintered and was easily damaged when handled.

By adding alumina particles to the nickel powder, in a 10wt% proportion of the nickel and aluminium needed to form NiAl, the porosity required in the preform was reduced to 51%. This was achieved in preform P7, using PSD2 nickel, a compaction pressure of 41MPa and a sintering temperature of 700°C for half an hour, Figure 9.4. The resulting preform had a porosity of 52%, and had undergone a more severe sintering programme than P6. This was the preform used in the subsequent reactive liquid metal infiltration attempt. Figure 9.4 showed that the porosity and alumina reinforcement were distributed uniformly in the preform, though the larger alumina particles (V) appeared to block some of the channels between the nickel (H).

9.3.2 Reactive Liquid Metal Infiltration

The calibration curves showed that a die wall temperature of 680°C was needed to raise the aluminium to 700°C. As soon as this was reached, a pressure of 149MPa was

applied to the aluminium to force it through the alumina mat and into the preform. The die was allowed to cool before the preform was recovered.

The die was designed so that the end-plate could be detached and the preform could be pushed out. However, the bolts securing the end-plate were difficult to turn and once the plate had been removed, it was found that aluminium had penetrated into the bolt threads and between the die and the end-plate. It was impossible to push out the preform, and the die had to be sectioned along its axis, which revealed more aluminium on top of the plug. An inspection of the bore of the die found that the regions around the reactants and plug had buckled during the infiltration.

The preform had been sectioned longitudinally with the die and this provided a cross sectional view of the infiltration of aluminium through the mat and the preform. The alumina mat had become attached to the top of the preform and Figure 9.5 shows that it was infiltrated by a phase (A), identified as aluminium by EPMA, Table 9.2.

SEM and EPMA of the preform revealed that this had been infiltrated with aluminium which had reacted with the nickel and formed a variety of intermetallic phases. Three

Preform Region	Phase	Ni (at%)		Al (at%)		O (at%)		Alloy/ Compound
		Mean	SD	Mean	SD	Mean	SD	
Mat	A	0.1	0.0	98.6	0.7	1.3	0.7	Al
	V	0.2	0.1	40.7	1.8	59.1	2.4	Al_2O_3
Top	H	94.0	2.2	4.5	2.0	1.5	0.9	Ni
	J	65.7	1.7	33.1	1.7	1.2	0.4	Ni_5Al_3
	L	38.4	0.2	60.8	0.3	0.8	0.1	Ni_2Al_3
	M	24.2	0.2	74.3	0.1	1.5	0.4	$NiAl_3$
	V	2.4	1.8	39.1	2.8	58.5	2.2	Al_2O_3
Middle	H	96.1	3.2	3.2	2.9	0.6	0.7	Ni
	I	76.0	1.3	23.5	1.4	0.5	0.5	Ni_3Al
	L	38.4	0.1	61.6	0.1	0.4	0.2	Ni_2Al_3
	M	24.7	0.1	75.3	0.1	0.0	0.0	$NiAl_3$
	V	1.3	0.6	38.9	0.7	59.8	0.7	Al_2O_3
Bottom	H	100.0	0.0	0.0	0.0	0.0	0.0	Ni
	J	63.8	0.9	35.0	0.6	1.2	1.0	Ni_5Al_3
	L	38.3	0.9	60.3	1.2	1.4	1.1	Ni_2Al_3
	M	24.5	0.1	75.1	0.1	0.3	0.3	$NiAl_3$
	V	2.1	1.6	38.3	0.8	59.6	1.3	Al_2O_3

Table 9.2 EPMA data of infiltrated preform

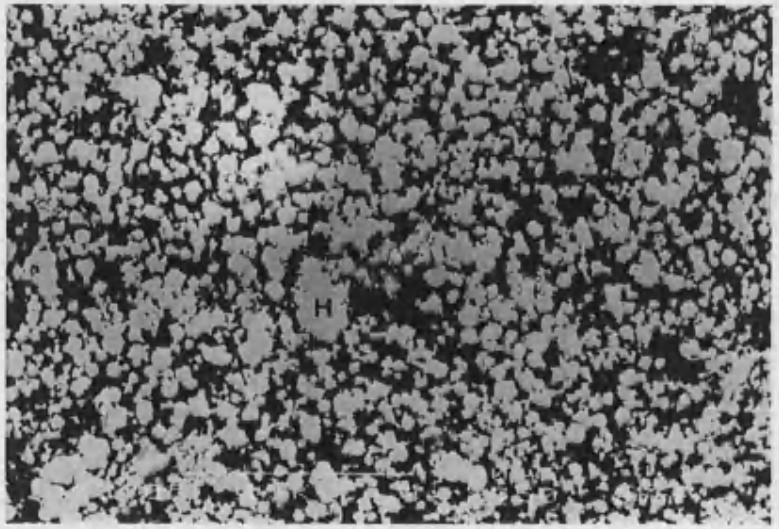

Figure 9.3 Porous nickel preform
100μm

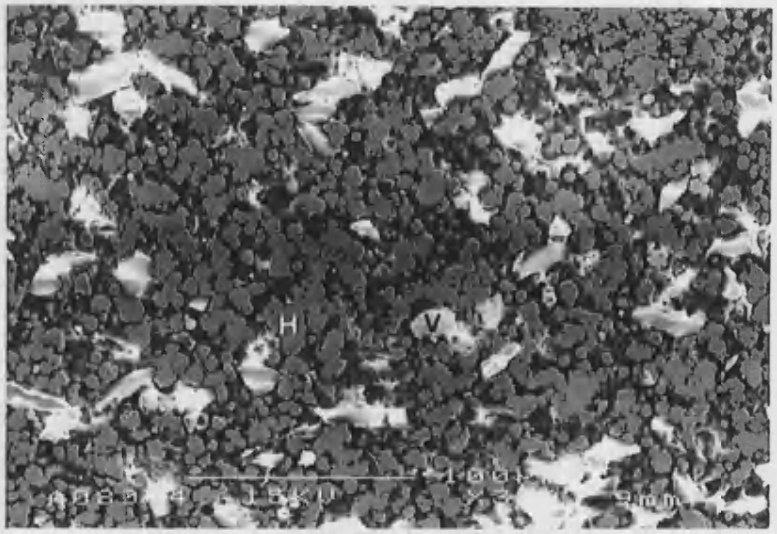

Figure 9.4 Porous nickel/alumina preform
H-Ni, V-Al_2O_3 100μm

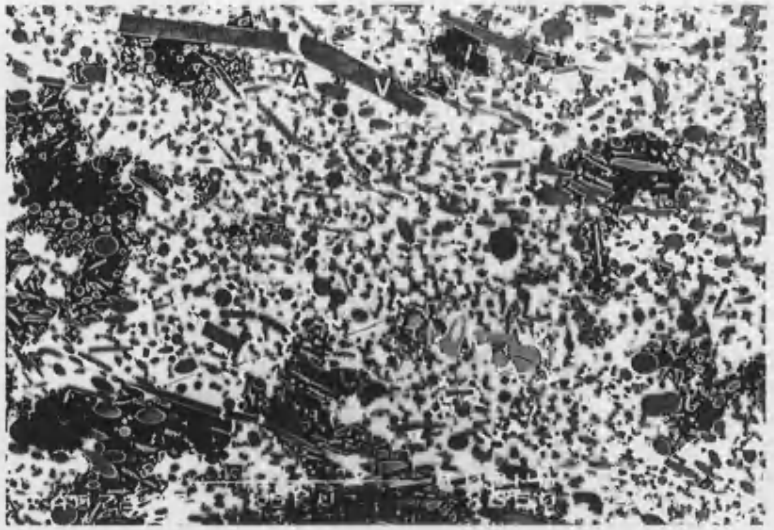

Figure 9.5 Infiltrated alumina mat
A-Al, V-Al_2O_3 100μm

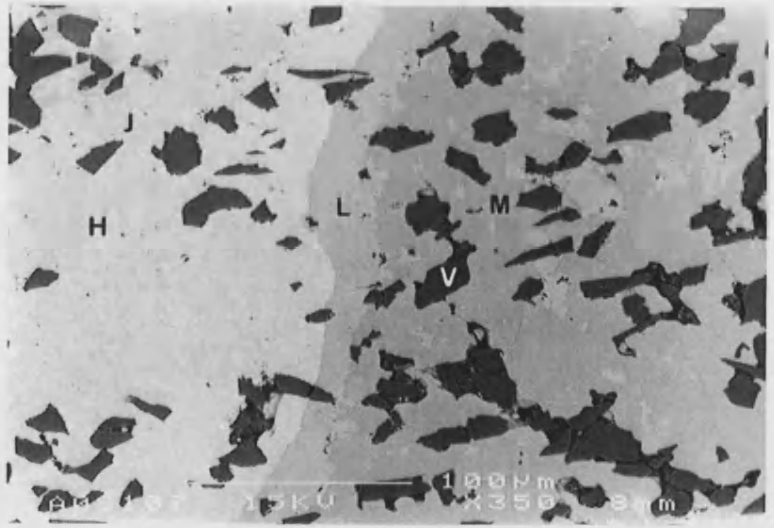

Figure 9.6a Microstructure of top and bottom of infiltrated preform
H-Ni rich, J-Ni_5Al_3, L-Ni_2Al_3, M-$NiAl_3$,V-Al_2O_3 100μm

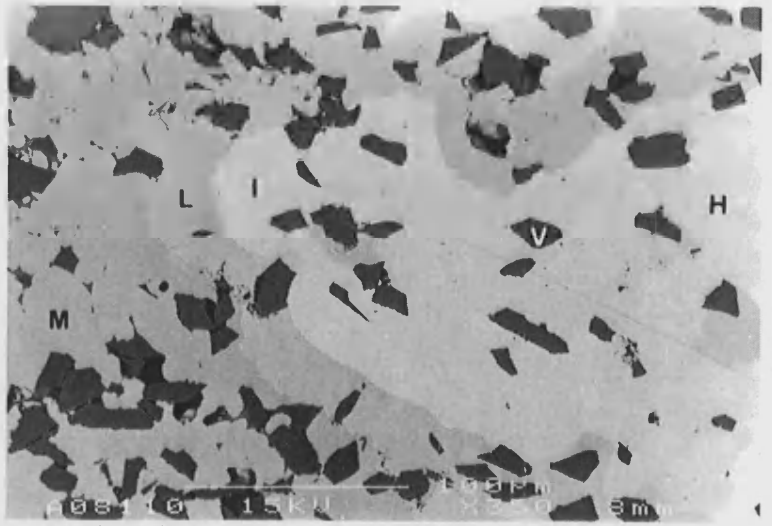

Figure 9.6b Microstructure of middle of infiltrated preform
H-Ni, I-Ni_3Al, L-Ni_2Al_3, M-$NiAl_3$, V-Al_2O_3 100μm

separate regions were examined in the infiltrated preform, a region near the top surface, one in the middle of the preform and one near the bottom surface.

The top surface of the compact contained five distinct phases, Figure 9.6a. Large regions of a dark phase (M) identified as $NiAl_3$ were surrounded by a layer of Ni_2Al_3 (L) and both were distributed throughout a matrix of nickel rich phases. This matrix contained the Ni_5Al_3 phase (J) and nickel rich cores along (H). The final phase (V) was the alumina reinforcement which had remained inert during the infiltration. EPMA also revealed the presence of a variety of compositions between the nickel and Ni_5Al_3 phases. No fixed composition was obtained and it was assumed that a thin Ni_3Al phase existed between the two. However, it was too thin to sample individually and varying quantities of the surrounding phases were also included in EPMA measurements.

There was a change in the phases present in the middle region, Figure 9.6b. The same dark phases of $NiAl_3$ (M) and Ni_2Al_3 (L) were present, but the matrix of nickel rich phases contained regions of Ni_3Al (I) and nickel rich cores (H). Alumina (V) was distributed throughout the region.

The phases in the bottom region were the same as those in the top, Figure 9.6a. The only noticeable difference was in an increase in the amount of $NiAl_3$ phase.

The alumina was uniformly distributed throughout the infiltrated preform and only a few agglomerations were found. Porosity measurements taken in the infiltrated preform were found to be low, less than 1.0% (SD 0.1%) and no gas pores were found, only a lack of consolidation of the matrix around alumina agglomerations. The large number of phases gave a wide variation in microhardness values, 330Hv (SD 150Hv). Macrohardness values were also varied, but the low porosity of the sample gave a similar average value of 359Hv (SD 150Hv).

9.4 Discussion

9.4.1 Fabrication of Porous Preforms

The preforms were required to withstand the infiltration pressure and retain their porosity long enough to allow sufficient aluminium to enter to form NiAl. The compressive strengths of the preforms were increased by compacting the powders

under higher pressures and by sintering at higher temperatures for longer times. However, this decreased the porosity.

The correct porosity was achieved in an unreinforced preform by lightly compacting the nickel and sintering it at a low temperature for a short time. But the resulting preform was powdery to the touch and easily damaged and it was thought that this would collapse during the infiltration. A reinforced preform, containing the correct porosity, was produced using a higher compaction pressure. This was used since it appeared to be more able to withstand the infiltration pressure.

An additional concern with the preforms was whether the porosity they contained was either connected or closed. This was difficult to deduce from the SEM images of the sintered preforms since they were only 2-D representations and the preparation had caused some smearing of the nickel which closed pores. Connected porosity was preferred since this would allow the aluminium to penetrate easily into the preform. Closed porosity would hinder infiltration, but it was hoped that if the molten aluminium would dissolve some of the nickel and open up further pores deeper into the preform.

9.4.2 Reactive Liquid Metal Infiltration

The liquid metal infiltration attempt only succeeded in forcing some of the aluminium into the preform and distributed the remainder around the apparatus. As aluminium infiltrated the preform it filled the porosity and reacted with the nickel. This reaction formed a liquid phase which prevented the channels between the pores from becoming blocked. However, since a greater proportion of the nickel reacted to form the liquid phase, the compressive strength of the preform was reduced and it began to collapse under the infiltration pressure. The combination of aluminium infiltration and preform collapse reduced the porosity and increased the pressure required to force further aluminium into the preform. At some point during the infiltration, this pressure exceeded the pressure required to force the aluminium around the plug and between the die and the end-plate.

The molten aluminium was able to travel around the plug at 700°C because thermal expansion had ruined the tolerances specified in the die design. The thermal expansion

end-plate. Thermal expansion was also responsible for the infiltrated preform becoming wedged in the die after it had cooled. The pressure caused the preform to expand radially to fill the diameter of the die at 700°C. During cooling, the die contracted around the preform as the silver steel had a larger coefficient of thermal expansion than the intermetallic phases in the preform.

The stresses produced in the die by this contraction may have caused the die bore to buckle. Another possibility was that the low yield strength of the steel at 700°C allowed the aluminium to deform the die as it was forced past the plug.

The actual mechanism of reactive infiltration of the preform was unclear as the thermocouple in the die wall was too distant from the reaction to measure any changes in temperature arising from an exothermic reaction. It was clear that the first aluminium entering the preform produced a reactive synthesis reaction with the nickel. This raised the temperature sufficiently to produce some liquid phase and kept the pores open for further infiltration of aluminium[85].

Only the correct amount of aluminium to form NiAl with the nickel and alumina preform was placed in the die. Therefore, the aluminium found below the die and above the plug indicated that the preform was rich in nickel. The lack of a single phase matrix suggested that the reactive infiltration was quenched before the reaction had continued to completion. This was brought about by a low rate of heat accumulation and a high rate of heat loss. The rate of heat accumulation was affected by an initially small area of reaction in the nickel rich preform as the aluminium infiltrated between the nickel particles. The rate of heat loss was increased by the surrounding metal die and the application of pressure to the preform. The pressure increased contact between the preform and the die walls and increased the thermal conductivity of the infiltrated preform.

An approximate reaction route was produced from a study of the phases formed during the infiltration and of the nickel-aluminium phase diagram, Figure 1.4. The initial aluminium entering the preform reacted with the nickel to form $NiAl_3$ and an aluminium rich liquid. The rate of heat loss from the compact was too great to allow the temperature to increase above the melting point of $NiAl_3$ and a layer of this intermetallic formed between the remaining nickel cores and the liquid phase. The

liquid was forced into the remaining pores where it formed $NiAl_3$ on any new nickel particles it encountered.

Once all the pores had either been filled with liquid or closed by the pressure, a significant amount of solid-state diffusion took place as the die cooled to room temperature. The die was allowed to cool in the furnace and coupled with its large mass, the preform took several hours to cool. The large area of contact between the small nickel particles and the $NiAl_3$ layer also promoted solid-state diffusion.

The top and middle regions formed Ni_5Al_3 when thin aluminium rich strips were sandwiched between two nickel cores. The intermediate compositions between the Ni_5Al_3 and the nickel cores indicated the presence of a layer of Ni_3Al, but his was too thin to resolve. The more porous regions of the original preform formed $NiAl_3$, since there were fewer nickel cores present to supply nickel. And an intermediate layer of Ni_2Al_3 was formed around them[86]. The aluminium took the longest time to reach the middle of the preform, which allowed the pressure to close a large number of pores before they could be infiltrated. This resulted in thinner strips of $NiAl_3$ between the nickel cores and solid-state diffusion was able to convert this to Ni_3Al as the preform cooled.

Since the alumina was still held by the unreacted nickel during the infiltration, it had little chance to be redistributed around the preform. The few agglomerations of alumina in the preform were not penetrated by the matrix and resulted in the only porosity in the sample. The hardness values reflected the low porosity of the sample and the range of phases in the matrix.

9.4.3 Summary

A preform containing the correct porosity to form NiAl was successfully produced by lightly compacting and sintering nickel and alumina powders. However, the preform was crushed by the infiltration pressure once the aluminium had started to react with nickel structure. This reduced the porosity of the preform and resulted in a nickel rich sample.

The reaction was quenched by the high rate of heat loss resulting from the surrounding die and the pressure applied. This formed a multiphase microstructure by a

nickel structure. This reduced the porosity of the preform and resulted in a nickel rich sample.

The reaction was quenched by the high rate of heat loss resulting from the surrounding die and the pressure applied. This formed a multiphase microstructure by a combination of liquid-state reactions, during infiltration and solid-state diffusion, as the die was cooled. The resulting sample was free from pores and possessed a uniform distribution of alumina.

The silver steel die lacked sufficient strength and stiffness at 700°C to withstand the stresses set up during the liquid metal infiltration. It also contracted around the preform which was impossible to remove without destroying the die.

A reduction in the infiltration pressure would have been beneficial. It would have reduced the loss of porosity in the preform and the rate of heat loss from the reaction. It would have also reduced the distortion of the die and prevented aluminium from escaping the reaction chamber. However, the pressure would have still needed to be sufficient to force the aluminium into the preform. A change in the die material to increase its strength and to insulate the reaction and a change in its design to allow easy removal of the preform would also have been preferable.

Section 10

SUMMARY AND FURTHER WORK

It was found that the formation of transition metal aluminides by a solid-state diffusion route was time consuming and resulted in a porous microstructure. A reactive synthesis route initiated a reaction between the reactants required to form the aluminide phase and used the energy released to sustain the reaction. A liquid phase was required during the reaction to allow liquid-state reactions to occur to rapidly form the aluminides. The correct quantities of well mixed reactants were required to form the desired aluminide phases.

Two reactive synthesis routes were investigated, these being the thermal explosion of powder compacts and the reactive infiltration of porous preforms. The extent of reaction was dependent on the rate of heat accumulation and the rate of heat loss. The rate of heat accumulation was affected by the energy available for release, the proportion of liquid formed, the dimensions of the reactants, the green density of the compact, the rate of heating and the application of pressure. The rate of heat loss was affected by the surroundings and the application of pressure. The porosity in the final materials was dependent on the initial density of the reactant mixtures, the amount of liquid formed during the reaction and the application of pressure during the reaction.

It was found that the nickel-aluminium system produced the highest extent of reaction and the lowest porosity. The small nickel powders and the large proportion of liquid formed by this system produced a large area of reaction, which increased the rate of heat accumulation and thus the extent of reaction. Also, the formation of the intermetallic phases was more exothermic than the other two systems investigated and this contributed to the higher rate of heat accumulation. The large proportion of liquid formed during the reactive synthesis reduced the final porosity.

The addition of reinforcing phases to the nickel and titanium-aluminium systems had differing effects. Alumina and carbon additions remained inert to the reactants and

diluted the reactions. This reduced the extent of reaction and increased the porosity of the final materials. Silicon carbide additions interacted with the reactants to form a variety of phases and increased the porosity of the final materials.

A method to introduce continuous reinforcements into a matrix was developed from a combination of a thermal explosion and a liquid metal infiltration. But the pressure used to infiltrate the preforms had to be limited to avoid quenching the thermal explosion. The pressure used in the reactive liquid metal infiltration also had to be limited to avoid crushing the porous preforms and reducing their porosity.

Several areas of this investigation may benefit from further work.

The thermal explosions in Section 6 need to be optimised for the iron and titanium-aluminium systems to produce homogeneous materials. This may be achieved by reducing the size of the transition metal powders, increasing the green density of the compacts, increasing the rate of heating of the compacts and reducing heat loss from the reactions. The porosities of all the final materials also need to be decreased. Porosities due to a lack of consolidation of the matrix may be reduced by increasing the proportion of liquid formed during the thermal explosion. But, the application of pressure to reduce porosity has to be carefully controlled to avoid quenching the reaction. A possible method of reducing gas porosity would be to degas the powders prior to the reaction.

The addition of alumina to the thermal explosions would also benefit from this work. The extent of reaction and the proportion of liquid formed in the titanium-aluminium compact need to be increased to form a lower porosity material. Whilst the proportion of liquid phase formed in the nickel-aluminium system needs to be reduced to avoid the uneven distribution of alumina particles. This may be achieved by adding more diluents to the reaction.

A careful balance of preform density and infiltration pressure has to be found in Section 8. A pressure high enough to infiltrate a continuous fibre preform without quenching the matrix forming reaction is required.

Finally, the reactive liquid metal infiltration route requires a large amount of additional work. A preform containing the correct porosity and able to withstand the infiltration pressures in the die is required. The rate of heat loss from the reaction between the

pressures in the die is required. The rate of heat loss from the reaction between the aluminium and the preform also has to be lowered to allow it to continue to completion. This may be accomplished by lowering the infiltration pressure and insulating the reaction. If the die is to be reused, the material and its design need to be altered to prevent it from being damaged when pressure is applied to the aluminium and to allow the infiltrated preform to be easily removed.

References

1 R.L.Fleischer. High-strength, high-temperature intermetallic compounds. Journal of Materials Science, (1987), vol.22, pp.2281-2288.

2 E.A.Feest and J.H.Tweed. Comparative viability of processing routes for intermetallic based materials. Materials Science and Technology, (1992), vol.8, pp.308-316.

3 F.H.Froes, C.Suryanarayana and D.Eliezer. Review: Synthesis, properties and applications of titanium aluminides. Journal of Materials Science, (1992), vol.27, pp.5113-5140.

4 D.M.Dimiduk, D.B.Miracle and C.H.Ward. Development of intermetallic materials for aerospace systems. Materials Science and Technology, (1992), vol.8, pp.367-375.

5 S.Naka, M.Thomas and T.Khan. Potential and prospects of some intermetallic compounds for structural appplications. Materials Science and Technology, (1992), vol.8, pp.291-298.

6 M.Taya and R.J.Arsenault. Metal matrix composites: thermomechanical behaviour. Oxford: Pergamon Press, 1989.

7 Y.W.Kim and F.H.Froes. The physical metallurgy of titanium aluminides. In: High Temperature Aluminides and Intermetallics, 1990, (S.H.Wang, C.T.Liu, D.P.Pope and J.O.Stiegler eds.), pp.465-492.

8 C.Koeppe, A.Bartels, J.Seeger and H.Mecking. General aspects of the thermomechanical treatment ot two-phase intermetallic TiAl compounds. Metallurgical Transactions A, (1993), vol.24A, pp.1795-1806.

9 C.T.Liu and K.S.Kumar. Ordered intermetallic alloys, part 1: nickel and iron aluminides. JOM, (1993), vol.45, pp.38-44.

10 U.Prakash, R.A.Buckley, H.Jones and C.M.Sellars. Structure and properties of ordered intermetallics based on the Fe-Al system. ISIJ International, (1991), vol.31, pp.1113-1126.

11 D.Hull and D.J.Bacon. Introduction to dislocations, 3rd ed. Oxford: Pergamon Press, 1984.

12 K.S.Kumar and G.Bao. Intermetallic-matrix composites: an overview. Composites Science and Technology, (1994), vol.58, pp.1-24.

13 D.L.Joslin, D.S.Easton, C.T.Liu, S.S.Babu and S.A.David. Processing of Fe_3Al and FeAl alloys by reaction synthesis. Intermetallics, (1995), vol.3, pp.467-481.

14 C.C.Wang and S.A.Akbar. Diffusion in ordered alloys and intermetallic compounds. Acta Metallurgica, (1993), vol.41, pp-2807-2813.

15 Y.Kim. Intermetallic alloys based on γ titanium aluminide. JOM, (1989), vol.41, pp.24-30.

16 H.E.Maupin and J.C.Rawers. Metal-intermetallic composites formed by reaction-sintering elemental powders. Journal of Materials Science Letters, (1993), vol.12, pp.540-541.

17 J.C.Rawers and H.E.Maupin. Metal-intermetallic composites formed by reaction sintering metal foils. Journal of Materials Science Letters, (1993), vol.12, pp.637-639.

18 M.E.Eberhart, D.P.Clougherty and J.M.Maclaren. Bonding-property relationships in intermetallic alloys. Journal of Materials Research, (1993), vol.8, pp.438-448.

19 W.O.Soboyejo, K.T.Venkateswara Rao, S.M.L.Sastry and R.O.Ritchie. Strength, fracture and fatigue behaviour of advanced high-temperature intermetallics reinforced with ductile phases. Metallurgical Transactions A, (1993), vol.24A, pp.585-600.

20 E.W.Collings. The physical metallurgy of titanium alloys. Metals Park, Ohio: American Society for Metals, 1984.

21 W.Betteridge. The Nimonic alloys. London: Edward Arnold, 1959.

22 J.H.Westbrook and R.L.Fleischer eds. Intermetallic compounds: principles and practices. Chichester: John Wiley and Sons, 1994.

23 J-P.Lebrat, A.Varma and P.J.McGinn. Mechanistic studies in combustion synthesis of Ni_3Al and Ni_3Al-matrix composites. Journal of Material Reserves, (1994), vol.9, pp.1184-1192.

24 G.Sauthoff. Creep of intermetallics. Materials Science and Technology, (1992), vol.8, pp.363-366.

25 B.H.Rabin and R.N.Wright. Microstructure and tensile properties of Fe_3Al produced by combustion synthesis/hot isostatic pressing. Metallurgical Transactions A, (1992), vol.23A, pp.35-40.

26 C.T.Liu and C.G.McKamey. Environmental embrittlement - a major cause for low ductility of ordered intermetallics. In: High Temperature Aluminides and Intermetallics, 1990, (S.H.Wang, C.T.Liu, D.P.Pope and J.O.Stiegler eds.), pp.133-151.

27 C.A.Hippsley and M.Strangwood. Embrittlement and crack growth in high temperature intermetallics. Materials Science and Technology, (1992), vol.8, pp.350-358.

28 M.Hansen. Constitution of binary alloys. New York: Mcgraw-Hill Book Company, 1958.

29 O.Klein and I.Baker. Effect of heat treatment on the tensile behaviour of iron-rich FeAl and FeAl+B. Scripta Metallurgica et Materialia, (1994), vol.30, pp.627-632.

30 N.S.Stoloff. Toughening mechanisms in intermetallics. Metallurgical Transactions A, (1993), vol.24A, pp.561-567.

31 J.R.Knibole, R.N.Wright, C.L.Trybus and V.K.Sikka. Microstructure and mechanical properties of Fe_3Al alloys with chromium. Journal of Materials Science, (1993), vol.28, pp.2040-2048.

32 C.Barrett and T.B.Massalski. Structure of metals. 3rd revised ed. Oxford: Pergamon Press,1980.

33 D.B.Miracle. Overview No.104: The Physical and Mechanical Properties of NiAl. Acta Metallurgica, (1993), vol.41, pp.649-684.

34 D.E.Alamn and N.S.Stoloff. Powder fabrication of monolithic and composite NiAl. The International Journal of Powder Metallurgy, (1991), vol.27, pp.29-41

35 C.Nishimura and C.T.Liu. Reactive sintering of Ni_3Al under compression. Acta Metallurgica et Materialia, (1993), vol.41, pp.113-120.

36 K.J.Hemker and W.D.Nix. High-temperature creep of the intermetallic alloy Ni_3Al. Metallurgical Transactions A, (1993), vol.24A, pp.335-341.

37 T.Cheng. Effects of refined microstructures on ductility and toughness at room temperature in nickel-rich NiAl. Journal of Materials Science, (1993), vol.28, pp.5909-5916.

38 M.Chen, S.Patu, J.N. Shen and C.X.Shi. Effects of chromium ion implantation on the oxidation of Ni_3Al. Journal of Materials Research, (1993), vol.8, pp.734-735.

39 M.Yamaguchi. High temperature intermetallics - with particular emphasis on TiAl. Materials Science and Technology, (1992), vol.8, pp.299-307.

40 T.Khan, P.Caron and S.Naka. Mechanical behaviour of Ni_3Al-based intermetallics and the need for designing multiphase alloys. In: High Temperature Aluminides and Intermetallics, 1990, (S.H.Wang, C.T.Liu, D.P.Pope and J.O.Stiegler eds.), pp.219-241.

41 M.W.Brumm and H.J.Grabke. Oxidation behaviour of NiAl-II. Cavity formation beneath the oxide scale on NiAl of different stoichiometeries. Corrosion Science, (1993), vol.34, pp.547-561.

42 M.W.Brumm, H.J.Grakabe and B.Wagemann. The oxidation of NiAl-III. Internal and intergranular oxidation. Corrosion Science, (1994), vol.36, pp.37-53.

43 H.J.Grabke, M.Brumm and M.Steinhorst. Development of oxidation resistant high temperature intermetallics. Materials Science and Technolgy, (1992), vol.8, pp.339-344.

44 G.H.Meier and F.S.Pettit. High temperature oxidation and corrosion of intermetallic compounds. Materials Science and Technology, (1992), vol.8, pp.331-338.

45 L.H.Edelson and R.O.Ritchie. Microstructural characterisation of $\alpha_2 + \beta_2$ titanium aluminide intermatallic (super α_2) using transmission electron microscopy. Materials Science and Engineering A, (1990), vol.130, pp.193-203.

46 J.Subrahmanyam. Cyclic oxidation of aluminised Ti-14Al-24Nb alloy. Journal of Materials Science, (1988), vol.23, pp.1906-1910.

47 J.Nack, J.Y.Kim and W.S.Cho. Morphological effect on the mechanical behaviour of a two-phase Ti_3Al-Nb alloy. Metallurgical Transactions A, (1993),vol.24A, pp.1785-1793.

48 R.Gnanamoorthy, Y.Mutoh, N.Masahashi and M.Matsuo. High temperature strength and fracture toughness in γ titanium aluminides. Journal of Materials Science, (1993), vol.28, pp.6631-6638.

49 H.H.Tian, Z.Huang and C.Q.Chen. Stability of lamellar structure in a Ti-47.8at%Al alloy. Scripta Metallurgica et Materialia, (1994), vol.30, pp.165-168.

50 K.Taguchi, M.Ayada, K.N.Ishihara and P.H.Shingu. Near-net shape processing of TiAl intermetallic compounds via pseudoHIP-SHS route. Intermetallics, (1995), vol.3, pp.91-98.

51 J.C.Rawers and W.Wrzesinski. Heat treatment of reaction-sintered hot-pressed TiAl. Scripta Metallurgica et Materialia, (1990), vol.24, pp.1985-1990.

52 P.Pouly, M.Hua, C.I.Garcia and A.J.DeArdo. Isothermal transformation behaviour of near γ TiAl alloys. Scripta Metallurgica et Materialia, (1993), vol.29, pp.1529-1534.

53 D.L.Davidson and J.B.Campbell. Fatigue crack growth through the lamellar microstructure of an alloy based on TiAl at 25°C and 800°C. Metallurgical Transactions A, (1993), vol.24A, pp.1555-1574.

54 D.I.Kimm and J.Wolfenstine. Effect of grain size on the creep behaviour of fully transformed γ-TiAl. Scripta Metallurgica et Materialia, (1994), vol.30, pp.615-619.

55 R.W.Hayes and P.A.McQuay. A first report on the creep deformation and damage behaviour of a fine grained fully transformed lamellar γ TiAl alloy. Scripta Metallurgica et Materialia, (1994), vol.30, pp.259-264.

56 C.H.Ward, J.C.Williams and A.W.Thompson. Dynamic environmental embrittlement of an α_2 titanium aluminide. Scripta Metallurgica et Materialia, (1993), vol.28, pp.1017-1021.

57 J.Subrahmanyam. Cyclic oxidation of aluminised Ti-14Al-24Nb alloy. Journal of Materials Science, (1988), vol.23, pp.1906-1910.

58 A.Gil, H.Hoven, E.Wallura and W.J.Quadakkers. The effect of microstructure on the oxidation behaviour of TiAl-based intermetallics. Corrosion Science, (1993), Vol.34, pp.615-630.

59 E.A.Brandes ed. Smithells metals reference book. 6th ed. London: Butterworths, 1983.

60 A.R.West. Solid state chemistry and its applications. Chichester: John Wiley and Sons, 1984.

61 C.T.Liu and Y-W.Kim. Room-temperature environmental embrittlement in a TiAl alloy. Scripta Metallurgica et Materialia, (1992), Vol.27, pp.599-603.

62 Kwai and S.Chan. Hydrogen tolerance of a Ti_3Al based alloy. Metallurgical Transactions A, (1993), vol.24A, pp.1095-1105.

63 J.Subrahmanyam, M.Vijaykumar and S.Ranganath. Thermochemistry of self propagating high temperature synthesis of titanium diboride composites. Metals Materials and Processes, (1989), vol.1, pp.105-112.

64 J.Lebrat and A.Varma. Self-propagating high-temperature synthesis of Ni_3Al. Combustion Science and Technology, (1992), vol.88, pp.211-221.

65 M.Atzmon. The effect of interfacial diffusion barriers on the ignition of self-sustained reactions in metal-metal diffusion couples. Metallurgical Transactions A, (1992), vol.23A, pp.49-53.

66 S.Ranganath, M.Vijayakumar and J.Subrahmanyam. Combustion-assisted synthesis of Ti-TiB-TiC composite via the casting route. Materials Science and Engineering, (1992), vol.A149, pp.253-257.

67 J.B.Holt and Z.A.Munir. Combustion synthesis of titanium carbide: theory and experiment. Journal of Materials Science, (1986), vol.21, pp.251-259.

68 H.C.Yi and J.J.Moore. Self-propagating high-temperature (combustion) synthesis (SHS) of powder-compacted materials. Journal of Materials Science, (1990), vol.25, pp.1159-1168.

69 S.Miura and C.T.Liu. Effects of aluminium concentration and compact thickness on reaction synthesis of Ni_3Al-NiAl alloys. Intermetallics, (1994), vol.2, pp.297-313.

70 H.C.Yi, A.Petric and J.J.Moore. Effect of heating rate on the combustion synthesis of Ti-Al intermetallic compounds. Journal of Materials Science, (1992), vol.27, pp.6797-6806.

71 S.Ranganath, T.L.Prakash and J.Subrahmanyam. Synthesis of iron aluminide under thermal explosion conditions. Materials Letters, (1990), vol.10, pp.215-217.

72 D.C.Dunand. Reactive synthesis of aluminide intermetallics. Materials and Manufacturing Processes, (1995), vol.10, pp.373-403.

73 W.R.Wrzesinski and J.C.Rawers. Self-propagating high-temperature synthesis of Ti-Al-SiC and Ti-Al-Al_2O_3 intermetallic composites. Journal of Materials Science Letters, (1990), vol.9, pp.432-435.

74 B.M.Vol'pe, D.AGarkol', V.V.Evstignee and A.B.Mukhachev. Interaction of the nickel-aluminium system in an SHS process studied by means of high-temperature brightness pyrometry. Combustion, Explosion and Shock Waves, (1994), vol.30, no.3, pp.319-325.

75 M.V.Fedorishcheva, V.P.Lyubivoi, V.E.Ovcharenko, L.I.Trishkina, B.S.Semukhin, Y.A.Sazanov and E.V.Kozlov. Compositon and fine structure of an intermetallic prepared by the SHS method. Powder Metallurgy and Metal Ceramics, (1993), vol.32, pp.501-504.

76 J.Lebrat and A.Varma. Self-propagating high-temperature synthesis of Ni_3Al. Combustion Science and Technology, (1992), vol.88, pp.211-221.

77 K.A.Philpot, Z.A.Munir and J.B.Holt. An investigation of the synthesis of nickel aluminides through gasless combustion. Journal of Materials Science, (1987), vol.22, pp.159-169.

78 J.B.Holt and S.D.Dunmead. Self-heating synthesis of materials. Annual Review of Materials Science, (1991), vol.21, pp.305-334.

79 D.L.Joslin, D.S.Easton, C.T.Liu and S.A.David. The effects of varaibles on reaction synthesis of Fe-Al alloys. Materials Research Society Symposium Proceedings, (1995), vol.364, pp.103-108.

80 A.Bose, B.Moore, R.M.German and N.S.Stoloff. Elemental approaches to Ni_3Al-matrix composites. Journal of Metals, (1988), vol.40, pp.14-17.

81 J.C.Rawers, J.S.Hansen, D.E.Alamn and J.A.Hawk. Formation of sheet metal-intemetallic composites by self-propagating high-temperature reactions. Journal of Materials Science Letters, (1994), vol.13, pp.1361-1363.

82 D.E.Alman, J.A.Hawk, A.V.Petty and J.C.Rawers. Processing intermetallic composites by self-propagating, high-temperature synthesis. Journal of Metals, (1994), March, pp.31-35.

83 D.C.Dunand, J.L.Sommer and A.Mortenesen. Reactive infiltration of nickel preforms with molten aluminium. Processing and Fabrication of Advanced Materials for High Temperature Applications-II. V.A.Ravi and T.S.Srivatsan eds. Warrendale, PA: The Minerals, Metals and Materials Society, 1993.

84 H.Fukunaga, X.Wang and Y.Aramaki. Preparation of intermetallic compound matrix composites by reaction squeeze casting. Journal of Materials Science Letters, (1990), vol.9, pp.23-25.

85 H.Chen, M.Kaya and R.W.Smith. Near net-shape long fibre reinforced intermetallic matrix composites produced by reactive infiltration process. Materials Letters, (1992), vol.13, pp.180-183.

86 D.C.Dunand, J.L.Sommer and A.Mortensen. Synthesis of bulk and reinforced nickel aluminides by reactive infiltration. Metallurgical Transactions A, (1993), vol.24A, pp.2161-2170.

87 I.Song and N.N.Thadhani. Shock-induced chemical reactions and synthesis of nickel aluminides. Metallurgical Transactions A, (1992), vol.23A, pp.41-48.

88 A.Bose, B.Moore, R.M.German and N.S.Stoloff. Elemental approaches to Ni_3Al-matrix composites. Journal of Metals, (1988), vol.40, pp.14-17.

89 D.L.Joslin, D.S.Easton, C.T.Liu and S.A.David. Reaction synthesis of Fe-Al alloys. Materials Science and Engineering A, (1995), vol. 192/193, pp.544-548.

90 R.M.German and R.G.Iacocca. Powder processing of intermetallics and intermetallic matrix composites. Processing and Fabrication of Advanced Materials for High Temperature Applications-II, V.A.Ravi and T.S.Srivatasan eds. Warrendale, PA: The Minerals, Metals and Materials Society, 1993.

91 S.B.Margolis. The asymptotic theory of gassless combustion synthesis. Metallurgical Transactions A, (1992), vol.23A, pp.15-22.

92 C.Hu and T.N.Baker. The liquid volume control in the ISM process applied to the Al-Fe system. Acta Metallurgica et Materialia, (1994), vol.42, pp.51-56.

93 G.X.Wang, M.Dahms, G.Leitner and S.Schultrich. Titanium aluminides from cold-extruded elemental powders with Al-contents of 25-75at% Al. Journal of Materials Science, (1994), vol.29, pp.1847-1853.

94 J-P.Lebrat, A.Varma and A.E.Miller. Combustion synthesis of Ni_3Al and Ni_3Al-matrix composites. Metallurgical Transactions A, (1992), vol.23A, pp.69-76.

95 D.M.Matson and Z.A.Munir. Combustion synthesis of intermetallic compounds usind titanium, nickel and copper wires. Materials Science and Engineering, (1992), A135, pp.700-705.

96 R.Armstrong. Theoretical models for the combustion of alloyable materials. Metallurgical Transactions A, (1992), vol.23A, pp.2339-2347.

97 Z.A.Munir. Reaction synthesis processes: mechanisms and characteristics. Metallurgical Transcations A, (1992), vol.23A, pp.7-13.

98 M.G.Lakshimikantha, A.Bhattacharya and J.A.Sekhar. Numerical modelling of solidification combustion synthesis. Metallurgical Transactions A, (1992), vol.23A, pp.23-34.

99 S.Sampath, S.Khatri, E.Shtessel and M.Koczak. Reactive processing of nickel based metal matrix composites. Processing and Fabrication of Advanced Materials for High Temperature Applications - II, V.A.Ravi and T.S.Srivatasan eds. Warrendale, PA: The Minerals, Metals and Materials Society, 1993.

100 J.J.Moore, D.W.Readey, H.J.Feng, K.Monroe and B.Mishra. The combustion synthesis of advanced materials. Jornal of the Minerals, Metals and Materials Society, (1994), vol.46, pp.72-78.

101 J.R.W.Warn. Concise chemical thermodynamics: in SI units. London: Van Nostrand Reinhold (Int.), 1988.

102 D.Palmer. Heat treatment of 7475 aluminium alloy for golf club shafts. BP internal report, (1992).

103 D. Loty and R.Abbaschian. Reactive hot compaction and "in-situ" reinforcement coating for intermetallic matrix composites. In: Ceramic Matrix Composites and Other Systems - proceedings of the Ninth International Conference on Composite Materials (ICCM/9): Madrid, 1993, (A.Miravete ed.), pp.891-905.

104 K.S.Chan. Toughening mechanisms in titanium aluminides. Metallurgical Transactions A, (1993), vol.24A, pp.569-583.

105 S.Nourbakhash and H.Margolin. Fabrication of high temperature fiber reinforced intermetallic matrix composites. In: Metal & Ceramic Matrix Composites: Processing, Modeling and Mechanical Behaviour, 1990, (R.B.Bhagat, A.H.Clauer, P.Kumar and A.M.Ritter eds.), pp.75-89.

106 S.K.Mukherjee and G.P.Khanra. Development of nickel aluminide - carbon fibre intermetallic composite by reaction sintering. Journal of Material Science Letters, (1991), vol.10, pp.1222-1224.

107 A.K.Misra. Modification of the fiber/matrix interface in aluminide-based intermetallic-matrix composites. Composites Science and Technology, (1993), vol.50, pp.37-48.

108 K.S.Kumar and J.D.Whittenberger. Discontinuously reinforced intermetallic matrix composites via XD synthesis. Materials Science and Technology, (1992), vol.8, pp.317-330.

109 S.M.Jeng, J.M.Yang and J.A.Graves. Effect of fibre coating on the mechanical behaviour of SiC fibre-reinforced titanium aluminide composites. Journal of Materials Research, (1993), vol.8, pp.905-916.

110 E.A.Feest. Interfacial phenomena in metal-matrix composites. Composites, (1994), vol.25, pp.75-86.

111 R.A.Mackay, S.L.Draper, A.M.Ritter and P.A.Siemers. A comparison of the mechanical properties of intermetallic matrix composites fabricated by two different methods. Metallurgical and Materials Transactions A, (1994), vol.25A, pp.1443-1455.

112 S.Nourbakhsh and H.Margolin. Processing of continuous-ceramic-fibre-reinforced intermetallic composites by pressure casting. Materials Science and Engineering, (1991), vol.A144, pp.133-141.

113 P.S.Korinko and D.J.Duquette. The thermal stability of TiB_2 in Ni-43at%Al. Scripta Metallurgica et Materialia, (1994), vol.30, pp.287-290.

114 J.D.Rigney and J.J.Lewandowski. Chemical stability of titanium diboride reinforcement in nickel aluminide matrices. Journal of Materials Science, (1993), vol.28, pp.3911-3922.

115 G.L.Povrik, J.A.Horton, C.G.Mckamey, T.N.Tiegs and S.R.Nutt. Interfaces in nickel aluminide/alumina fibre composites. Journal of Materials Science Letters, (1988), vol.23, pp.3945-3950.

116 R.M.German and A.Bose. Fabrication of intermetallic matrix composites. Materials Science and Engineering, (1989), vol.A107, pp.107-116.

117 T.C.Chou. Interfacial reactions between Ni_3Al and SiC. Scripta Metallurgica et Materialia, (1990), vol.24, pp.409-414.

118 H.Mabuchi, H.Tsuda and Y.Nakayama. Combustion synthesis of TiAl-matrix composites in the Ti-Al-BN system. Scripta Metallurgica et Materialia, (1995), vol.32, pp.253-257.

119 J.C. Rawers and W.R. Wrzesinski. Melt infiltration of selected intermetallics into SiC. Journal of Materials Science Letters, (1990), vol.9, pp.503-505.

120 T.F.Stephenson, J.A.E.Bell and J.Roy. Nickel-coated carbon fibre preforms for metal matrix composites. Internal report for INCO Ltd.

121 M.Dahms, F.Schmelzer, J.Seeger and B.Wildhagen. Microstructure and mechanical properties of gamma base titanium aluminide produced from extruded elemental powders. Materials Science and Technology, (1992), vol.8, pp.359-362.

122 C.T.Liu, E.H.Lee, E.P.George and A.J.Duncan. Intergranular fracture tendency in NiAl doped with boron and carbon. Scripta Metallurgica et Materialia, (1994), vol.30, pp.387-392.

123 P.J.Goodhew and F.J.Humphreys. Electron microscopy and analysis. 2nd ed. London: Taylor & Francis, 1988.

124 R.E.Reed-Hill. Physical Metallurgy Principals. 2nd ed. New York: D.Van Nostrand Company, 1973.

125 S.B.Jung, Y.Minamino, T.Yamane and S.Saji. Reaction diffusion and formation of Al_3Ni and Al_3Ni_2 phases in the Al-Ni system. Journal of Materials Science Letters, (1993), vol.12, pp.1684-1686.

126 M.M.P.Janssen. Diffusion in the nickel-rich part if the Ni-Al system at 1000C to 1300C; Ni3Al layer growth, diffusion coefficients and interface concentrations. Metallurgical Transactions, (1973), vol.4, pp.1625-1633.

127 F.N.Rhines. Phase diagrams in metallurgy: their development and application. New York: Mcgraw-Hill Book Company, 1956.

128 I.J.Polmear. Light alloys: metallurgy of the light metals. 2nd ed. London: Edward Arnold, 1989.

129 V.B.Rao and C.R.Houska. Reactions and diffusion between an Al film and a Ti substrate. Metallurgical Transactions A, (1983), vol.14A, pp.61-66.

130 A.K.Sarkhel and L.L.Seigle. Interdiffusion coefficients in the Ni_2Al_3 (γ) phase of the Ni-Al system. Metallurgical Transactions A, (1982), vol.13A, pp.1313-1314.

131 A.J.Hickl and W.R.Heckel. Kinetics of phase layer growth during aluminide coating of nickel. Metallurgical Transactons A, (1975), vol.6A, pp.431-440.

132 S.Shankar and L.L.Seigle. Inter-diffusion and intrinsic diffusion in the NiAl (δ) phase of the Ni-Al system. Metallurgical Transactions A, (1978), vol.9A, pp.1467-1476

133 D.L.Joslin, D.S.Easton, C.T.Liu and S.A.David. The effects of variables on reaction synthesis of Fe-Al alloys. Materials Research Society Symposium Proceedings, (1995), vol.364, pp.103-108.

134 B.Zhang, J.Wang, X.Wan and W.Chen. A study of the β and Ω phases in a Ti-Al-Cr alloy. Scripta Metallurgica et Materialia, (1994), vol.30, pp.399-404.

135 I.Barin, O.Knacke and O.Kubaschewski. Thermochemical properties of inorganic substances: 1977 supplement. Berlin: Springer-Verlag, 1977.

136 Hultgern, Desai, Hawkins, Gleiser and Kelley. Selected values of the thermodynamic properties of binary alloys. Ohio: American Society of Metals, 1973.

137 C.H.Henager and J.L.Brimhall. Solid state displacement reaction synthesis of interpenetrating-phase Ni-Al/Al_2O_3 composites. Scripta Metallurgica et Materialia, (1993), vol.29, pp.1597-1602.

Appendix A. Alphabetical Designation of Phases

A list of the letters used to identify the phases encounterd in this investigation is provided below.

A	-	Al
B	-	Fe
C	-	$FeAl_3$
D	-	FeAl
E	-	$FeAl_2$
F	-	Fe_2Al_5
G	-	$FeAl_3$
H	-	Ni
I	-	Ni_3Al
J	-	Ni_5Al_3
K	-	NiAl
L	-	Ni_2Al_3
M	-	$NiAl_3$
N	-	Ti
O	-	Ti_3Al
P	-	$TiAl/Ti_3Al$
Q	-	TiAl
R	-	$TiAl_2$
S	-	$TiAl_3$
T	-	$Ti_4Al_2C_2$
U	-	Ti_5Si_3
V	-	Al_2O_3
W	-	SiC
X	-	C

Appendix B. Alloying Elements

The tables below display details of the alloying elements which have been added to the XAl and X_3Al iron, nickel and titanium aluminides.

Alloying Elements	Compound	Effect	References
B	FeAl	Increases grain boundary strength and ductility	9,10,30,122
C	Fe_3Al	Reduces ductility	10
Cr	Fe_3Al	Increases ductility and fracture strength, reduces yield strength and environmental sensitivity	10,25,30,31
Mo	FeAl	Increases elevated temperature strength / reduces ductility	9,10
Mo	Fe_3Al	Increases elevated temperature strength / reduces ductility	9,10,31
Nb	Fe_3Al	Increases elevated temperature strength / reduces ductility	9,31
Si	Fe_3Al	Increases elevated temperature strength / reduces ductility	10,31
Ti	Fe_3Al	Increases elevated temperature strength	10
Zr	FeAl	Increases yield strength	10

Alloying additions to FeAl and Fe_3Al

Alloying Elements	Compound	Effect	References
B	NiAl	Increases strength	26
B	NiAl	Reduces ambient temperature intergranular fracture	9
B	Ni_3Al	Suppresses intergranular fracture and increases ambient temperature ductility	4,5,26,27,30, 39,40,122
Be	Ni_3Al	Increases ambient temperature ductility	26
C	NiAl	Increases strength	33
Cr	NiAl	Promotes surface alumina formation	33,44
Cr	NiAl	Changes ambient temperature fracture mode from intergranular to transgranular	30
Cr	Ni_3Al	Reduces high temperature embrittlement by oxygen, thus increasing ductility	9,26,38,40
Fe	NiAl	Increases UTS	33
Fe	NiAl	Increases ambient temperature ductility	30
Fe	Ni_3Al	Increases ambient temperature ductility	9
Fe	Ni_3Al	Improves hardness and corrosion resistance	9
Ga	NiAl	Increases UTS and ambient temperature ductility	33
Hf	NiAl	Increases oxidation resistance	9
Hf	NiAl	Improves creep resistance	9
Hf	Ni_3Al	Increases strength	9
Mn	Ni_3Al	Increases UTS	26
Mo	NiAl	Increases UTS	9,33
Mo	NiAl	Increases ambient temperature ductility	9,33
Y	NiAl	Increases oxidation resistance by improving adherence of oxide scale	9,33
Zr	NiAl	Increases tensile and creep strength	9
Zr	NiAl	Improves adherence of oxide scale and thus oxidation resistance	9,33
Zr	Ni_3Al	Increases strength	9
Zr	Ni_3Al	Increases grain boundary cohesion, but increases environmental embrittlement	9

Alloying additions to NiAl and Ni_3Al

Alloying Elements	Compound	Effect	References
B	Ti_3Al	Controls grain size	3
C	TiAl	Reduces ductility	15,27
C	TiAl	Increases creep strength	7,15
Cr	TiAl	Increases ductility	3,8,15,30,39,7
Cr	TiAl	Increases fracture toughness	48
Cr	TiAl	Reduces oxidation resistance	7,15,134
Cr	Ti_3Al	Increases strength	3,7
Er	TiAl	Lowers ductile/brittle transition temperature	27
H_2	Ti_3Al	Increases strength but reduces ductility and fracture toughness	3
Hf	TiAl	Reduces ductility	7,15
Mn	TiAl	Increases ductility	3,7,8,15,30
Mn	TiAl	Reduces oxidation resistance	7,15
Mo	TiAl	Improves oxidation resistance	3,39
Mo	Ti_3Al	Improves oxidation resistance	3,7
Mo	Ti_3Al	Increases strength and ductility	3
Mo	Ti_3Al	Increases creep strength but reduces fracture toughness	3,7
N	TiAl	Reduces ductility	27
Nb	TiAl	Reduces ductility	7,15
Nb	TiAl	Increases strength	3,7
Nb	TiAl	Improves oxidation resistance	3,7,8,15,39
Nb	Ti_3Al	Increases ambient temperature ductility	3,27,47
Nb	Ti_3Al	Increases strength	7
Nb	Ti_3Al	Improves oxidation resistance	3,7,57
Nb	Ti_3Al	Increases creep strength and fracture toughness	3,7
O_2	TiAl	Reduces ductility	3,15,27
O_2	Ti_3Al	Increases ambient and intermediate strengths but lowers ductility	3,7

Alloying additions to TiAl and Ti_3Al (continued overleaf)

Alloying Elements	Compound	Effect	References
Si	TiAl	Improves oxidation resistance	39
Si	Ti_3Al	Increases creep strength	3,7
Ta	TiAl	Reduces ductility	7,15
Ta	TiAl	Increases strength	3,7
Ta	TiAl	Improves oxidation resistance	3,7,8,15
Ta	Ti_3Al	Improves oxidation resistance	3,7
Ta	Ti_3Al	Increases strength and ambient temperature ductility	3,7
V	TiAl	Increases ductility	3,7,8,15,30
V	TiAl	Decreases oxidation resistance	7,15
V	Ti_3Al	Increases ambient temperature ductility	3
W	TiAl	Reduces ductility	7,15
W	TiAl	Improves oxidation resistance	7,8,15
W	TiAl	Increases creep strength	7,15
W	Ti_3Al	Improves oxidation resistance	57
Y	Ti_3Al	Controls grain size	3
Y	TiAl	Lowers ductile/brittle transition temperature	27
Zr	TiAl	Reduces ductility	7,15
Zr	Ti_3Al	Increases strength and ductility	3
Zr	Ti_3Al	Increases creep resistance	3,7

Alloying additions to TiAl and Ti_3Al

Appendix C. Thermodynamic Calculations

The thermodynamic calculations in Section 1.4 were used to produce plots of adiabatic temperature and molar fraction of molten product against initial reactant temperature. A brief explanation of the calculations for these plots is given below. The thermodynamic data used in the following equations, are included at the end of this section.

NiAl Formed at the Initiation Temperature

The thermal explosions were initiated once a liquid phase was formed and the lowest temperature that this occurred in the nickel-aluminium system was 639.9°C. The enthalpy of formation of NiAl at this temperature, $\Delta H_{f,912.9}(NiAl)$, was calculated using equation (5):

$$\Delta H_{f,912.9}(NiAl) = \Delta H_{f,298}(NiAl) + \int_{298}^{912.9}[C_p(NiAl) - C_p(Ni) - C_p(Al)]dT + [-L(Ni)_{ss}]$$

All temperatures have been converted to Kelvin and nickel undergoes a solid/solid phase transformation at 630K.

To calculate the adiabatic temperature, T_{ad}, for varying quantities of alumina reinforcement, equation (9) was used:

$$-\Delta H_{f,912.9} = (1-x)\left[\int_{912.9}^{Tad} C_p(NiAl)dT + \nu L_m(NiAl) + \int_{Ts}^{912.9}[C_p(Ni) + C_p(Al)]dT + \underset{Ts<630}{L}(Ni)_{ss}\right] + x\left[\int_{Ts}^{Tad} C_p(Al_2O_3)dT\right]$$

The solid/solid transformation temperature for nickel was only included if the initial temperature of the reactants, T_s, was less than 630K. Initially ν was set at zero and T_{ad} was calculated using an iterative method on a spreadsheet. Once T_{ad} reached 1913K, the melting point of NiAl, then T_{ad} was set at 1913K and ν was calculated as the extra energy available began to melt the NiAl. When ν reached a value of one, all

the NiAl had been melted, and the temperature of the melt was raised. The new T_{ad} was calculated by setting ν to a value of one and using an iterative method.

NiAl Formed at its Melting Point

The melting point of NiAl is 1913K and $\Delta H_{f,1913}(NiAl)$ was calculated using:

$$\Delta H_{f,1913}(NiAl) = \Delta H_{f,298}(NiAl) + \int_{298}^{1913}[C_p(NiAl) - C_p(Ni) - C_p(Al)]dT + [-L(Ni)_{ss}] + [-L(Ni)_m - L(Al)_m]$$

Both reactants are molten at 1913K and their enthalpies of melting were included. The enthalpy of melting of NiAl was not included as it was assumed that solid NiAl was formed and the energy generated was used to melt it.

Equation (10) was used to calculate the adiabatic temperatures and molar fraction of molten NiAl formed:

$$-\Delta H_{f,1913}(NiAl) = (1-x)\left[\int_{1913}^{Tad} C_p(NiAl)dT + \nu L(NiAl)_m + \int_{Ts}^{1913}[C_p(Ni) + C_p(Al)]dT + \underset{Ts<630}{L}(Ni)_{ss} + L(Ni)_m + L(Al)_m\right] + x\left[\int_{Ts}^{Tad} C_p(Al_2O_3)dT\right]$$

Once again, the enthalpy of the solid/solid transformation in nickel was only included if T_s was less than 630K. T_{ad} was calculated by initially setting ν to zero. If T_{ad} was less than 1913K, then the reaction was not self-sustaining as the reactants were not raised to the formation temperature of NiAl. ν and T_{ad} values greater than 1913K were calculated as before.

TiAl Formed at the Initiation Temperature

The lowest temperature that a liquid phase formed in the titanium-aluminium system and thus the initiation temperature, was 933.1K, the melting point of aluminium. $\Delta H_{f,933.1}(TiAl)$ was calculated accordingly:

$$\Delta H_{f,933.1}(TiAl) = \Delta H_{f,298}(TiAl) + \int_{298}^{933.1}[C_p(TiAl) - C_p(Ti) - C_p(Al)]dT + [-\underset{Ts<933.1}{L}(Al)_m]$$

The enthalpy of melting of aluminium, $L(Al)_m$ was included into the equation as the aluminium had to be molten to initiate the reactive synthesis. No corresponding term was included when calculating $\Delta H_{f,912.9}(NiAl)$ as the thermodynamic model could not accommodate intermediate phases. However, the calculations were not affected by this difference as $L(Al)_m$ was also included in the equation to calculate T_{ad} and the molar fraction of molten TiAl, in the term calculating the energy required to raise the reactants to the initiation temperature. This cancelled out $\Delta H_{f,933.1}(TiAl)$ in the above equation. $L(Al)_m$ was not present in either of the corresponding equations for NiAl:

$$-\Delta H_{f,933.1} = (1-x)\left[\int_{933.1}^{Tad} C_p(TiAl)dT + \nu L_m(TiAl) + \int_{Ts}^{933.1}[C_p(Ti) + C_p(Al)]dT + \underset{Ts<933.1}{L}(Al)_m\right] + x\left[\int_{Ts}^{Tad} C_p(Al_2O_3)dT\right]$$

T_{ad} and the molar fraction of liquid TiAl were calculated using the same method as for NiAl.

TiAl Formed at its Melting Point

The melting point of TiAl is 1733K and $\Delta H_{f,1733}(TiAl)$ was calculated as follows:

$$\Delta H_{f,1733}(TiAl) = \Delta H_{f,298}(TiAl) + \int_{298}^{1733}[C_p(TiAl) - C_p(Ti) - C_p(Al)]dT + [-L(Ti)_{ss}] + [-L(Al)_m]$$

It was assumed that solid TiAl was formed at 1733K and the energy released by its formation was used to melt it:

$$-\Delta H_{f,1733}(NiAl) = (1-x)\left[\int_{1733}^{Tad} C_p(TiAl)dT + \nu L(TiAl)_m + \int_{Ts}^{1733}[C_p(Ti) + C_p(Al)]dT + L(Ti)_{ss} + L(Al)_m\right] + x\left[\int_{Ts}^{Tad} C_p(Al_2O_3)dT\right]$$

Prop	T_{ss} (K)	L_{ss} (KJ/mol)	T_m (K)	L_m (KJ/mol)	$\Delta H_{f,298}$ (KJ/mol)	C_p (KJ/mol) a	b	c	Temp. range
Al	-	-	933.1	10.47	-	4.94	2.96	0.00	(298-933.1)
						7.00	0.00	0.00	(933.1-2767)
Ni	630	0.58	1726	17.16	-	4.06	7.04	0.00	(298-639)
						6.00	1.80	0.00	(630-1726)
						9.20	0.00	0.00	(1726-2200)
Ti	1155	3.34	1940	17.50	-	5.28	2.40	0.00	(298-1155)
						4.74	1.90	0.00	(1155-1350)
NiAl	-	-	1913	63.00	-118.50	10.00	3.30	0.00	(198-1913)
						17.00	0.00	0.00	(1913-2100)
TiAl	-	-	1733	60.00	-74.00	13.37	1.42	-1.80	(298-1733)
						15.00	0.00	0.00	(1733-2152)
Al_2O_3	-	-	2327	-	-	24.82	6.28	-6.95	(298-800)
						28.80	2.20	-11.56	(800-2327)

Selected thermodynamic data[28,59,72,135,136]

$C_p = 4.1868(a+b10^{-3}T+c10^{5}T^{-2})$

T_{ad} and the molar fraction of liquid TiAl were calculated using the same method as for NiAl.

A slightly higher NiAl melting point was used in this section compared to the one given in Section 1. This was a result of using different data sources.

Appendix D. Polishing Routines

The polishing routines of all the samples produced in this investigation are listed below. Wheel direction refers to the direction the surface rotated with respect to the rotating sample holder. Complementary (Comp) and both were rotating in the same direction, contrary (Contra) and they were rotating in opposite directions.

Sample Preparation Routines for Section 3

Diffusion couples (Fe-Al, Ni-Al, Ti-Al)
Sectioned on Abrasimet 2 using 06TRE wheel, mounted in conductive phenolic resin

Surface	Abrasive Type and Size	Load per Sample (lbs)	Wheel Speed (rpm)	Wheel Direction	Time (mins)
SiC Paper	P320	5	150	Comp	Till Plane
SiC Paper	P1000	5	150	Contra	4
Metlap 4	9μm OB	5	25	Comp	4
Texmet	3μm OB	5	240	Comp	4
Texmet	1μm OB	5	240	Comp	1.5
Chemomet	Colloidal Silica	2.5	80	Contra	1

Sample Preparation Routines for Section 4

Iron/nickel powders added to molten aluminium
Sectioned on Abrasimet 2 using 06TRE wheel, mounted in conductive phenolic resin

Surface	Abrasive Type and Size	Load per Sample (lbs)	Wheel Speed (rpm)	Wheel Direction	Time (mins)
SiC Paper	P320	5	150	Comp	Till Plane
SiC Paper	P1000	5	150	Comp	1
Metlap 4	9μm OB	5	25	Comp	4
Texmet	3μm OB	5	240	Comp	4
Texmet	1μm OB	5	240	Comp	4
Chemomet	Colloidal Silica	2.5	80	Comp	2

Titanium powder added to molten aluminium
Sectioned on Abrasimet 2 using 06TRE wheel, mounted in conductive phenolic resin

Surface	Abrasive Type and Size	Load per Sample (lbs)	Wheel Speed (rpm)	Wheel Direction	Time (mins)
SiC Paper	P320	5	150	Comp	Till Plane
Silk	3µm OB	5	240	Comp	4
Texmet	1µm OB	5	240	Comp	4
Chemomet	Colloidal Silica	2.5	80	Comp	1

Sample Preparation Routines for Section 5

Reacted titanium-aluminium powder mixture
Sectioned on Abrasimet 2 using 06TRE wheel, mounted in conductive phenolic resin, vacuum impregnated with epoxy resin

Surface	Abrasive Type and Size	Load per Sample (lbs)	Wheel Speed (rpm)	Wheel Direction	Time (mins)
SiC Paper	P200	5	150	Comp	Till Plane
SiC Paper	P320	5	150	Comp	2
Metlap 4	9µm OB	5	25	Contra	8
Texmet	PC 3µm WB + Colloidal Silica	5	240	Comp	8
Texmet	PC 1µm OB + Colloidal Silica	5	150	Comp	4
Chemomet	Colloidal Silica	2.5	80	Comp	1

Sample Preparation Routines for Section 6

Green Fe-Al, Ni-Al and Ti-Al powder compacts
Sectioned on Isomet 2000 using a diamond edged blade, vacuum impregnated with epoxy resin and mounted in conductive phenolic resin

Surface	Abrasive Type and Size	Load per Sample (lbs)	Wheel Speed (rpm)	Wheel Direction	Time (mins)
SiC Paper	P320	5	150	Comp	Till Plane
Perf Tex	9µm WB PC	5	240	Comp	4
RAM	3µm WB PC	5	240	Comp	4
Chemomet	Colloidal Silica	5	100	Comp	5

Reacted iron-aluminium powder compacts
Sectioned on Isomet 2000 using a diamond edged blade, mounted in conductive phenolic resin and vacuum impregnated with epoxy resin

Surface	Abrasive Type and Size	Load per Sample (lbs)	Wheel Speed (rpm)	Wheel Direction	Time (mins)
SiC Paper	P180	5	150	Comp	Till Plane
Metlap 4	9µm OB	5	25	Contra	8
Texmet	3µm WB PC + Colloidal Silica	5	240	Comp	8
Texmet	1µm WB PC + Colloidal Silica	5	240	Comp	4
Chemomet	Colloidal Silica	2.5	100	Comp	1

Reacted nickel-aluminium powder compacts
Sectioned on Isomet 2000 using a diamond edged blade, mounted in conductive phenolic resin and vacuum impregnated with epoxy resin

Surface	Abrasive Type and Size	Load per Sample (lbs)	Wheel Speed (rpm)	Wheel Direction	Time (mins)
SiC Paper	P180	5	150	Comp	Till Plane
Metlap 6	9µm OB	5	120	Comp	4
Nylon	3µm WB PC + Colloidal Silica	5	240	Comp	10
Texmet	1µm WB PC + Colloidal Silica	5	240	Comp	10
Chemomet	Colloidal Silica	2.5	100	Comp	2

Reacted titanium-aluminium powder compacts
Sectioned on Isomet 2000 using a diamond edged blade, mounted in conductive phenolic resin and vacuum impregnated with epoxy resin

Surface	Abrasive Type and Size	Load per Sample (lbs)	Wheel Speed (rpm)	Wheel Direction	Time (mins)
SiC Paper	P180	5	150	Comp	Till Plane
SiC Paper	P320	5	150	Comp	0.5
Metlap 4	9µm WB	5	25	Comp	4
Texmet	3µm WB	5	240	Comp	4
Texmet	1µm WB	5	240	Comp	4
Chemomet	Colloidal Silica	5	100	Comp	4

Sample Preparation Routines for Section 7

Green alumina reinforced powder compacts
Sectioned on Isomet 2000 using a diamond edged blade, vacuum impregnated with epoxy resin and mounted in conductive phenolic resin

Surface	Abrasive Type and Size	Load per Sample (lbs)	Wheel Speed (rpm)	Wheel Direction	Time (mins)
SiC Paper	P180 + wax	5	150	Comp	Till Plane
SiC Paper	P320 + wax	minimum	150	Comp	1
Perf Tex	9µm WB PC	5	240	Comp	4
Ultrapol	3µm WB PC	5	240	Comp	8
Chemomet	Colloidal Silica	5	100	Comp	3

Green silicon carbide reinforced powder compacts
Sectioned on Isomet 2000 using a diamond edged blade, vacuum impregnated with epoxy resin and mounted in conductive phenolic resin

Surface	Abrasive Type and Size	Load per Sample (lbs)	Wheel Speed (rpm)	Wheel Direction	Time (mins)
SiC Paper	P240 + wax	5	150	Comp	Till Plane
SiC Paper	P240 + wax	minimum	150	Comp	0.5
Metlap 4	9µm WB	5	25	Comp	4
Texmet	3µm WB	5	240	Comp	8
Chemomet	Colloidal Silica	5	100	Comp	3

Reacted nickel-aluminium-alumina powder compacts
Sectioned on Isomet 2000 using a diamond edged blade, mounted in conductive phenolic resin and vacuum impregnated with epoxy resin

Surface	Abrasive Type and Size	Load per Sample (lbs)	Wheel Speed (rpm)	Wheel Direction	Time (mins)
SiC Paper	P180	5	150	Comp	Till Plane
Metlap 10	15µm OB	5	120	Comp	8
Ultrapad	15µm WB	5	240	Comp	20
Ultrapol	6µm WB	5	240	Comp	15
Ultrapol	3µm WB	5	240	Comp	15
Chemomet	Colloidal Silica	5	100	Comp	1

Reacted titanium-aluminium-alumina powder compacts
Sectioned on Isomet 2000 using a diamond edged blade, mounted in conductive phenolic resin and vacuum impregnated with epoxy resin

Surface	Abrasive Type and Size	Load per Sample (lbs)	Wheel Speed (rpm)	Wheel Direction	Time (mins)
SiC Paper	P180	5	150	Comp	Till Plane
Metlap 4	9µm OB	5	25	Contra	5
Texmet	3µm WB PC	5	240	Comp	10
Ultrapol	1µm WB PC + Colloidal Silica	10	240	Comp	15
Chemomet	Colloidal Silica	2.5	100	Comp	2

Reacted nickel-aluminium-silicon carbide powder compacts
Sectioned on Isomet 2000 using a diamond edged blade, mounted in conductive phenolic resin and vacuum impregnated with epoxy resin

Surface	Abrasive Type and Size	Load per Sample (lbs)	Wheel Speed (rpm)	Wheel Direction	Time (mins)
SiC Paper	P180	5	150	Comp	Till Plane
Metlap 4	9µm OB	5	25	Comp	6
Texmet	3µm WB PC + Colloidal Silica	10	240	Comp	10
Texmet	1µm WB PC + Colloidal Silica	10	240	Comp	15
Chemomet	Colloidal Silica	2.5	100	Comp	2

Reacted titanium-aluminium-silicon carbide powder compacts
Sectioned on Isomet 2000 using a diamond edged blade, mounted in conductive phenolic resin and vacuum impregnated with epoxy resin

Surface	Abrasive Type and Size	Load per Sample (lbs)	Wheel Speed (rpm)	Wheel Direction	Time (mins)
SiC Paper	P180	5	150	Comp	Till Plane
Metlap 4	9µm OB	5	25	Contra	10
Texmet	3µm WB PC + Colloidal Silica	10	240	Comp	5
Chemomet	Colloidal Silica	5	100	Comp	1

Sample Preparation Routines for Section 8

Reacted nickel-aluminium-carbon/alumina compacts
Sectioned on Isomet 2000 using a diamond edged blade, mounted in conductive phenolic resin and vacuum impregnated with epoxy resin

Surface	Abrasive Type and Size	Load per Sample (lbs)	Wheel Speed (rpm)	Wheel Direction	Time (mins)
SiC Paper	P200	5	150	Comp	Till Plane
SiC Paper	P320	5	150	Comp	0.5
Metlap 4	9μm WB PC	5	25	Contra	4
Texmet	3μm WB PC	5	240	Comp	4
Chemomet	Colloidal Silica	5	100	Comp	2

Sample Preparation Routines for Section 9

Porous nickel preform
Sectioned on Isomet 2000 using a diamond edged blade, mounted in conductive phenolic resin and vacuum impregnated with epoxy resin

Surface	Abrasive Type and Size	Load per Sample (lbs)	Wheel Speed (rpm)	Wheel Direction	Time (mins)
SiC Paper	P240	5	150	Comp	Till Plane
Metlap 8	9μm OB	5	120	Comp	4
Metlap 4	9μm OB	5	50	Contra	4
Texmet	3μm OB	5	100	Comp	4
Texmet	Colloidal Silica	5	100	Contra	3
Mastertex	Colloidal Silica	2.5	80	Comp	4

Porous nickel/alumina preform
Sectioned on Isomet 2000 using a diamond edged blade, mounted in conductive phenolic resin and vacuum impregnated with epoxy resin

Surface	Abrasive Type and Size	Load per Sample (lbs)	Wheel Speed (rpm)	Wheel Direction	Time (mins)
SiC Paper	P320	5	150	Comp	Till Plane
Metlap 8	9µm OB	5	120	Comp	4
Metlap 4	9µm OB	5	50	Contra	4
Texmet	3µm OB	5	100	Comp	4
Texmet	Colloidal Silica	5	100	Contra	3
Chemomet	Colloidal Silica	5	100	Comp	3

Infiltrated nickel/alumina preform
Sectioned on Isomet 2000 using a diamond edged blade, mounted in conductive phenolic resin

Surface	Abrasive Type and Size	Load per Sample (lbs)	Wheel Speed (rpm)	Wheel Direction	Time (mins)
SiC Paper	P320	5	150	Comp	Till Plane
Perf Tex	9µm WB PC	5	240	Comp	4
Ultrapol	3µm WB PC	5	240	Comp	8
Chemomet	Colloidal Silica	5	100	Comp	3

Appendix E. Programme Listings

Calculation of Interfacial Lengths

To calculate the interfacial lengths between the transition metal and aluminium powders in the green compacts in Sections 6 and 7, the following macro was written for Optimas 6 image analysis software by Mr Mark Deven.

```
/* ========== CONTACT3a.MAC ==========================================
author:         Mark Deven, University of Bath, School of Materials Science.
date:           December-1996
comments:       This macro prompts for stored images from a file and uses the GetAutoThreshold()
ALI function (previous versions called Athld.mac) to calculate thresholds for two phases of a three
phase image (ignores pore phase ). It then processes the first phase and builds an outline of the phase;
this is stored in Arithmetic Ops. The second phase is similarly processed and logically ANDed with
the first to give an image of common interface. Line lengths are autocreated and shown overlayed on
the original image. Calibrated line lengths are extracted and summed and displayed in message box.
Note: this macro utilises Optimas6 functionality and can only be run under windows95/optimas6.
Calls           NONE
Version         3a
================================================================== */

MacroMessage ("This is the Interfacial Contact Macro Version 3a.\n\t MJD 6/12/96.");

OpenConfiguration ("C:\\OPTIMAS6\\config\\Default.cfg");// add the relevant .cfg

/* Image Placement */
NewImageOnFileOpenOptions[ 0 ] = -2;
ImageFileDestinationRoi = 1;
ImageFilePlaceSource = 0;
ImageFileScaling = 3;
/* High Bit Active Luminance Range */
FileActiveRangeMethod = 2 : -1 : 0 : 0;
FileOpenLuminanceCast = 2;
/* High Bit Viewed Luminance Range */
NewViewedRangeMethod = 3 : -1 : 0 : 0;
KeepExistingViewedRange = FALSE;

ClearScreen ();
OpenImage ();

if ( Prompt( "The current calibration is " : ActiveCalibration
                        : ".\nDo you want to change it?",0x1002) )/*yes/no buttons, no as default */
        {
                Calibrate(); /* call up dialog if user wants to calibrate */
                ChangeCursor ();/* Back to pointer */
                while( IsWindow("Calibrate Spatial") ) ; /* do nothing til closed */
        }

// Copy image to ArithOps
```

```
StatusBar = "Storing Image...";
ROIToList (, "Original Image");


/***** Get the AutoThreshold values for three phases *****/
/***** 6 = Minimise within segment variance (method of Otsu). *****/
/***** 3 = Suggested number of threshold pairs to find. *****/

REAL rPairs[,];

Histogram();
rPairs = GetAutoThreshold(ArROIHistogram,6,3,,ActiveLuminanceRange,);
if ( rPairs && 2 < GetShape(rPairs)[0] )

                {
                        // successful autothreshold

                        cLuminance = ToText(rPairs[1,0]:rPairs[1,1]);
                        StatusBar = "Threshold for Dark phase set at " : cLuminance;


                        /***** Process Dark phase first *****/

                        StatusBar = "Finding Dark phase...";
                        GrayToBinary (,rPairs[1,0],rPairs[1,1]);

                        BINB_iIterations = 2;
                        //  Binary Opening [erode then dilate]
                        ErodeFilter(,BINB_iIterations,128,255);
                        DilateFilter(,BINB_iIterations,128,255);

                        OutlineFilter(,128,255);

                        BINB_iIterations = 1;
                        //Increase line thickness to give contact between phases
                        DilateFilter(,BINB_iIterations,128,255);

                        //Copy the outline image to ArithOps
                        StatusBar = "Storing Image.";
                        ROIToList (, "Dark phase outline");
                        ArithmeticOp ("Copy", "Original Image", , , "Clip", FALSE, FALSE);

                        /************************END*****************************/


                        /**** Process Light phase ****/

                        cLuminance = ToText(rPairs[2,0]:rPairs[2,1]);
                        StatusBar = "Threshold for Light phase set at " : cLuminance;

                        StatusBar = "Finding Light phase...";
                        GrayToBinary (,rPairs[2,0],rPairs[2,1]);

                        BINB_iIterations = 2;
                        //  Binary Opening [erode then dilate]
                        ErodeFilter(,BINB_iIterations,128,255);
                        DilateFilter(,BINB_iIterations,128,255);
```

```
                    OutlineFilter(,128,255);

                    BINB_iIterations = 1;
                    //Increase line thickness to give contact between phases
                    DilateFilter(,BINB_iIterations,128,255);

                    //Copy the outline image to ArithOps
                    StatusBar = "Finding shared interface...";
                    ROIToList (, "Light phase outline");
                    ArithmeticOp ("And", "Dark phase outline", , , "Clip", FALSE, FALSE);

                    /************************END*****************************/
                }

else            {
                    Delete(rPairs);
                    Pause();
                    // end it here!

                }

/*****Set No of phases to binary and find light phase*****/
Histogram();
rPairs      =       GetAutoThreshold(ArROIHistogram[0..(VectorLength(ArROIHistogram)-1)]      :
0,6,2,,ActiveLuminanceRange,);
if ( rPairs && 1 < GetShape(rPairs)[0] )
                {
                    // successful autothreshold

                    Threshold(rPairs[1,0]:rPairs[1,1]);

                    CreateLine (, , TRUE);
                    StatusBar = "Copying back original image.";
                    ArithmeticOp ("Copy", "Original Image", , , "Clip", FALSE, FALSE);

                    SetExport (mLnLength, 2, TRUE);
                    MultipleExtractAll (TRUE);

                    /* Show the result */
                    MacroMessage("The Total Interface for your Image
                                        is\n\t",Sum(mLnLength),
                    GetOrSetField(ActiveCalibration, 103),);
                }

/*****delete variables and stored images*****/

                Delete (BINB_iIterations);
                Delete (rPairs);
                Delete (cLuminance);
                DeleteImage ("Dark phase outline");
                DeleteImage ("Light phase outline");
                DeleteImage ("Original Image");

        /************************THE END*****************************/
```

Temperature Recording Programme

The programme used to record the time/temperature profiles of the thermal explosions in Sections 6 and 7 was written by Mr Simon Bowman and is listed below.

```
#include <conio.h>
#include <dos.h>
#include <bios.h>
#include <stdlib.h>
#include <stdio.h>
#include <string.h>
#include "textlib.h"
#include "pc27.h"

const int ESC = 0x011B;
const int CTRLS = 0x1F13;
const int B_KEY = 0x3000;

#define PRE             50
#define FIRE    2000


// Base interrupt time is 1mS

const int pretime = 100;    // Milliseconds
#if defined SHORTTIME
const int firetime = 10;   // 20 seconds collection
#else
const int firetime = 20;    // 40 seconds collection
#endif

int Time = 300;                 // Initial timer

extern ValueReady;
extern Value;

//
//      Temperatures breaks bins for 12 bit acquisition 4V range
//      gain = 100. These are 16 bit bins for 4V biploar
//

int degrees[] =    {0, 52, 97, 137, 175, 210, 245, 278,
                                        310, 342, 372, 403, 432, 462, 491, 519,
                                        548, 575, 604, 631, 658, 684, 711, 737,
                                        763, 789, 815, 840, 864, 889, 913, 937,
                                        962, 986, 1009, 1033, 1057, 1080, 1102, 1125,
                                        1148, 1169, 1193, 1216, 1238, 1260, 1283, 1305,
                                        1327, 1349, 1371, 1393, 1415, 1438, 1460, 1482,
                                        1504, 1526, 1549, 1571, 1593, 1615, 1638, 1661,
                                        1684, 1707, 1731, 1754};

int elements = sizeof(degrees)/sizeof(degrees[0]) - 1;

int GetKey(void);
char filename[96];
int pretrigger[PRE];            // Value before fire (5 secs at 10 per sec)
```

```
int data[FIRE];                    // 20 secs at 100 per sec
void ExitProgram ();

void main(int argc, char *argv[])
{
        int key;
        int i, T;
        float perbit;

        SetChannel(0);                    // Use channel 0
        SetPC27ClockRate();  // Interrupt every 1ms

        if (argc != 2)      {
                cputs("Usage: EXO filename");
                return;
        }
        strcpy(filename,argv[1]);

        FILE *f = fopen(filename, "rb");
        if (f) {
                puts("File already exists!");
                return;
        }
        fclose(f);

        if ((f = fopen(filename, "wb")) == NULL) {
                puts("Unable to create file");
                return;
        }

        cursoff();
        clrscr();

        gotoxy(22, 10);
        cputs("Temperature = ");
        gotoxy(22, 12);
        cputs("Press B to begin acquisition");
        gotoxy(20, 14);
        cputs("Press Ctrl+S to halt acquisition");

        SetVector(5);
        EnableIRQ(5);

        do {
                if (ValueReady) {
                        i = Value/16;              // Get array index into lookup table
                        if (i > elements-1)
                                T = degrees[elements];
                        else {
                                perbit = (degrees[i+1] - degrees[i])/16.0; // C/bit
                                T = perbit * (Value - i*16) + degrees[i];
                        }
                        gotoxy(36, 10);
                        cprintf("%-4i", T);
                        ValueReady = 0;
                }
                key = GetKey();
                if (key == ESC || key == CTRLS) {
```

```
                unlink(filename);
                ExitProgram();;
        }
} while ((key & 0xFF00) != B_KEY);

clrscr();

gotoxy(27,12);
cputs("Loading pre-trigger array");

do {
        if (ValueReady == 1)
                break;
} while (1);

Time = pretime;
ValueReady = 0;


for (i = 0; i < PRE; i++) { // Load the pretrigger array
        do {
                if (ValueReady == 1)
                        break;
        } while (1);
        pretrigger[i] = Value;
        ValueReady = 0;
}

clrscr();

gotoxy(22,12);
cputs("Temperature = ");

int fire = 0;
int abort = 0;
int j = 0;

while (!abort && !fire)    {
        if (ValueReady) {
                memmove(&pretrigger[0], &pretrigger[1], sizeof(int)*(PRE-1));
                pretrigger[PRE-1] = Value;
                ValueReady = 0;
                if (pretrigger[PRE-1] - pretrigger[PRE-11] > 12) {    // About 10C at 600C
                        fire = 1;
                        Time = firetime;
                        break;
                }
                if (GetKey() == CTRLS) {
                        abort = 1;
                        break;
                }
                if (j++ == 10)     {
                        j = 0;
                        i = pretrigger[PRE-1]/16;
                        if (i > elements-1)
                                T = degrees[elements];
                        else {
                                perbit = (degrees[i+1] - degrees[i])/16.0; // C/bit
```

```
                                        T = perbit * (pretrigger[PRE-1] - i*16) + degrees[i];
                                }
                                gotoxy(36, 12);
                                cprintf("%-4i", T);
                        }
                }
        }

        if (fire) {
                gotoxy(22,14);
                cputs("Collecting data");
                for (i = 0; i < FIRE; i++) {
                        do {
                                if (ValueReady == 1)
                                        break;
                        } while (1);
                        data[i] = Value;
                        ValueReady = 0;
                }
                float time = 0;
                for (j = 0; j < PRE; j++) {
                        i = pretrigger[j]/16;
                        if (i > elements-1)
                                T = degrees[elements];
                        else {
                                perbit = (degrees[i+1] - degrees[i])/16.0; // C/bit
                                T = perbit * (pretrigger[j] - i*16) + degrees[i];
                        }
                        fprintf(f, "%-4.2f, %i\r\n", time, T);
                        time += (float)pretime/1000;
                }
                for (j = 0; j < FIRE; j++) {
                        i = data[j]/16;
                        if (i > elements-1)
                                T = degrees[elements];
                        else {
                                perbit = (degrees[i+1] - degrees[i])/16.0; // C/bit
                                T = perbit * (data[j] - i*16) + degrees[i];
                        }
                        fprintf(f, "%-4.2f, %i\r\n", time, T);
                        time += (float)firetime/1000;
                }
                fclose(f);
        }
        ExitProgram();
}

void ExitProgram ()
{
        curson();
        DisableIRQ(5);
        RestoreVector(5);
        exit(0);
}

int GetKey(void)
{
        if (bioskey(1) == 0)
```

```
                return 0;
        else
                return bioskey(0);
}
```

Appendix F. Engineering Drawings

Engineering drawings of the apparatus used to prepare and react powder compacts are displayed in this section.

The die in which the powders were compacted in Section 6 to 9 is shown in the first two drawings.

Die-i and die-ii are included in the next two drawings.

The final three drawings cover the die used for liquid metal infiltration in Section 9.

Die Wall

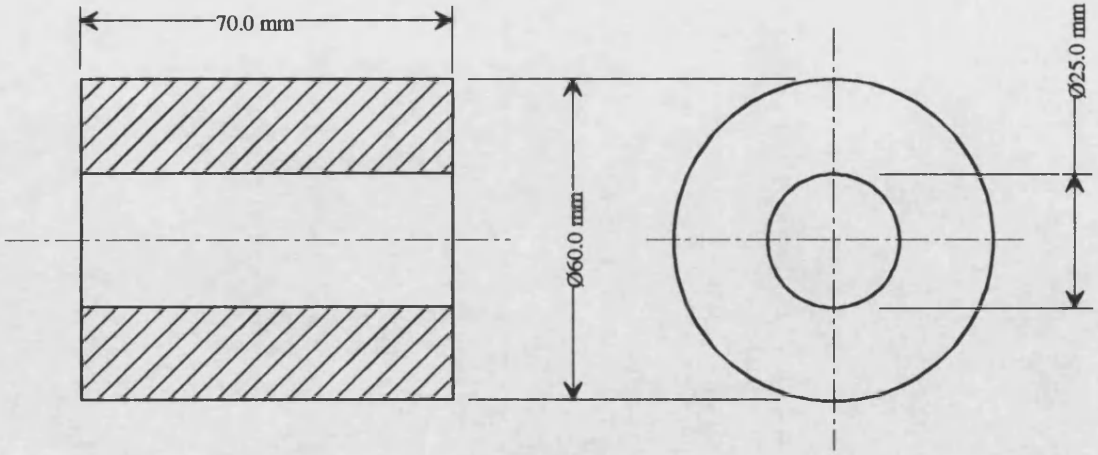

Plug

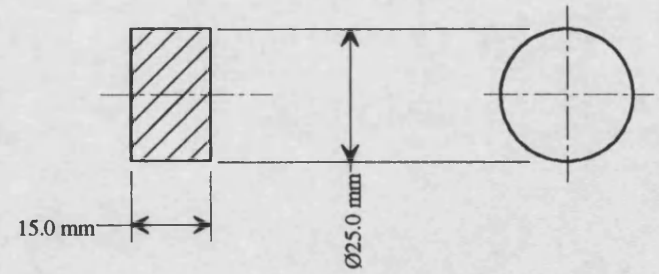

Platen to have a normal run (f7) fit within the 25mmØ bore

Powder Compactor	D. Palmer	1993-97	Scale 7:10	Dimensions: mm
Tolerances: ±0.2mm	Material: H13 Tool Steel (Heat treated)		Finish: Bore and insert as smooth as possible, remaining surfaces machine turned finish.	

End Plate

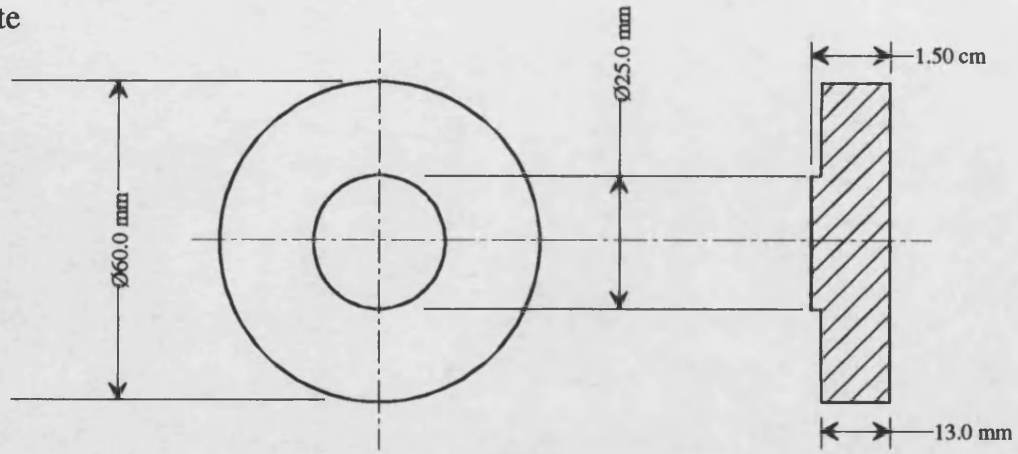

End plate to have a normal run (f7) fit within the 25mmØ bore

Plunger

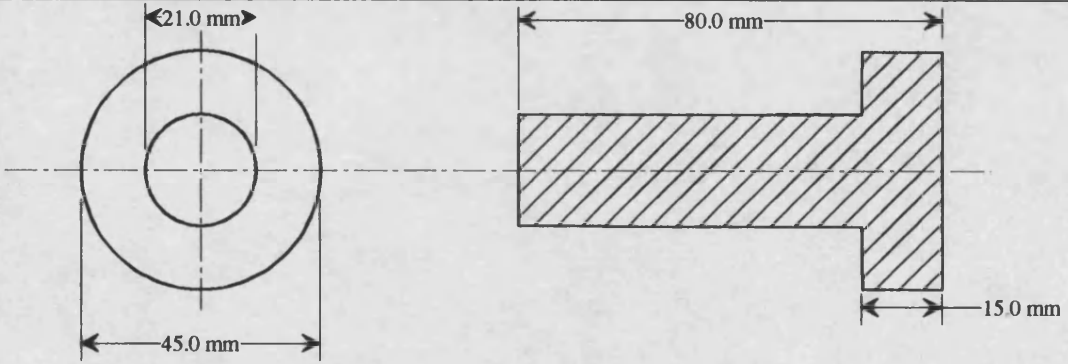

Powder Compactor	D. Palmer	1993-97	Scale 7:10	Dimensions: mm
Tolerances: ±0.2mm	Material: H13 Tool Steel (Heat treated)		Finish: Surfaces machine turned finish.	

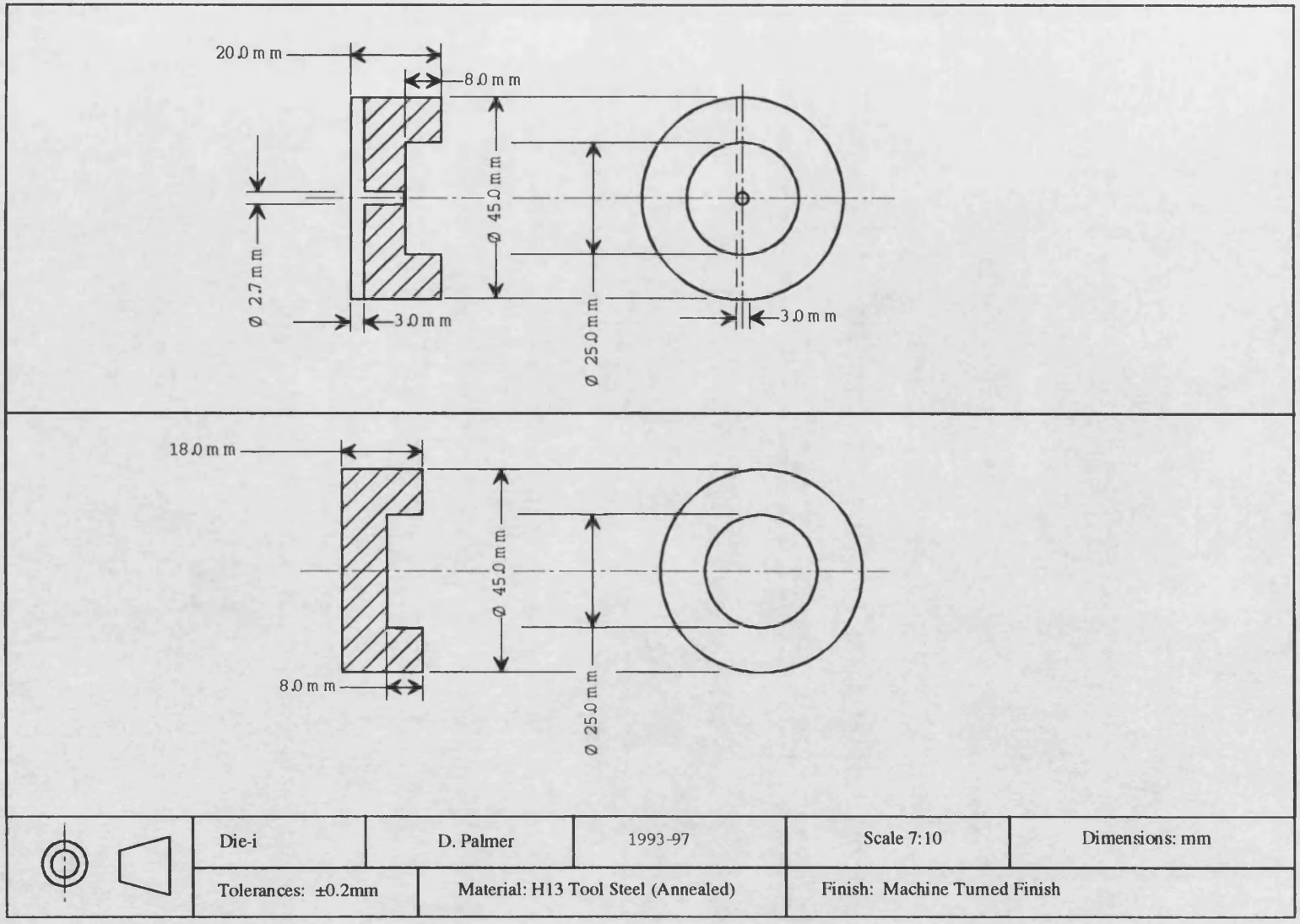

Die-i	D. Palmer	1993-97	Scale 7:10	Dimensions: mm
Tolerances: ±0.2mm	Material: H13 Tool Steel (Annealed)		Finish: Machine Turned Finish	

Die Wall

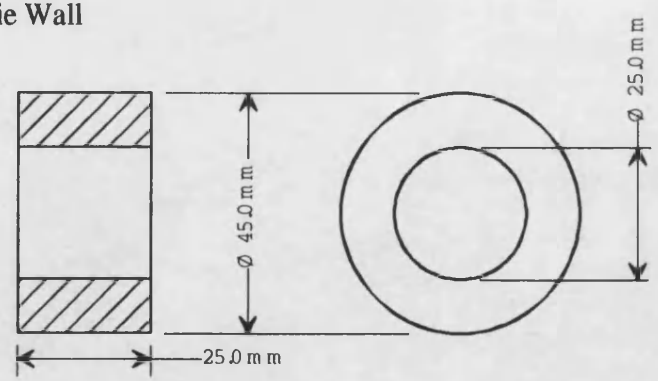

Plunger

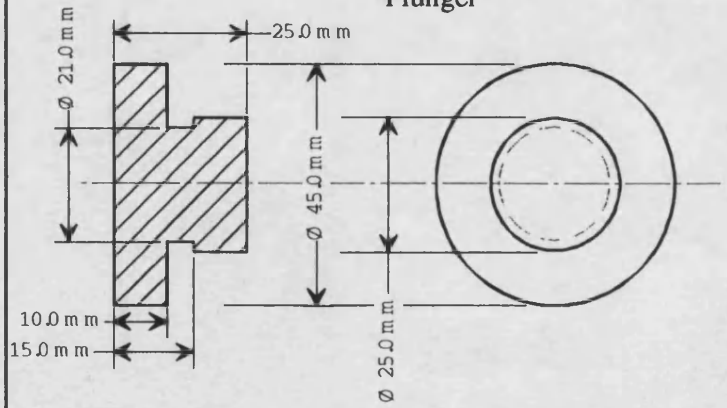

Ø 25.0mm to have k6 fit into bore of die wall

End Plate

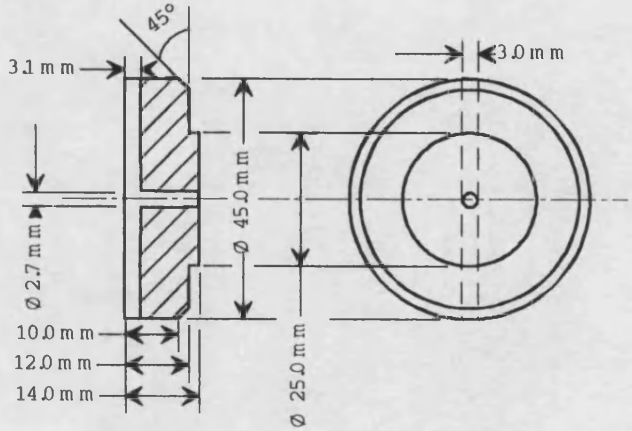

Ø 25.0mm to have a f7 fit into bore of die wall

	Die-ii.	D. Palmer	1993-97	Scale 7:10	Dimensions: mm
	Tolerances: ±0.2mm	Material: H13 Tool Steel (Heat Annealed)	Finish: Machine Turned Finish		

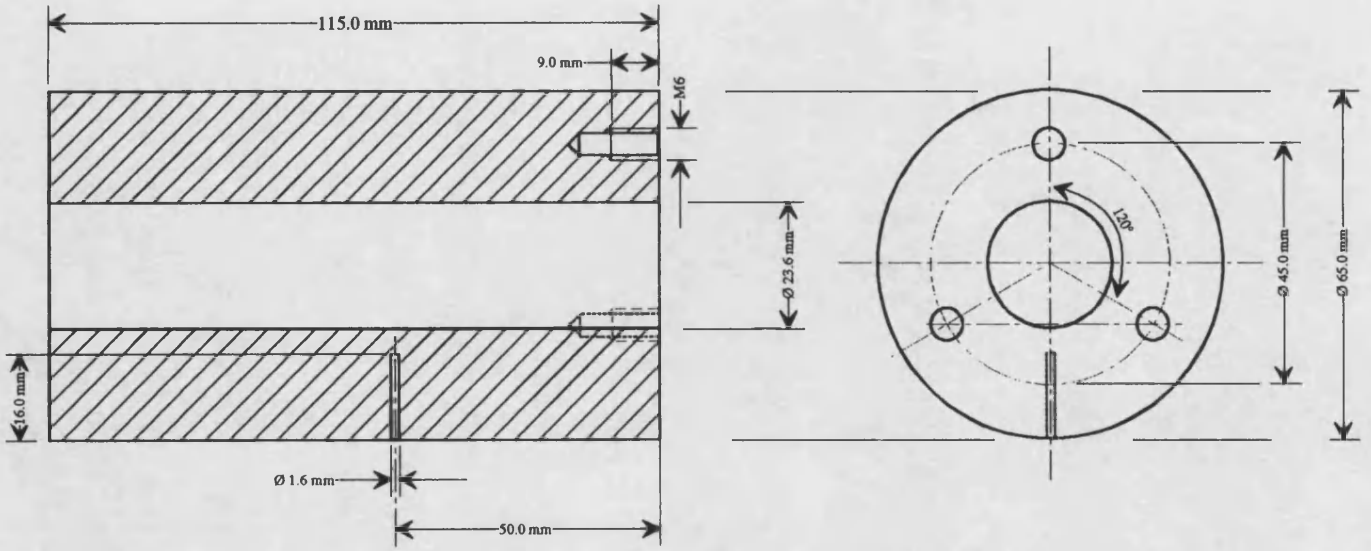

LMI Body	D. Palmer	1993-97	Scale 7:10	Dimensions: mm
Tolerances: ±0.2mm	Material: Silver Steel		Finish: Bore Ground Finish, Rest Machine Turned Finish	

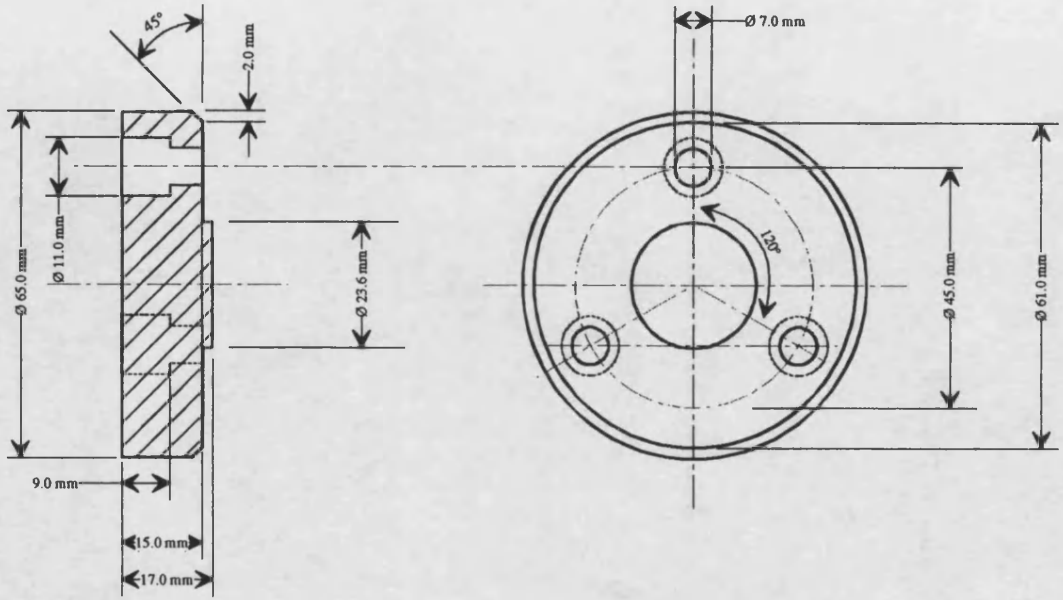

Note: 23.6mm Ø projection, free run fit (e9) into bore in body

	LMI End Plate	D. Palmer	1993-97	Scale 7:10	Dimensions: mm
	Tolerances: ±0.2mm	Material: Silver Steel		Finish: Machine Turned Finish	

Plug

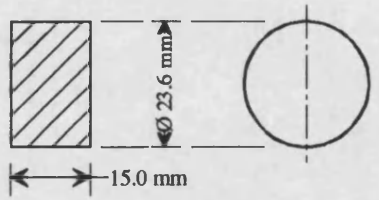

Disc to have a H8 push fit into bore in drawing 1.

Plunger

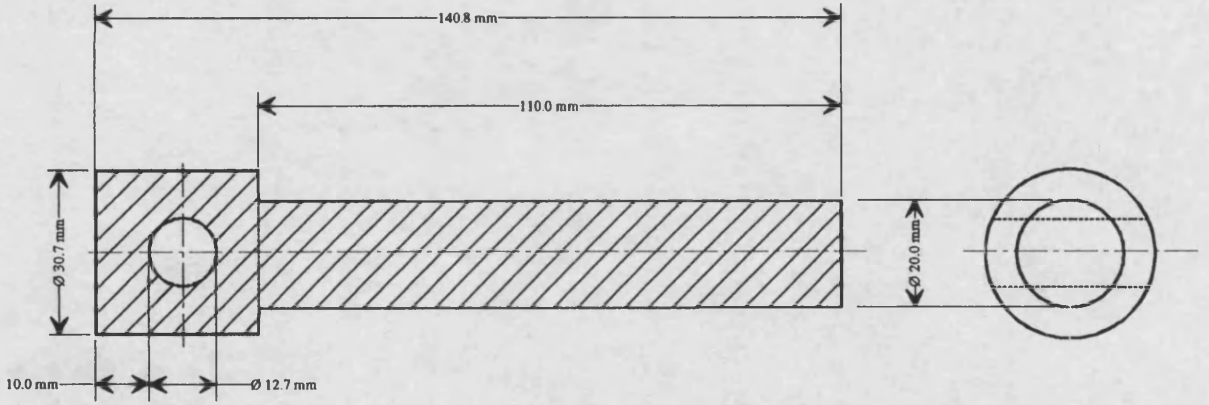

	LMI Plug & Plunger	D. Palmer	1993-97	Scale 7:10	Dimensions: mm
	Tolerances: ±0.2mm	Material: Silver Steel		Finish: Ground Finish	